

FINAL REPORT

Vapor Intrusion From Entrapped NAPL Sources and Groundwater Plumes: Process Understanding and Improved Modeling Tools for Pathway Assessment

SERDP Project ER-1687

July 2014

Tissa Illangasekare
Benjamin Petri
Radek Fučík
Carolyn Sauck
Luke Shannon
Toshihiro Sakaki
Kathleen Smits
Abdullah Cihan
John Christ
Paul Schulte
Brent Putman
Yaoguo Li
Colorado School of Mines

Distribution Statement A

This document has been cleared for public release



REPORT DOCUMENTATION PAGE

Form Approved
OMB No. 0704-0188

Public reporting burden for this collection of information is estimated to average 1 hour per response, including the time for reviewing instructions, searching existing data sources, gathering and maintaining the data needed, and completing and reviewing this collection of information. Send comments regarding this burden estimate or any other aspect of this collection of information, including suggestions for reducing this burden to Department of Defense, Washington Headquarters Services, Directorate for Information Operations and Reports (0704-0188), 1215 Jefferson Davis Highway, Suite 1204, Arlington, VA 22202-4302. Respondents should be aware that notwithstanding any other provision of law, no person shall be subject to any penalty for failing to comply with a collection of information if it does not display a currently valid OMB control number. **PLEASE DO NOT RETURN YOUR FORM TO THE ABOVE ADDRESS.**

1. REPORT DATE (DD-MM-YYYY) 15/05/2014	2. REPORT TYPE Draft Final Report	3. DATES COVERED (From - To) April 2009- July 2014
--	---	--

4. TITLE AND SUBTITLE Vapor Intrusion From Entrapped NAPL Sources and Groundwater Plumes - Process Understanding and Improved Modeling Tools for Pathway Assessment	5a. CONTRACT NUMBER
	5b. GRANT NUMBER
	5c. PROGRAM ELEMENT NUMBER

6. AUTHOR(S) Illangasekare, Tissa H; Petri, Benjamin; Fučík, Radek; Sauck, Carolyn; Shannon, Luke; Sakaki, Toshihiro; Smits, Kathleen; Cihan, Abdullah; Christ, John; Schulte, Paul; Putman, Brent; Li, Yaoguo.	5d. PROJECT NUMBER ER-1687
	5e. TASK NUMBER
	5f. WORK UNIT NUMBER

7. PERFORMING ORGANIZATION NAME(S) AND ADDRESS(ES) Colorado School of Mines, Center for Experimental Study of Subsurface Environmental Processes 1500 Illinois Street Golden, Colorado 80401	8. PERFORMING ORGANIZATION REPORT NUMBER
--	---

9. SPONSORING / MONITORING AGENCY NAME(S) AND ADDRESS(ES)	10. SPONSOR/MONITOR'S ACRONYM(S)
	11. SPONSOR/MONITOR'S REPORT NUMBER(S)

12. DISTRIBUTION / AVAILABILITY STATEMENT
Approved for Public Release, Distribution is Unlimited

13. SUPPLEMENTARY NOTES

14. ABSTRACT
Factors that contribute to the uncertainty and variability of measured vapor concentrations in buildings and structures resulting from subsurface VOC sources were investigated. Mechanisms controlling vapor generation and subsequent migration through the subsurface in naturally heterogeneous subsurface under various physical and climatic conditions were investigated using laboratory and modeling studies. Experiments were conducted in test systems varying from bench to intermediate scale. Concurrently with the experiments, modeling tools were developed. This research established that subsurface vapor pathways are dynamic and complex, sometimes contributing to counter-intuitive cause-effect relationships. Infiltration was found to affect vapor signals in indoor air, with the time-scales and the strength of the vapor signals depending on the interplay of the intensity, duration of rainfall, and subsurface heterogeneity. Water table fluctuation imparts very complex transport behavior within the capillary fringe that has significant effects on vapor loading from the groundwater plumes that defied simplified models used in screening. Trapped sources in the unsaturated zone are capable of loading significant mass into the unsaturated zone, but the loading rate is a strong function of the moisture distribution in the vicinity of the source. Indoor sampling strategies need to factor in the transients associated with climate and weather. This has to be done in conjunction with subsurface characterization methods to identify potential dynamic pathways. Novel characterization methods such as electrical

15. SUBJECT TERMS
Vapor intrusion; volatile organics; indoor air quality; improved conceptual models; monitoring strategies

16. SECURITY CLASSIFICATION OF:			17. LIMITATION OF ABSTRACT	18. NUMBER OF PAGES 188	19a. NAME OF RESPONSIBLE PERSON
a. REPORT	b. ABSTRACT	c. THIS PAGE			19b. TELEPHONE NUMBER (include area code)

This report was prepared under contract to the Department of Defense Strategic Environmental Research and Development Program (SERDP). The publication of this report does not indicate endorsement by the Department of Defense, nor should the contents be construed as reflecting the official policy or position of the Department of Defense. Reference herein to any specific commercial product, process, or service by trade name, trademark, manufacturer, or otherwise, does not necessarily constitute or imply its endorsement, recommendation, or favoring by the Department of Defense.

Table of Contents

LIST OF ACRONYMS	viii
MATHEMATICAL NOMENCLATURE	x
LIST OF FIGURES	xi
LIST OF TABLES	xv
ACKNOWLEDGEMENTS	xvi
ABSTRACT.....	xvii
1. INTRODUCTION	1
1.0. Introduction.....	1
1.1. Relevant Background.....	1
1.2. Research Questions.....	4
1.3. Project objectives and approach.....	5
1.4. References.....	6
2. BACKGROUND	9
2.0. Introduction.....	9
2.1. Present Standard of Practice for Vapor Intrusion Assessment	9
2.1.1. Vapor attenuation and “attenuation factors”	10
2.2. Scientific fundamentals of vapor transport	10
2.2.1. Advective transport	11
2.2.2. Diffusive and dispersive transport	13
2.2.3. Reactive transport processes	14
2.2.4. Effects of heterogeneity and the built environment	18
2.3. Current models of vapor intrusion	19
2.3.1. Analytical models of VI.....	20
2.3.2. Numerical modeling studies of VI	24
2.4. Enhanced characterization methods.....	26
2.5. Limitations of the current knowledge base.....	27
2.6. References.....	27
3. MODELING APPROACHES	39
3.0. Introduction.....	39
3.1. Current and proposed VI models	39

3.2. Modeling approaches	40
3.3. General model formulation	41
3.4. References	44
4. MATERIALS AND METHODS	47
4.1. Project approach.....	47
4.2. General Analytical Methods and Materials	47
4.2.1. Apparatus	47
4.2.2. Analytical Methods	48
4.2.3. Common Materials.....	50
4.3. NAPL Volatilization Experiments	51
4.3.1. Objectives.....	51
4.3.2. Apparatus and approach	51
4.3.3. Case 1 “occluded” NAPL experimental procedure.....	54
4.3.4. Case 1 “exposed” NAPL experimental procedure	55
4.4. Capillary fringe volatilization experiments	55
4.4.1. Objectives.....	55
4.4.2. Apparatus	55
4.4.3. Experimental procedure	57
4.5. Soil moisture dynamic experiments with heat and rain	58
4.5.1. Objective	58
4.5.2. Apparatus	59
4.5.3. Experimental Procedure	61
4.6. Integrated dynamic flow and vapor transport experiments.....	62
4.6.1. Objective	62
4.6.2. Apparatus	62
4.6.3. Experimental Procedure	65
4.7. Geophysical tank experiment.....	68
4.7.1. Objectives.....	68
4.7.2. Apparatus	68
4.7.3. Experimental Procedure	69
4.8. Site demonstration of infiltration effect	70
4.8.1. Objective	70
4.8.2. Site background.....	71

4.8.3. Technical Approach	72
4.9. Scenario Simulations	74
4.9.1. Approach	74
4.10. References	76
5. RESULTS AND DISCUSSION	79
5.0. Introduction	79
5.1. Vadose zone NAPL volatilization experiments	79
5.1.1. Occluded NAPL experimental results (case 1)	79
5.1.2. Comparison of experimental and numerical results for occluded NAPL case	81
5.1.3. Exposed source experimental results (case 2)	83
5.2. Capillary fringe volatilization experiments	86
5.3. Dynamic air pathway experiments	89
5.3.1. Infiltration experiment results	90
5.3.2. Heat experiment results	92
5.3.3. Comparison to numerical results	93
5.3.4. Case Studies with Different Degrees of Heterogeneity	96
5.3.5. Discussion	98
5.4. Integrated dynamic flow and vapor transport experiments	100
5.4.1. Homogeneous case	100
5.4.2. Heterogeneous case	108
5.4.3. Mass balance calculations	109
5.5. Model analysis of rain infiltration and water table fluctuation experiments	111
5.5.1. Model testing	111
5.5.2. Steady-state analysis of the intermediate scale tank system	113
5.5.3. Rainfall infiltration simulation	118
5.5.4. Water table fluctuation simulation	121
5.6. Two-dimensional geophysical tank experiment	127
5.7. Site demonstration of geophysical methods and observation of infiltration effect	137
5.7.1. Site-specific historical soil moisture events	138
5.7.2. Observed temperature and soil moisture content values	139
5.7.3. ERT inversions	139
5.7.4. Comparison of ERT inversions to VI signal observations	141

5.8. Practical implications of transient vapor dynamics through simulation of hypothetical scenarios	143
5.8.1. Scenario characteristics and steady-state simulation	145
5.8.2. Rainfall scenarios	148
5.8.3. Water table reduction scenarios	151
5.9. References	154
6. SUMMARY, CONCLUSIONS AND RECOMMENDATIONS.....	157
6.1. Summary of research	157
6.2. General conclusions	159
6.3. Practical implications	162
6.4. Recommendations for future work	164
APPENDIX A: SUPPORTING DATA	166
A.1. Introduction	166
A.2. Data sets from integrated dynamic flow and vapor transport experiments	166
A.3. Development and testing of an efficient model for simulation of vapor transport	167
APPENDIX B: LIST OF SCIENTIFIC/TECHNICAL PUBLICATIONS....	185

List of Acronyms

2-D	-	Two dimensional
3-D	-	Three dimensional
AER	-	Air exchange rate (in a house or building)
AFB	-	Air Force Base
AFCEE	-	Air Force Center for Engineering and the Environment
BTX	-	Benzene, toluene, and xylene
°C	-	degrees Celsius
CDPHE	-	Colorado Department of Public Health and Environment
CERCLA	-	Comprehensive Environmental Response, Compensation, and Liability Act
CESEP	-	Center for Experimental Study of Subsurface Environmental Processes
cm	-	Centimeter
COMSOL	-	COMSOL Multiphysics v3.5a (finite element method simulator)
CSM	-	Colorado School of Mines
DC	-	Direct Current
DCE	-	Dichloroethylene
D.I.	-	deionized water
DNAPL	-	dense nonaqueous phase liquid
DOD	-	Department of Defense
DOE	-	Department of Energy
DURIP	-	Defense University Research Instrumentation Program
EM	-	Electromagnetic
EPA	-	Environmental Protection Agency
Eqn.	-	equation
ERT	-	Electrical resistivity tomography
ESTCP	-	Environmental Security Technology Certification Program
ET	-	Evapotranspiration
FEHM	-	Finite Element Heat and Mass Transfer Code
GC	-	gas chromatography
GW	-	ground water
hr	-	hour
IP	-	Induced Polarization
ITRC	-	Interstate Technology Regulatory Council
JE	-	Johnson and Ettinger
m	-	Meter
MCL	-	maximum concentration limits
min	-	minutes
MODFLOW	-	Modular groundwater model
mos	-	months
NAPL	-	nonaqueous phase liquid
NSF	-	National Science Foundation
PCE	-	tetrachloroethylene
RCRA	-	Resource Conservation and Recovery Act
TDR	-	Time Domain Reflectometry
SERDP	-	Strategic Environmental Research and Development Program

SLPM	-	Standard Liters Per Minute (mass flow rate of a gas corrected to standard temperature (25°C) and pressure (1 atm))
SON	-	Statement of Need
SVE	-	soil vapor extraction
TCE	-	Trichloroethylene
USAF	-	United States Air Force
USEPA	-	United States Environmental Protection Agency
VI	-	Vapor intrusion
VOC	-	Volatile Organic Compounds
Yr	-	Year
mL	-	milliliter

Mathematical Nomenclature

ρ_b	-	bulk density
ρ_w	-	water density
ρ_g	-	density of the gas phase
θ_w	-	volumetric water content
θ_g	-	volumetric gas content
ϕ	-	porosity
S_w	-	water saturation
S_g	-	gas saturation
S_n	-	NAPL saturation
P_w	-	pressure of water
P_g	-	pressure of gas
P_c	-	capillary pressure
q_w	-	Darcy flux for water
q_g	-	Darcy flux for gas
k_i	-	intrinsic permeability
k_{rw}	-	water relative permeability
k_{rg}	-	gas relative permeability
μ_w	-	viscosity of water
μ_g	-	viscosity of gas
R	-	gas constant
T	-	temperature
M_w	-	molecular weight of water
M_a	-	molecular weight of air
M_n	-	molecular weight of NAPL
α_L	-	longitudinal dispersivity (m)
α_T	-	transverse dispersivity (m)
α	-	van Genuchten parameter [1/cm] or attenuation coefficient [1]
n	-	van Genuchten parameter
R_{gw}^w	-	mass transfer term for water vapor between water and gas phases
R_{gw}^n	-	mass transfer term for NAPL vapor between the gas and water phases
R_{wn}^n	-	mass transfer term for NAPL dissolution between NAPL and water phases
a	-	subscript for air phase
w	-	subscript for water phase
n	-	subscript for NAPL phase
w_i	-	mass ratio for each component (mass of component i divided by total mass)
$D_{m,i}$	-	molecular diffusion coefficient of NAPL in phase i ($m^2 s^{-1}$)
$\delta_{i,j}$	-	Kronecker Delta function.
H_T	-	dimensionless Henry's Law constant corrected for system temperature T (K)
C_b	-	effective heat capacity per unit volume of soil
C_w	-	specific heat capacity of water
C_g	-	specific heat capacity of gas
C_s	-	specific heat capacity of solid phase
λ_T	-	effective thermal conductivity
L	-	latent heat coefficient.

List of Figures

Figure 1.1:	Conceptual model of the vapor intrusion pathway and related zones	3
Figure 1.2:	Flow chart depicting approach of the ER-1687 project	6
Figure 2.1:	Process based conceptual model of the vapor intrusion pathway.....	11
Figure 2.2:	Illustrations of the surface conditions of a VI site in an urban / suburban setting.....	19
Figure 3.1:	Current pathway conceptual model of the subsurface component of the VI pathway	40
Figure 4.1:	Conceptual diagram of NAPL source configurations within the vadose zone pore space.....	52
Figure 4.2:	Experimental Apparatus and Tank Packing for NAPL volatilization experiments.....	53
Figure 4.3:	Schematic of capillary fringe volatilization experimental apparatus.....	56
Figure 4.4:	Capillary fringe volatilization experiments packing configuration and cases 1-4 description.....	57
Figure 4.5:	Primary drainage, secondary drainage, and wetting curves for #20/30 Accusand.....	57
Figure 4.6:	Aqueous phase sampling locations within the tank.	58
Figure 4.7:	Schematic view of the two-dimensional tank for dynamic soil moisture experiments	60
Figure 4.8:	Photo of the two-dimensional tank.	60
Figure 4.9:	Conceptual model for intermediate scale tank for integrated dynamic flow and vapor transport experiments with tank schematic.....	63
Figure 4.10:	Detailed schematic of tank design and configuration	63
Figure 4.11:	Photo of the tank apparatus.....	64
Figure 4.12:	Schematic of the geophysical tank experiment apparatus	69
Figure 4.13:	Schematic of geophysical sand tank packing configurations	70
Figure 4.14:	Map with field demonstration site location (indicated by red star) located adjacent to Hill AFB, UT	71
Figure 4.15:	Schematic of VI monitoring locations with exterior and interior monitoring points and ERT profiles indicated.	72
Figure 4.16:	Schematic of subsurface geologic composition at field demonstration site in Utah.....	73
Figure 4.17:	Schematic of water table elevations across field demonstration site.....	73

Figure 5.1:	Measured TCE effluent vapor concentration versus time for occluded NAPL experiments	80
Figure 5.2:	Comparison of steady-state model with steady-state experimental effluent concentration values for case 1 runs.	82
Figure 5.3:	Simulated concentration profile and diffusion / dispersion tensor magnitude profile for run #12.....	83
Figure 5.4:	Concentration versus time for exposed source NAPL systems	84
Figure 5.5:	Estimated van Genuchten saturation, Mualem air and water relative permeability and Millington-Quirk effective diffusivity curves for the 20/30 Accusand	87
Figure 5.6:	Effluent vapor concentration over time for all 4 cases.	88
Figure 5.7:	Aqueous TCE concentrations in the capillary fringe from experiment 3.	89
Figure 5.8:	Soil water saturation by layer and total surface flow fraction (Rainfall experiment).	91
Figure 5.9:	Total air inflow, individual layer air outflow rates and precipitation rate (Rainfall experiment)	91
Figure 5.10:	Soil water saturation and surface flow fraction (Heat experiment).	92
Figure 5.11:	Air inflow and outflow rates and precipitation rate (Heat experiment).....	93
Figure 5.12:	Vertical water saturation profile along sensor array C at $t = 3$ hours (when the rainfall stopped) and at $t = 9$ hours.	94
Figure 5.13:	Soil water saturation distribution and air flow field (left) $t = 3$ hours, (right) $t = 9$ hours.....	94
Figure 5.14:	Transient change in soil water saturation in layers 1-4 in column C.....	95
Figure 5.15:	Transient change in airflow rates	96
Figure 5.16:	Schematic images of air flow pathway dynamics under different climatic conditions at the soil surface.....	97
Figure 5.17:	Fraction of subsurface- and surface-origin air flows under varied degree of heterogeneity (soil property contrast).	98
Figure 5.18:	Effluent vapor concentrations over the entire 106 day homogeneous experiment.	101
Figure 5.19:	Observed average air pressure distributions for high flow and medium flow periods.....	103
Figure 5.20:	TCE airflow concentrations and water saturations a sensor array 5 during water table fluctuation three (WT3).....	105
Figure 5.21:	TCE airflow concentrations, water saturations, airflow, and air pressure data from rain event 2 (R2)	107
Figure 5.22:	Effluent vapor concentrations over the entire 106 day heterogeneous experiment.....	109

Figure 5.23:	COMSOL model and C++ model compared to each other simulating the experiments in section 5.1.....	111
Figure 5.24:	COMSOL model compared against McCarthy and Johnson (1996) data and analytical model.....	113
Figure 5.25:	Effect of friction losses on airflow streamlines within the tank	115
Figure 5.26:	Simulated vs. observed data for airflow rates in the 4 flux chambers.	116
Figure 5.27:	Water saturation profiles for model(s) and experimental data as a function of sensor array elevation	119
Figure 5.28:	Comparison of model and experimental concentration responses in the effluent airflow from the tank	121
Figure 5.29:	Model and experimental comparison of mean soil moisture values in array 5 during the water table fluctuation event.....	123
Figure 5.30:	Comparison of experiment and model for TCE concentrations at tank outlet. ...	124
Figure 5.31:	Comparison of water saturations at array 5 for the hysteresis model, non-hysteresis model and data for the water table rise.	125
Figure 5.32:	Model and experiment comparison for only water table reduction.	126
Figure 5.33:	Mass balance and boundary fluxes from the model for the water table reduction.....	127
Figure 5.34:	Schematic of packing configuration #1 and the calibrated volumetric moisture content data with the water table set at the upper, mid and lower elevations.....	129
Figure 5.35:	Schematic of packing configuration #2 and the calibrated volumetric moisture content data with the water table set at the upper, mid and lower elevations.....	130
Figure 5.36:	Schematic of packing configuration #3 and the calibrated volumetric moisture content data with the water table set at the upper, mid and lower elevations.....	131
Figure 5.37:	Schematic of packing configuration #1 and the soil gas diffusivity simulations with the water table set at the upper, mid and lower elevations.	132
Figure 5.38:	Schematic of packing configuration #2 and the soil gas diffusivity simulations with the water table set at the upper, mid and lower elevations.	133
Figure 5.39:	Schematic of packing configuration #3 and the soil gas diffusivity simulations with the water table set at the upper, mid and lower elevations.	134
Figure 5.40:	Schematic of packing configuration #1 and the ERT inversions with the water table set at the upper, mid and lower elevations.	135
Figure 5.41:	Schematic of packing configuration #2 and the ERT inversions with the water table set at the upper, mid and lower elevations.	136
Figure 5.42:	Schematic of packing configuration #3 and the ERT inversions with the water table set at the upper, mid and lower elevations.	137
Figure 5.43:	MET station precipitation data from field site and statistical analysis of local precipitation events from field site.	138

Figure 5.44:	Temperature and volumetric moisture content changes in response to simulated moisture event.....	139
Figure 5.45:	Time-series snap shots of ERT surveys capturing initial site conditions and the infiltrating wetting front induced by our simulated precipitation event	140
Figure 5.46:	Graph of the VI signal entering study site building over a five-day window that included our field demonstration and simulated precipitation event	142
Figure 5.47:	Graph of the VI signal entering study site building over 1-day window during our ERT field demonstration with ERT time-series snap shots overlaid on the VI signal timeline.....	142
Figure 5.48:	Timescales of typical hydrologic cycle dynamic events and remediation activities.....	144
Figure 5.49:	Steady-state initial condition for scenarios	146
Figure 5.50:	Effect of rainfall intensity on TCE concentrations of soil gas entering the building.....	148
Figure 5.51:	Scenarios showing effect of precipitation rate on airflow rate into a building....	149
Figure 5.52:	Effect of infiltration at 1 mm/hr for 24 hours on vapor signals in sandy clay loam scenario.	150
Figure 5.53:	Effect of water table drop rate on subslab vapor concentrations	151
Figure 5.54:	Effect of water table depth on subslab vapor concentrations from a water table dropping at a rate of 1 m/year in sandy soil.....	152
Figure 5.55:	Effect of water table reduction on airflow rate. Initial water table depth is 3m and sandy soil media.....	153

List of Tables

Table 2.1:	Summary of Analytical Models Addressing VI.....	21
Table 2.2:	Numerical Models of Vapor Intrusion.....	22
Table 4.1:	Characteristics of experimental apparatus	48
Table 4.2:	Properties of Porous Media used in this study ¹	50
Table 4.3:	Trichloroethylene Properties at 20°C (Cowen and Mercer, 1993)	51
Table 4.4:	Experimental test cases for capillary fringe experiments	58
Table 4.5:	Homogeneous case water table fluctuations and rain events.....	66
Table 4.6:	Heterogeneous test cases.....	67
Table 4.7:	Proposed scenarios demonstrating the effect of individual processes on vapor intrusion	75
Table 5.1:	Summary of experimental results	81
Table 5.2:	Volatilization Mass Transfer Correlations.....	85
Table 5.3:	Experimental Results Cases 1-4.....	87
Table 5.4:	Airflow in atmospheric chambers during steady-state periods (SLPM).....	103
Table 5.5:	Comparison of model fit to mean steady-state air pressure values as a function of airflow	116
Table 5.6:	Characteristics differentiating this study’s model from previous scenario simulations	143
Table 5.7:	Soil properties of media used in scenario simulations.....	147
Table 5.8:	Water table fluctuation scenarios.....	153
Table 6.1:	Practical implications of weather and climate factors for VI.	163
Table 6.2:	Factors suggested for future analysis.....	165

Acknowledgements

The authors gratefully acknowledge the support through Strategic Environmental Research and Development Program (SERDP) Grant ER-1687. The research team also wishes to acknowledge the programmatic support provided by SERDP program managers and the staff of HydroGeoLogic, Inc. The experimental research required the extensive use of existing testing facilities at the Center for Experimental Study of Subsurface Environmental Processes (CESEP) at Colorado School of Mines. A number of funding sources provided support to develop this facility. These includes past SERDP funding (CU-1294), National Science Foundation, Army Research Office, DoD's Defense University Research Instrumentation Program (DURIP), National Security Science and Engineering Faculty Fellows (NSSEFF) program through Air Force office for Scientific Research (AFOSR) and AMAX Endowment through Colorado School of Mines.

Czech Science Foundation, Transport in Subsurface Environmental Applications KONTAKT ME10009, Czech Ministry of Education, Youth and Sports for providing funding for partial support for Dr. Radek Fučík for the model development. Michal Beneš, Prof. Dr. Ing., Czech Technical University in Prague, Faculty of Nuclear Sciences and Physical Engineering, Department of Mathematic provided useful guidance in the model development effort.

The authors also gratefully acknowledge and thank Professor Paul Johnson, Arizona State University, Research Assistant Professor Hong Luo, and their research group for the access provided to the field site at Hill Air Force Base and assistance to conduct the geophysical study.

The authors are also grateful to the U.S. Air Force Academy, who provided funding for cadets Michael Glatthar, who assisted in our laboratory in summer 2011.

The help provided by undergraduate student, Alex Maul, Department of Mechanical Engineering at Colorado School of Mines in designing the intermediate test tank is gratefully acknowledged.

ABSTRACT

Objectives

This research addressed the problem of intrusion of hazardous chemical vapors from subsurface sources to surface and subsurface structures. Volatile organic compounds (VOC) are commonly found entrapped as non-aqueous phase liquids (NAPLs) in the soil pores or dissolved in groundwater at industrial waste sites, refineries and DOE and DOD complexes. Vapors emitted from these contaminant sources readily disperse into the atmosphere, into air-filled void spaces within the soil, and migrate below surface structures, leading to the intrusion of contaminant vapors into indoor air. Although it has been recognized for some time that VI is potential exposure pathway, a complete understanding of the basic mechanisms and methods to characterize have been lacking. Existing approaches to managing the VI pathway have often neglected the complex factors associated with the atmosphere-subsurface boundary, a dynamic water table at the unsaturated-saturated zone interface, subsurface heterogeneity, and NAPL source zone conditions. These may significantly influence VI behavior, suggesting a need to evaluate whether existing knowledge is directly transferable to VI studies. *The primary objective of this completed study was to improve our understanding of factors that contribute to the uncertainty and variability of measured vapor concentrations in subsurface buildings and structures resulting from subsurface VOC sources.* Mechanisms controlling vapor generation and subsequent migration through the subsurface in naturally heterogeneous subsurface under various physical and climatic conditions were investigated using laboratory and modeling studies. The viability of using shallow surface geophysical methods for the identification of VI pathways was investigated.

Technical Approach

The basic premise under which the technical study was planned was that it is not feasible to control and quantify all the climatic and hydrogeologic factors that contribute to the VI in field settings to get accurate data to improve our basic understanding. Also, findings from site-specific case studies cannot be generalized for all sites with diverse climate and geology. Experiments were conducted in test systems varying from small bench scale to intermediate scale. The bench scale experiments were designed to obtain data for the improvement of fundamental process understanding. Experiments conducted in a 16-ft long, highly instrumented intermediate scale tank integrated vapor generation, transport and intrusion under the influence of rainfall, water table fluctuation and NAPL volatilization. Concurrently with the experiments, research level modeling tools were developed to interpret data and to obtain new insights for improving conceptual understanding and to provide the basis for the development of more comprehensive models. Even though it was not within the scope of this project, the development of a comprehensive model that can be used for predictions was initiated. The research models that were tested for their ability to capture the responses observed in the experiments were used to conduct a limited set of hypothetical scenario simulations with the goal of demonstrating the practical implications of the research findings that will lead to guideline development and better monitoring of VI sites.

Results/Findings

The results of the study clearly demonstrated that numerical modeling based on improved conceptual models and observations in the intermediate scale test tanks were informative to understand the processes that govern VI in complex systems. This research established that subsurface VI pathways are dynamic and complex, sometimes contributing to counter-intuitive

cause-effect relationships. If these relationships are not well understood, it will lead to deficient monitoring strategies, wrong interpretation of monitoring data, poor decision-making, and risk assessment. The complexity can be attributed to the interaction of climate and geologic heterogeneity. The naturally heterogeneous soil profile controls the rates of wetting front propagation and transient soil moisture distribution during and after a precipitation event. The propagating front triggers the movement of the vapor in the soil pores partitioned from the contaminated soil-water. The rate at which the vapor eventually moves to the building depends on the relative permeability of the air phase that directly depends on the dynamics of the spatial distribution of the soil moisture. The time-scales and the strength of the vapor signals observed in indoor air will depend on the interplay of the intensity and duration of the rainfall event and the site-specific subsurface heterogeneity. Even though the specific scenarios of pavements around the building was not investigated, some of the tank studies where soil at the land surface was kept at high saturation resulting in capping the soil, resulted in the air that potentially carry the vapor from subsurface sources preferentially moving through the subsurface to the building. This suggests that the urban infrastructure associated with the building will have an effect on the VI pathway development.

Another finding of this work that has important practical implications is that water table fluctuation imparts very complex transport behavior within the capillary fringe that has significant effects on vapor loading from the groundwater plumes that defied simplified models used in screening. The results demonstrate the important role capillary fringe plays in loading of contaminant mass from the groundwater plume to the VI pathway in the unsaturated zone. The capillary fringe is a critical interface between the saturated zone containing the dissolved contaminant and the unsaturated zone with potential VI pathways. As diffusion through the capillary fringe creates rate-limited conditions, the primary mechanism that contributes to temporal variability is the fluctuation of the water table, but not necessarily the concentrations in the groundwater plume.

Trapped NAPL sources in the unsaturated zone are capable of loading significant mass into the unsaturated zone, but the loading rate is a strong function of the moisture distribution within and in the vicinity of the source, suggesting again the importance of climate factors in vapor generation. Intermediate scale experiments suggested that climate and weather dependent transient thermal boundary conditions at the soil surface would not have any significant effects on subsurface vapor transport. Shallow surface geophysical methods may have the potential to provide tracking of soil moisture distributions in field soils, but further development is needed.

The findings from this study have implications on monitoring VI sites and buildings. Sampling strategies need to factor in the transients associated with climate and weather. This has to be done in conjunction with subsurface characterization methods to identify potential preferential pathways that are dynamic.

Benefits

At the time this project was initiated, little was known about the practical effect of weather and climate factors affecting VI and indoor air quality. The new knowledge gained has lead to improved conceptual models of the pathway, giving insights into how these factors influence VI. Benefits to the DOD include improved management guidance for VI sites, ultimately leading to the reduction in risk to subsurface structures and homes plagued by indoor air pollution issues, and more informed regulatory decision-making on contaminant clean-up levels. The research also has provided the foundation to develop comprehensive models that after field validation can be used for prediction and monitoring and remediation design.

Chapter 1: Introduction

1.0 Introduction

The intrusion of vapor phase contamination into buildings from contaminated soil and groundwater represents a potential risk to human health that has received increased attention at remediation sites. Protocols for screening, monitoring and mitigating this exposure pathway have been developed and implemented. However, spatial and temporal variability in indoor air concentrations continue to make assessment of this pathway difficult. It has been hypothesized that factors such as weather, climate, subsurface heterogeneity, and water table dynamics may be among the contributors to spatial and temporal variability. Yet few studies, either laboratory or field, have evaluated these factors in a controlled manner, and there are few datasets upon which to validate mathematical models of VI, especially against the dynamic systems that impart temporal variability. The project described in this report was initiated to explore the role these factors may play in the VI pathway through laboratory experimentation at varied scales, development and application of numerical models, and a field demonstration in collaboration with another project (SERDP project ER-1686). While a majority of scientific studies of vapor intrusion emphasize field site data collection or modeling investigations, this project is unique in that it contains a large laboratory experimental component. Experimentation was employed because a great deal of control over conditions may be obtained at the laboratory scale that is lost at the field scale, including factors such as infiltration rates, water table fluctuations, soil heterogeneity and others. The advantage of experimentation over a modeling-only approach is that experiments inherently contain the physical processes at play during vapor migration, whereas models must be built on assumptions about physical theory. The approach used in this project explores experiments and models as complementary so that both physical and theoretical aspects of the VI pathway may be validated. The result is a yield of important observations of vapor plume dynamics and intrusion behavior under the influence of water table fluctuations, rain events, NAPL and dissolved phase contaminant sources, and spatially heterogeneous soil properties. These observations in turn support the development of an improved conceptual model of the vapor intrusion pathway, and improved site decision-making and modeling. This new knowledge and tools will help in better addressing the problems of VI in risk assessment, monitoring and remediation.

1.1 Relevant Background

Historically, much of the subsurface contamination and remediation attention has focused on water contamination and water-related exposure pathways that pose risks to human health. Many remedial actions focused on reducing the threat to groundwater or surface water supplies by targeting maximum contaminant levels (MCLs) promulgated by USEPA for drinking water as remediation standards. However, less attention was traditionally given to vapor phase contamination, which may contaminate indoor air in homes and businesses overlying contaminated soil and groundwater. This is referred to as the vapor intrusion (VI) exposure pathway, which describes the transport of volatile contaminant vapors from subsurface sources through foundations and into buildings, whereupon the vapors mix with the indoor air causing an inhalation pathway risk. Though this exposure pathway has long been recognized (Nazeroff et al.

1987; Johnson and Ettinger, 1991; Moseley and Meyer, 1992), several high profile VI sites have prompted a more thorough evaluation of the VI pathway, especially in the last decade (Moseley and Meyer, 1992; Obmascik, 2000; Fitzpatrick and Fitzgerald, 2002; GSI 2007; Folkes et al. 2009). According to ITRC (2007) guidelines, “*state and federal regulators are now in the process of examining older remedial decisions involving groundwater contamination to assess whether the vapor intrusion pathway warrants reopening closed cases.*” New regulatory drivers require that the potential for VI be evaluated when volatile chemicals are present in soil or groundwater in the vicinity of homes and businesses (USEPA, 2002; CDPHE, 2004; ITRC, 2007, USDoD 2009). This regulatory and public interest has turned vapor intrusion into a major consideration in the management of contaminated lands. It is now common for remediation project managers to screen buildings around contaminated lands for VI risk, and follow through with indoor air sampling and mitigation measures for buildings with a confirmed VI problem.

The primary focus of these VI investigations has been on VOCs commonly found at industrial sites, gas stations, drycleaners, refineries and DOE and DOD complexes. These waste chemicals may be entrapped as non-aqueous phase liquids (NAPLs) in the subsurface, sorbed to soil solids, or dissolved in groundwater. The vapor phase can readily disperse into air-filled void spaces within the soil, migrate below surface structures or disperse into the atmosphere. Because many building foundations contain construction joints, cracks, openings, and unfinished crawl spaces, vapor can enter the building through a combination of advection and diffusion through these openings (Johnson and Ettinger, 1991). Significant soil gas advection in the vicinity of a building can occur due to heating and ventilation equipment, as well as atmospheric pressure fluctuations (Nazaroff et al. 1987). All of these factors combine to complete the vapor intrusion pathway, which is illustrated in figure 1.1.

However, despite the renewed emphasis on vapor intrusion and additional data collection (especially indoor air sampling), wide variability observed in the field (McHugh et al. 2004; McHugh et al. 2007; Folkes et al. 2009) raises questions over how to identify buildings with a VI risk and which factors control the VI pathway. Regulatory guidance emphasizes use of screening values based on the Johnson and Ettinger (1991) model to assist in determining which buildings to investigate for VI. This is generally implemented with default values for the “attenuation coefficient,” which expresses the estimated indoor air concentration as a fraction of the source concentration (ITRC 2007, USDoD 2009). Buildings that exceed the allowable indoor concentration based on the default attenuation coefficient are often targeted for indoor air sampling. However, indoor air data gathered from VI investigations often show wide spatial and temporal variability, and values depart significantly from the Johnson and Ettinger model (McHugh et al. 2004; McHugh et al. 2007; Folkes et al. 2009). Field studies have indicated that the existence of an identifiable source of contamination does not necessarily lead to higher indoor air concentrations (Olson and Corsi 2002), suggesting that other factors also contribute to indoor contaminant concentrations. This has led to higher decision uncertainty about VI risk to specific buildings, and research is needed to investigate the sources of this uncertainty.

A number of studies explored factors related to buildings, such as interior background sources and variation in building construction (Abreu and Johnson, 2005; McHugh et al. 2006; Mills et al. 2007; Dawson and McAlary 2009; Gorder and Dettenmaier, 2011). These factors that contribute to variability raise challenges for the “building-centric” approach to VI assessment that often focuses on indoor air sampling. As a result, in a USEPA review article, Tillman and

Weaver (2005) state, “due to difficulty in conclusively identifying the soil-to-indoor pathway via indoor sampling, researchers have suggested moving the focus of VI investigations outside the home.” This suggests the need for a more thorough understanding of subsurface processes that lead to vapor intrusion and sources of variability that influence VI. Yet relatively little information is available on the sources of variability in the VI pathway that originate outside the home. Based on limited field observations, weather and climate factors have been suggested to play a role in temporal variability, and heterogeneity a role in spatial variability, but their cause effect relationships are not well delineated.

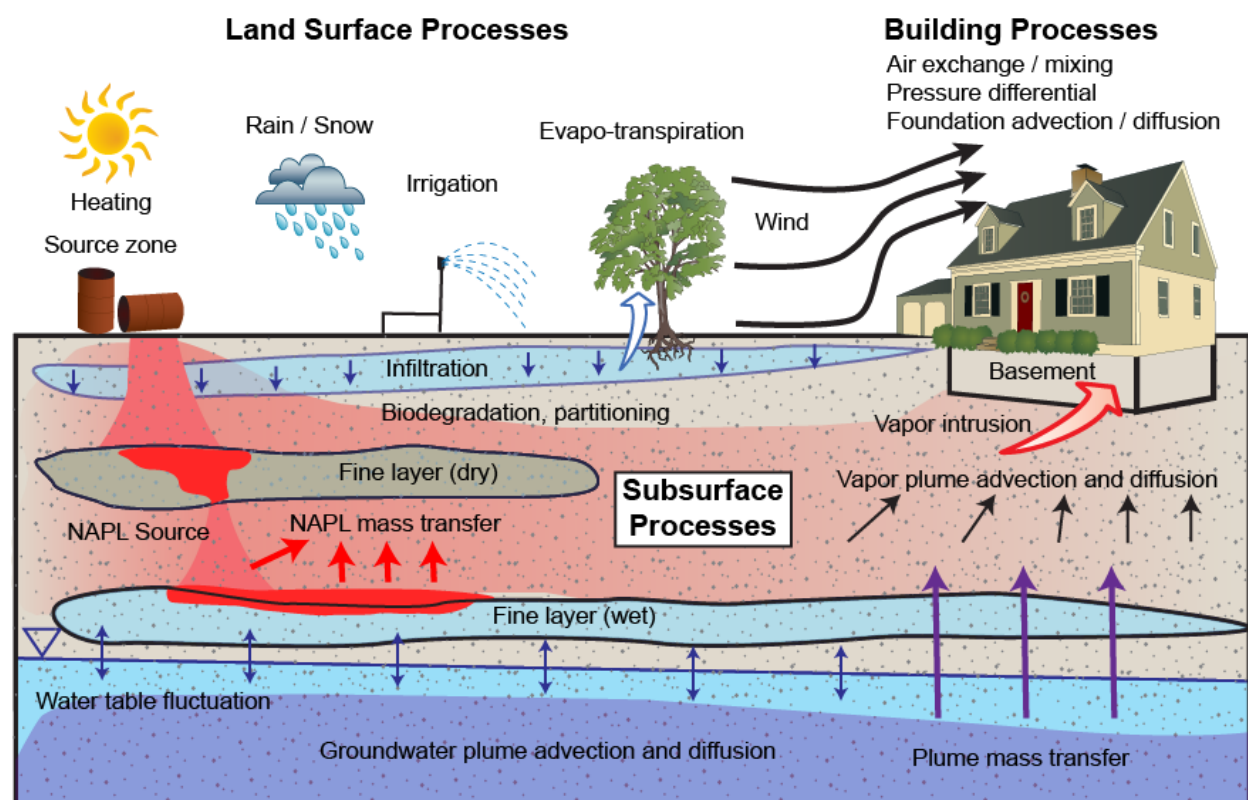


Figure 1.1: Conceptual model of the vapor intrusion pathway and related zones.

As with other applications involving risk assessment, analytical and numerical models that simulate the basic processes that govern vapor transport can play a role in VI analysis. One limitation of commonly used VI models, many of which were developed some time ago, is that they typically assume steady-state and often homogenous conditions in the subsurface, which has the effect of overlooking spatial and temporal variability. However, such variability has often been observed when sampling indoor air in houses and buildings (Johnston, 2012). *Spatial variability* reflected by differences in vapor concentrations varying from house to house can be the result of a number of factors that include naturally occurring variability of soil properties and vadose zone boundary conditions (Hers et al., 2000; Folkes et al., 2009; Bozkurt et al., 2009). *Temporal variability* may result from transient heat, wind, ambient pressure and water flux boundary conditions at the land-atmospheric interface (Folkes et al., 2009; Luo et al., 2009; Johnston, 2012). Fluctuating water table conditions controlled by recharge, pumping, and stream-aquifer interactions may also contribute to the transient vapor flux generation at the sources (McCarthy and Johnson, 1993; Thomson et al., 1997). A number of physical and geo-chemical processes may attenuate the vapor in the subsurface along the pathways from the

sources to the building. Figure 1.1 identifies four zones that influence the contaminant pathway: (1) the groundwater zone, which typically is the source of contaminant vapors, (2) the vadose zone where vapor migration primarily occurs, (3) the atmospheric zone where vapor and water fluxes enter or exit the vadose zone, and (4) the building zone which represents the risk receptor. Though these four zones are delineated separately, they are highly coupled to each other and these couplings are essential to include in the design of an effective research approach. Further exploration of the processes between these zones is necessary to build better conceptual models of the VI pathway, and understand the causes and effects of variability along the VI pathway.

1.2 Research Questions

A considerable knowledge base already exists in surface and subsurface hydrology, irrigation water management and subsurface remediation (e.g. soil vapor extraction and air sparging). This knowledge can be used to address basic scientific questions, and to develop new technologies and models for applications. However, existing approaches to managing the VI pathway have often neglected the complex factors associated with the atmosphere-subsurface boundary, a dynamic water table at the unsaturated-saturated zone interface, subsurface heterogeneity, and NAPL source zone conditions. These may significantly influence VI behavior, suggesting a need to evaluate whether existing knowledge is directly transferable to VI studies. In this context, a set of questions evolved into a research plan and methods to evaluate the effect of these complex factors on VI.

- Is the assumption of equilibrium interphase partitioning (i.e., volatilization) between the NAPL, water and/or gas phases appropriate in VI scenarios with environmentally relevant gas-phase pressure gradients?
- Do dynamic water table fluctuations affect VOC volatilization, and hence the contaminant mass flux generated at a significant level?
- Do changes in the air/water interface area at pore-scale due to dynamic water table fluctuations significantly affect the rate and amount of contaminant partitioning to the gas phase?
- Will changes in conditions at the land-atmosphere interface due to climate change (e.g., severe storms, wider range of temperature variability) significantly influence the potential for VI?
- Do dynamic effects associated with short-term changes in weather conditions (wind velocity, pressure fluctuations, temperature, diurnal cycles, heat flux, etc.) at the land surface (land-atmospheric interface) significantly affect soil moisture and hence air permeability, particularly through high air permeable preferential channels?
- What are the limitations of screening models such as the ones that have been developed by Johnson and Ettinger (1991) for pathway assessment? Are there ways to incorporate more comprehensive models in the VI decision-making process that can capture the relevant processes and yield meaningful insights?
- If more sophisticated modeling methods are needed, what new site characterization and monitoring methods need to be developed to obtain necessary input parameters? Can

these new, more sophisticated models, be employed to re-design simplified screening tools?

1.3 Project objectives and approach

To probe the research questions posed in section 1.2, a series of experimental and modeling tasks were completed. The main objective of this work was an improved understanding of the processes and mechanisms controlling vapor generation from entrapped NAPL sources and groundwater plumes, their subsequent migration through the subsurface, and their attenuation in naturally heterogeneous vadose zones under various natural physical, climatic, and geochemical conditions. Experiments conducted at multiple scales were integrated with analytical and numerical modeling and field data to test new and existing VI theories and models. The section below presents a summary of the methodology used for each task. More details are documented in the chapters to follow in the report. Figure 1.2 presents a flow chart for the project approach.

- 1) **Studies of vapor generation** – *Objective: Obtain a fundamental understanding of the mechanisms of vapor generation from source zones (NAPL and dissolved) under varying hydrogeologic and climatic conditions.* This task investigated the nature of mass transfer (i.e. vapor generation) from NAPL sources and dissolved phase VOC plumes through experiments and modeling. In particular, the roles of soil moisture and water table dynamics were explored for their impact on contaminant loading to vapor plumes.
- 2) **Studies of soil moisture variability** – *Objective: to determine the role of soil moisture variability and heating on vapor pathway dynamics.* This series of experiments explored the affect of infiltration and heat flux at the land surface on vapor transport pathways. Testing was performed in a large 2-D tank with heterogeneous porous media.
- 3) **Development and evaluation of models for vapor transport and attenuation** – *Objective: Investigate and develop modeling methods for up-scaling vapor attenuation behavior characterized at the laboratory scale to the field scale.* A numerical model was developed to up-scale vapor generation, transport and attenuation behavior. The model was validated against data generated in tasks 1 and 2 and refined to facilitate up-scaling for field prediction of vapor behavior.
- 4) **Studies of coupled flow and transport at the intermediary scale** – *Objective: Generate a comprehensive data set capturing VI pathway processes to validate models.* An experiment using a intermediate scale tank system was conducted. This experiment integrated the phenomena identified from project components (1) and (2) above to examine the observed physical processes in a more realistic setting, and make conclusions about the practical effect of dynamics on VI. Specific objectives were to: (a) Observe vapor plume behavior under physically dynamic conditions including rainfall and water table fluctuation, (b) Generate quantitative data that may be used to validate numerical models of VI, and (c) test our conceptual model of the pathway.
- 5) **Model application through a series of practical scenarios** – *Objective: To evaluate the adequacy of screening and other existing models for field applications under complex physical, climatic, and/or geochemical conditions.* Data and phenomena identified from all previous experiments as well as the upscaled model were compared with the present screening-level models to provide guidance on their application. The product was a series of

scenarios and guidance to help remediation professionals come to better decisions with regard to the VI pathway.

6) Characterization and monitoring of vapor pathways – *Objective: Develop strategies for cost-effective characterization and monitoring of vapor pathways using hard and soft data assimilation methods.* The improved conceptual model developed by the previous tasks may require new or improved site-characterization methods for implementation. In this task, data collection techniques including both “hard” data (e.g. sampling) and “soft” data (e.g. subsurface geophysics) were refined for characterization and monitoring of vapor pathways using electrical resistance tomography (ERT).

7) Field demonstration – *Objective: Field study to demonstrate developed knowledge and validate conceptual model.* The final stage is to demonstrate the conceptual model and decision support developed in the previous tasks at the field scale. Improved characterization methods (ERT) were demonstrated as well.

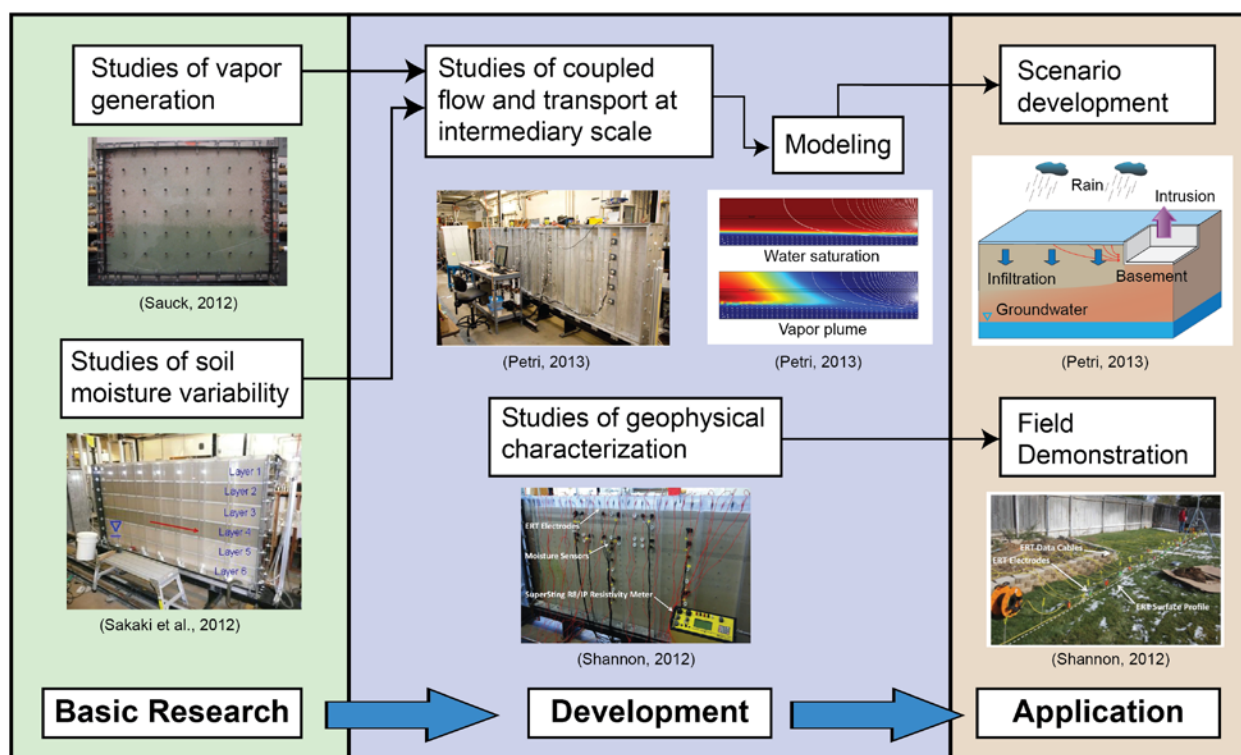


Figure 1.2: Flow chart depicting approach of the ER-1687 project.

The remainder of this report presents more detailed background on the VI pathway and science issues that need to be further explored, the materials, methods and models employed in this project, the results obtained from each project component and relevant discussion of observations, and conclusions and practical implications that can be inferred from this work.

1.4 References:

Abreu, L. D. V., and Johnson, P. C. (2005). "Effect of Vapor Source-Building Separation and Building Construction on Soil Vapor Intrusion as Studied with a Three-Dimensional Numerical Model." *Environmental Science & Technology*, 39(12), 4550-4561.

- Bozkurt, Ozgur, Kelly G. Pennell, and Eric M. Suuberg. 2009. "Simulation of the Vapor Intrusion Process for Nonhomogeneous Soils using a Three-Dimensional Numerical Model." *Ground Water Monitoring and Remediation* no. 29 (1):92-104.
- Colorado Department of Public Health and Environment. 2004. Draft Indoor Air Guidance. Hazardous Materials and Waste Management Division,. 58 p
- Dawson, Helen E., and Todd A. McAlary. 2009. "A compilation of statistics for VOCs in post-1990 indoor air concentration studies in North American residences unaffected by subsurface vapor intrusion." *Ground Water Monitoring and Remediation* no. 29 (1):60-69.
- Fitzpatrick, Nancy A., and John J. Fitzgerald. 2002. "An evaluation of vapor intrusion into buildings through a study of field data." *Soil & Sediment Contamination* no. 11 (4):603-623.
- Folkes, David, William Wertz, Jeffrey Kurtz, and Theodore Kuehster. 2009. "Observed Spatial and Temporal Distributions of CVOCs at Colorado and New York Vapor Intrusion Sites." *Ground Water Monitoring and Remediation* no. 29 (1):70-80.
- Gorder, Kyle A., and Erik M. Dettenmaier. 2011. "Portable GC/MS Methods to Evaluate Sources of cVOC Contamination in Indoor Air." *Ground Water Monitoring and Remediation* no. 31 (4):113-119.
- GSI Environmental Inc. (2007). "Environmental Security Technology Certification Program (ESTCP) Final Report, Detailed Field Investigation of Vapor Intrusion Processes."
- Hers, Ian, Jim Atwater, Loretta Li, and Reidar Zapf-Gilje. 2000. "Evaluation of vadose zone biodegradation of BTX vapours." *Journal of Contaminant Hydrology* no. 46 (3-4):233.
- Interstate Technology Regulatory Council. (2007). "Vapor Intrusion Pathway: A Practical Guideline." 172.
- Johnson, P. C., and Ettinger, R. A. (1991). "Heuristic model for predicting the intrusion rate of contaminant vapors into buildings." *Environmental Science & Technology*, 25(8), 1445-1452.
- Johnston, Jill E. 2012. Spatio-temporal variability of tetrachloroethylene (PCE) in indoor air due to vapor intrusion: A community based, longitudinal approach. Presentation at National Environmental Monitoring Conference, at Washington, D.C.
- Luo, H., Paul Dahlen, Paul C. Johnson, Tom Peargin, and T. Creamer. 2009. "Spatial variability of soil-gas concentrations near and beneath a building overlying shallow petroleum hydrocarbon-impacted soils." *Ground Water Monitoring and Remediation* no. 29 (1):81-91.
- McCarthy, Kathleen A., and Richard L. Johnson. 1993. "Transport of Volatile Organic Compounds Across the Capillary Fringe." *Water Resour. Res.* no. 29 (6):1675-1683.

- McHugh, Thomas E., John A. Connor, and Farrukh Ahmad. 2004. "An Empirical Analysis of the Groundwater-to-Indoor-Air Exposure Pathway: The Role of Background Concentrations in Indoor Air." *Environmental Forensics* no. 5:33-44.
- McHugh, Thomas E., Phillip C. de Blanc, and Roger J. Pokluda. 2006. "Indoor Air as a Source of VOC Contamination in Shallow Soils Below Buildings." *Soil & Sediment Contamination* no. 15:103-122.
- McHugh, Thomas E., Tim N. Nickels, and Samuel Brock. 2007. Evaluation of Spatial and Temporal Variability in VOC Concentrations at Vapor Intrusion Investigation Sites. Paper read at Proceedings of Air & Waste Management Association's Vapor Intrusion: Learning from the Challenges, September 26-28, 2007, at Providence, RI.
- Mills, W. B., Liu, S., Rigby, M. C., and Brenner, D. (2007). "Time-Variable Simulation of Soil Vapor Intrusion into a Building with a Combined Crawl Space and Basement." *Environmental Science & Technology*, 41(14), 4993-5001.
- Moseley, C. L., and Meyer, M. R. (1992). "Petroleum contamination of an elementary school: a case history involving air, soil-gas, and groundwater monitoring." *Environmental Science & Technology*, 26(1), 185-192.
- Nazaroff, William W., Steven R. Lewis, Suzanne M. Doyle, Barbara A. Moed, and Anthony V. Nero. 1987. "Experiments on Pollutant Transport From Soil into Residential Basements by Pressure-Driven Airflow." *Environ. Sci. Technol.* no. 21:459-466.
- Obmascik, Mark. 2000. "Snafu lets toxins run amok." *Denver Post*, December 31, 2000.
- Olson, D. A., and Corsi, R. L. (2002). "Fate and Transport of Contaminants in Indoor Air." *Soil & Sediment Contamination*, 11(583-601).
- Thomson, N. R., J. F. Sykes, and D. Van Vliet. 1997. "A numerical investigation into factors affecting gas and aqueous phase plumes in the subsurface." *Journal of Contaminant Hydrology* no. 28 (1-2):39.
- Tillman, F. D., and Weaver, J. W. (2005). "Review of Recent Research on Vapor Intrusion, EPA/600/R-5/1006." US EPA Office of Research and Development, Washington DC.
- United States Department of Defense. 2009. DoD Vapor Intrusion Handbook. 171 p
- United States Environmental Protection Agency. (2002). "Draft Guidance for Evaluating the Vapor Intrusion to Indoor Air Pathway from Groundwater and Soil." Office of Solid Waste and Emergency Response, ed., 178.

Chapter 2: Background

2.0 Introduction

In order to develop an improved conceptual model of the vapor intrusion exposure pathway under dynamic conditions, it is important to review the current knowledge base and standard of practice for assessing VI. First a brief review of the current typical approach to vapor intrusion pathway assessment will be discussed. This is followed by a review of scientific fundamentals relevant to the vapor intrusion pathway. Also, a critical review and discussion of the presently available vapor intrusion models is presented highlighting areas where further work was found to be needed for better VI pathway understanding. Finally some discussion potential alternate site characterization methods are discussed. The following literature review reveals that no study has yet evaluated the full behavior of the pathway schematic indicated in figure 1.1, especially under the influence of complex factors including rain, water table fluctuation and heterogeneity.

2.1 Present Standard of Practice for Vapor Intrusion Assessment

Within the last decade, a variety of regulatory agencies at the federal and state levels promulgated various approaches for assessing the potential for vapor intrusion into buildings at contaminated sites (USEPA 2002; CDPHE 2004; ITRC 2007; USEPA 2008; DoD 2009). The approaches vary by agency and state, but generally follow three major stages. The first is an initial screening stage, in which potentially VI-impacted buildings are determined from site-specific data that is available or augmented by additional characterization. At this stage, the decision-making rationale for potentially at-risk buildings may originate from conservative application of a screening model (especially the model presented by Johnson and Ettinger, 1991), or application of another screening standard such as groundwater MCLs. Once a building is found possibly at-risk, most regulatory guidance encourages direct engagement of the property owner or occupants of the at-risk building in the second stage, including offers to sample the indoor air for VOCs. If consent is granted, indoor air sampling is conducted, typically as a 24 hour composite sample drawn into a Summa gas canister (ITRC 2007). Considerable efforts to minimize indoor sources of contaminants (e.g. temporary removal of cleaning chemicals, other products containing VOCs) are often incorporated to minimize interfering sources of contamination when determining the risk posed to a given building (Gorder and Dettenmaier, 2011). To build further evidence confirming or negating a complete vapor intrusion pathway, it is generally desirable to obtain a “subslab” soil gas sample at the same time as the indoor air sampling (ITRC 2007; DoD 2009). The “subslab” sampling involves drilling a hole in a basement floor to access and analyze the gas in the vadose zone directly beneath the building foundation. This sample provides further evidence of a connected vapor pathway if contaminants are detected. The final assessment stage (third stage) involves a decision on whether action is required based on data gathered. These typically fall into the categories of “no action” if no risk is suspected or, “long term monitoring” if the building does not appear affected, but is proximal enough that future risk cannot be ruled out, and active mitigation if the risk pathway is complete and vapor concentrations must be reduced (ITRC 2007). These steps may be conducted in an

iterative manner depending on data collection and conceptual site model refinement and interpretation.

2.1.1 Vapor attenuation and “Attenuation Factors”

There are a number of natural subsurface processes that attenuate vapor mass as they pass from the source to the building. As a result, measured indoor air concentrations are generally much lower than what is observed in the subsurface. This attenuation behavior is typically quantified empirically as an “attenuation factor” or alpha value (Johnson and Ettinger, 1991; ITRC, 2007), which is the ratio of the indoor air concentration to the source concentration (Johnson and Ettinger, 1991) given:

$$\alpha = \frac{C_{indoor}}{C_{source}} \quad (1)$$

This alpha value quantifies the magnitude of effect that subsurface and building processes have on the indoor air concentration. Many analytical and numerical modeling studies, as well as field investigations report their results in the form of alpha (attenuation factor) values (Abreu et al., 2009; Bozkurt et al., 2009; Yu et al., 2009). The “source” concentration represents the concentration of the media from which measurements or predictions are made, and is expressed as the equivalent concentration in air at equilibrium with the source. Source concentrations may be measured in the field or assumed based on limited field data. Thus, if the source is a NAPL, the saturation vapor pressure is assumed to represent the concentration of the source, while if the source is a NAPL dissolved in groundwater, the concentration is assumed to be the equilibrium concentration determined by Henry’s Law. If vadose zone soil gas concentrations are available, then no adjustment is made. A lower alpha value describes a higher attenuation between the source and building. Because the α value empirically embeds many physical, chemical and biological processes (e.g. those outlined in figure 1.1), alpha values are highly dependent on where the subsurface sample is taken and what media is sampled (Johnson et al., 2002; ITRC, 2007). Thus an alpha estimated from subslab soil gas will generally be higher than an alpha from groundwater data, because typically the concentration of soil gas underneath a building will be much closer to the indoor air concentration than the concentration in groundwater, which may be some considerable distance away. Selection of sampling locations is specified by regulatory guidance that is often specific to each US State (ITRC, 2007).

2.2 Scientific Fundamentals of Vapor Transport

Vapor transport in the subsurface is controlled by a series of physical, chemical and biological processes that merit further exploration in order to understand the full complexity and interactions of the process-based conceptual model. Transport of vapors is influenced by the flow and distribution of air, water and NAPL phases, as well as by the porous media hydraulic properties. Furthermore, mass transfer governs the partitioning of organic contaminants between these phases, while solute advection, diffusion and dispersion govern the transport within each phase. Finally, reactive processes that occur within these phases, especially including biotic and abiotic degradation reactions, influence vapor fate. This section summarizes much of the understanding of these processes and their influence on vapor intrusion.

The generation, transport and intrusion of contaminant vapors are ultimately driven by solute transport within multiple phases within the vadose zone. A process-based conceptual model is illustrated in figure 2.1. This model incorporates major solute transport processes. Reactions are represented by source or sink terms that may include mass transfer between other phases, or transformative reactive processes that degrade or change the contaminant, such as biodegradation, within a phase. The generic solute transport equation that captures the processes and mass balance is given by:

$$R_i \phi \frac{\partial C_i}{\partial t} = D_{i,e} \nabla \cdot \nabla C_i - \nabla \cdot \mathbf{q}_i C_i + source / sink \tag{18}$$

Where, C_i is the concentration in phase i , R_i is a coefficient defining sorption for phase i , $D_{i,e}$ is the combined effective diffusion / dispersion coefficient for phase i , and \mathbf{q}_i is the Darcy flux vector for phase i . The importance of these processes and existing understanding of their role in the vapor intrusion pathway are described in the sections below. More detailed discussion of the processes that appear in eq. 18 as applied to vapor transport is presented below.

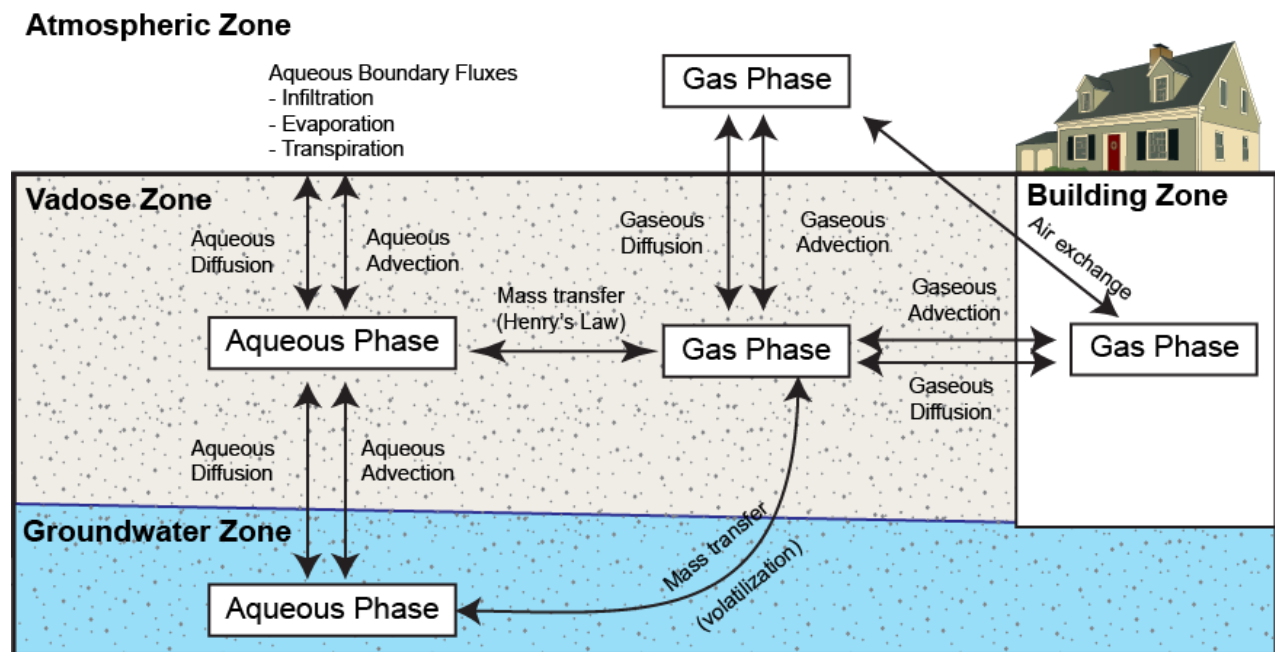


Figure 2.1: Process based conceptual model of the vapor intrusion pathway.

2.2.1 Advective transport

Advective transport of VOCs within the vadose zone is driven by bulk-phase (e.g., air or water) fluid flow. Thus, advection is strongly coupled to multiple phase flow, which is modeled using Darcy’s Law that is assumed to govern fluid flow in the porous medium. Many of the same physical descriptions used in other applications to flow in porous media are used in vadose zone transport, such as Brooks-Corey (1966) or Van Genuchten (1980) retention and relative permeability models. However, advection in the vadose zone differs substantially from

advection in the saturated zone. In the saturated zone, groundwater flow is primarily driven by regional scale hydraulic gradients within groundwater aquifers, often resulting in horizontal flow. In contrast, in the vadose zone, advection occurs primarily on a vertical basis driven by boundary conditions at the land-atmospheric interface. For instance, daily diurnal barometric pressure changes in the atmosphere drive cyclical flow of soil gas into and out of soil at the land surface via barometric pumping (Auer et al., 1996; Parker, 2003; Tillman et al., 2003). Since this process is cyclic, the net gas phase displacement over long time periods tends to be minimal, but this causes enhanced mechanical dispersion for which Fickian dispersion models have been proposed (Auer et al., 1996). The model by Auer et al. (1996) found that this barometric dispersion in certain systems could exceed the natural diffusion of the gas phase, especially when water saturation of the porous media was high (e.g. 0.95) or when the vadose zone was very deep. Wind at the land-atmospheric boundary has also been proposed to impact VOC subsurface transport, especially when interacting with surface structures, which cause enhanced subsurface airflow on the windward side of a building (Luo et al., 2009). Buildings themselves also drive advection in the soil gas phase, as heating, ventilation and air-conditioning (HVAC) equipment may create higher or lower pressures within a building, driving flow through permeable openings in building foundations (Nazaroff et al., 1987; Robinson et al., 1997; Garbesi et al., 1993). For example, Nazaroff et al. (1987) conducted a field test where building underpressures of 25-50 Pa were observed to induce gas flow rates in the subsurface in excess of 1 meter per hour. Robinson et al (Robinson et al., 1997) found that even in absence of active building ventilation systems, barometric effects on the foundation itself could result in long term vapor flow rates equivalent to a rate driven by a steady 0.4 Pa building underpressurization. Advection is not limited to just the gas phase in the vadose zone; infiltration, evapotranspiration and water table fluctuation impart water phase fluxes that can transport, dilute, or alter the advective flow of contaminants (Imhoff et al., 1994; Szatkowski et al., 1995; Thomson et al., 1997; Tillman and Weaver, 2007). Air and water flow also interact as shown in a study by Sakaki et al. (2012) performed as a part of this project that found that in response to infiltration at the land surface, the gas phase relative permeability dropped in surface layers, resulting in diversion of airflow around water wet regions. Aqueous flow also influences water content and distribution, affecting basic transport parameters like tortuosity and effective diffusion coefficients (Millington and Shearer, 1971; Werner et al., 2004; Poulsen et al., 2006; Carr et al., 2010).

The aforementioned advection processes are all driven by boundary conditions and the fluid flow results from fluxes across these boundaries. However, there are also advection processes that are driven by solute transport and mass transfer. These include density driven advection, as well as advection due to the volatilization (expansion) of a nonaqueous phase liquids (Falta et al., 1989; Mendoza and Frind, 1990a; Mendoza and Frind, 1990b; Lenhard et al., 1995; Jang and Aral, 2007). Many VOCs, especially if emanating from a NAPL source, evolve a gas phase with a significantly higher density than that of air. This causes a density gradient that causes the gas plume to sink. Density can have significant effects on plume development; a sensitivity analysis by Mendoza and Frind (1990b) found that plumes under the influence of density driven advection compress vertically, which resulted in lower upward diffusive fluxes out of the land-atmospheric interface due to density advection acting in opposition. Furthermore, they found that simulated density plumes could spread laterally on the water table resulting in a plume up to twice as large as a plume that was simulated using diffusion alone. The effect of density was found in their analysis to become significant when the density of the soil gas exceeded that of air by a factor of 1.15, and was also permeability dependent becoming more dominant when gas

phase permeabilities exceeded $1 \times 10^{-11} \text{ m}^2$. Falta et al. (1989) found density advection had effects on NAPL mass transfer in a similar permeability range ($6 \times 10^{-11} \text{ m}^2$) where volatilization rates were a factor of 4 higher when density advection was considered over diffusion alone. Volatilization itself can also induce advection due to the expansion of a comparatively dense NAPL into a much less dense vapor, though the sensitivity analysis by Mendoza and Frind (1990b) found this to be of minor importance. Unlike the advection processes outlined in the previous paragraph, these latter processes are more complex and difficult to incorporate into numerical models because the solute transport equation is strongly coupled to the fluid flow equations requiring simultaneous solution.

Within this experimental study, air and water flow, as well as density advection, are anticipated to play key roles in the transport of VOCs. These processes are incorporated into a numerical model using Darcy's Law and the Van Genuchten (1980) retention and relative permeability model, as described in chapter 3.

2.2.2 Diffusive and dispersive transport

Another component of multiphase solute transport is diffusion and dispersion. These processes are typically modeled together in the ADE, but represent two different processes. Molecular diffusion represents the spreading of a solute due to a concentration gradient, and is described by Fick's Law, while dispersion refers to the spreading of a solute during flow through a porous network. Thus, dispersion is ultimately an advection process within pores that depends on the flow characteristics of the system, while diffusion occurs independent of flow characteristics. In vapor intrusion systems, molecular diffusion is an important process because within gases, diffusion coefficients are typically orders of magnitude higher than in aqueous systems. For example, the molecular diffusion coefficient for trichloroethylene is $8.75 \times 10^{-6} \text{ m}^2/\text{s}$ in air versus $1.00 \times 10^{-10} \text{ m}^2/\text{s}$ in water (Lugg, 1968; Rabideau et al., 1999). Many simple vapor intrusion models simulate subsurface vapor transport as a diffusive only process (Johnson and Ettinger, 1991; Jeng et al., 1996; Olson and Corsi, 2001; Davis et al., 2009). Given this very large difference in diffusion coefficients, and that within the pore space both the air and water phases are present simultaneously, it is generally recognized that the "effective" diffusion coefficient of the system is dependent on phase saturation and the tortuosity of the phases (Millington and Shearer, 1971; Werner et al., 2004; Shen and Chen, 2007). Millington and Quirk (1961) and Millington and Shearer (1971) proposed a relationship to adjust the bulk effective diffusion coefficient in a two-phase system using:

$$D_{eff} = D_g \frac{\theta_g^{3.33}}{\phi^2} + \left(\frac{D_w}{H_i} \right) \frac{\theta_w^{3.33}}{\phi^2} \quad (23)$$

where, D_{eff} is the effective diffusion coefficient, D_g is the gas phase molecular diffusion coefficient, D_w is the aqueous phase molecular diffusion coefficient, θ_g is the soil gas content, θ_w is the soil water content, H_i is the dimensionless Henry's constant, and ϕ is the porosity. This relationship represents one of the most commonly implemented diffusion models for two-phase systems. However, this model does not always fit experimentally measured values of the diffusion coefficient, and thus modified or alternative formulations have been proposed and used (Werner et al., 2004; Poulsen et al., 2006; Shen and Chen, 2007).

Meanwhile, dispersion is a more difficult process to simulate. Dispersion is typically segmented into longitudinal and transverse components with different coefficients. These coefficients are empirical due to the complicated nature of the subsurface heterogeneity. In the vadose zone barometric pumping with a back and forth movement of soil gas can also enhance dispersion, and in some cases can be quite significant (Auer et al., 1996; Parker, 2003).

2.2.3 Reactive transport processes

Reactive processes transform the mass distribution between phases. As described in the following sections, these include phase mass transfer, sorption, and biotic / abiotic degradation reactions.

2.2.3.1 Mass transfer between phases: In principle, there are two basic approaches to simulating mass transfer: the local-equilibrium and non-equilibrium approaches. Under the equilibrium approach, the phases are assumed to be in direct equilibrium, such as with Henry's Law between air and water phases:

$$p = k_H C_w \quad (20)$$

where, k_H is the Henry's Law constant (a function of temperature), p is the partial pressure of the contaminant in the gas phase, and C_w is the aqueous concentration of the contaminant. Similarly, for single component NAPLs, the local equilibrium assumption for air and water phases entails assuming the concentration in air is at the saturation vapor pressure (p_{sat}) and the solubility limit ($C_{w,sat}$), respectively. If the NAPL is a multicomponent NAPL, Raoult's Law must be used to estimate the effective solubility limit or effective saturation vapor pressure for each component because the NAPL composition itself may change with time. Henry's Law constants, saturation vapor pressures and solubility limits are dependent on temperature (Boublík et al., 1973; Heron et al., 1998).

Theoretically, the equilibrium condition holds true at contacts between phases. However as mass transfer is upscaled, this mass-transfer behavior can exhibit behavior that is "effectively" rate-limited. As a result, non-equilibrium mass transfer is often proposed in the form of empirically derived Gilliland-Sherwood mass transfer models (Miller et al., 1990; Imhoff et al., 1994; Powers et al., 1994; Szatkowski et al., 1995; Wilkins et al., 1995; Yoon et al., 2002; Nambi and Powers, 2003; Illangesakare et al., 2010). These non-equilibrium models assume mass transfer occurs across a boundary layer between phases and is driven by diffusion and advection within this boundary layer. A concentration gradient is assumed to be the driving force for mass transfer, while a mass transfer rate coefficient describes the properties of the boundary layer. Mathematically, for an air-water system this is given by (21) and (22). Physical system parameters relating to phase velocities, diffusion coefficients, length scales and other factors are generally rolled into the correlation through dimensionless numbers such as the Peclet, Schmidt or Reynold's, or Modified Sherwood numbers.

$$source / sink|_{gas} = k \left(\frac{C_w}{K_H} - C_g \right) \quad (21)$$

$$\text{source/sink}|_{\text{water}} = k(C_g K_H - C_w) \quad (22)$$

where, the source/sink terms for the respective phases are incorporated into the ADE, k is a mass transfer rate coefficient, C_w is the aqueous VOC concentration, and C_g is the gas phase VOC concentration.

The break point between equilibrium and non-equilibrium models can be dependent on system parameters and phase distribution. For instance, Seagren et al. (1999) compared local-equilibrium and non-equilibrium assumptions for NAPL-to-water mass transfer from a NAPL pool. They found that if the product of the Schmidt and Modified Sherwood numbers was greater than 400, then the local equilibrium and non-equilibrium models converged on the same solution. Below this number, the solutions diverged, suggesting non-equilibrium models would be more appropriate for higher velocity, higher dispersion systems. Correlations have been proposed for air-water mass transfer (Szatkowski et al., 1995; Braida and Ong, 1998; Chao et al., 2008), Air-NAPL systems (Wilkins et al., 1995; Yoon et al., 2002; Harper et al., 2003), and NAPL-water systems (Miller et al., 1990; Imhoff et al., 1994; Saba and Illangasekare, 2000; Nambi and Powers, 2003). One challenge in using non-equilibrium models relates to their being developed empirically for a certain system; extrapolating beyond that system can lead to erroneous mass transfer rate estimates. For example, Gililand-Sherwood correlations that are developed from 1-dimensional porous media column studies where a mobile phase (e.g. water, air) is forced through an immobile phase (e.g. NAPL, water) may overestimate mass transfer from multidimensional real world systems where flowing phases may naturally bypass zones of low saturation (Saba and Illangasekare, 2000). Furthermore, some of the previous mentioned correlations were derived for active remediation technologies such as soil vapor extraction and air sparging (Wilkins et al., 1995; Yoon et al., 2002), where the airflow regime represents a system of forced advection. Yet under typical conditions during vapor intrusion, where airflow is driven by generally weak indoor air or atmospheric pressure gradients, the rates of advection may be considerably lower than in these other systems, and it is unknown how these correlations will perform if used for the investigation of VI.

In this study, both local equilibrium and non-equilibrium models are employed to describe the transport behavior of the experiments. With NAPL, especially under complex soil moisture conditions, non-equilibrium modeling is necessary to predict mass transfer. However, in other portions of the study, equilibrium may be assumed.

2.2.3.2 Sorption: This section describes the partitioning of contaminants to solid phase porous media, including adsorption of VOCs to mineral surfaces and soil organic matter (Smith et al., 1990; Ong and Lion, 1991; Shonnard et al., 1993; Conklin et al., 1995; Ruiz et al., 1998; Kim et al., 2005). These sorption processes can have a complex effect on contaminant migration and are generally a strong function of soil moisture content. Organic compound sorption to inorganic soil minerals has been shown to be a significant process under very dry soil conditions (e.g. below field capacity), where the sorption capacity decreases with increasing water content and gas phase humidity (Smith et al., 1990; Shonnard et al., 1993; Ruiz et al., 1998; Thoma et al., 1999). This phenomenon is attributed to the displacement of the VOC by water molecules at mineral sorption sites, resulting in nonlinear sorption isotherms under low moisture conditions (Shonnard et al., 1993; Thoma et al., 1999). As the water content in the soil increases above the field

capacity, other processes begin to dominate, such as air-water partitioning of the VOC via Henry's Law (Conklin et al., 1995). Sorption of organics to soil organic matter has been shown to be a factor, with sorption generally increasing with organic content in the soil (Ong, 1991; Kim et al., 2005). In this study, the laboratory sands are clean, washed silica sands with negligible organic content, and were saturated at well above field capacity, so sorption is not anticipated to affect the laboratory results.

Simulation of sorption processes can be accomplished through incorporation of the retardation (R) factor into the advection-dispersion equation. It is common in some studies to neglect aqueous advection and treat the water as an immobile sorbent and thus incorporate Henry's Law partitioning into the R value (Conklin et al., 1995; Kim et al., 2005). However, for this study it is important to simulate the aqueous and air phases separately as both will be mobile. While nonlinear sorption of VOCs to inorganic minerals may be significant in dry environments (Shonnard et al., 1993; Thoma et al., 1999), it is presumed that these conditions will only be present in soils in the very shallow surface layer, or in very dry climates. Therefore, the R factor may be estimated using linear relations from the methods of Conklin et al. (1995) and Kim et al. (2005), given by equation (19):

$$R_g = 1 + \frac{\rho_b}{\theta_g} \frac{K_D}{K_H} + \frac{a_i K_i}{\theta_g} \quad (19)$$

where, θ_g is the air content, K_H is the Henry's Law constant, K_D is the organic phase – water partitioning coefficient ($K_D \approx K_{OC} f_{OC}$), K_{OC} is the organic carbon partitioning coefficient, f_{OC} is the organic carbon fraction, a_i is the specific interfacial surface area, and K_i is the adsorption constant for the air-water interface. In describing these terms, the first term ("1") accounts for mass in the gas phase, the second term accounts for mass in the soil organic matter phase, and the final term describes the air-water interfacial adsorption process.

2.2.3.3 Biotic and abiotic degradation: The degradation of organic contaminants within the vadose zone includes biotic and abiotic mechanisms, and is known to affect the migration of vapor plumes within the subsurface. Aerobic biodegradation can be particularly important since many vadose zone environments have significant exposure to oxygen fluxes from the land-atmospheric interface (Ostendorf and Kampbell, 1991; Lahvis et al., 1999).

However, the susceptibility of contaminants to biodegradation depends in part on the type of contaminant. LNAPL contaminants, such as total petroleum hydrocarbons (TPH) and benzene, toluene and xylene (BTX) are known to be quite susceptible to aerobic biodegradation (Lahvis et al., 1999; Bouchard et al., 2008), and incorporation of biodegradation kinetics into reactive transport models is a common practice (Hers et al., 2000; Gaganis et al., 2004; Broholm et al., 2005). Furthermore, simple inclusion of kinetic expressions for LNAPL contaminant degradation may not be sufficient to adequately describe the biodegradation that occurs; instead, some reactive transport models now include separate transport modules for microbial growth substrates, oxygen diffusion and carbon dioxide transport to improve prediction of contaminant transport and degradation (Ostendorf and Kampbell, 1991; Battistelli, 2004; DeVauil, 2007). Using a 1-D transport model calibrated to field and experimental data, Ostendorf and Kampbell (1991) found that oxygen levels at a ground water table 5 m below the surface were extremely

low as oxygen diffusing from above was nearly completely consumed by biodegradation of LNAPL compounds in the vadose zone. The cumulative effect of these biodegradation processes may be to limit the spread of a vapor plume. Indeed, the U.S. Environmental Protection Agency has indicated that the models supporting their guidance document (USEPA 2002) may be too conservative for typical underground storage tank (UST) sites containing hydrocarbon pollutants, in part due to this biodegradation effect.

Chlorinated VOCs (CVOCs) may also undergo biodegradation reactions. For trichloroethylene (TCE), a representative CVOC, several biodegradation pathways have been identified (Pant and Pant, 2010). These include: 1) aerobic co-metabolism, where trichloroethene and other chlorinated solvents are aerobically degraded by organisms expressing certain enzymes, such as methane monooxygenase (Fogel et al., 1986; Alvarez-Cohen and McCarty, 1991; Arvin, 1991), 2) anaerobic reductive dechlorination, where TCE is used as an electron acceptor and in the process is dehalogenated to *cis*-1,2-dichloroethylene, vinyl chloride and ethene (Maymo-Gatell et al., 1997; Yang and McCarty, 1998; Hendrickson et al., 2002) and 3) aerobic direct oxidation, whereby the microbe directly uses the VOC as a carbon source and electron donor (Olaniran et al., 2008). With respect to the vadose zone, the aerobic mechanisms are more likely to be active than anaerobic processes due to the higher potential for exposure to oxygen, though modeling studies by Verginelli and Baciocchi (2011) did indicate the potential for significant anaerobic degradation under some conditions.

However, while biodegradation reactions can act as significant sinks for contaminants, quantitative prediction of biodegradation performance is challenging *in situ* because the microbial populations are sensitive to environmental variables. Temperature, pH, and a suitable combination of electron acceptors, electron donors and growth substrates must be present for the microbes to effectively degrade contaminants (Alexander, 1999). Furthermore, the presence of contaminants in high concentrations may be toxic to microbes (Ely et al., 1997; Yang and McCarty, 1998). Thus, incorporation of site-specific biodegradation data is generally necessary to predict biodegradation rates *in situ*. The California Environmental Protection Agency recommends that data on oxygen consumption and carbon dioxide production be gathered before including biodegradation in their vapor intrusion models (DTSC 2005).

Several abiotic contaminant reaction mechanisms may also be present in natural systems. For instance, 1,1,1-trichloroethane and several other chloroalkanes are susceptible to hydrolysis reactions that accelerate with increasing temperature (Jeffers et al., 1989). Some reduced iron-bearing minerals have also been shown to reductively dechlorinate trichloroethylene and tetrachloroethylene (Liang et al., 2009), though such minerals are less likely to persist under an oxic vadose zone. Even oxygen itself can react abiotically with TCE (Knauss et al., 1998), though the reaction is very slow at typical groundwater temperatures. For instance, Knauss et al (1998) investigated the kinetic and thermodynamic parameters of this reaction and found that while at 90 °C, kinetic rates of oxidation were high enough that this pathway could lead to considerable degradation in thermal desorption systems, yet at 25 °C, the reaction was slower by a factor of about 2500, and almost 25000 at 10 °C.

Within the tank systems used in this work, neither biotic or abiotic degradation mechanisms are anticipated to play a major role. This is because the sands used in the laboratory are a very pure silica sand with minimal reactivity, and the water sources, chemicals and media used in the tank

contain minimal nutrients or growth substrates making significant biological growth and biodegradation unlikely. However, these could be major processes at field scale.

2.2.4 Effects of heterogeneity and the built environment

The previous discussion has provided the theoretical framework to describe subsurface vapor generation and migration. Implementation of this theory requires parameterizing models in such a manner that they represent a real system. However, natural subsurface geologic systems are rarely homogeneous. Instead, many subsurface systems have naturally extensive lithographic heterogeneities that impact mass transfer, advection, diffusion and pathway development. Many attempts to upscale these parameters have been made (Bakr et al., 1978; Gelhar et al., 1979; Dagan, 1984; Sposito et al., 1986; Russo, 1992; Rajaram and Gelhar, 1995; Liu and Molz, 1997), yet field-scale simulation of heterogeneous sites remains challenging. Furthermore, heterogeneities in VI systems may extend beyond the natural environment to include numerous subsurface engineering systems. For example, pavement, foundations, French drains, and subsurface utilities all have potential implications for vadose zone contaminant transport by affective fluid movement and phase saturation. This infrastructure is expected at many or most vapor intrusion sites since these generally reside in urban areas. Yet many modeling studies of vapor intrusion have focused on isolated individual houses (Abreu and Johnson, 2005; Abreu and Johnson, 2006; Abreu et al., 2009; Bozkurt et al., 2009; Yu et al., 2009). Thus, the authors are unaware of any study that has included typical urban infrastructure in the conceptual model. Generally vapor-impacted houses reside in an urban or suburban area, where surface and subsurface interference by surrounding houses, paved streets and sidewalks, subsurface utilities and other infrastructure have implications for multiphase flow and solute transport. This built environment may be important to consider with respect to vapor migration. As a demonstration, Figure 2.2 is a GoogleEarth™ snapshot taken from a small part of the well-known vapor-impacted neighborhood surrounding the Redfield's site in Denver, Colorado (Folkes et al., 2009). This site has nearly 500 VI-impacted houses and Figure 2.2 shows 44 of these (Identified from Folkes et al., 2009). From the GoogleEarth™ image, a simplified diagram by Petri (2014) depicts the surface conditions. The grey areas represent individual houses within a 2-block area, while the black area represents apparent paved surfaces, consisting of streets, driveways, sidewalks, and patios. The remaining green area represents the actual area where an open atmospheric contact and interaction may exist. This represents a much different land surface condition for vapor intrusion than the single house in isolation. Paved and overbuilt areas block or alter land-atmospheric exchange, such as rain infiltration and vadose zone off gassing to the atmosphere. Thus, if a "uniform" rain event occurs at a VI site, the infiltration condition is far from uniform. Under an irrigation case, the infiltration is even less uniform, as irrigation occurs at different times and different intensities depending on the homeowners' landscaping preferences. Such surface conditions should, in theory, represent a much different situation than a single house in isolation, as is the present VI modeling approach. This boundary condition alone represents a form of heterogeneity.



Figure 2.2: Illustrations of the surface conditions of a VI site in an urban / suburban setting

The conceptual model of the subsurface for VI sites also needs to consider the impact of common urban subsurface infrastructure. In a neighborhood like the one shown above, there will also likely be large diameter sanitary sewers running the length of each street. Each house on the street will have a sewer connection to the main. It is common practice for these sewers to be laid within porous bedding materials, especially gravel, which allows for limited expansion and contraction of the pipes and to avoid pipe collapse. Furthermore, many houses may have French drains installed around their perimeter to disperse drainage from the roofs of the houses away from the structure. All of these represent strong, artificially planted heterogeneities that are common and may have the potential to redistribute both soil vapor and infiltration. Because these processes are located adjacent to or underneath vapor-impacted buildings, it is plausible that they may have as much potential to affect VI as natural heterogeneities.

2.3 Current Models of Vapor Intrusion

Many attempts have been made to predict and study the behavior of vapor intrusion through the use of analytical and numerical models. Some models may simulate the entire VI pathway from source to indoor air, while others may focus only on components of the VI pathway, such as indoor air mixing or subsurface fluxes. The results of VI modeling studies can be expressed in many ways, including predicted indoor air or subslab soil gas concentrations, contaminant fluxes, or quite frequently in terms of an “alpha” value (attenuation factor). As with most models, many simplifying assumptions are often made to facilitate solution of the model and focus on specific processes. Table 2.1 contains a summary of analytical models employed for VI, while Table 2.2 contains a summary of numerical models of VI.

2.3.1 Analytical Models of VI

Analytical models of VI are common despite the widespread simplifications that they make, because of their limited input parameters and ease of application. One analytical model in particular, the Johnson and Ettinger (1991) model, has become widely adopted and is incorporated into many regulatory guidance documents (Johnson, 2002; ITRC 2007; USEPA 2008; DOD 2009). Several common features are noteworthy in the analytical models of VI. First, in regards to subsurface transport, these models almost exclusively assume 1-dimensional vertical transport of soil vapors through the subsurface, typically via either diffusion alone or a combination of advection and diffusion. Of the analytical models reviewed, the only exceptions were models by Krylov and Ferguson (1998) and McHugh et al. (2010), who focused primarily on indoor air mixing and treated the subsurface as a compartment, neglecting subsurface advection and diffusion entirely. A majority of the models assume steady-state conditions and present results either in terms of alpha factors or indoor air concentrations. The primary difference between these studies is the different types of building foundations (e.g. basement construction versus slab-on-grade or crawlspace systems), intrusion pathway parameters (e.g. crack area, crack configuration, crack permeability and diffusivity), building parameters (air exchange rate, single and multiple room models), subsurface properties (permeability, diffusivity, domain length, water content, and others) and the inclusion of subsurface biodegradation into the model. Since most of the models assume steady-state conditions, the contaminant source is usually assumed to be a constant and is typically situated on the water table. A few of the models solve for transient conditions allowing for a time-variant source, such as an exponentially decaying source in the case of Jeng et al. (1996) or more complex source signals in the case of Mills et al. (2007).

In general, analytical models have emphasized the diffusive transport of the soil vapors, with diffusion being included in every analytical VI model with the exception of the two mixing models. This represents a departure from traditional contaminant hydrology modeling in the saturated zone, where transport is often advection-dominated. As a result, many of the analytical models have examined soil parameters (porosity, retention characteristics, etc.) to determine their effect on diffusivity, especially as predicted by the Millington-Quirk (1961) relationship (23).

Comparatively fewer models include advective transport in any form. The models by Parker (Parker et al., 2003; Parker, 2003) were modified to account for the additional dispersive transport that can occur due to barometric pumping cycles, and related parameters such as soil permeability and pressure fluctuations. However, these models does not specifically solve for advection but rather the incorporation of a dispersion term into the effective diffusion coefficient. Little et al. (1992) presented a series of models that could include an advection term, but these models focused on highly theoretical scenarios such as pulse sources, or advection dominated systems that do not correspond well with most conceptual models of the VI pathway. Only the model by Mills et al. (2007) includes advection as a separate term in in the transport model in a manner that may be solved directly owing to their use of Laplace methods.

Table 2.1: Summary of Analytical Models Addressing VI

Study	Model Type	Solution type	Subsurface transport processes	Vapor source	Building characteristics	Independent variables evaluated by study	Description
Davis et al 2009	1D	SS	DIFF	constant source	None	Effective diffusion coefficient	Model of oxygen and hydrocarbon diffusion with first order or instantaneous reactions. High moisture content layers at field site deviated from model.
Devault 2007	1D	SS	DIFF	constant source	Crack area, AER		Analytical model of oxygen-limited aerobic biodegradation. Two layer model (lower anaerobic, non degrading layer; upper aerobic degrading layer) with advection and mixing into building.
Jeng et al 1996	1D	TR	DIFF	decaying source	1-compartment model, AER	water content, source and degradation kinetics	1-D diffusion model, but with decaying source and first order biodegradation.
Johnson and Ettinger 1991	1D	SS + TR	DIFF	constant source	Building area, crack properties	dimensionless groups relating crack diffusion to crack advection	Most commonly used model of VI and the basis for risk assessment. Assumes 1-D diffusion of vapor in vadose zone from source to a building, followed by advection through a foundation crack.
Krylov and Ferguson 1998	indoor mixing model	SS	none	soil surface	Subfloor construction	Wind speed, air exchange rates, soil concentration	Mixing model looking at airflow within buildings with subfloors. Models affect of wind on windward and leeward sides of a building
Little et al 1992	1D	SS + TR	DIFF ADV	constant source	Crack area, AER		3 analytical models presented: 1) transient solution for a sudden source of vapor diffusing to a house, 2) transient radial diffusion to a house from an initially uniformly contaminated vadose zone, 3) a steady-state system with advection only
McHugh et al 2006	indoor mixing model	TR	none	pulse source	AER, Crack properties		Presents a mixing model for a source VOCs inside a building to demonstrate that indoor air can contaminate the subsurface below a building, resulting from cyclical fluctuations in building pressure.
Mills et al 2007	1D	TR	DIFF ADV	transient source	Foundation type (crawl space, basement), multiple rooms	Monti Carlo sensitivity analysis with 10% variation in all parameters	Transient solution of advection and diffusion with first-order decay. Strong emphasis on crawl space construction compared to the JE model. Analytical model is solved in the Laplace space, allowing time variable inputs, and inverted numerically
Olson and Corsi 2001	1D	SS	none	none	2-compartment mixing model	basement air exchange rate	Model provided considers mixing in the building between the basement and the rest of the building. Subsurface transport model similar to JE model
Parker 2003a	1D	SS	DIFF DISP ADV	none	None	frequency, magnitude of barometric cycles, permeability, depth to groundwater	Model for modification of the dispersion coefficient for barometric pumping, as well as cyclical water table effects (e.g. tides). Sensitivity analysis revealed barometric pumping dispersion more significant in less permeable soils, deeper vadose zone systems.
Parker 2003b	1D	SS	DIFF ADV	transient source		Sensitivity analysis	Transport model similar to JE model with 1-D diffusion, with additional mixing and dilution parameters near the building. Includes additional parameters for biodegradation, multicomponent NAPLs, and barometric pumping.
Verginelli and Baciocchi 2011	1D	SS	DIFF	constant source	Basement	Aerobic and anaerobic biodegradation rates, source depth, concentration	Model includes both anaerobic and aerobic biodegradation, with reaction zone thickness coupled with oxygen transport. Sensitivity analysis revealed that while generally aerobic degradation would dominate, anaerobic degradation could be significant under some conditions, including lower concentrations and deeper sources.

"1D" = 1-dimensional soil transport model, "SS" = steady-state model solution, "TR" = transient model solution, "DIFF" = diffusive transport included, "ADV" = advective transport included, "DISP" = dispersion transport included, "AER" = air exchange rate (for the building).

Table 2.2: Numerical Models of Vapor Intrusion

Study	Model	Method	Type	Solution	Soil type	Vapor Source	Building parameters	Independent variables	Description
Abreu and Johnson 2005	A&J 2005	FD	3D	SS	Hom	WT	SOG, basement, perimeter crack	Source depth and lateral offset, crack width, building pressure, porosity, water content, soil permeability, Foundation type	Model simulated vapor plume evolution and alpha as a function of source lateral separation, source depth, building parameters and others. Source depth and offset had strong effects on VI, as did factors that affected the soil flow rate (e.g. pressurization, crack parameters, soil permeability). Some biodegradation modeling presented. Foundation had a minor effect, with slab on grade construction generally more sensitive to other parameters, but slightly lower VI rates compared to basements
Abreu and Johnson 2006	A&J 2005	FD	3D	SS	Hom	WT	SOG, basement, perimeter crack,	Biodegradation rate, depth of source, source concentration, foundation type	Evaluated aerobic biodegradation coupled with oxygen transport from the atmosphere. Biodegradation rate had a generally stronger effect for deeper vapor sources. Significant differences in intrusion were observed between basement and slab-on-grade scenarios with the latter more sensitive. The crack location at the building perimeter was not investigated in a sensitivity analysis. Many vapor plumes under the house looked quite similar despite large changes in biodegradation rate, and it is feasible that a crack located deep under the building would have seen higher vapor concentrations and less sensitivity
Abreu et al 2009	A&J 2005	FD	3D	SS	Hom	WT	SOG, basement, perimeter crack	Source depth, concentration, biodegradation rate, foundation type	Included rate-limited biodegradation and oxygen transport in a simulation of soil vapor adjacent to a building. At high source concentrations, vapor intrusion rates were high despite biodegradation due to the rate-limitation. At lower concentrations, considerably more attenuation observed. Biodegradation interacted strongly with depth to source and foundation type due to oxygen diffusion path distances. Deeper sources and lower concentrations promote attenuation
Bozkurt et al 2009	COMSOL	FE	3D	SS	Het	WT	Basement, perimeter crack	Soil permeability, 9 different structured lithologies	Same model as in Pennell et al 2009, but with heterogeneous cases. Cases included various layered systems with variable permeability, a discontinuous clay layer system, and a system with scattered obstacles (e.g. utilities). The layered systems indicated that the sequence of low permeability layers had a strong control on VI through the combination of advection and diffusivity. Systems with high permeability soil near the building had high airflow and high vapor intrusion rates, despite the lowest subslab concentrations. Low permeability soils near foundation had high subslab concentrations, but vapor flow was low resulting in less intrusion.
Hers et al 2000	VADBIO	FD	2D	TR	Het	WT	SOG, perimeter crack	Biodegradation solution method, heterogeneity	Evaluated oxygen limited biodegradation in a homogeneous system and a system with a high moisture surface layer. 4 different kinetic approaches presented: 1) 1st-order, 2) combined zero-order and 1st-order, 3) instantaneous stoichiometric reaction (rate-limited by O ₂ transport), 4) zero-order and 1st-order with fully coupled O ₂ transport. Differences between models less apparent for homogeneous soil than heterogeneous system, where the location of the reaction front differed by model and was affected by the moist surface. Compared model to field data.
Pennell et al 2009	COMSOL	FE	3D	SS	Hom	WT	Basement	Building configurations (building with garage, with gravel sub base, 2 buildings, paved surface)	Equation system consists of air-phase Darcy flow coupled with advection-dispersion equation in gas phase. Simulates airflow to a perimeter crack, with extensive discussion of meshing necessary to account for different length scales.

Table 2.2: Numerical Models of Vapor Intrusion (continued)

Study	Model	Method	Type	Solution	Soil type	Vapor Source	Building parameters	Independent variables	Description
Tillman and Weaver 2007	HYDRUS-2D	FE	2D	TR	Hom	None	SOG	Rain fall rate, history, soil texture	Study uses HYDRUS0-2D with Richard's Equation to simulate the soil moisture distribution around a building using 1-hour time-variable rainfall data from a site in New Jersey. This is then used to compare subslab moisture content to moisture content outside the building, and tests the sensitivity of average moisture content on the J-E model. Sites underneath the building were considerably drier and less variable than outside the building footprint and expressed higher risk in the J-E model due to higher diffusivity. The situation was exacerbated by finer soil textures where the diffusivity differences between wet and dry soils is greater. Field characterization data compared.
Wang and Ward 2000	FLUENT	FE	3D	SS	Hom	Distrib.	Basement, perimeter crack, permeable floor	Different crack / floor parameters	Gas advection and diffusion, first order decay, 1-phase flow, energy equation Simulated radon transport into a basement with a commercial simulator. System solved using coupled heat, flow and advection dispersion equations. Solution is only for 1 phase flow.
Yu et al 2009	Comp-flowbio	FD	2D	TR	Het	NAPL	Basement, "effective crack"		2 phase air + water flow Presents application of COMPFLOWBIO model to Bordon heterogeneous aquifer. Demonstrates that mass transfer from the groundwater to vadose zone is limited by advection and diffusion in gas phase, but further model findings are compromised by an assumed boundary condition at the atmospheric interface. The model assumed only advective fluxes could cross the land-atmospheric boundary and neglected diffusive fluxes. Included infiltration but only as a steady low rate. Basement modeled as one or several grid-blocks with no mesh refinement.

"A&J 2005" = model by Abreu and Johnson (2005). "FE" = Finite element model, "FD" = finite difference model, "3D" = 3-dimentional domain, "2D" = 2-dimentional domain, "SS" = steady-state solution, "TR" = transient solution, "hom" = homogeneous soil domain, "het" = heterogeneous soil domain, "WT" = water table is source of VOCs, "distributed" = source is uniformly distributed throughout vadose zone, "NAPL" = source is a NAPL located in the vadose zone, "SOG" = slab-on-grade foundation type included in model, "basement" = basement foundation type included in model, "perimeter crack" = a crack around the perimeter serves as the connection between the building and the subsurface. "effective crack" = vapor intrusion through the crack simulated as an average flux through the basement slab with no mesh refinement.

2.3.2 Numerical Modeling studies of Vapor Intrusion

Compared to the available analytical models of vapor intrusion, the numerical models have been used to study a wider array of processes, employed a wider variety of approaches, and investigated more complex vapor intrusion scenarios. These are summarized in Table 2.2. These studies employed an array of models, including codes specifically developed for vapor intrusion, such as that by Abreu and Johnson (2005), or commercially available platforms developed for more versatile applications, such as COMSOL Multiphysics® by COMSOL Inc. (Bozkurt et al., 2009; Pennell et al., 2009), FLUENT® by Ansys, Inc. (Wang and Ward, 2002), and HYDRUS-2D® by PC-Progress (Tillman and Weaver, 2007). The advantage of these models compared to the analytical models in Table 2.1 is that they give more insight into how the complexity of real systems may affect vapor intrusion at the field scale. Of all the numerical studies, only Hers et al. (2000) applied a numerical model to a field site and compared the model to data. The remainder of the studies focused on fictitious scenarios of vapor intrusion into a building, though in the case of Yu et al (2009), the model domain used a soil distribution representative of the Bordon site, and Tillman and Weaver (2007) used hourly precipitation data from a site in New Jersey.

Many numerical modeling studies investigated the affect of building construction and configuration, typically including basements and slab-on-grade foundations. Most assumed that the soil gas flows through a “perimeter” crack that runs along the edge of the building, justifying this as a common location for construction joints between basement walls and a floor slab. This assumed location for a crack is where the model directs the soil gas flow due to the assumed under-pressurization of the building. Likewise, basement floor slabs and walls are generally assumed to be no flux boundaries. Numerically, such a situation poses a challenge to model as very fine discretization is required next to the crack, or the crack must be upscaled in some effective parameter representation. Many studies employ this approach, though Yu et al. (2009) averaged the flux out over the entire slab. It is surprising however that few of the studies considered the possibilities of cracks, joints or openings in locations other than the perimeter. Many of the models showed the highest concentrations underneath the center of a building, rather than at the edges, raising the question whether VI from openings in those regions may pose a higher risk. Only the study by Wang and Ward (2002) considered a complex building foundation configuration with joints in mid-slab. However, with only one realization, it is impossible to know how the intrusion location affects the concentrations next to the building. Nevertheless, vapor intrusion rates into Slab-on-Grade structures were generally observed to be more sensitive to subsurface conditions than basements, though overall rates and behavior were similar. This sensitivity may be due to the very short subsurface pathway between the atmospheric boundary and the perimeter crack when compared to basements where the transport pathway from the land surface to the crack is longer and deeper in the subsurface.

Most of the studies simulated airflow as a one-phase flow problem, making assumptions about relative permeability and effective diffusivity based on assumed water contents. Only two studies incorporated multiphase flow, in the case of Tillman and Weaver (2007) by using Richard’s Equation, and a fully three phase flow model (air-water-NAPL) in the case of Yu et al (2009). Both models included infiltration, though approaches differed significantly. In the case of Yu et al (2009), a steady-state yearly infiltration flux was assumed at the land surface and thus the model makes no conclusions about the transient effects of infiltration. Only the model of Tillman and Weaver (2007) simulated transient infiltration and made note of fluctuations in

water content near a building. Their key observation was that the building creates a considerable infiltration shadow, and therefore the soil moisture distribution under the building was considerably drier than the soil outside the building footprint. However, the model of Tillman and Weaver (2007) did not solve a coupled advection-dispersion equation to predict vapor concentrations in the subsurface, but simply incorporated updated soil gas diffusivities based on moisture distribution into the 1-dimensional Johnson and Ettinger (1991) model to predict the effect on vapor intrusion. Thus their predictions of VI still do not represent a fully coupled system where rain infiltration can impart vapor displacement and mass transfer behavior upon the system.

Of the systems that included heterogeneity, most studies used artificial discrete heterogeneities (often layers) that are otherwise isotropic, with only the study by Yu et al (2009) including realizations of a randomized field. All of the studies that evaluated heterogeneity noted significant effects. Bozkurt et al. (2009) highlighted that concentrations adjacent to a slab alone do not strictly control VI risk, as the soil gas flux rate into the building must also be considered. They showed in several layered systems that high permeability soils near the building could result in lower concentrations, but higher fluxes than a corresponding low permeability system. The heterogeneity of the system explored by Hers et al (2000) reflected a real field system, but was incorporated into the model as a simple layer. Their study was particularly focused on biodegradation and predicted an interesting interaction between heterogeneity and biology due to the effects on oxygen transport. In a homogeneous, dry system, the location of the “front” where biodegradation and oxygen consumption was occurring was relatively insensitive to the kinetic methods they tested. Yet when a wet layer at the surface restrained oxygen diffusion, the reaction front location shifted, suggesting that wet layers may effect the location of biological productivity due to their effects on oxygen transport. Perhaps the most comprehensive attempt to model a heterogeneous vapor intrusion system is the model of Yu et al. (2009), who simulated multiple realizations of a random field based on the Bordon site geostatistics. Their model also included a fully coupled three-phase-flow constitutive model based on the method of Stone (1973) and incorporating solute transport. They simulated NAPL sources in both the vadose zone and saturated zone and resulting groundwater and vapor plumes. In their flow model, they noted that heterogeneity could cause upward or downward migration of groundwater flow in the vicinity of the capillary fringe, which has implications for the mass transfer across the fringe. However, their solute transport results appear to be compromised by a boundary assumption. When solving the solute transport equation for vadose zone vapor migration, nearly all studies (e.g. Hers et al., 2000; Abreu and Johnson, 2005; Abreu and Johnson, 2006; Abreu et al., 2009; Bozkurt et al., 2009; Pennell et al., 2009) assume that the VOC concentration at the land-atmospheric boundary is either zero or at a background level in recognition of the free exchange of both advective and diffusive fluxes with atmospheric air. In the model of Yu et al (2009) it appears that this is not incorporated. Their flow equations allow free exchange of advective fluxes with the atmosphere, with inflowing air set to a zero concentration and outflowing air set to the subsurface concentration, but they do not allow a diffusive flux. The concentration contours in their plots meet the land-atmospheric boundary at apparent right angles. This approach results in an unrealistic accumulation of vapors within the vadose zone, as well as a much longer retention time of VOCs.

2.4 Enhanced Characterization Methods:

One objective of this project was to explore the use of enhanced and innovative characterization methods to support the new conceptual model that was developed by the project. Site characterization is a necessary and important component of VI assessment in order to develop a good site-specific conceptual model for analysis of vapor risk. Traditional VI site characterization methods emphasize common field sampling methods such as use of boreholes and logging, and soil gas and groundwater sampling (ITRC, 2007). These methods do provide valuable data for VI assessment, but they are also limited in that they generally only provide information at discrete and sparsely distributed locations at a site. Some sites with geologic conditions defined by high heterogeneity may require a very large number of sample points to get an accurate characterization of the site geology and other parameters that contribute to VI. As a result, advanced characterization methods that are less intrusive and yet provide more detailed information are of interest. Recent work by Professor Mark Brusseau under ESTCP project ER-201125 “*Use of Mass-Flux Measurement and Vapor Phase Tomography to Quantify Vadose Zone Source Strength and Distribution*” has explored the use of targeted vapor extraction and mass flux analysis to obtain detailed characterization of source zones entrapped in the vadose zone (Carroll et al., 2012; Brusseau et al., 2012; Carroll et al., 2013). His work emphasizes the analysis of historic SVE data, coupled with cyclic contaminant mass discharge (CMD) tests where SVE is applied to multiple wells in a sequential fashion to obtain a detailed characterization of the overall vapor source (Carroll et al., 2013). Geophysical methods originally developed for other applications may yield important information about site characteristics for vapor investigations. A review of field methods indicated that geoelectrical techniques, particularly electrical resistance tomography (ERT), have been used to define subsurface structures and phase distributions in applications including hydrogeological studies, mining exploration, engineering projects, and environmental investigations (Griffiths et al., 1990; Griffiths and Barker, 1993; Dahlin and Loke, 1997; Olayinka, 1999; Olayinka and Yaramanci, 1999; Amidu and Olayinka, 2006; Aizebeohai et al., 2010). ERT methods are based on the theory that electric fields, caused by introducing a current into the ground, can be observed and interpreted to represent material properties of subsurface compositions (*R.E. Sheriff, 2004*). By rearranging a series of electrodes in varied arrays, and measuring the electric fields that result, a representation of subsurface properties can be gained from the data (*Dahlin and Loke, 1997*).

To date, the authors are unaware of any laboratory studies that have used ERT methodologies to directly address a vapor intrusion related problem. However, in the past decade and a half several studies have performed ERT evaluations in laboratory experiments that have investigated subsurface processes that are indirectly related to vapor intrusion. Several laboratory studies using intermediate scale tanks have used ERT to capture key vapor intrusion related parameters such as soil moisture content (*Daily et al., 1995; Slater et al., 2002; Franz et al., 2010; Redwan, 2010*). *Daily et al. (1995)* were able to demonstrate the utility of ERT in environmental applications including delineation of contaminant distributions in the subsurface, monitoring remediation processes such as radius of influence from air sparging wells, and detecting leaks from underground storage tanks. *Franz et al. (2010)* also quantified soil moisture contents using ERT techniques from a rapid infiltration event in a 3-dimensional tank, and made comparisons to semi-analytical and numerical models. Meanwhile, the study by *Slater et al. (2002)* used ERT to

capture solute transport processes by tracing progress of sodium chloride plume. These studies provide a scientific basis for inferring that ERT may provide insights into the vapor intrusion process as well, such as by detecting preferential vapor pathways and heterogeneous soil moisture distributions.

Field investigations with ERT also support the notion that ERT may provide useful information for VI studies. As with laboratory investigations, no direct studies of VI using ERT have been conducted, but other studies give indirect support that ERT may provide insights into soil moisture content and soil horizons [Zhou *et al.*, 2001; Michot *et al.*, 2003; Rein *et al.*, 2004; Ozcep *et al.*, 2007; Rings *et al.*, 2008; Schwartz *et al.*, 2008; Besson *et al.*, 2010; Brunet *et al.*, 2010; Garre *et al.*, 2011; Laloy *et al.*, 2011; Franz *et al.*, 2011]. For example, Michot *et al.* [2001] investigated the ability of ERT to capture the change in shallow soil water content of an irrigated corn crop by tracking water uptake by roots and the progression of the infiltration front with preferential flow zones. Meanwhile, Schwartz *et al.* [2008] and Brunet *et al.* [2010] successfully used ERT methods quantify soil moisture profiles on two-dimensional vertical planes. The aforementioned field studies illustrate the documented performance of ERT to quickly and effectively capture the dynamic changes in soil moisture contents that the unsaturated zone undergoes, as well as soil horizons at the spatial and temporal scales that are required for effective vapor intrusion modeling. The research conducted within this project paper builds on the previous work performed using ERT in hydrogeological applications by addressing the need to develop novel approaches to improve VI characterization techniques.

2.5 Limitations of the current knowledge base

The literature discussed above forms the current basis of understanding for the vapor intrusion pathway and vapor plume transport. While these studies have addressed many important issues with the VI pathway, there still remain many gaps where new knowledge is necessary. One of these gaps lies in the understanding of how vapor behaves in a dynamic vadose zone system. Many of the models and studies have focus their efforts on steady-state solutions to the vapor problem, and make the implicit assumption that the vadose zone is essentially a constant with time. They also often neglect the complexity of multiphase flow, and its important interactions with mass transport. However, field data often shows temporal variability, and the cause and significance of this variability is often unknown. Our hypothesis is that some of this variability may originate from weather and hydrologic cycle dynamics, such as surface heating, rainfall and water table fluctuation. The experimental and modeling initiatives in this project seek to add the knowledge base by probing these dynamics and learning about their implications for the VI pathway.

2.6 References:

- Abreu, L. D. V., R. A. Ettinger, et al. (2009). "Simulated soil vapor intrusion attenuation factors including biodegradation for petroleum hydrocarbons." Ground Water Monitoring and Remediation **29**(1): 105-117.
- Abreu, L. D. V. and P. C. Johnson (2005). "Effect of vapor source-building separation and building construction on soil vapor intrusion as studied with a three-dimensional numerical model." Environmental Science & Technology **39**(12): 4550-4561.

- Abreu, L. D. V. and P. C. Johnson (2006). "Simulating the effect of aerobic biodegradation on soil vapor intrusion into buildings: Influence of degradation rate, source concentration, and depth." Environmental Science & Technology **40**(7): 2304-2315.
- Aizebeokhai A.P., Olayinka Al., Singh V.S. 2010. Application of 2D and 3D geoelectrical resistivity imaging for engineering site investigation in a crystalline basement terrain, southwestern Nigeria. Journ. Environ. Earth Scien., DOI: 10.1007/s12665-010-0474-z, p. 1481.
- Amidu S. A., Olayinka Al. 2006. Environmental assessment of sewage disposal systems using 2-D electrical resistivity imaging and geochemical analysis: A case study from Ibadan, Southwestern Nigeria. Environ. Eng. Geosci., 7(3):261-272.
- Alexander, M. (1999). Biodegradation and bioremediation. New York, New York, Academic Press.
- Alvarez-Cohen, L. and P. L. McCarty (1991). "A cometabolic bio-transformation model for halogenated aliphatic compounds exhibiting product toxicity." Environmental Science & Technology **25**(8): 1381-1387.
- Arvin, E. (1991). "Biodegradation kinetics of chlorinated aliphatic hydrocarbons with methane oxidizing bacteria in an aerobic fixed biofilm reactor." Water Research **7**: 873-881.
- Auer, L. H., N. D. Rosenberg, et al. (1996). "The effects of barometric pumping on contaminant transport." Journal of Contaminant Hydrology **24**(2): 145.
- Bakr, A. A., L. W. Gelhar, et al. (1978). "Stochastic analysis of spatial variability in subsurface flows: 1. Comparison of one- and three-dimensional flows." Water Resour. Res. **14**(2): 263-271.
- Battistelli, A. (2004). "Modeling biodegradation of organic contaminants under multiphase conditions with tmvobio." Vadose Zone Journal **3**: 875-883.
- Boublík, T., V. Fried, et al. (1973). The vapour pressures of pure substances: Selected values of the temperature dependence of the vapour pressures of some pure substances in the normal and low pressure region. New York, Elsevier.
- Bouchard, D., D. Hunkeler, et al. (2008). "Carbon isotope fractionation during diffusion and biodegradation of petroleum hydrocarbons in the unsaturated zone: Field experiment at vaerlose airbase, denmark, and modeling." Environmental Science & Technology **42**(2): 596-601.
- Bozkurt, O., K. G. Pennell, et al. (2009). "Simulation of the vapor intrusion process for nonhomogeneous soils using a three-dimensional numerical model." Ground Water Monitoring and Remediation **29**(1): 92-104.

- Braida, W. and S. K. Ong (1998). "Air sparging: Air-water mass transfer coefficients." Water Resour. Res. **34**(12): 3245-3253.
- Broholm, M. M., M. Christophersen, et al. (2005). "Compositional evolution of the emplaced fuel source in the vadose zone field experiment at airbase værløse, denmark." Environmental Science & Technology **39**(21): 8251-8263.
- Brooks, R. H. and A. T. Corey (1966). "Properties of porous media affecting fluid flow." J. Irrig. Drain. Div. Amer. Soc. Civil Eng. **92**(IR2): 61-88.
- Brunet P., Clement R., Bouvier C. 2010. Monitoring soil water content and deficit using electrical resistivity tomography (ERT) – A case study in the Cevennes area, France. J. of Hydrology. 380(1-2): 146-153.
- Brusseau, M; Carroll, K; Truex, M; and Becker, D. (2012) "Characterization and remediation of chlorinated volatile organic contaminants in the vadose zone." Vadose Zone Journal, doi:10.2136/vzj2012.0137. 1-17.
- Carr, D. B., L. C. Levy, et al. (2010). Vadose zone profiling to better understand vadose zone processes related to vapor intrusion.
- Carroll, K; Oostrom, M; Truex, M; Rohay, V; and Brusseau, M. (2012) "Assessing performance and closure for soil vapor extraction: Integrating vapor discharge and impact to groundwater quality." J. Contam. Hydrol., **128**, 71-82.
- Carroll, K; Truex, M; Brusseau, M; Parker, K; Mackley, R; Rohay, V. (2013) "Characterization of persistent volatile contaminant sources in the vadose zone." Groundwater Monitoring and Remediation. **33**(2) 68-84.
- Chao, K.-P., S. K. Ong, et al. (2008). "Mass transfer of vocs in laboratory-scale air sparging tank." J. Hazard. Mater. **152**: 1098-1107.
- Colorado Department of Public Health and Environment (2004). Draft indoor air guidance, Hazardous Materials and Waste Management Division, : 58.
- Conklin, M. H., T. L. Corley, et al. (1995). "Nonequilibrium processes affecting forced ventilation of benzene and xylene in a desert soil." Water Resources Research **31**: 1355-1365.
- Dagan, G. (1984). "Solute transport in heterogeneous porous formations." J. Fluid. Mech. **145**: 151-177.
- Dahlin T., Loke M.H. 1997. Quasi-3D imaging-mapping of three-dimensional structures using two-dimensional DC resistivity techniques. Proceedings of the 3rd Meeting of the Environ. Eng. Geophy. Soc.: 143-146.

- Davis, G. B., B. M. Patterson, et al. (2009). "Evidence for instantaneous oxygen-limited biodegradation of petroleum hydrocarbon vapors in the subsurface." Ground Water Monitoring and Remediation **29**: 126-137.
- Davis, G. B., J. L. Rayner, et al. (2005). "Measurement and modeling of temporal variation in hydrocarbon vapor behavior in a layered soil profile." Vadose Zone Journal **4**: 225-239.
- Department of Defense (2009). *Dod vapor intrusion handbook*: 171.
- Department of Toxic Substances Control (DTSC) (2005). *Guidance for the evaluation and mitigation of subsurface vapor intrusion in indoor air*. California Environmental Protection Agency.
- DeVaul, G. E. (2007). "Indoor vapor intrusion with oxygen-limited biodegradation for a subsurface gasoline source." Environmental Science & Technology **41**(9): 3241-3248.
- Ely, R. L., J. K. Williamson, et al. (1997). "Cometabolism of chlorinated solvents by nitrifying bacteria: Kinetics, substrate interactions, toxicity effects and bacterial response." Biotechnology and Bioengineering **54**(6): 520-534.
- Falta, R. W., I. Javandel, et al. (1989). "Density-driven flow of gas in the unsaturated zone due to the evaporation of volatile organic compounds." Water Resour. Res. **25**(10): 2159-2169.
- Fitzpatrick, N. A. and J. J. Fitzgerald (2002). "An evaluation of vapor intrusion into buildings through a study of field data." Soil & Sediment Contamination **11**(4): 603-623.
- Fogel, M. M., A. R. Taddeo, et al. (1986). "Biodegradation of chlorinated ethenes by a methane-utilizing mixed culture." Applied and Environmental Ecology **51**(4): 720-724.
- Folkes, D., W. Wertz, et al. (2009). "Observed spatial and temporal distributions of cvocs at colorado and new york vapor intrusion sites." Ground Water Monitoring and Remediation **29**(1): 70-80.
- Gaganis, P., P. Kjeldsen, et al. (2004). "Modeling natural attenuation of multicomponent fuel mixture in the vadose zone: Use of field data and evaluation of biodegradation effects." Vadose Zone Journal **3**: 1262-1275.
- Gelhar, L. W., A. L. Gutjahr, et al. (1979). "Stochastic analysis of macrodispersion in a stratified aquifer." Water Resour. Res. **15**(6): 1387-1397.
- Gorder, K. A. and E. M. Dettenmaier (2011). "Portable gc/ms methods to evaluate sources of cvoc contamination in indoor air." Ground Water Monitoring and Remediation **31**(4): 113-119.
- Griffiths D.H., Barker R.D. 1993. Two dimensional resistivity imaging and modeling in areas of complex geology. J. Appl. Geophy., 29: 211-226.

- Griffiths D.H., Turnbull J, Olayinka Al. 1990. Two-dimensional resistivity mapping with a complex controlled array. First Break, 8: 121-129.
- Harper, B. M., W. H. Stiver, et al. (2003). "Nonequilibrium nonaqueous phase liquid mass transfer for soil vapour extraction systems." Journal of Environmental Engineering **129**(8): 745-754.
- Hendrickson, E. R., J. A. Payne, et al. (2002). "Molecular analysis of dehalococcoides 16s ribosomal DNA from chloroethene-contaminated sites throughout north america and europe." Applied and Environmental Microbiology **68**: 485-495.
- Heron, G., T. H. Christensen, et al. (1998). "Henry's law constant for trichloroethylene between 10 and 95 °c." Environ. Sci. Technol. **32**: 1433-1437.
- Hers, I., J. Atwater, et al. (2000). "Evaluation of vadose zone biodegradation of btx vapours." Journal of Contaminant Hydrology **46**(3-4): 233.
- Ho, C. K. and K. K. Udell (1992). "An experimental investigation of air venting of volatile liquid hydrocarbon mixtures from homogeneous and heterogeneous porous media." Journal of Contaminant Hydrology **11**(3-4): 291.
- Illangasekare, T. H., E. J. Armbruster, et al. (1995a). "Non-aqueous phase fluids in heterogeneous aquifers: An experimental study." Journal of Environmental Engineering **121**: 571-579.
- Illangasekare T.H., Frippiat C.C. and Fučík R. (2010) Dispersion and Mass Transfer Coefficients in Groundwater of Near-surface Geologic Formations, in Handbook of Chemical Mass Transport in the Environment, Editors L. J. Thibodeaux and D. Mackay, CRC Press/Taylor and Francis Group.
- Illangasekare, T. H., J. L. Ramsey, Jr., et al. (1995b). "Experimental study of movement and distribution of dense organic contaminants in heterogeneous environments." J. Contam. Hydrol. **20**: 1-25.
- Imhoff, P. T., P. R. Jaffé, et al. (1994). "An experimental study of complete dissolution of a nonaqueous phase liquid in saturated porous media." Water Resources Research **30**(2): 307-320.
- Interstate Technology Regulatory Council (2007). Vapor intrusion pathway: A practical guideline: 172.
- Jang, W. and M. M. Aral (2007). "Density-driven transport of volatile organic compounds and its impact on contaminated groundwater plume evolution." Transport in Porous Media **67**: 353-374.

- Jeffers, P. M., L. M. Ward, et al. (1989). "Homogeneous hydrolysis rate constants for selected chlorinated methanes, ethanes, ethenes and propanes." Environ. Sci. Technol. **23**(1): 965-969.
- Jeng, C. Y., V. J. Kremesec, et al. (1996). Models of hydrocarbon vapor diffusion through soil and transport into buildings. Petroleum Hydrocarbons and Organic Chemicals In Groundwater: Prevention, Detection, and Remediation Conference, Houston, TX, National Ground Water Association.
- Johnson, P. C. (2002). Identification of critical parameters for the Johnson and Ettinger (1991) vapor intrusion model. Soil and Groundwater Research Bulletin Number 17, American Petroleum Institute: 39.
- Johnson, P. C. and R. A. Ettinger (1991). "Heuristic model for predicting the intrusion rate of contaminant vapors into buildings." Environmental Science & Technology **25**(8): 1445-1452.
- Johnson, P. C., R. A. Ettinger, et al. (2002). Migration of soil gas vapors to indoor air, American Petroleum Institute: 10.
- Johnson, P. C., R. A. Ettinger, et al. (2009). "Empirical assessment of ground water-to-indoor air attenuation factors for the CDOT-MTL Denver site." Ground Water Monitoring and Remediation **29**(1): 153-159.
- Kim, H., S. Lee, et al. (2005). "Gas transport of volatile organic compounds in unsaturated soils: Quantitative analysis of retardation processes." Soil Sci. Soc. Am. J. **69**: 990-995.
- Knauss, K. G., M. J. Dibley, et al. (1998). Aqueous oxidation of trichloroethene (tce): A kinetic and thermodynamic analysis. First International Conference on Remediation of Chlorinated and Recalcitrant Compounds, Monterey, California, Battelle Press.
- Krylov, V. V. and C. C. Ferguson (1998). "Contamination of indoor air by toxic soil vapors: The effects of subfloor ventilation and other protective measures." Building and Environment **33**(6): 331.
- Lahvis, M. A., A. L. Baehr, et al. (1999). "Quantification of aerobic biodegradation and volatilization rates of gasoline hydrocarbons near the water table under natural attenuation conditions." Journal of Contaminant Hydrology **19**: 47-67.
- Lenhard, R. J., M. Oostrom, et al. (1995). "Investigation of density-dependent gas advection of trichloroethylene: Experiment and a model validation exercise." Journal of Contaminant Hydrology **19**(1): 47.
- Liang, X., R. P. Philip, et al. (2009). "Kinetic and isotope analysis of tetrachloroethylene and trichloroethylene degradation by model Fe(II)-bearing minerals." Chemosphere **75**: 63-69.

- Little, J. C., J. M. Daisey, et al. (1992). "Transport of subsurface contaminants into buildings." Environmental Science & Technology **26**(11): 2058-2066.
- Liu, H. H. and F. J. Molz (1997). "Block-scale dispersivity for heterogeneous porous media characterized by stochastic fractals." Geophysical research letters **24**(17): 2239-2242.
- Lugg, G. A. (1968). "Diffusion coefficients of some organic and other vapors in air." Anal. Chem. **40**(7): 1072-1077.
- Luo, H., P. Dahlen, et al. (2009). "Spatial variability of soil-gas concentrations near and beneath a building overlying shallow petroleum hydrocarbon-impacted soils." Ground Water Monitoring and Remediation **29**(1): 81-91.
- Maymo-Gatell, X., Y. Chien, et al. (1997). "Isolation of a bacterium that reductively dechlorinates tetrachloroethene to ethene." Science **276**(5318): 1568-1571.
- McHugh, T. E., R. Davis, et al. (2010). "Evaluation of vapor attenuation at petroleum hydrocarbon sites: Considerations for site screening and investigation." Soil & Sediment Contamination **19**: 725-745.
- McHugh, T. E., P. C. de Blanc, et al. (2006). "Indoor air as a source of voc contamination in shallow soils below buildings." Soil & Sediment Contamination **15**: 103-122.
- McHugh, T. E., T. N. Nickels, et al. (2007). Evaluation of spatial and temporal variability in voc concentrations at vapor intrusion investigation sites. Proceedings of Air & Waste Management Association's Vapor Intrusion: Learning from the Challenges, Providence, RI.
- Mendoza, C. A. and E. O. Frind (1990a). "Advective-dispersive transport of dense organic vapors in the unsaturated zone: 1. Model development." Water Resour. Res. **26**(3): 379-387.
- Mendoza, C. A. and E. O. Frind (1990b). "Advective-dispersive transport of dense organic vapors in the unsaturated zone: 2. Sensitivity analysis." Water Resour. Res. **26**(3): 388-398.
- Michot D. et al. 2003. Spatial and temporal monitoring of soil water content with an irrigated corn crop cover using surface electrical resistivity tomography. Water Resour. Res. **39**(5): Article #1138.
- Miller, C. T., M. M. Poirier-McNeill, et al. (1990). "Dissolution of trapped nonaqueous phase liquids: Mass transfer characteristics." Water Resour. Res. **26**(11): 2783-2796.
- Millington, R. J. and J. P. Quirk (1961). "Permeability of porous solids." Trans. Faraday. Soc. **57**: 1200-1207.

- Millington, R. J. and R. C. Shearer (1971). "Diffusion in aggregated porous media." Soil Science **111**: 372-378.
- Mills, W. B., S. Liu, et al. (2007). "Time-variable simulation of soil vapor intrusion into a building with a combined crawl space and basement." Environmental Science & Technology **41**(14): 4993-5001.
- Moseley, C. L. and M. R. Meyer (1992). "Petroleum contamination of an elementary school: A case history involving air, soil-gas, and groundwater monitoring." Environmental Science & Technology **26**(1): 185-192.
- Nambi, I. M. and S. E. Powers (2003). "Mass transfer correlations for nonaqueous phase liquid dissolution from regions with high initial saturations." Water Resources Research **39**(2).
- Nazaroff, W. W., S. R. Lewis, et al. (1987). "Experiments on pollutant transport from soil into residential basements by pressure-driven airflow." Environ. Sci. Technol. **21**: 459-466.
- Olaniran, A. O., D. Pillay, et al. (2008). "Aerobic biodegradation of dichloroethenes by indigenous bacteria isolated from contaminated sites in africa." Chemosphere **73**(1): 24-29.
- Olayinka Al. 1999. Advantage of two-dimensional geoelectrical imaging for groundwater prospecting: case study from Ira, southwestern Nigeria. *Water Res. J. Nig. Assoc. Hydrogeol.* 10: 103-113.
- Olayinka Al., Yaramanci U. 1999. Choice of the best model in 2-D geoelectrical imaging: case study from a waste dump site. *Eu. J. Environ. Eng. Geophy.*, 3: 221-244.
- Olson, D. A. and R. L. Corsi (2001). "Characterizing exposure to chemicals from soil vapor intrusion using a two-compartment model." Atmospheric Environment **35**(24): 4201.
- Ong, S. K., T. B. Culver, et al. (1992). "Effects of soil moisture and physical-chemical properties of organic pollutants on vapor-phase transport in the vadose zone." Journal of Contaminant Hydrology **11**(3-4): 273.
- Ong, S. K. and L. W. Lion (1991). "Effects of soil properties and moisture on the sorption of trichloroethylene vapor." Water Research **25**(1): 29.
- Ostrom, M., J. H. Dane, et al. (2005). "Removal of carbon tetrachloride from a layered porous medium by means of soil vapor extraction enhanced by dessication and water table reduction." Vadose Zone Journal **4**: 1170-1182.
- Ostendorf, D. W. and D. H. Kampbell (1991). "Biodegradation of hydrocarbon vapors in the unsaturated zone." Water Resour. Res. **27**(4): 453-462.
- Ozcep F., Tezel O., Asci M. 2009. Correlation between electrical resistivity and soil-water content: Istanbul and Golcuk. International Journal of Physical Sciences. 4 (6): 362-365.

- Pant, P. and S. Pant (2010). "A review: Advances in microbial remediation of trichloroethylene (tce)." Journal of Environmental Sciences **22**(1): 116-126.
- Parker, B., J. A. Cherry, et al. (2003). "Review and analysis of chlorinated solvent dense nonaqueous phase liquid distributions in five sandy aquifers." Vadose Zone Journal **2**: 116-137.
- Parker, J. C. (2003). "Physical processes affecting natural depletion of volatile chemicals in soil and groundwater." Vadose Zone Journal **2**: 222-230.
- Pennell, K. G., O. Bozkurt, et al. (2009). "Development and application of a three-dimensional finite element vapor intrusion model." J. Air & Waste Manage. Assoc. **59**(4): 447-460.
- Petri, B. (2014 - in preparation) "Improved understanding of dynamic vapor plume behavior for vapor intrusion pathway assessment: fundamental transport process interactions driven by variable soil moisture." PhD dissertation, Colorado School of Mines. Advisor: Tissa Illangasekare.
- Poulsen, M. M. and B. H. Kueper (1992). "A field experiment to study the behavior of tetrachloroethylene in unsaturated porous media." Environmental Science & Technology **26**(5): 889-895.
- Poulsen, T. G., P. Moldrup, et al. (2006). "Bimodal probability law model for unified description of water retention, air and water permeability, and gas diffusivity in variably saturated soil." Vadose Zone Journal **5**: 1119-1128.
- Powers, S. E., L. M. Abriola, et al. (1994). "Phenomenological models for transient napl-water mass-transfer processes." Journal of Contaminant Hydrology **16**: 1-33.
- Rabideau, A. J., J. M. Blayden, et al. (1999). "Field performance of air-sparging system for removing tce from groundwater." Environ. Sci. Technol. **33**: 157-162.
- Rajaram, H. and L. W. Gelhar (1995). "Plume-scale dependent dispersion in aquifers with a wide range of scales of heterogeneity." Water Resour. Res. **31**(10): 2469-2482.
- Rivett, M. O., G. P. Wealthall, et al. (2011). "Review of unsaturated zone transport and attenuation of volatile organic compound (voc) plumes leached from shallow source zones." J. Contam. Hydrol. **123**: 130-156.
- Robinson, A. L., R. G. Sextro, et al. (1997). "Soil-gas entry into an experimental basement driven by atmospheric pressure fluctuations-measurements, spectral analysis, and model comparison." Atmospheric Environment **31**(10): 1477-1485.
- Ruiz, J., R. Bilbao, et al. (1998). "Adsorption of different voc onto soil minerals from gas phase: influence of mineral, type of voc, and air humidity." Environmental Science & Technology **32**(8): 1079-1084.

- Russo, D. (1992). "Upscaling of hydraulic conductivity in partially saturated heterogeneous porous formation." Water Resour. Res. **28**(2): 397-409.
- Saba, T. and T. H. Illangasekare (2000). "Effect of groundwater flow dimensionality on mass transfer from entrapped nonaqueous phase liquid contaminants." Water Resour. Res. **36**(4): 971-979.
- Sakaki, T., P. E. Schulte, et al. (2012). "Airflow pathway dynamics in heterogeneous subsurface influenced by land surface boundary conditions." Vadose Zone Journal: in review.
- Schwartz B.F., Schreiber M.E., Yan T.T. 2008. Quantifying field-scale soil moisture using electrical resistivity imaging. J. of Hydrology. 362(3-4): 234-246.
- Seagren, E. A., B. E. Rittman, et al. (1999). "A critical evaluation of the local-equilibrium assumption in modeling npl-pool dissolution." Journal of Contaminant Hydrology **39**: 109-135.
- Sheriff R.E. 2004. Encyclopedic Dictionary of Exploration Geophysics, Geophysical Reference Series 1, Fourth Edition.
- Shen, L. and Z. Chen (2007). "Critical review on the impact of tortuosity on diffusion." Chemical Engineering Science **62**(14): 3748-3755.
- Shoemaker, C. A., T. B. Culver, et al. (1990). "Analytical models of the impact of two-phase sorption on subsurface transport of volatile chemicals." Water Resour. Res. **26**(4): 745-758.
- Shonnard, D. R., R. L. Bell, et al. (1993). "Effects of nonlinear sorption on the diffusion of benzene and dichloromethane from two air-dry soils." Environmental Science & Technology **27**(3): 457-466.
- Siegel, L. (2009). "Stakeholders' views on vapor intrusion." Ground Water Monitoring and Remediation **29**(1): 53-57.
- Smith, J. A., C. T. Chiou, et al. (1990). "Effect of soil moisture on the sorption of trichloroethene vapor to vadose-zone soil at picatinny arsenal, new jersey." Environmental Science & Technology **24**(5): 676-683.
- Sposito, G., W. A. Jury, et al. (1986). "Fundamental problems in the stochastic convection-dispersion model of solute transport in aquifers and field soils." Water Resour. Res. **22**(1): 77.
- Stone, H. L. (1973). "Estimation of three phase relative permeability and residual oil data." J. Can. Pet. Technol. **12**(4): 53-61.

- Szatkowski, A., P. T. Imhoff, et al. (1995). "Development of a correlation for aqueous-vapor phase mass transfer in porous media." Journal of Contaminant Hydrology **18**: 85-106.
- Thoma, G., J. Swofford, et al. (1999). "Effect of dynamic competitive sorption on the transport of volatile organic chemicals through dry porous media." Water Resour. Res. **35**(5): 1347-1459.
- Thomson, N. R., J. F. Sykes, et al. (1997). "A numerical investigation into factors affecting gas and aqueous phase plumes in the subsurface." Journal of Contaminant Hydrology **28**(1-2): 39.
- Tillman, F. D., J.-W. Choi, et al. (2003). "A comparison of direct measurement and model simulation of total flux of volatile organic compounds from the subsurface to the atmosphere under natural field conditions." Water Resour. Res. **39**(10): 1284.
- Tillman, F. D. and J. W. Weaver (2007). "Temporal moisture content variability beneath and external to a building and the potential effects on vapor intrusion risk assessment." Science of The Total Environment **379**(1): 1.
- United State Environmental Protection Agency (2002). Draft guidance for evaluating the vapor intrusion to indoor air pathway from groundwater and soil. Office of Solid Waste and Emergency Response: 178.
- United State Environmental Protection Agency (2008). "Epa on-line tools for site assessment calculation." Retrieved February 29, 2008, from http://www.epa.gov/ATHENS/learn2002model/part-two/onsite/jne_background_reverse.htm.
- Ursino, N., T. Gimmi, et al. (2001). "Combined effects of heterogeneity, anisotropy, and saturation on steady state flow and transport: A laboratory sand tank experiment." Water Resour. Res. **37**(2): 201-208.
- van Genuchten, M. T. (1980). "A closed-form analytical equation for predicting the hydraulic conductivity of unsaturated soils." Soil Sci. Soc. Am. J. **44**(5): 892-898.
- Verginelli, I. and R. Baciocchi (2011). "Modeling of vapor intrusion from hydrocarbon-contaminated sources accounting for aerobic and anaerobic biodegradation." J. Contam. Hydrol. **126**: 167-180.
- Wang, F. and I. C. Ward (2002). "Radon entry, migration and reduction in houses with cellars." Building and Environment **37**: 1153-1165.
- Werner, D., P. Grathwhol, et al. (2004). "Review of field methods for the determination of the tortuosity and effective gas-phase diffusivity in the vadose zone." Vadose Zone Journal **3**: 1240-1248.

- Wilkins, M. D., L. M. Abriola, et al. (1995). "An experimental investigation of rate-limited nonaqueous phase liquid volatilization in unsaturated porous media: Steady state mass transfer." Water Resour. Res. **31**(9): 2159-2172.
- Yang, Y. and P. L. McCarty (1998). "Competition for hydrogen within a chlorinated solvent dehalogenating anaerobic mixed culture." Environmental Science & Technology **32**: 3591-3597.
- Yoon, H., J. H. Kim, et al. (2002). "Effect of water content on transient nonequilibrium napl-gas mass transfer during soil vapor extraction." Journal of Contaminant Hydrology **54**: 1-18.
- Yu, S., A. J. A. Unger, et al. (2009). "Simulating the fate and transport of tce from groundwater to indoor air." Journal of Contaminant Hydrology **107**: 140-161.

Chapter 3: Modeling Approaches

3.0 Introduction

Since models play an integral role in vapor intrusion screening and analysis, we considered it important to explore new and existing models to determine what role weather and climate may play in the VI pathway. Our objective was to review current VI models for use as the baseline for model development and testing with project experiments. Based on these models, we can then make suggestions for how weather and climate factors affect VI, and discuss limitations of existing models as well as improved modeling approaches.

3.1 Current and proposed VI models

Current conceptual models of vapor transport in the vadose zone commonly assume a steady-state diffusion-dominated process (Johnson and Ettinger, 1991; Abreu and Johnson, 2005; DeVaul, 2007; Davis et al., 2009) (see chapter 2.3 for a review of current VI models). The steady-state assumption is usually made because short-term temporal variability (~days) in vapor concentrations is often not significant at depths greater than about 1.3 m (4 ft) (Hartmen, 2006; ITRC, 2007). In the absence of strong gas phase advection, diffusion is assumed to dominate (Rivett et al., 2011). Figure 3.1 illustrates the current, most commonly applied VI pathway conceptual model. This model is usually applied in a one-dimensional transport regime (Johnson and Ettinger, 1991; DeVaul 2007; Davis et al., 2009), though more recent numerical models have explored two- and three-dimensional effects and heterogeneities (Abreu et al., 2005; Bozkurt et al., 2009; Yao et al., 2011). In the model, the source of VOCs is usually a shallow groundwater plume assumed to be in equilibrium with the vadose zone. This elutes a vapor phase, which then diffuses through the vadose zone environment and towards the atmospheric surface where soil gas may exchange with the atmosphere (Johnson and Ettinger, 1991, Abreu and Johnson, 2005, Bozkurt et al., 2009). Soil gas advection may be included in the conceptual model within the immediate proximity of a building foundation, where pressure differentials between indoor air and soil gas commonly drive soil gas flow into the building (Nazaroff et al., 1987; Abreu and Johnson, 2005; Bozkurt et al., 2009). Advection within the rest of the vadose zone is typically neglected (Johnson and Ettinger, 1991; DeVaul, 2007; Davis et al., 2009; Verginelli and Baciocchi, 2011), though the role of barometric pumping and related dispersion has been acknowledged (Parker, 2003; Parker et al., 2003).

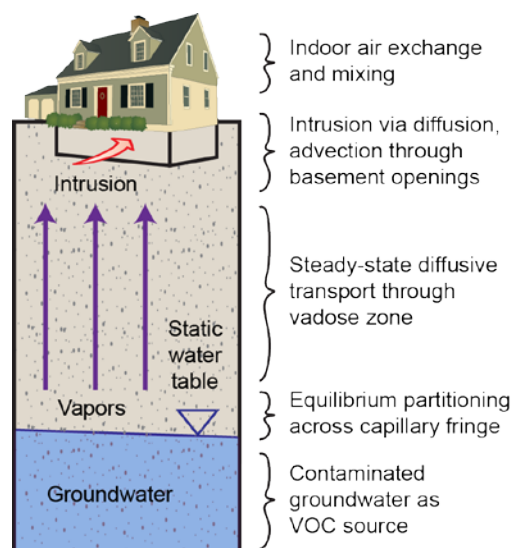


Figure 3.1: Current pathway conceptual model of the subsurface component of the VI pathway.

However, despite the wide application of the VI conceptual model in figure 3.1 (especially Johnson and Ettinger, 1991), field data suggest a more spatially and temporally complex system (McHugh et al., 2004, McHugh et al., 2007, Folkes et al., 2009). A more comprehensive description of environmental factors that may help explain some of this spatial and temporal variability was presented in figure 1.1 discussed earlier. These must be translated into a capable model to enable exploration of these processes. This project is primarily focused on the subsurface portion of this model, and thus will not fully explore the factors within the building zone as well as the atmosphere. To explore the subsurface component of the pathway, the model must incorporate multiple phase flow for air, water, and/or NAPL phases, advective and diffusive transport of VOCs within the air and water phases, mass transfer between air, water and NAPL phases, and in some cases heat transport. A process conceptual diagram of this proposed model was in Figure 2.1. The following sections describe the numerical formulation that implements these processes.

3.2 Modeling approaches

Because this study involved multiple experiments with multiple objectives, and the modeling goals included exploration of different modeling approaches, the models developed needed flexibility in formulation. This flexibility eliminated the opportunity to use traditional transport models that are “hard” coded in terms of governing equations and constitutive relations. For instance, some commercially available groundwater modeling packages may solve unsaturated flow equations using the Richards Equation, which incorporates the assumption that gas pressure is atmospheric throughout the unsaturated domain. However, this approach does not allow for the exploration of advection effects in the gas phase. To achieve the required flexibility, two models were used throughout the project. The first model was a research model developed within COMSOL Multiphysics, v3.5a, which is a software program that numerically solves systems of coupled, non-linear differential equations using a MATLAB platform. The primary advantage of this software is increased flexibility in applying and changing the governing equations that the model solves, which in turn allows a user to more easily explore complex

physical processes. The primary disadvantage of such a modeling approach is that in order for the numerical solvers to have sufficient flexibility to solve highly complex problems, computational efficiency and stability are often reduced. Thus the COMSOL modeling approach is largely a research tool for exploring physical behavior, but is not a “production” code. This can make sensitivity analysis challenging because of long model run times or stability issues with individual test cases. The second model used was developed in collaboration with the Czech Technical University, and is intended to be used as a more efficient production code for future exploration. It was beyond the scope of this project to fully verify and validate this separate model since it was produced through independent collaboration with the objective of doing a more thorough exploration of upscaled vapor transport in more realistic heterogeneous field conditions in the future. This model is further described in appendix A.

3.3 General model formulation

This section summarizes the formulation of the models used throughout the project at the general level. This formulation includes macroscopic mass, momentum and energy balance equations. It is assumed that water and gas phases are mobile, and the NAPL phase is immobile. The gas phase is assumed to be compressible and is an ideal gas mixture of organic vapor, water vapor and dry air. The water phase is assumed contain dissolved NAPL and water. The NAPL phase is assumed to contain a pure single component. Advection, diffusion and dispersion processes are considered for the fate of NAPL vapor in the gas phase and dissolved NAPL in the water phase assuming non-equilibrium mass transfer reactions among NAPL-water, NAPL-gas and water-gas phases.

However, the model formulations were customized for each series of experiments. For instance, the dynamic soil moisture experiments described in section 4.5 explored infiltration of water in heterogeneous media along with heat-induced evaporation, but did not contain any contaminant vapor. Therefor in the model, only the air and water flow equations, and the heat transport equation were solved. Meanwhile, in the large tank experiments described in section 4.6, heat was not incorporated (the experiment was essentially isothermal), while contaminant transport and mass transfer were included. Thus, the heat equation was neglected, but solute transport was included.

The mass balance equation for an incompressible mobile water phase in a non-deformable porous medium (Bear, 1972) is given by

$$\frac{\partial \theta_w}{\partial t} + \nabla \cdot (\mathbf{q}_w) = -\frac{R_{gw}^1}{\rho_w} \quad (1)$$

where ρ_w is the water density, θ_w is the water content, and R_{gw}^1 is the phase change rate for water vapor between water and gas phases. \mathbf{q}_w is the macroscopic velocity for water that is expressed by a momentum balance using Darcy’s law:

$$\mathbf{q}_w = -\frac{k_{rw} k_s}{\mu_w} \cdot \nabla (p_w + \rho_w \mathbf{g}z) \quad (2)$$

where k_s is the saturated permeability, k_{rw} is the relative permeability and μ_w is the viscosity of water, p_w is the pressure of water. Mass balance for the compressible mobile gas phase can be written

$$\rho_g \frac{\partial \theta_g}{\partial t} + \theta_g \frac{\partial \rho_g}{\partial t} + \nabla \cdot (\rho_g \mathbf{q}_g) = 0 \quad (3)$$

where ρ_g is the density of the gas phase, θ_g is the volumetric gas content and q_g is the Darcy velocity for gas, expressed as:

$$\mathbf{q}_g = -\frac{k_{rg} k_s}{\mu_g} \cdot \nabla (p_g + \rho_g \mathbf{g}z) \quad (4)$$

where k_{rg} is the relative permeability of gas and μ_g is the viscosity of gas, p_g is the pressure of gas. Water and gas pressures are coupled by the macroscopic capillary pressure relationship $p_c(S_w) = p_g - p_w$ where S_w is the water saturation. The constitutive relationship $p_c - S_w$ curve relates p_c to S_w (or, equivalently, the gas saturation). To compute the saturation and relative permeability of the gas and water phases from p_c , van-Genuchten water retention [van Genuchten, 1980] and van-Genuchten-Mualem relative permeability models [Mualem, 1976] were used. The conservation of mass for the immobile NAPL phase can be expressed as

$$\rho_n \frac{\partial \theta_n}{\partial t} = R_{nw} - R_{ng} \quad (5)$$

The immobilized NAPL phase can dissolve in water phase or volatilize into the air phase. The first term on the right hand side is the mass transfer rate between water and NAPL, and the second term represents the mass transfer rate between NAPL and gas. The two-phase (air-water) capillary pressure-saturation relationship, $f(p_c)$, is assumed to hold in the presence of an immobile NAPL phase and expressed by modifying the van Genuchten (1984) water retention function:

$$\frac{\theta_w - \theta_{rw}}{\theta_s - \theta_{rw} - \theta_n} = f(p_c) = \left[1 + (\alpha h_c)^n \right]^{-(1-1/n)}; \quad h_c = \frac{p_c}{\rho_w g} \quad (6)$$

Substitution of Eq. (6), equations (1) and (3) can be rewritten as

$$\frac{\partial \theta_w}{\partial p_c} \frac{\partial p_c}{\partial t} - f(p_c) \frac{\partial \theta_n}{\partial t} + \nabla \cdot (\mathbf{q}_w) = -\frac{R_{gw}}{\rho_w} \quad (7)$$

$$-\rho_g \frac{\partial \theta_w}{\partial p_c} \frac{\partial p_c}{\partial t} - \rho_g [1 - f(p_c)] \frac{\partial \theta_n}{\partial t} + \theta_g \frac{\partial \rho_g}{\partial t} + \nabla \cdot (\rho_g \mathbf{q}_g) = 0 \quad (8)$$

If there is no NAPL phase in the domain, the second terms on the left hand side involving the NAPL time derivative become zero. Based on the Ideal gas law for the mixture of water vapor, air and NAPL vapor, the density of the gas can be expressed as

$$\rho_g = \frac{(p_g + p_{atm})/(RT)}{1/M_w + w_a(1/M_a - 1/M_w) + w_n(1/M_n - 1/M_w)} \quad (9)$$

where R is the gas constant, T is the temperature, M_w is the molecular weight of water, M_a is the molecular weight of air, and M_n is the molecular weight of NAPL. w_i is the mass ratio for each component (mass of component i divided by total mass), and sub-indices a , w and n stand for air, water and NAPL. For the three component gas phase,

$$w_a + w_w + w_n = 1 \quad (10)$$

Transport of the components in the gas phase is described using the advection-dispersion equation (ADE). For a three-component system, there must be two ADEs, and the third phase mass ratio is computed from Eq. (10). The ADE for water vapor is

$$\frac{\partial \rho_g w_w \theta_g}{\partial t} + \nabla \cdot (\rho_g w_w \mathbf{q}_g - D_{wg} \theta_g \rho_g \nabla w_w) = R_{gw}^1 \quad (11)$$

where D_{wg} is the hydrodynamic dispersion equal to the sum of effective diffusion and dispersion coefficients. This is commonly defined by eq (12).

$$\mathbf{D}_i = (\alpha_L - \alpha_T) \frac{\mathbf{u}_i \mathbf{u}_i^T}{|\mathbf{u}_i|} + \left(\alpha_T |\mathbf{u}_i| + D_{m,i} \frac{\theta_i^{10/3}}{\phi^2} \delta_{ij} \right) \quad i = g, w \quad (12)$$

where, α_L is the longitudinal dispersivity (m), α_T is the transverse dispersivity (m), $D_{m,g}$ is the molecular diffusion coefficient of TCE in phase i ($\text{m}^2 \text{s}^{-1}$), θ_i is volumetric content of phase i , and $\delta_{i,j}$ is the Kronecker Delta function.

The ADE for NAPL vapor in the gas phase is

$$\frac{\partial \rho_g w_n \theta_g}{\partial t} + \nabla \cdot (\rho_g w_n \mathbf{q}_g - D_{ng} \theta_g \rho_g \nabla w_n) = R_{gw}^2 + R_{ng} \quad (13)$$

where R_{gw}^2 is the mass transfer rate of NAPL vapor between the gas and water phases. Mass balance for dissolved NAPL is also described by the ADE:

$$\frac{\partial c_n \theta_w}{\partial t} + \nabla \cdot (c_n \mathbf{q}_w - D_{mw} \theta_w \nabla c_n) = -R_{gw}^2 - R_{mw} \quad (14)$$

Different approaches may be used to solve for mass transfer between phases. The simplest model assumes local equilibrium between air and water phases to hold throughout the entire model

domain. Local equilibrium between gas and water phase NAPL (e.g. TCE) concentrations may be expressed by Henry's Law:

$$H_T = \frac{c_g}{c_w} \quad (15)$$

where H_T is the dimensionless Henry's Law constant corrected for system temperature T (K). When this assumption is employed, Eq. (14) can be expressed in terms of the gas phase concentration and then added into Eq. (13), effectively reducing two differential equation to one. However, if non-equilibrium exists between the gas and water, or NAPL and gas, then Eq. (13) and Eq. (14) must be coupled through a separate rate equation for R_{gw} ² and R_{nw} .

Energy conservation in a macroscopic system containing water, gas and solid phases can be expressed as

$$\frac{\partial \rho_b C_b T}{\partial t} + \nabla \cdot (C_g \rho_g T \mathbf{q}_g + C_w \rho_w T \mathbf{q}_w - \lambda_T \nabla T) = -LR_{gw} \quad (12)$$

where ρ_b is the bulk density, C_b is the effective heat capacity per unit volume of soil, C_w , C_g , and C_s are the specific heat capacities of water, gas, and solid, respectively, λ_T is the effective thermal conductivity, and L is the latent heat coefficient. In this study, C_b is estimated based on the averaging of the specific heat capacities of water (C_w), gas (C_g), and solid (C_s) weighted with density values and volumetric water contents. The second term on the left hand side of Eq. (14) includes convection due to the flow of gas and water, and heat conduction. The effective soil thermal conductivity, λ_T , is generally estimated using empirical correlations [*de Vries*, 1963; *Chung and Horton*, 1987; *Campbell et al.*, 1994]. The empirical model presented by *Campbell et al.* [1994], which improves upon the *de Vries* [1963] model by taking temperature variations into account, was used in this study.

These served multiple purposes throughout the study. One purpose was to test the models and their formulations to determine when they could properly predict the vapor plume behavior or otherwise gain an insight as to whether other physical processes need to be incorporated. Another purpose was to assist in data analysis, because the models allow prediction and estimation of physical processes, such as diffusion, which cannot be readily measured or visually observed. Through the use of these models, many important observations and findings were made and are incorporated into the results and discussion.

3.4 References:

- Abreu, L. D. V. and P. C. Johnson (2005). "Effect of vapor source-building separation and building construction on soil vapor intrusion as studied with a three-dimensional numerical model." *Environmental Science & Technology* **39**(12): 4550-4561.
- Bear, J. (1972). *Dynamics of fluids in porous media*. New York, Elsevier.

- Bozkurt, O., K. G. Pennell, et al. (2009). "Simulation of the vapor intrusion process for nonhomogeneous soils using a three-dimensional numerical model." *Ground Water Monitoring and Remediation* **29**(1): 92-104.
- Campbell, G.S., J.D. Jungbauer, W.R. Bidlake, and R.D. Hungerford. 1994. Predicting the effect of temperature on soil thermal-conductivity. *Soil Sci.* 158:307-313.
- Chung, S.O., and R. Horton (1987), Soil heat and water-flow with a partial surface mulch. *Water Resour. Res.*, 23:2175-2186.
- Davis, G. B., B. M. Patterson, et al. (2009). "Evidence for instantaneous oxygen-limited biodegradation of petroleum hydrocarbon vapors in the subsurface." *Ground Water Monitoring and Remediation* **29**: 126-137.
- DeVaull, G. E. (2007). "Indoor vapor intrusion with oxygen-limited biodegradation for a subsurface gasoline source." *Environmental Science & Technology* **41**(9): 3241-3248.
- de Vries, D.A. 1963. Thermal properties of soils. p. 210-235. In W. R. van Wijk. (ed.) *Physics of plant environment*. North-Holland Publishing Company, Amsterdam, the Netherlands.
- Folkes, D., W. Wertz, et al. (2009). "Observed spatial and temporal distributions of VOCs at Colorado and New York vapor intrusion sites." *Ground Water Monitoring and Remediation* **29**(1): 70-80.
- Hartman, B. (2006). "How to collect reliable soil gas data for risk-based applications, specifically vapor intrusion: Part 4 - updates on soil gas collection and analytical procedures." *L.U.S.T Bulletin* **53**.
- Interstate Technology Regulatory Council (2007). *Vapor intrusion pathway: A practical guideline*: 172.
- Johnson, P. C. and R. A. Ettinger (1991). "Heuristic model for predicting the intrusion rate of contaminant vapors into buildings." *Environmental Science & Technology* **25**(8): 1445-1452.
- McHugh, T. E., J. A. Connor, et al. (2004). "An empirical analysis of the groundwater-to-indoor-air exposure pathway: The role of background concentrations in indoor air." *Environmental Forensics* **5**: 33-44.
- McHugh, T. E., T. N. Nickels, et al. (2007). *Evaluation of spatial and temporal variability in VOC concentrations at vapor intrusion investigation sites*. Proceedings of Air & Waste Management Association's Vapor Intrusion: Learning from the Challenges, Providence, RI.
- Mualem, Y. (1976). "A new model for predicting the hydraulic conductivity of unsaturated porous media." *Water Resour. Res.* **12**(3): 513-522.
- Nazaroff, W. W., S. R. Lewis, et al. (1987). "Experiments on pollutant transport from soil into residential basements by pressure-driven airflow." *Environ. Sci. Technol.* **21**: 459-466.

- Parker, B., J. A. Cherry, et al. (2003). "Review and analysis of chlorinated solvent dense nonaqueous phase liquid distributions in five sandy aquifers." *Vadose Zone Journal* **2**: 116-137.
- Parker, J. C. (2003). "Physical processes affecting natural depletion of volatile chemicals in soil and groundwater." *Vadose Zone Journal* **2**: 222-230.
- Rivett, M. O., G. P. Wealthall, et al. (2011). "Review of unsaturated zone transport and attenuation of volatile organic compound (voc) plumes leached from shallow source zones." *J. Contam. Hydrol.* **123**: 130-156.
- van Genuchten, M. T. (1980). "A closed-form analytical equation for predicting the hydraulic conductivity of unsaturated soils." *Soil Sci. Soc. Am. J.* **44**(5): 892-898.
- Verginelli, I. and R. Baciocchi (2011). "Modeling of vaporintrusion from hydrocarbon-contaminated sources accounting for aerobic and anaerobic biodegradation." *J. Contam. Hydrol.* **126**: 167-180.
- Yao, Y., R. Shen, et al. (2011). "Comparison of the johnson-ettinger vapor intrusion screening model predictions with full three-dimensional model results." *Environ. Sci. Technol.* **45**: 2227-2235.

Chapter 4: Materials and Methods

4.1 Project approach

To probe the research questions and objectives posed in section 1.2 and 1.3, a series of experimental and modeling tasks were performed. Recall, the main objective of this work was an improved understanding of the processes and mechanisms controlling vapor generation from entrapped NAPL sources and groundwater plumes, their subsequent migration through the subsurface, and their attenuation in naturally heterogeneous vadose zones under various natural physical, climatic, and geochemical conditions. Toward this end, experiments conducted at multiple scales were integrated with analytical and numerical modeling and field data to test new and existing VI theories and models. The overall project approach was outlined in section 1.3. This chapter presents more details on the objectives of each study component, as well as the methodology and materials employed. Since there was much overlap of materials and methodologies between each specific set of experiments, the first section of this chapter is devoted to general analytical methods that were utilized across all of the studies. Following this review, a specific description of each experiment, apparatus and procedure is given.

4.2 General Analytical Methods and Materials

Throughout the project, a series of experimental apparatuses, materials and methodologies were used to investigate vapor mass transfer, flow, transport and intrusion. In many cases, these materials, methods and equipment were identical or similar. These equipment and methods are summarized in the section below.

4.2.1 Apparatus:

Throughout the project, a variety of experimental apparatus at varied scales were used to test the hypothesis and explore the research questions outlined in chapter 1. In general, these apparatus can be described as either “bench-scale” or “intermediate-scale.” At the “bench-scale”, physical and chemical processes may be explored under tightly controlled conditions, and often multiple sets of independent experiments may be conducted. For this project, the “bench-scale” consisted of experiments conducted in small flow cells packed with porous media. The “intermediary-scale” (also referred to as intermediate scale) represents an experimental scale that is between the bench and the field scale (Ostrom et al., 2006; 2007), which allows observation and testing of larger-scale interacting phenomena than can be observed at the bench scale, or reliably controlled at the field scale. For instance, infiltration and water table fluctuation are important factors that manifest themselves at the field scale, and intermediate-scale testing allows the investigation of how they affect vapor transport. Because of the larger complexity of the intermediate scale, typically fewer experiments are run, but those experiments are generally longer, more intensively instrumented and monitored than at the bench scale. Table 4.1 presents the dimensions of the various apparatus that were used.

Table 4.1: Characteristics of experimental apparatus:

	NAPL volatilization	Capillary Fringe volatilization	Dynamic soil moisture / ERT tank	Integrated dynamic flow and vapor transport
Scale	Bench	Bench	Intermediate	Intermediate
Tank Dimensions (m, L x H x D)	0.28m x 0.15m x 0.025m	0.40m x 0.30m x 0.05m	2.44m x 1.22m x 0.076m	4.88m x 1.22m x 0.057m
Tank Materials	glass, aluminum	acrylic	acrylic	glass, aluminum

4.2.2 Analytical methods

A variety of analytical methods were used throughout the project to measure various physical and chemical parameters important to each experimental system. These are summarized below.

4.2.2.1 Gas phase TCE analysis: Since the overall emphasis of the project was evaluation of vapor phase contamination in soil gas and indoor air, a reliable, repeatable method for VOC analysis in air was necessary. Trichloroethylene (TCE) was used as a model volatile organic contaminant (VOC) throughout the project since it is a common target of vapor intrusion investigations, and previous studies in our laboratory have built a knowledge base from working with TCE (Illangasekare et al. 2006; Siegrist et al. 2006; Lowry et al. 2012). However, many challenges in analyzing for gas phase TCE concentrations were initially encountered as much of our previous experience focused on groundwater analysis. One challenge posed by our unique experimental apparatuses developed for this study is that only very small sample sizes (~1 mL or less) are practical for grab samples. Pulling larger sample volumes generally disturbs the airflow fields. Thus, methods like EPA TO-15 tend to be impractical at this laboratory scale. Some initial studies using gas phase grab sampling with gastight syringes and manual injection into a gas chromatograph (GC) indicated problems with calibration and repeatability. To surmount this challenge, a shift in sampling methodology and experimental approach was made by purchasing a fully automated gas sampling valve system for the GC. This system (HP6890 GC, flame ionization detector, automated gas sampling valve, split/splitless inlet, and Zebron ZB-624 30 m x 0.53 mm polysiloxane column) allowed direct connection of the GC to the experimental apparatus, removed all manual handling of gas samples, and proved far more repeatable and reliable. This adjustment also shifted the sampling focus away from limited grab sampling at discrete points in time and space toward high temporal resolution sampling (e.g. every 4-8 minutes round the clock) of an effluent gas stream. This shift facilitated the production of accurate TCE breakthrough curves for further analysis. The specific analytic details were: GC inlet isothermal at 150 °C, column oven and sampling valve isothermal at 80 °C, runtimes of 4-8 minutes, FID detector at 250 °C, carrier gas (helium) flowrate of 5.8 mL/min, with a 1:1 split ratio. A mass flow controller (Cole Parmer, 16 Series Mass Flow Controller, 0-50 SCCM range) was used to maintain a constant flow and constant pressure gas-sampling stream through the GC for good repeatability. All airflow connections between the flow-making device, the tank and the gas chromatograph consisted of 3.2 mm stainless steel tubing and fittings. Calibration curves for trichloroethylene were generated using professionally prepared gas phase standards (Matheson Tri-Gas) of TCE in nitrogen at concentrations of 10.8, 210.6 and 2000 ppm_v. The method detection limit was approximately 0.5 ppb_v.

4.2.2.2 Aqueous phase TCE analysis: Analysis of aqueous TCE concentrations in the dissolved groundwater plume was also necessary for multiple experiments. A TCE solvent extraction in liquid hexane method that has been used extensively in other projects (Illangasekare et al. 2006; Siegrist et al. 2006; Siegrist et al. 2010) was selected for this purpose. This is a grab sampling method where a liquid water sample (typically 100 μ L) is withdrawn in a gastight syringe and extracted with HPLC grade hexane in a gas tight analysis vial. The hexane phase is then analyzed via GC (HP6890 GC, micro electron capture detector [μ ECD], split/splitless inlet, and Zebron ZB-624 30 m x 0.53 mm polysiloxane column). The analytic details were: inlet temperature 150 $^{\circ}$ C, oven isothermal at 80 $^{\circ}$ C for 3 minutes, ramp to 200 $^{\circ}$ C in 4 minutes, then isothermal at 200 $^{\circ}$ C for 2 minutes, 9 minute total run time, with a 50:1 split ratio and a column flow of 5.8 mL/min helium. The method detection limit was approximately 5 ppb.

4.2.2.3 Soil water content and Temperature: Because the distribution and flow of air and water phases were expected to play an important role in the VI pathway, especially in relation to the weather and climate factors evaluated by this project, an effective method for measuring soil water content as a function of time was necessary. For these experiments a series of soil moisture probes produced by Decagon Devices, Inc. were used. Two probe styles were employed, the EC-5 soil moisture probe, and the 5TE coupled soil moisture and temperature probe. Both probe styles measure the dielectric constant of the media, which can be calibrated to the water content of the media using the method of Sakaki et al. (2011a). The 5TE probe also includes a temperature measurement probe. In experiments where the 5TE probe was unavailable, a separate EC-T probe was used to monitor temperature. All of the aforementioned sensors were connected to data-loggers (Em50, Decagon Devices, Inc.) to gather data at a rate of up to once per minute.

4.2.2.4 Air pressure: Air pressure measurements were also critical to characterizing the flow pathways through the unsaturated porous media employed in these studies. Thus, many experimental apparatus were instrumented with air pressure sensors that measured differential pressure relative to the atmosphere. Atmospheric pressure in Golden Colorado averages about 82,000 Pa. Pressure measurement included insertion of a hydrophobic-treated porous cup (using the methodology of Sakaki et al. 2011b) into the experimental tanks, and connecting these via plastic tubing to electronic air pressure sensors (PX138-001D5V, Omega Engineering Inc, Stamford, CT). These sensors were monitored every 1 minute by a datalogger (NI USB-6225, National Instruments Inc, Austin, TX), and calibrated via manometers with a 7 point calibration curve.

4.2.2.5 Electrical Resistance Tomography (ERT): To analyze the utility of “soft” data in assisting characterization and observation of the VI pathway, the geophysical method electrical resistance tomography (ERT) was investigated. This method entails passing a current through the subsurface between electrodes installed at the ground surface, and measuring the resistance. With proper inverse modeling, resistance can be translated into either two-dimensional sections or 3-dimensional maps of resistance in the subsurface. In an unsaturated zone setting, zones of low water content pose higher electrical resistance than zones of higher water content, and thus this method has potential to map the soil moisture profile of the vadose zone. However, its potential use for VI had not been documented. A controlled laboratory and a field experiment were both conducted with this unit. The equipment involved a SuperSting R8 IP 8-channel earth resistivity

meter (Advanced Geosciences Inc., Austin, TX) with 28 stainless steel electrodes (8cm length by 1cm in diameter), which was used to perform ERT surveys along surface profiles in the sand tank apparatus. The electrodes were inserted directly into the sand surface. The SuperSting main data cable was connected to the electrodes using plastic coated 18-gauge aluminum wire and secured using aluminum alligator clips.

4.2.3 Common Materials

4.2.3.1 Porous media: Many of the experimental investigations were conducted in porous materials. In an effort to simplify and enhance data interpretation and modeling between studies, many used the same well-characterized porous media. The majority of these materials were different mesh sizes of the brand Accusand™ (Unimin, Inc.), which are very uniform sands. These were used because their uniformity allows them to be packed into multiple experimental apparatuses and achieve high repeatability in terms of their hydraulic and retention properties. Properties of the various sands are given in table 4.2. The values in this table were also used in subsequent modeling of the experiments.

Table 4.2: Properties of Porous Media used in this study¹

Sand (tightly packed)	d50 ² (mm)	Dry Bulk Density (g/cm ³)	Porosity	Saturated hydraulic conductivity (cm/s) ⁴	Cycle ⁶	Residual Water Saturation ³	Maximum Water Saturation ³	van Genuchten α (1/cm) ⁵	van Genuchten n ($m=1-1/n$) ⁵
12/20	1.04	1.82	0.312	0.376	PD	0.054	1.000	0.10	9.21
					I	0.054	0.827	0.11	6.00
					SD	0.054	0.827	0.15	9.50
20/30	0.75	1.78	0.330	0.237	PD	0.082	1.000	0.07	15.68
					I	0.082	0.712	0.14	5.10
					SD	0.082	0.712	0.08	10.46
30/40	0.52	1.77	0.334	0.106	PD	0.084	1.000	0.06	17.81
					I	0.084	0.725	0.09	6.50
					SD	0.084	0.725	0.06	14.70
40/50	0.36	1.74	0.335	0.052	PD	0.087	1.000	0.04	10.18
					I	0.087	0.812	0.08	4.20
					SD	0.087	0.812	0.05	7.66
70	0.20	1.56	0.413	0.014	PD	0.080	1.000	0.02	11.53
					I	0.080	n/a	n/a	n/a
					SD	0.080	n/a	n/a	n/a

¹values from Smits (2010)

²Estimated from sieve data provided by the manufacturer

³Measured in a separate 1-dimensional long column experiment

⁴Measured in a separate hydraulic conductivity test

⁵Estimated using RETC (van Genuchten et al., (1991)

⁶PD = primary drainage, I = imbibition, SD = secondary drainage

4.2.3.2 Test chemicals: Relatively few chemical reagents were required for the various studies. Analytical grade (T341-500, >99.5%, stabilized, Certified ACS) trichloroethylene was purchased from Fisher Chemical, and used as the sole source of TCE for all experiments in which TCE was present as a VOC. Select properties of trichloroethylene are given in Table 4.3. In experiments where TCE was present in a NAPL phase, the TCE was dyed red with Sudan IV at an approximate concentration of 100 mg in 1 liter of TCE. In the vapor generation experiments (described in sections 4.3 and 4.4), Millipore water (>18 M Ω /cm) was used for all water sources in the experiment. However, due to the large volumetric water requirements for the large tank experiments (sections 4.5 and 4.6), it was impractical to use deionized water and therefore these experiments employed tap water supplied to the lab.

Table 4.3: Trichloroethylene Properties at 20°C (Cowen and Mercer, 1993)

Property	TCE
Molecular weight (g/mol)	131.39
Density (g/mL)	1.46
Absolute viscosity (cp)	0.57
Vapor pressure (Pa)	7710
Dimensionless Henry's Law Constant	0.299
Total gas density (g/L)	1.52
Water diffusion coefficient (cm ² /s)	8.3 x 10 ⁻⁶
Air diffusion coefficient (cm ² /s)	8.11 x 10 ⁻²

4.3 NAPL volatilization experiments

4.3.1 Objectives

The objective of the NAPL volatilization studies was to determine how variable soil moisture conditions influence volatilization from NAPL source zones. In principle, any NAPL source located in the vadose zone will produce a vapor plume, but the rate of mass loading to the plume and the source longevity will be determined by the volatilization (mass transfer) rate. However, the soil moisture content of the source zone and its interfaces may control the volatilization rate because transport of the vapor in the gas and water phases is subject to differing rates of diffusion and advection. This is particularly relevant in the scenario of a fluctuating water table that may periodically expose or swamp a NAPL source zone, or in the case of NAPL sources that have become entrapped in fine porous media layers. The objective of this study was to test NAPL volatilization under two soil moisture scenarios: 1) a source zone fully occluded from the bulk air phase (e.g. NAPL entrapped in a water saturated fine soil layer) and 2) with the NAPL directly exposed to the bulk air phase (e.g. a perched NAPL pool or NAPL floating on the capillary fringe). These scenarios differ because in the occluded case, the contaminant must transfer through the water phase first via diffusion or advection prior to volatilization, whereas the exposed source may transfer directly into the vapor phase. The former case has potential for significant rate-limitations in mass transfer because of the orders of magnitude difference in diffusion coefficients between air and water (see table 4.3). The outcome of this study improves the conceptual understanding of how NAPL sources may behave under variable soil moisture conditions. Figure 4.1 provides an illustration of these differing configurations within the pore space.

4.3.2 Apparatus and Approach

Two separate series of experiments were performed. The first series evaluated mass transfer from an “occluded” NAPL source (case 1 - figure 4.2) while the second explored an exposed (free) NAPL source (case 2 – figure 4.2). Exploring both NAPL configurations independently enabled the comparison of mass transfer characteristics between the two. Both experiments were conducted using the same apparatus, instrumentation and analytical methods, but differed in source creation procedure, sand pack geometry and experimental procedure. An important procedural difference was that the occluded (case 1) experiments were run until mass transfer reached pseudo steady-state because the slow mass transfer rates requires exceptionally long experimental run times (month to years) to completely deplete the NAPL sources. For the

exposed (case 2) NAPL sources, mass transfer was rapid and transient (days), and therefore these experiments were run until complete NAPL source depletion.

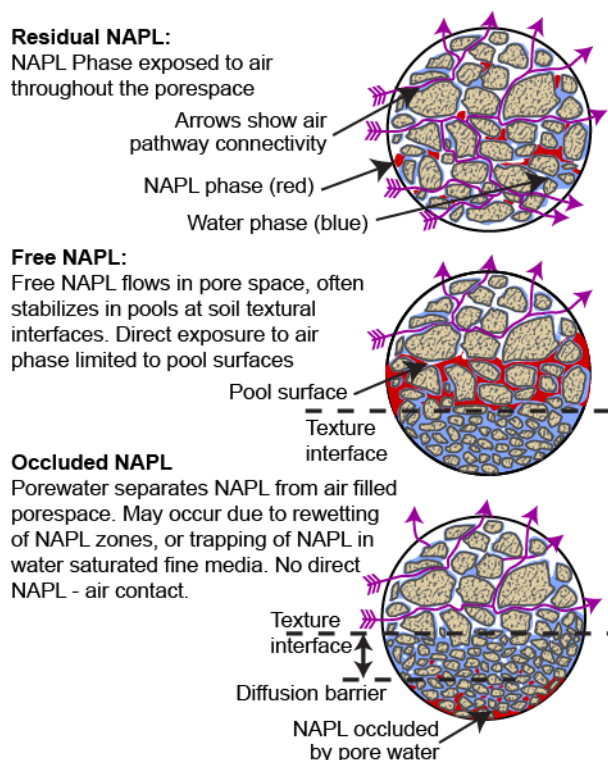


Figure 4.1: Conceptual diagram of NAPL source configurations within the vadose zone pore space.

Both experiments were conducted in a 2-dimensional sand-packed flow tank [internal dimensions: 28 x 15.5 x 2.5 cm (height x length x depth)] constructed from aluminum plates, sealed with polyethylene gaskets and a plate glass window at the front, enabling visual observation of the experiment (figure 4.2). The rear face of the tank contained a grid of injection ports sealed with PTFE-lined septa through which TCE NAPL could be injected to create the desired trapping configuration. The porous media used to pack the tank were as indicated in figure 4.2. The tank was initially wet packed with sand and deionized water in accordance with the procedure outlined in Sakaki and Illangasekare (2007). Tank packing and source zone characteristics differ between case 1 and case 2 (see figure 4.2). The tank was drained (drainage details to follow) to a specified head under hydrostatic conditions to establish an unsaturated zone within the tank. Following drainage, a known mass of TCE NAPL was injected into the source zone and controlled airflow was started immediately through the tank. The airflow was introduced into the tank through the left gravel well screen and exited the tank at the right gravel well screen. A bentonite clay cap prevented the escape of air through the surface. Air (grade zero) from a compressed gas cylinder provided the airflow source, which was controlled using a mass flow controller (Cole Parmer, 16 Series Mass Flow Controller, 0-50 SCCM range). The airflow was bubbled through a water column to humidify the air prior to injection to prevent evaporative losses from soil water and maintain a steady water saturation profile throughout each experiment. The airflow range tested by this apparatus equates to average pore velocities of around 3 to 145 m/day in the unsaturated zone, and is considerably lower than velocities

previously studied in soil vapor extraction (~100 to 10,000 m/d Ho and Udell, 1992; Wilkins et al., 1995; Yoon et al., 2002; Oostrom et al., 2005) and in air sparging (~100-100,000 m/d Braida and Ong, 1998; Braida and Ong, 2000; Rogers and Ong, 2000). The entire apparatus operated under positive pressure, and two electronic air pressure sensors (see section 4.2.1.4) were located within the inlet and effluent manifolds, continuously monitoring the tank pressure. The internal tank pressure range for the tank experiment ranged 82,090 – 87,171 Pa. The higher tank pressures were associated with positive pressurization of the tank that occurs due to the constriction of higher gas flow rates through the effluent tubing and GC. Two temperature sensors (see section 4.2.1.3) were attached to the back aluminum face of the tank and the average of these two temperature sensors was reported as the ambient temperature of the apparatus. The overall average room temperature for all experiments was 22.6 ± 0.7 °C.

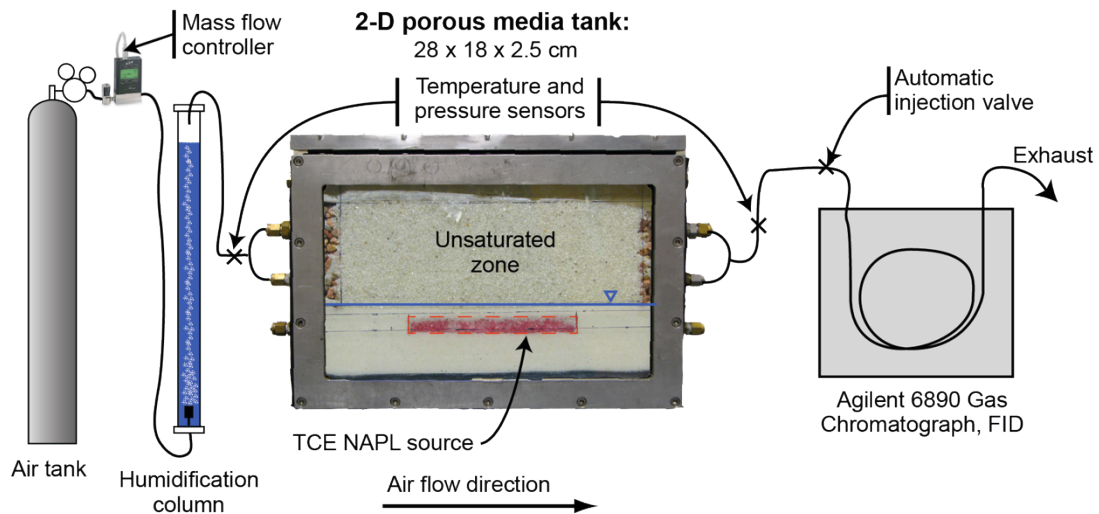
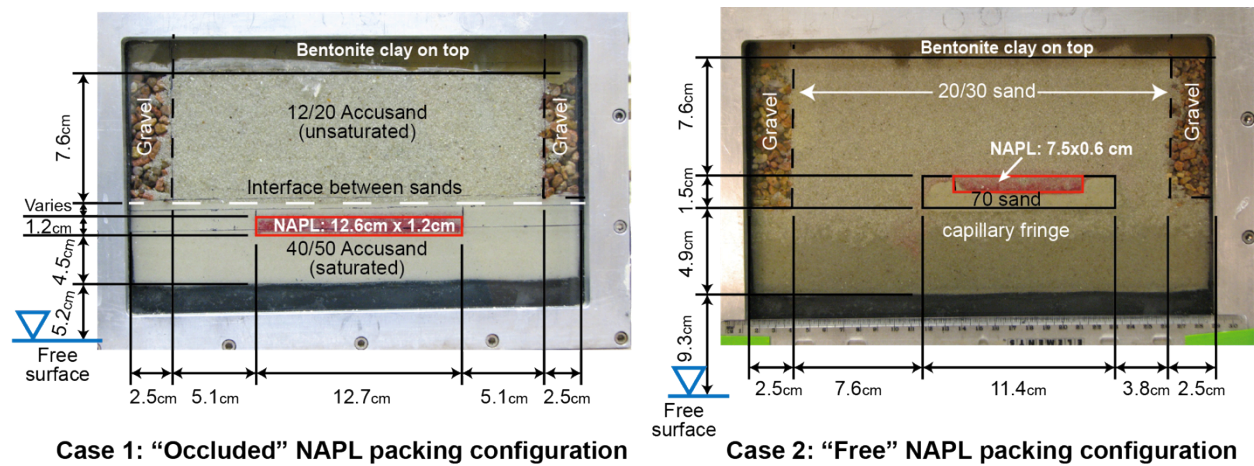


Figure 4.2: Experimental Apparatus and Tank Packing for NAPL volatilization experiments. Case 1 presents the occluded NAPL experiment (see section 4.3.3) and case 2 presents the exposed NAPL experiment (see section 4.3.4). The free surface elevation relative to the bottom of the tank is presented in the figures, and in both cases is below the tank bottom (under suction).

From the effluent manifold, the air stream was directed into a gas chromatograph (GC) for analysis via the gas phase TCE analysis method (described in 4.2.1.1). All airflow connections between the flow-making device, the tank and the gas chromatograph consisted of 3.2 mm stainless steel tubing and fittings. The 8-minute runtime of the GC method resulted in continuous measurement of effluent TCE concentration approximately every 8 minutes for the duration of the experiment.

4.3.3 Case 1 “occluded” NAPL experimental procedure:

The occluded case experiments tested different occlusion layer thicknesses and air phase velocities to examine the mass transfer relationship to the length of the diffusion pathway across the occlusion and bulk diffusion and advection away from the occluded source. The tank was wet-packed with two sands (see section 4.2.2.1 for properties): a fine sand (#40/50) in the lower section of the tank, and a coarse sand (#12/20) in the upper section of the tank (see figure 4.2). During packing, a coarse sand block (#12/20), 12.7cm x 1.2cm was emplaced within the lower section of fine sand to serve as the NAPL source zone. This packing produces a narrow band of fine sand between the coarse upper tank section and the coarse NAPL source zone (see dimension marked “variable” in figure 4.2). This band is the occlusion layer, and two thicknesses were tested: 1) 13.9 mm which was denoted the “thick” occlusion system, and 2) 8.5 mm which was denoted the “thin” occlusion system. Zones of pea gravel were located at the left and right boundaries to serve as well screens and evenly distribute the air flow. The top of the tank was sealed with bentonite clay and an aluminum plate to ensure that the tank was airtight.

After packing was complete, the tank was drained by lowering the water table to 5.2 cm below the bottom boundary of the tank; this is accomplished by attaching a constant -head water reservoir to the lowest right-hand port, and setting the head to this desired level. This creates a suction of approximately 12 cm of water at the interface between the upper coarse sand section and the lower fine sand section. Because of the difference in air entry values for the coarse and fine sands (7.1 cm-H₂O and 19.4 cm-H₂O respectively), the drainage results in a sharp saturation front at the interface between coarse and fine sand such that the upper coarse sand is drained and the lower fine sand is fully water saturated under tension. Because air entry into the fine sand has not occurred, the coarse sand NAPL source zone also remains fully saturated.

After 24 hours of drainage to a hydrostatic condition, the constant head device was isolated via a shutoff valve, and NAPL was injected into the source zone. A known mass of TCE was slowly injected through 5 injection ports with the goal of making as high and uniform a NAPL saturation as possible without allowing any NAPL to escape the source zone. The NAPL was effectively occluded from the gas phase by the water saturated fine sand surroundings the source region. The NAPL injection volumes for the “thick” and “thin” occlusion systems corresponded to 11.3 g and 12.3 g, which equate to approximately 52% and 55% NAPL saturation in the source, the remaining pore space being saturated with water. Immediately after NAPL injection, airflow through the tank started and continuous effluent concentration sampling began. Because mass-transfer from NAPLs is affected by the velocity of the mobile phase (Miller et al., 1990; Powers et al., 1994; Saba and Illangasekare, 2000), various airflow rates were tested. These alternative flow rates were achieved using a step-wise approach that allowed the system to reach steady-state (each run was typically 1-2 days), which was determined by observing that no changes in effluent concentration were occurring, before adjusting the flow rate and achieving a

new state-state operation. In this manner, 6 different flow rates were tested for both the “thick” and “thin” occlusion systems without stopping the experiment (table 5.1 in the results depicts the flow rates in terms of the effective average pore velocity).

4.3.4 Case 2: “Exposed” NAPL experimental procedure:

The objective of the case 2 experiments was to evaluate mass transfer from an “exposed” NAPL pool as a basis for comparison to the case 1 experiments. For the high saturation “exposed” NAPL packing configuration (case 2), the tank was uniformly wet packed with water and medium sand (#20/30), except for a small NAPL source “trough” of very fine sand (#70) 7.6 cm long in the center of the tank (see figure 4.2). This trough was aligned with three ports for NAPL injection. The trough was bounded at its upstream and downstream ends by a 0.6 cm lip to contain the lateral spread of the NAPL. Similar to case 1, pea gravel on the left and right sides of the tank were included as a well screen, and bentonite was used to seal the top of the tank. Also similar to case 1, the tank was drained through suction applied at a known pressure head (9.3 cm-water below the tank bottom). However, unlike case 1 which produces a sharp water saturation front, the case 2 packing produced a capillary fringe in the bottom of the tank. Only the trough remains fully saturated due to the high air-entry pressure of very fine #70 sand (41.2 cm). After drainage was complete, 2.93 g (2.0 mL) of trichloroethylene NAPL was slowly injected into the source trough where it settled, forming a NAPL pool with approximate dimensions of 7.6 x 2.5 x 0.6 cm (length x width x depth) and an estimated 50% average saturation of the trough pore space. Following NAPL injection, airflow was immediately started in the tank and effluent gas concentrations were monitored as described in case 1. The experiment continued until all NAPL was depleted through visual observation from the system and effluent concentrations declined to less than 1% of initial values.

4.4 Capillary Fringe volatilization experiments

4.4.1 Objectives:

The objective of these experiments was to test the hypothesis that volatilization from groundwater across the capillary fringe, especially under dynamic conditions, may play a critical role in mass loading to vapor plumes in the vadose zone. The exploration of this hypothesis at a small scale is necessary to understand the basic process physics, prior to upscaling to a more complex experimental system in the large tank experiments (section 4.6). A series of experiments were conducted where groundwater served as a source of TCE contamination, and volatilization behavior was measured as a function of groundwater fluctuation, heterogeneity and airflow velocity. This yielded insights into the mass transfer behavior from a falling water table, as well as across a capillary fringe and water saturated fine layers.

4.4.2 Apparatus:

The apparatus used in these experiments consisted of a 2-D sand tank where volatilization of TCE from groundwater is typically evaluated (see Figure 4.3). The tank was constructed using 1.5 cm thick plexiglass and its internal dimensions were 40 cm (length) by 30 cm (height) by 5 cm (width). Variables that could be controlled include air velocity in the vadose zone, the

dynamics of the capillary fringe (e.g. wetting vs. drying), and dynamics of the saturated zone underlying the vadose zone (e.g. static groundwater vs. flowing plume).

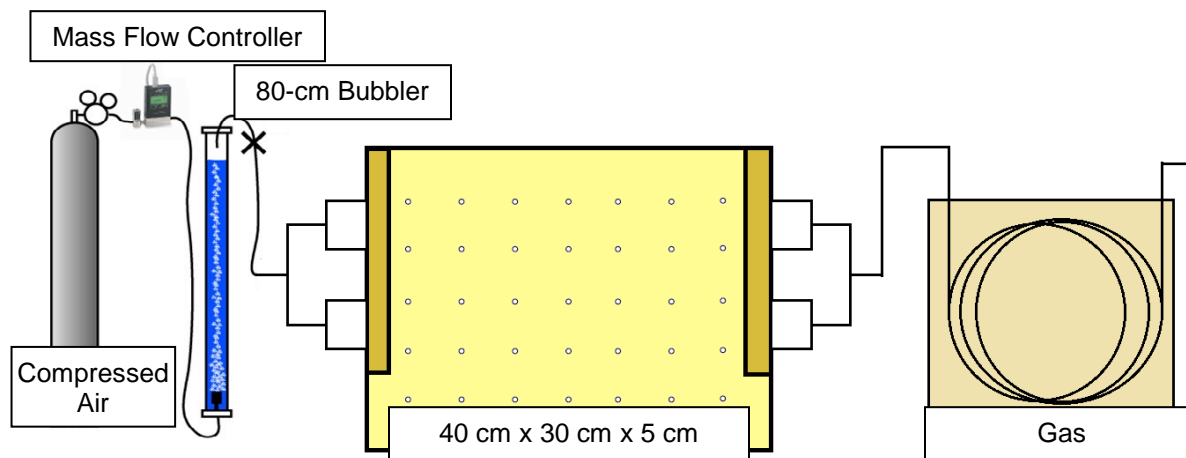


Figure 4.3: Schematic of capillary fringe volatilization experimental apparatus

4.4.2.1 Physical instrumentation: Temperature, pressure, airflow, and effluent TCE concentration were monitored throughout each experiment. Two electronic temperature sensors (see section 4.2.1.3) were adhered to the outside of the tank to monitor ambient temperature, which was assumed representative of the temperature inside the tank. The pressure drop across the tank was monitored using two air pressure sensors (see section 4.2.1.4) embedded within the influent and effluent gas manifold. Airflow through the tank was controlled using a mass flow controller (Cole Parmer, 16 Series Mass Flow Controller, 0-50 SCCM range). Effluent gas phase TCE concentrations were measured using the method described in section 4.2.1.1.

To generate the airflow through the tank, a mass flow controller was connected to a compressed Zero Grade air cylinder with 1/8" stainless steel tubing and Swagelok fittings. To maintain constant soil moisture content throughout the experiment, the airflow was humidified through an 80-cm bubbler. The tank effluent manifold was connected directly to the gas chromatograph (GC) automatic sampling valve using Swagelok fittings and 1/8" stainless steel tubing. A schematic of the full experimental set up can be seen in Figure 4.3.

4.4.2.2 Tank sand pack details: Two different sand packing configurations were used (figure 4.4). For homogeneous experiments, Accusand #20/30 was used to fill the entire tank aside from a thin gravel pack well screen at the left and right boundaries of the tank. For heterogeneous tank packing, a #70 fine sand lens was emplaced in the middle of the tank, with the remainder of the tank filled with #20/30 Accusand. Properties of the sands are in section 4.2.2.1. The tank was wet packed with clean deionized water following the method of Sakaki and Illangasekare (2007).

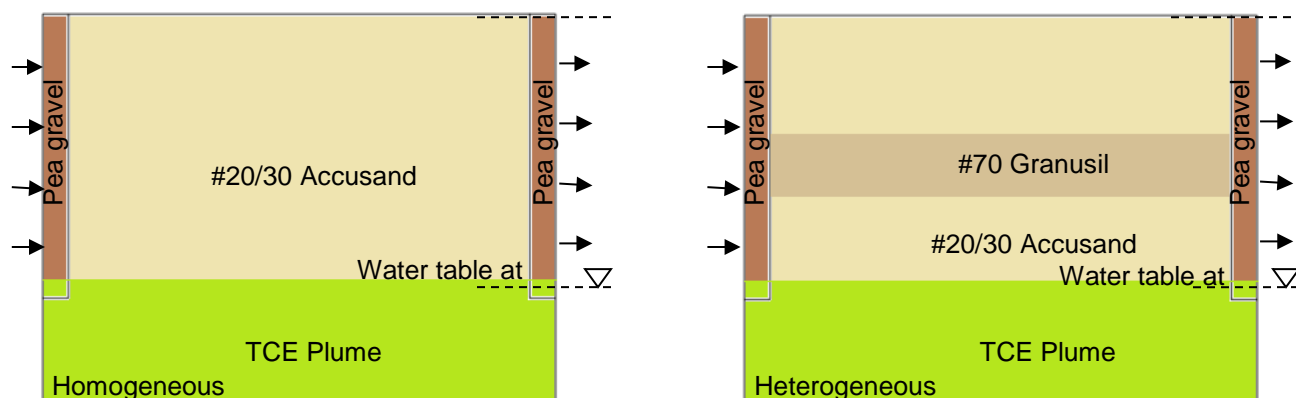


Figure 4.4: Capillary fringe volatilization experiments packing configuration and cases 1-4 description

4.4.3 Experimental Procedure

4.4.3.1 Creation of the contaminant plume: Pure trichloroethylene was mixed with deionized water for 24 hours to create a fully saturated TCE solution (approximately 1400 mg/L). This solution was diluted DI water to the concentration given table 4.4 for each test case. Aqueous TCE concentrations were measured using the method described in section 4.2.1.2. Using a peristaltic pump, 10 L of solution was pumped through the lowest port in the wet-packed fully saturated tank. This volume of water (~5 tank pore volumes) was sufficient to displace the initial clean deionized water within the tank, and achieve a uniform distribution of the TCE contaminated water. A dilute concentration of green food dye was added to the water to give visual confirmation of a uniform distribution of the TCE solution. After uniform saturation of the tank with TCE contaminated water, the peristaltic pump was shut off, as these experiments did not incorporate active groundwater flow. Using constant head reservoirs attached to the lowest port on either its side, the tank was then drained so that the water table dropped to the bottom of the tank, leaving a capillary fringe of approximately 12 cm that obeyed the primary drainage curve shown in figure 4.5. The top influent air port was then shut off and the air inside the tank was allowed to reach equilibrium with the water phase for 24 hours.

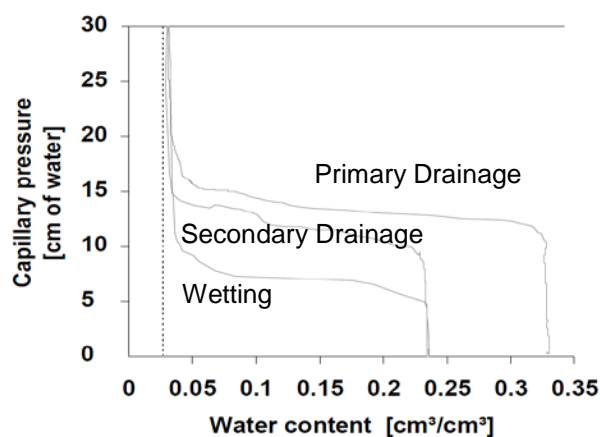


Figure 4.5. Primary drainage, secondary drainage, and wetting curves for #20/30 Accusand

4.4.3.2 Experimental procedure: After equilibration, airflow was introduced through the unsaturated zone of the tank. Several experimental test cases were conducted. These cases are summarized in 4.4, which presents the airflow rates, estimated average linear pore velocity in the unsaturated sand, and the starting aqueous TCE concentration. Effluent TCE concentrations in the air stream were monitored throughout each experiment. In several cases, aqueous TCE samples (see section 4.2.1.2) from within or below the capillary fringe were taken to obtain the profile of concentrations across the capillary fringe. These sampling locations are indicated in figure 4.6.

Table 4.4: Experimental test cases for capillary fringe experiments

Experiment	Tank packing	Airflow ($\text{cm}^3 \text{min}^{-1}$ at STP*)	Estimated average linear pore velocity in unsaturated sand (m d^{-1})	Initial aqueous TCE concentration (mg L^{-1})
Case 1	Homogeneous	2.0	0.86	429
Case 2	Homogeneous	50.0	21.6	389
Case 3	Heterogeneous	2.0	1.05	118
Case 4	Heterogeneous	50.0	26.3	410

*STP= standard temperature and pressure (1 atm, 70 °F [21.1 °C])

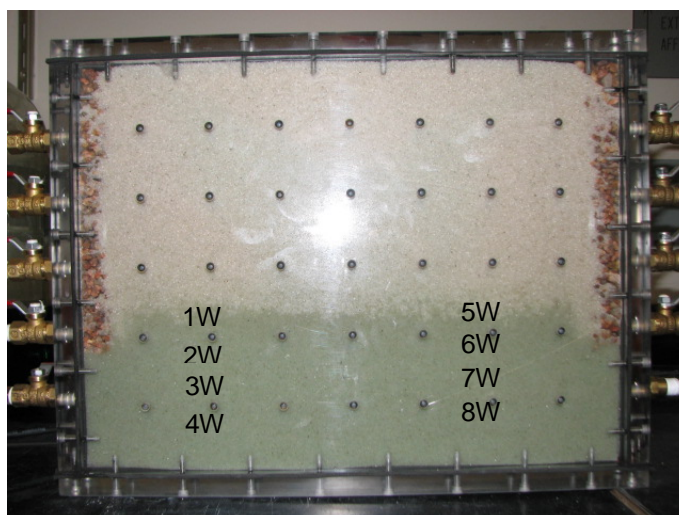


Figure 4.6: Aqueous phase sampling locations within the tank. Green color of the liquid indicates the groundwater zone and the clear sand shows the unsaturated zone where airflow occurs.

4.5. Soil moisture dynamic experiments with heat and rain boundary conditions

4.5.1. Objective

The goal of this series of experiments was to explore how the spatial and temporal variability of soil moisture dynamically affects vapor transport pathways. Lateral air pathway dynamics were tested in a heterogeneous vadose zone under various surface climate conditions (i.e., precipitation and heating). These experiments were conducted in a two-dimensional large sand

tank under laboratory conditions because of the inability to accurately control initial and boundary conditions at the field scale. These experiments were not designed to represent exact field conditions, which are much more complicated due to different soil types and more complex process interactions, rather they were conducted using well-characterized sands and simple packing configurations to generate data that can improve our fundamental understanding of the processes (e.g., under which more subsurface-origin air flows into a subsurface structure) and guide the development and use of a numerical model. This modeling can then provide further insight on how the “degree of heterogeneity” (i.e., different contrasts in soil properties) affects the evolution of preferential pathways of air and how these preferential pathways respond to soil moisture increases due to infiltration. For the numerical tool development, a finite-element based COMSOL multi-physics code was used. Note that in both experiments and modeling, we focused only on the physical flow dynamics of the air and water phase as affected by the heterogeneity and soil moisture conditions; chemical transport was not directly incorporated.

4.5.2 Apparatus

To demonstrate the spatial and temporal variability of airflow pathways subject to soil moisture dynamics, a series of experiments using an intermediate-scale two-dimensional tank were performed. The dimensions of the tank were 122 cm (height) \times 244 cm (length) \times 7.6 cm (width). The tank was packed with six soil layers for all experiments as shown in Figure 4.7, and a photograph of the tank is presented in figure 4.8. Layer 6 was always placed below the water table making it saturated. Soil moisture, temperature and air pressure sensors (described in section 4.2.1.3 and 4.2.1.4) were installed in 30 locations in the sand pack representing columns A-F and layers 1-5 (see figure 4.7). Two constant-head reservoirs were connected to the near-bottom corners of the tank for controlling the water table elevation. In typical VI problems, a pressure “drop” in the basement induces flow of air into a building. In our experiments, however, injecting air into the soil at a controlled flow rate for multiple hours was more practical (from a hardware point of view) than pulling air out of the soil. Therefore, in these experiments we injected constant airflow into layer 4 and monitored outflow rates at the downstream end of layers 1 through 4. These airflow dynamics created by air injection are analogous to those created by suction under VI except that the flow direction is reversed.

Four uniform specialty silica sands of differing mean grain size were used to pack the layers as indicated in figure 4.7. Although field soils are much more complex in composition, texture and structure, well-characterized sands were used to simplify the subsurface conditions, but still generate accurate data for model testing. The silica sands are identified by the effective sieve numbers; #12/20, #20/30, #30/40 and #40/50 (see section 4.2.2.1 for properties of porous media). The sand was carefully wet-packed into the tank and compacted via thorough tapping of the tank wall. For each layer, a predetermined amount of sand was poured and compacted to occupy the designed volume and ensure the porosity value specified in Table 4.2. The water table was initially established at the top surface of the entire aquifer during wet-packing (i.e. the land surface). The water table was then lowered by setting the two constant head reservoirs at an elevation 20 cm above the bottom boundary. The capillary fringe extended over the entire layer 5 (due to its air entry pressure of >20 cm of water) and mostly remained wet during the experiments. Two separate experiments were performed in this tank: 1) precipitation was applied (hereinafter, referred to as rainfall experiment) and air pathways were monitored and 2) heat was applied at the soil surface following a second precipitation event (hereinafter, referred

to as heat experiment) and air pathways were monitored. Before each experiment, soil water from the previous wetting event was allowed to drain overnight to re-equilibrate the system.

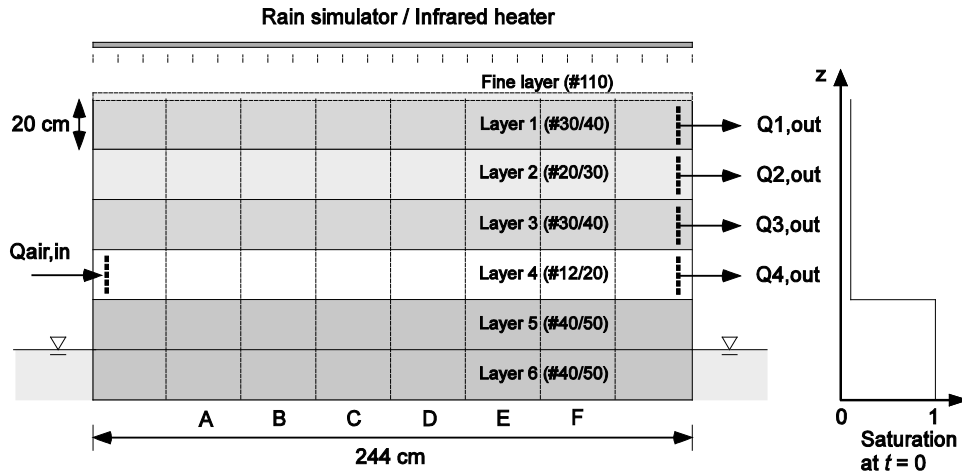


Figure 4.7: Schematic view of the two-dimensional tank for dynamic soil moisture experiments. Saturation profile is only schematic. Note that the air flow is reversed in the rainfall and heat experiments.



Figure 4.8: Photo of the two-dimensional tank apparatus.

Precipitation at the soil surface was induced using a rainfall simulator placed at the top of the tank. Four lines of soaker tubing (DripMaster®, outer diameter = 6.4 mm, Orbit Irrigation Products, Inc., North Salt Lake, UT) were aligned about 1.5 cm apart and fixed along and about 3 cm above the soil surface. The soaker tubing was connected to a water supply through a regulator and the flow rate was monitored with a water flowmeter (Micro-turbine Flo-Sensor, Model 101, range 0.2-5 L/min, McMillan Co., Georgetown, TX). The surface of the soaker tubing was treated with a water repellent compound to help the water drip more uniformly.

In the heat experiment, the temperature boundary was imposed using thermal irradiation at the soil surface to investigate the influence of heat-induced evaporation on dynamically developing airflow pathways. In order to create a wet surface condition, a layer of very fine sand with a thickness of 3 cm was added on top of layer 1 (Figure 4.7). An infrared heating element (Model

HSE 500-120, Salamander), together with a reflector, was positioned directly above the soil surface to obtain a nearly uniform heat flux distribution. The soil surface temperature was monitored with an infrared non-contact temperature sensor (Model IRt/c.03, Exergen Corp., Watertown, MA) connected to a temperature control system (Model 2104, Chromalox, Inc., Pittsburg, PA) to ensure that the soil surface temperature remained constant. In the heat experiment, the temperature at the surface was set to remain in the range of 68 - 70 °C. After some trial and error process, this high temperature was found to induce evaporation so that the important key features are observed within a reasonable experimental duration of ~0.5 days.

4.5.3 Experimental procedure

A large number of experimental test cases were run, totaling over 35 experiments. However, for discussion purposes, only two cases are emphasized, as a number of these were redundant and primarily aided in refining the experimental method. Throughout the course of all experiments, the water table was set to 20 cm above the bottom of the tank. In each experiment, air flow at 3,000 cm³/min was applied to layer 4 (which is the coarsest and expected to be the primary air flow path) at the left boundary at $t = -10$ min. The air flow reached steady state within a short period of time (< 1 minutes). This relatively high air flow rate was chosen so that changes in the pore air pressure were measurable on the order of ~1 kPa and air flow rates with time. As noted previously, this air injection simulates air flow into buildings as shown in **Figure 1** although the flow direction reversed while facilitating more accurate control of the air flow rate throughout the experiment. The air injection point mimics the cracks in the basement slabs through which soil air penetrates into a building such as in Figure 1.1.

4.5.3.1 Rainfall experiment: After a trial and error process, a rainfall intensity of 150 mm/hour was selected for the test. The selection of the appropriate rainfall rate was guided not by rates expected in field settings, but by the properties of the sands used and the specific packing configuration. This selected intensity led to changes in the subsurface soil moisture distribution leading to measurable effects on air pathway development. The intensity of 60 mm/hour or higher is considered as heavy rain in field settings. However, the high permeability of sand materials used in the experiments required the scaling of the rainfall rates to ensure an observable change in the soil moisture distribution. Use of a lower, but more realistic rainfall rate resulted in small soil moisture changes due to rapid infiltration. Thus, to understand the interaction between soil moisture distribution and air flow and to generate precision data sets for validating the numerical model which could then be run at more realistic rainfall rates, the above-mentioned rainfall intensity was employed. The rainfall was supplied at the surface for 3 hours and airflow into layer 4 was fixed at 3,000 standard cm³/min for approximately 9 hours. During the experiment, the air inflow rate into layer 4 and outflow rates from layers 1-4 were monitored using five air flow meters. It has to be emphasized that, for more realistic soils, soil moisture could increase sufficiently higher under realistic rainfall intensities.

4.5.3.2 Heat experiment: Precipitated water infiltrated rather quickly in the soil conditions used in the rainfall experiment and the heat boundary at the soil surface was expected to affect soil moisture only near the surface. Therefore, in the heat experiment, a 3 cm-thick fine sand layer (hereinafter, referred to as the surface fine layer) was added at the surface of the aquifer used in the previous rainfall experiment. Additionally, six soil moisture sensors and temperature sensors were embedded in this surface fine layer. Two relative humidity (RH) sensors were also

installed to monitor humidity inside the fine layer and at the soil surface. An infrared heating system was placed ~20 cm above the soil surface to control surface temperature. The boundary conditions were identical to those for the rainfall experiment described in the previous section. The only difference was that after the rainfall ceased at $t = 3$ hours, the heater was turned on for 7 hours to keep the surface soil temperature at 68-70 °C. Although a diurnal heating cycle is expected in practical settings, a monotonic heating pattern was employed in this study for a better control of the boundary condition.

4.6 Integrated dynamic flow and vapor transport experiments

The objective of these experiments was to couple the multiphase flow of air and water with vapor advection, diffusion and mass transfer, particularly under dynamic (transient) conditions at the intermediate scale. This testing allows the exploration of interactions between rainfall and vapor diffusion and advection, or capillary fringe mass transfer from a dynamic water table. To our knowledge, no data set exists that have rigorously experimented with a volatile contaminant under conditions where all of these interacting phenomena are present.

4.6.1 Objective

The hypothesis of the large tank experiments was that dynamic hydrologic events can impart complex transient effects in the vapor intrusion pathway, but determining the significance and duration of such effects requires building a knowledge base that includes experimental observations in addition to numerical models. With the objective of evaluating infiltration and water table fluctuation on this more complex pathway conceptual model, this study conducted a 2-D intermediate-scale tank experiment (4.8 m x 1.2 m x 0.05 m) to generate observations of vapor plume transport under conditions relevant to VI. The experiment was conducted in a way that treats the intermediate scale tank as a mock vapor intrusion setting, including a groundwater plume source and vapor flow into a “building”. Experimental studies offer the advantage of known and tightly controlled conditions that are often absent from field sites; this enables the exploration of fundamental physical processes and the testing of models to ensure that all relevant physics are considered. A numerical model was also used to enable examination of physical phenomena observed in the experiments. The objectives of this work were to: (a) observe vapor plume behavior under rainfall and water table fluctuation, (b) generate quantitative data for validation of numerical models of VI, and (c) test our conceptual model of the pathway. From this data, observations about vapor plume behavior under dynamic soil moisture conditions may be made.

4.6.2 Apparatus

The experimental system consisted of a 2-dimensional intermediate scale sand tank (interior dimensions 4.883m x 1.219m x 0.057m) sized to facilitate vapor plume experiments. Conceptually, the tank is set up as a simulated vadose zone system representing a micro-scale vapor intrusion setting, as shown in figure 4.9, and drawn in detail in figure 4.10. The tank itself was assembled from prefabricated tank wall segments that have been used in previous studies (Rodriguez, 2006; Moreno-Barbero et al., 2007). The front face of the tank was a 1/2 inch acrylic plastic sheet lined on the interior of the tank with 1/8 inch plate glass; this allows visual observation of the soil in the tank, but prevents VOC sorption to the acrylic material. The back

face of the tank was a 3/8 inch aluminum plate that has threaded holes drilled in it to allow the installation of soil moisture and air pressure sensors (see sections 4.2.1.3 and 4.2.1.4). These sensors were installed in 30 locations indicated with black circles in figure 4.10. Two temperature sensors were fixed to the external aluminum back plate of the tank to monitor the ambient laboratory temperature. A photo the tank apparatus is provided in figure 4.11.

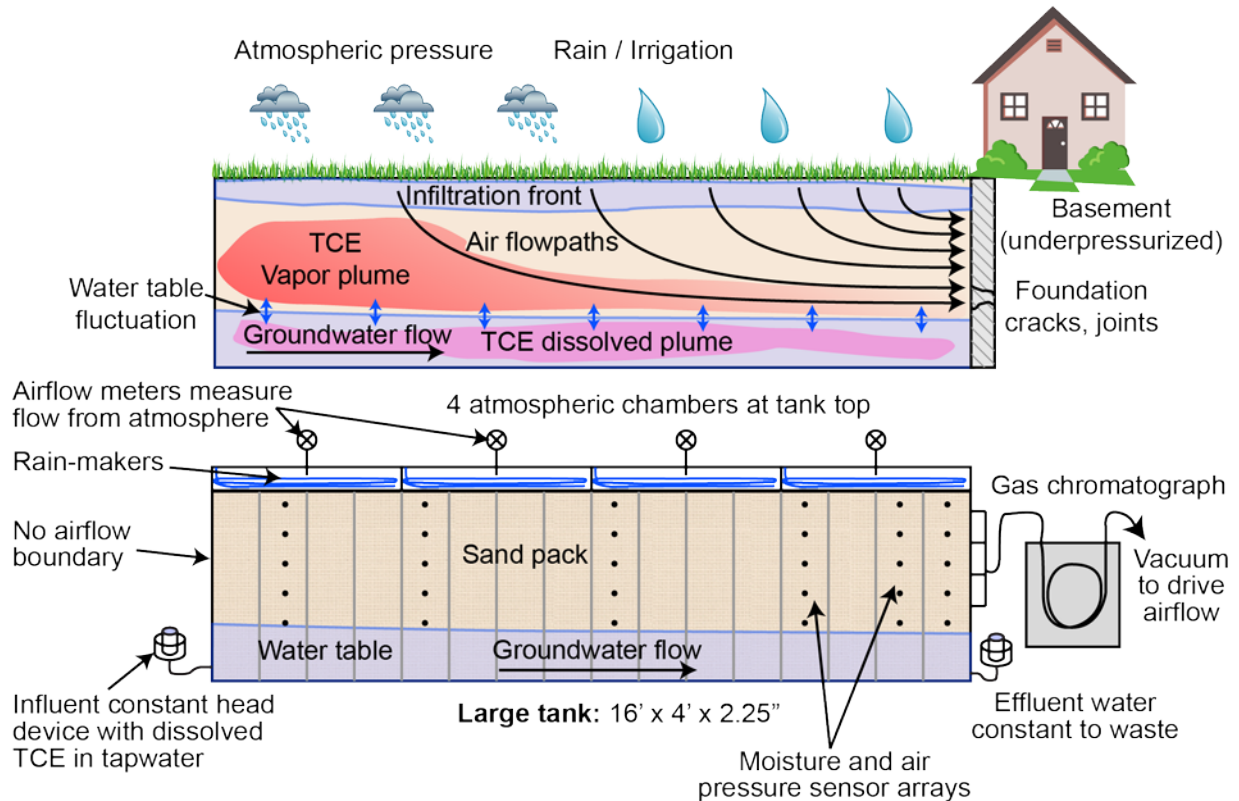


Figure 4.9: Conceptual model for intermediate scale tank for integrated dynamic flow and vapor transport experiments with tank schematic.

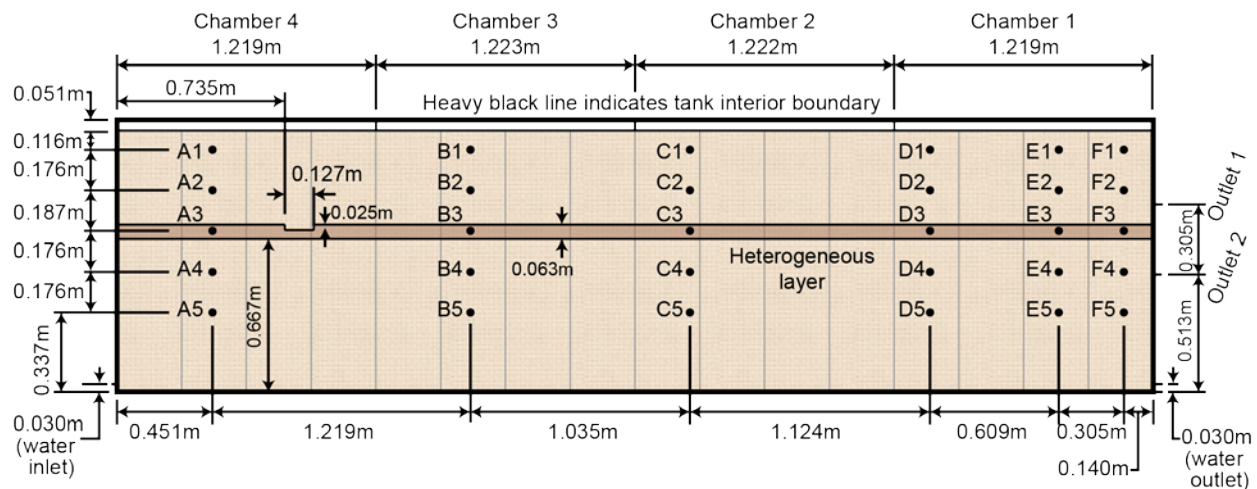


Figure 4.10: Detailed schematic of tank design and configuration.

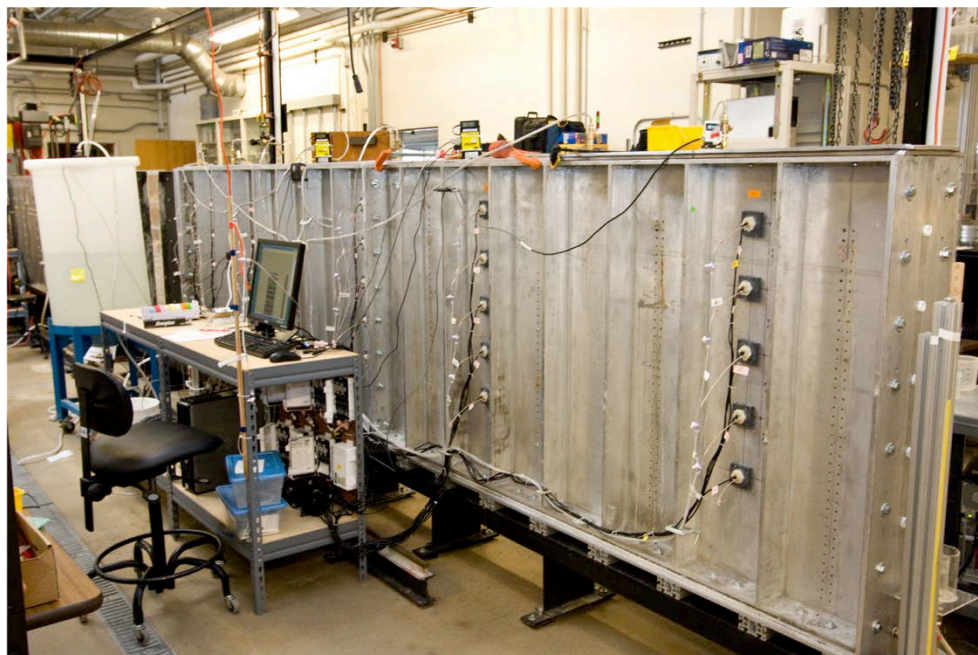


Figure 4.11: Photo of the tank apparatus

Two experiments with different packing geometry were performed, one a “homogeneous” tank and one a “heterogeneous” tank configuration. The properties of the sands used in packing both tanks were listed in table 4.2. Both experiments were carefully wet packed in accordance with the procedure outlined in Sakaki and Illangasekare (2007) to gain a tight packing without any air trapping. Tap water was used for all water sources throughout the experiment. In the homogeneous case the entire tank was uniformly packed with #40/50 Accusand. For the heterogeneous case, a single layer (shown in figure 4 as the “heterogeneous layer”) of #70 sand was included in the packing, while the remaining volume of the tank was packed with #40/50 Accusand. On the left side of the heterogeneous packing, a cutout within the fine grain layer creates a 0.127m x 0.025m notch in which NAPL may be injected.

In both the homogeneous and heterogeneous experiments, a 5.1 cm headspace existed between the top of the sand pack and the top of the tank, creating an atmospheric void. The atmospheric void allowed the creation of 4 separate atmospheric chambers (see figure 4) across the top of the tank. Airtight separations between the chambers were created by installing sheet metal dividers between compartments that keyed into the sand pack by 5 cm, and extended to the top of the tank. These were sealed with a silicone sealant. A rain-making device was installed in each of the 4 compartments that consisted of 3 lengths of irrigation soaker hose (DripMaster, 6.4-mm o.d., Orbit Irrigation Products) running the length of the compartment spaced 1.5 cm apart. Flow to the rain-making devices was measured via a turbine flowmeter (Micro-turbine Flo-Sensor, Model 101, range 0.2–5L min⁻¹, McMillan Co.). Shutoff valves to each compartment allowed spatially variable application of rain to any combination of compartments. A 1/4 inch acrylic plastic plate formed the top boundary to each compartment and was sealed into place with silicone sealant. Air inflow into each atmospheric chamber was driven by the vacuum pulled at the right side of the tank within the sand pack. The flowing air was humidified to reduce evaporative soil moisture losses from the tank, and measured by mass flow meters (FMA 1800 Series Flowmeters, size 20 (compartment 1), size 10 (compartment 2 and 3) and FLR1000 series

5-D (compartment 4), all by Omega Engineering Inc, Stamford, CT). Airflow to each chamber could be controlled via valves. Two outlets on the right side of the tank were used to draw the vacuum (shown as outlet 1 and 2 in figure 4) that drives airflow within the tank. Outlet 2 was used as the only location for applying vacuum for the majority of the experiments, while Outlet 1 was used only once at the end of the heterogeneous tank experiment for the NAPL volatilization experiment. A vacuum regulator on a laboratory vacuum supply line set the flow rate to this vacuum line, and the airflow through this vacuum line was also measured by a mass flowmeter (FMA 1800 Series Flowmeter, size 30 SLM, Omega Engineering Inc). All flowmeters within the tank logged data every minute to a datalogger (NI USB-6225, National Instruments Inc, Austin, TX). A small sample stream was diverted from the main vacuum line into a gas chromatograph (GC) with an automated sampling valve to analyze the outflowing air for trichloroethylene (see section 4.2.1.1.).

Constant head overflow devices were used to control the flow of the groundwater plume at both the inlet and outlet ends of the tank. A constant hydraulic gradient (7.5 cm drop over 4.88 m tank length) was maintained across the tank throughout all experiments, including throughout the water table fluctuations (e.g. the water table is raised but gradient held constant by raising inlet and outlet devices simultaneously). The water inlet and outlet ports are shown in figure 4.10, and were lined with a fine steel screen to prevent sand from exiting the tank. At the effluent end of the tank, the water flowed out the constant head device to waste. An influent mixing apparatus delivered a steady flow of tap water contaminated TCE to serve as the source of VOC vapors. The device consisted of a 20 L glass carboy on a magnetic stir plate that was kept full of water and had an excess (>100 mL) of NAPL phase TCE present to saturate the water with TCE. A peristaltic pump dilutes a flow of this TCE saturated solution into a 4L glass mixing container with clean water at about a 1:4 dilution rate, which then flows by gravity into the constant head device. Water samples were withdrawn daily from the influent and effluent and analyzed for TCE via the aqueous sampling method (see section 4.2.1.2). For the homogeneous tank experiment, this mixing device produced TCE contaminated water at a mean concentration of 317±19 mg/L (mean ± 95% CI). In the heterogeneous tank, it was determined that wear on one of the peristaltic pump heads caused the dilution factor to slowly decrease midway through the experiment, causing a significant increase in the influent concentration. For the first 45 days, the mean concentration was 433±19 mg/L (mean ± 95% CI), with a standard deviation of ±62 mg/L, while after 45 days the mean concentration increased by 13 mg/L per day, with a wider standard deviation of 29% of the mean value. At 87 days, the mean concentrations stabilized around 1000 mg/L.

4.6.3 Experimental Procedure

After apparatus preparation, but before experiment startup, a quality control step was taken to ensure that the tank was suitably airtight, as any unplanned leaks could affect data quality. First, the tank was drained with the constant head devices at their initial elevations. Then a flow of helium (~ 5 Lmin⁻¹) was passed across the entire tank (outlet 2 to chamber 4, see figure 4) under positive pressure, and the tank was scanned using an electron leak detector; this generally located large to medium leaks. For small leaks, all exterior joints of the tank were sprayed with a soapy water solution that bubbles in the presence of an air leak. Any detected leaks were sealed with silicone sealant. After leaks were sealed, the vacuum line was connected to outlet 2, and all atmospheric chambers opened for airflow. A mass balance calculation on all metered airflows

into and out of the tank was performed, and the tank was considered airtight once the mass balance was better than 99 +/- 2%.

4.6.3.1 Homogeneous case: The homogeneous case was run first. Initial elevations for the constant head devices were 9 cm on the influent side and 1.5 cm on the effluent side, with the datum at the tank bottom. The regulator setting on the vacuum line resulted in airflow of 3.815 SLPM. The tank was run at this initial flow rate to steady state for the first 21 days, after which the airflow was reduced to 0.980 SLPM. This reduction was made because experience gained through operating the new apparatus indicated that a lower airflow would be less likely to accidentally pull pore water into the vacuum line and possibly interfere with instrumentation. On day 66 of the experiment, an accidental adjustment of the vacuum regulator resulted in a reduced airflow of 0.428 SLPM. This was discovered on day 73 and corrected upwards to an airflow of 0.772 SLPM, where it remained until the end of the 106 day experiment. The airflow regime stabilized very quickly in response to a flowrate change, typically within minutes, but in each case at least a day was given to re-equilibrate the tank for changes to diffusive transport. Throughout this 106 day experiment, a series of 3 water table fluctuation events and 4 rain events were simulated. The conditions and timeframes for each of these transient events are given in table 4.5.

Table 4.5: Homogeneous case water table fluctuations and rain events.

Event	Abbreviation	Start day time	Description
Water Table Fluctuation 1	WT1	Day 24 2:45	1) Head devices raised by 18cm over 24hr 2) Head devices held at elevated position for next 24hr 3) Head devices lowered by 18cm over 24hr
Water Table Fluctuation 2	WT2	Day 38 16:15	Exact repeat of water table fluctuation 1 method
Water Table Fluctuation 3	WT3	Day 51 17:20	1) Head devices raised by 18cm over 48hr 2) Head devices held at elevated position for next 48hr 3) Head devices lowered by 18cm over 48hr
Rain event 1	R1	Day 65 17:45	5.0 min rain in all compartments, water flow of 1.0 LPM in each compartment
Rain event 2	R2	Day 74 19:30	6.5 min rain in all compartments, water flow of 1.0 LPM in each compartment
Rain event 3	R3	Day 81 20:45	5.3 min rain in all compartments, water flow of 1.0 LPM in each compartment
Rain event 4	R4	Day 87, 18:50	5.0 min rain in compartments 1 & 2 only, water flow of 1.0 LPM in each compartment

Water table fluctuations 1 and 2 were duplicate experiments conducting the full water table fluctuation over 3 days, while water table fluctuation 3 had the overall same magnitude, but was done more slowly over 6 days. When raising and lowering the constant head devices, a semi-continuous rate of rise was achieved by raising or lowering them 1.5 cm every 2hr for WT1 and WT2, and by 1.5cm every 4hr for WT3. A total rise of 18cm was used in all 3 water table fluctuations. With the rain events, the intent was to produce as uniform a wetting front as possible. However, during R1, excessive fingering of the water infiltration was observed in large part due to some drying of the sand pack that had occurred over the previous 65 days of the experiment, despite efforts to humidify the atmospheric air inflow. It was decided to sacrifice this rain event with the intent of rewetting the sand, and rain was applied at a heavy rate for several minutes afterward. Thus, the data for R1 should be considered qualitative. The tank was allowed to re-equilibrate, and the infiltration fronts in subsequent experiments did not observe

fingering. R2 and R3 were duplicates, and R4 tested the effect of non-uniform infiltration. After 106 days, the experiment was terminated.

4.6.3.2 Heterogeneous case: The heterogeneous case was run after the homogeneous case. The tank rested 1 month prior to repacking while continued vacuum flow occurred to flush VOC vapors from the tank. When the tank was repacked, the #40/50 Accusand was excavated to below the level of the heterogeneous layer. This sand was dried and reused. The tank was wet packed, drained, and sealed as described previously. In the heterogeneous case, the initial constant head devices were located at 31.7cm at the influent and at 11.7 cm at the effluent, higher than in the homogenous tank. It was discovered that some pore clogging had occurred in the inlet screen possibly due to microbial growth during the shutdown period. The inlet screen was scraped to remove as much of this growth as possible, but a higher head was necessary in the heterogeneous tank in order to force a flow that was similar to the homogeneous case. Unlike the homogeneous case where there were several intentional and unintentional airflow adjustments, the entire heterogeneous case was run at an airflow of 3.001 SLPM, except for the NAPL experiment where the location of airflow was changed. A total of 3 water table fluctuation events and 3 rain events were applied, as well as 1 NAPL injection experiment. These events are outlined in table 4.6.

Table 4.6: Heterogeneous test cases

Event	Abbreviation	Start day time	Description
Water Table Fluctuation 4	WT4	Day 23 9:30	A complex water table fluctuation. Procedure: 1) water level raised 9cm to 40.7cm over 24hr 2) water level held at 40.7cm for 24hr 3) water level lowered 18cm to 20.7 over 48hr 4) water level held at 20.7cm for 24hr 5) water level raised 9cm to 31.7cm over 24hr
Water Table Fluctuation 5	WT5	Day 43 0:30	A short increase and decrease 1) water level raised 9cm to 40.7cm over 24hr 2) water level held at 40.7cm for 24hr 3) water level lowered 9cm to 31.7 over 24hr
Water Table Fluctuation 6	WT6	Day 54 4:30	A short decrease and increase 1) water level lowered 9cm to 20.7 over 24hr 2) water level held at 20.7cm for 24hr 3) water level raised 9cm to 31.7cm over 24hr
Rain event 5	R5	Day 59 17:00	14.5 minutes rain applied, unequally to rewet the sand
Rain event 6	R6	Day 74 20:45	A second rain event to rewet the sand (qualitative)
Rain event 7	R7	Day 77 21:15	Unequal rain event due to rainmaker malfunction. Compartments 3 and 4 ponded water, compartments 1 and 2 had normal rain application at 1 LPM water for 5 minutes.
NAPL 1	N1	Day 89, 5:00	65.6 g of TCE injected into source zone trough. 4.5 days prior to NAPL injection, the water table was brought up to height of 73.7 cm (influent) and 53.7 cm (effluent), and stabilized. After NAPL injection, airflow is switched to pull from outlet 1. The water table is steady for 9 days. On day 98, at 5:30, the reduced by 15cm over 40 hrs

The water table fluctuations in the heterogeneous case were complicated by the presence of the heterogeneity, as well as the higher initial water table. As a result, a water table increase of only 9cm was possible without swamping the vacuum line. WT4 takes the form of a sine-wave shaped fluctuation, rising by 9cm, then falling 18cm, then returning to the initial position. WT5 takes the

form of just the first half of WT4, while WT6 takes the form of the second half. With regard to the rain events, problems with the rain-making devices only allowed the data to be used for qualitative analysis. R5 and R6 were both attempts to rewet the sand after it dried, but fingering was excessive in compartment 1. On the R7 rain attempt, the rainmaking devices in compartment 3 and 4 malfunctioned and resulted in a swamping boundary condition on top of the sand pack, while compartments 1 and 2 behaved normally. The flow-rate to the swamped compartments exceeded the flowmeter capacity and as a result an unknown volume was applied to the compartment. Because it was cost and time prohibitive to reopen the tank and fix the rain makers, and good rain data sets were gathered in the homogeneous tank, the rain experiments were abandoned in the heterogeneous tank.

4.7 Geophysical tank experiment

4.7.1 Objectives

One of the primary objectives of this task is to improve the spatial and temporal resolution of data sets associated with VI studies. We approached this objective by performing a series of intermediate-scale laboratory tests to evaluate the performance and limitations of electrical resistance tomography (ERT) under varying water table conditions and increasingly complex heterogeneous packing configurations. By evaluating ERT performance and limitations in a controlled laboratory environment, we are able to better design a proof of field test.

4.7.2 Apparatus

All ERT laboratory experimentation was performed in an intermediate-scale two-dimensional vertical sand tank apparatus. The testing tank apparatus was constructed using 5/8"-thick clear plexiglass panels for front, rear, bottom, and sides (length = 220 cm, width = 8.25 cm, height = 110 cm). The panels were sealed using clear silicone and bolted together using stainless-steel hardware. The top of the sand tank was left open to the atmosphere to allow access for geophysical instrumentation. The sides of the sand tank contained water drainage points connected to vertically adjustable external reservoirs (diameter = 8 cm, height = 15 cm), as seen in Figure 4.12. An array of soil moisture sensors (see section 4.2.1.3) were installed along vertical profiles (at depths of 4, 14, 25, 30, 35, 40, and 55 cm below ground surface {bgs}), as required to capture changes in soil moisture contents in response to the selected water table elevations. Given that ERT data is highly sensitive to the electrical properties of the material being investigated, recording accurate and precise soil moisture content values was crucial during all stages of experimentation. The soil moisture sensors were calibrated in accordance with the two point α -mixing model developed by Sakaki et al. (2011a).

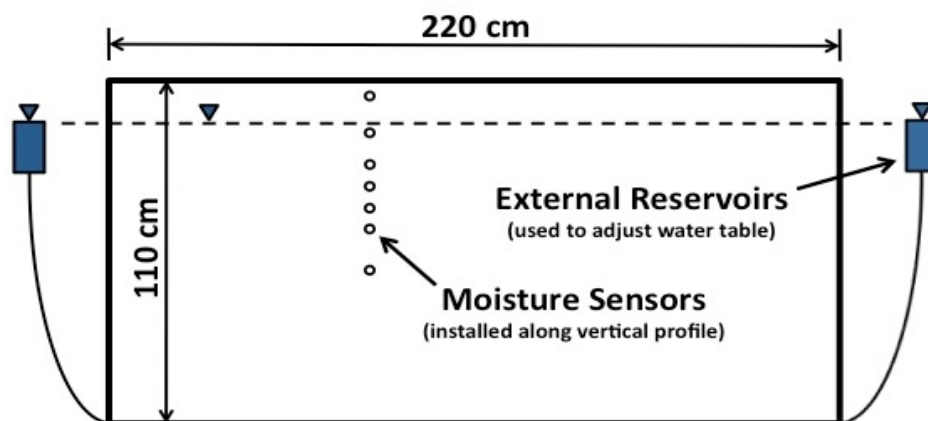


Figure 4.12: Schematic of the geophysical tank experiment apparatus with reservoirs used to control water table elevation and moisture sensors installed along a vertical profile. Moisture sensors were installed at vertical elevations of 4, 14, 25, 30, 35, 40, and 55 cm bgs (below ground surface). Total volume of sand tank apparatus is $163,350 \text{ cm}^3$.

All sensors used on this experiment were installed through the vertical walls of the test tank apparatus to avoid water channeling on the sensor wires. Temperature probes were installed through the walls of the sand tank apparatus at depths of 5 cm bgs and 80 cm bgs to capture any temperature variations throughout experimentation. Three uniform specialty silica sands, #12/20, #20/30, and Granusil #70 were used in different tank packings (see section 4.2.2.1 for porous media properties).

An earth resistivity meter with 28 stainless steel electrodes was used to perform ERT surveys along surface profiles in the sand tank apparatus (see section 4.2.1.5 for ERT equipment description). The electrodes were inserted directly into the sand surface. An electrode spacing of 6.25 cm was selected based on the spatial resolution and depth of investigation required to capture the sand-pack heterogeneities. For ERT investigations, as the electrode spacing decreases, the depth of investigation decreases proportionally and the resolution increases (Sheriff, 2004). Based on the packing configurations selected, our experiments required an approximate depth of investigation of 45 cm (to adequately capture the packed heterogeneities) and a spatial resolution fine enough to capture a horizontal layer as thin as 4 cm.-thick (used in our final sand-pack configuration). Several feasibility tests were performed to determine the optimal electrode array for the tank, and are described in Shannon (2012).

4.7.3 Experimental Procedure

To perform the ERT laboratory evaluations, the sand tank apparatus was carefully wet-packed using well-characterized crushed silica sands in three unique, heterogeneously-packed configurations to create three physical VI models as shown in Figure 4.13. During the wet-packing procedure, the sand was carefully poured into the sand tank apparatus using a sieve in incremental layers of approximately 2 cm. The depth of the water in the sand tank apparatus was kept constant at approximately 12 cm in order to minimize depositional layering. Maximum packing density was achieved by physically disturbing the wet-packed surface after each sand layer was deposited, and by tapping the walls of the sand tank during and after each sand layer

was deposited; this method has been documented to achieve higher packing density than the methods outlined by ASTM D 4253-00.

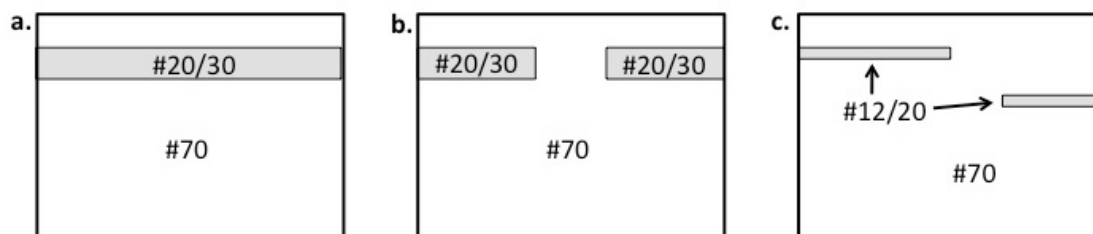


Figure 4.13 (a-c). Schematic of geophysical sand tank packing configurations: (a) *Configuration #1* – Fine matrix (#70 sand) with coarse continuous horizontal layer (#20/30 sand, 10 cm. thick). (b) *Configuration #2* – Fine matrix (#70 sand) with coarse discontinuous horizontal layer (#20/30 sand, 10 cm. thick). (c) *Configuration #3* - Fine matrix (#70 sand) with shallow and deep thin discontinuous horizontal layers (#12/20, 4 cm. thick). Figures not drawn to scale.

For each packing configuration (Figure 4.13), the water table was initially established at the top of the sand tank apparatus. Initial ERT profiles were taken under fully saturated conditions. The bottom and side boundaries of the sand tank apparatus were kept as no-flow boundaries throughout the experimentation. The water table was then lowered in incremental stages, allowed to equilibrate approximately 60 minutes, and resurveyed along the same surface profile used in the previous ERT test. Three water table elevations, fully saturated, at a vertical midpoint and a lower point (20-30 cm below the soil surface, respectively) were designed to capture three specific moisture distribution conditions within the heterogeneously-packed configurations. The second water table elevation (10-15 cm below the soil surface) was selected to allow for ERT evaluations under transitional moisture content conditions. The third and final water table elevation (20-30 cm below the soil surface) was set at a low point within the sand tank apparatus at approximately 20-30 cm below the area of interest (i.e. the vertical intersection of coarse and fine layers). This experimental procedure of evaluating ERT methods under three distinct water table elevations was repeated for all three heterogeneous sand-pack configurations. For the duration of each ERT experiment, water content, temperature and electrical conductivity were concurrently monitored and recorded at five-minute intervals using self-contained digital data loggers.

4.8 Geophysical Site Demonstration

4.8.1 Objective

A field demonstration was initiated to learn whether dynamic vapor intrusion behavior would be observed due to dynamic soil moisture events. This test employed a field site at Hill Air Force Base in Ogden, Utah in collaboration with the SERDP Project ER-1686 team. The field test involved the deployment of soil moisture sensors and the ERT geophysical scanning system along with a simulated precipitation event (applied through sprinklers) at a house with vapor intrusion to see if a vapor signal could be observed. Testing this in the field gained insight into the practical affect of dynamic soil moisture and may help inform future observation and analysis at VI sites.

4.8.2 Site Background

The site selected for field demonstrations is currently owned and operated as a SERDP-funded field study site by Professor Paul Johnson from Arizona State University (ASU). The field site is located in Layton, Utah, as seen in Figure 4.14.



Figure 4.14: Map with field demonstration site location (indicated by red star) located adjacent to Hill AFB, UT.

The site selected for this field demonstration is a residential home that has been converted to a field study site by Professor Johnson's research group from ASU. The site is adjacent to Hill Air Force Base (AFB) and is one of many homes in the area that the DoD has identified as a site with compromised indoor air quality due to VI related mechanism. Groundwater contamination on the site consists of a dissolved-phase chlorinated solvent plume containing trichloroethylene (TCE) as the primary chemical of concern (COC). This contaminated groundwater plume, along with the associated contaminated pore-water in the capillary zone produces observable VI signals on-site. Soil gas measurement points include interior sub-slab, above slab, interior ambient, and exterior subsurface locations (at three-foot depth increments from surface to groundwater elevation located at approximately 15 ft bgs). Professor Johnson's research group has installed a sensor and sampling network that covers the entire building envelope (interior and sub-slab) and six exterior subsurface regions around the building, as seen in Figure 4.15.

The sensor and sampling networks consist of O₂ sensors, pressure transducers, and soil-gas monitoring points in the unsaturated zone surrounding and below the building envelope. Their soil-gas monitoring program is autonomous and continuous. It employs an on-site soil-gas collection system, which automatically collects and runs samples through an on-site gas chromatograph/mass spectrometer (Hapsite GC/MS, Inficon, Syracuse, New York) every four

hours. The group has installed a MET station in the back yard to record key atmospheric data sets such as precipitation, rain, humidity, temperature, and wind speed.

4.8.3 Technical Approach

The technical approach used for the field demonstration incorporated an induced and controlled moisture event at the ground surface (using the available on-site garden sprinkler system), and observing the hydrologic response in the vadose zone using ERT (see section 4.2.1.5), while simultaneously monitoring the VI signal using an on-site GC/MS. Initial evaluations of site geology indicate highly heterogeneous conditions composed primarily of silts/clays with interbedded fine sand stringers that span from approximately 1 m below ground surface (bgs), to the water table, located approximately 3 m bgs across the site, as seen in Figure 4.16 and 4.17.

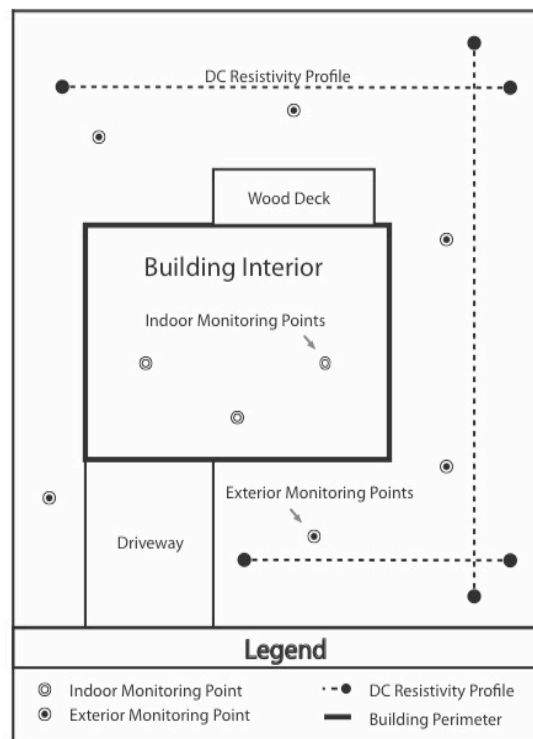


Figure 4.15: Schematic of VI monitoring locations with exterior and interior monitoring points indicated by concentric circles (oxygen concentrations, pressure potential, and soil gas sampling ports) and ERT profiles indicated by dashed lines with solid circular ends.

GEOLOGY

Silt/clay with numerous fine sand stringers

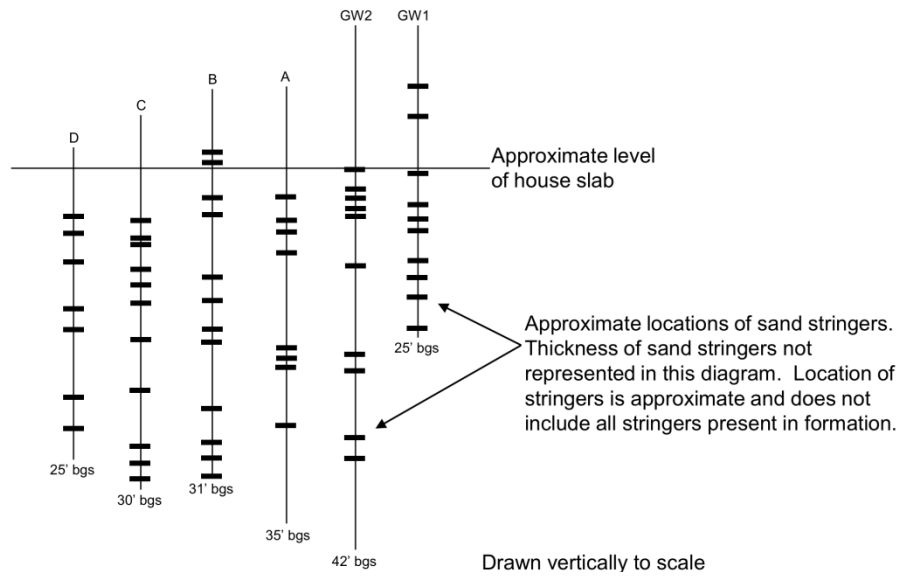


Figure 4.16: Schematic of subsurface geologic composition at field demonstration site in Utah [Ongoing VI site study by Johnson et al., 2010-2012].

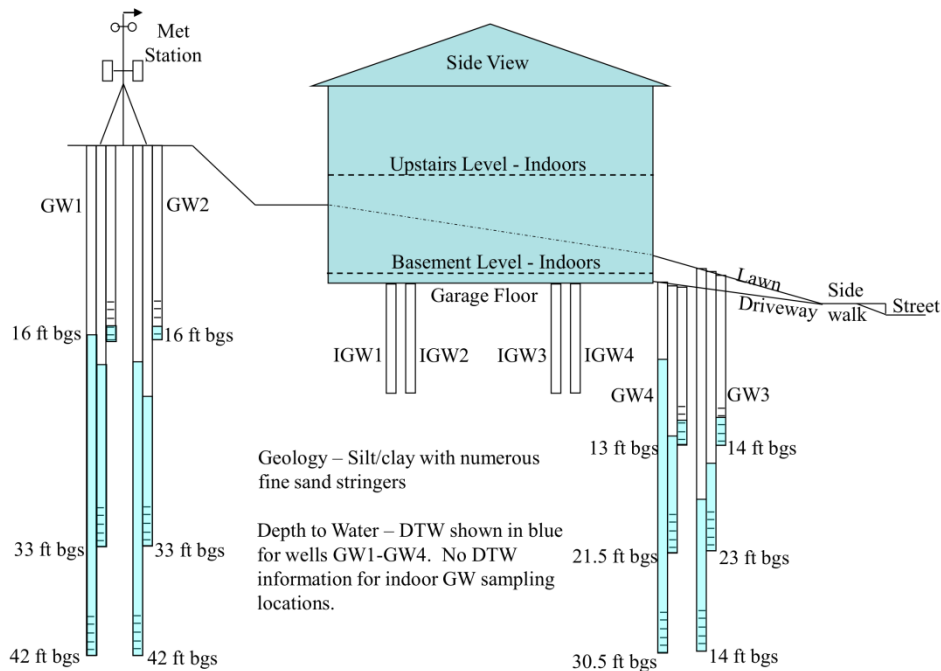


Figure 4.17: Schematic of water table elevations across field demonstration site [Ongoing VI site study by Johnson et al., 2010-2012].

To collect moisture and temperature gradients along the ERT profile selected, a small hole was manually excavated (adjacent to the selected ERT profile) and soil moisture and temperature sensors (see section 4.2.1.3) similar to those used in the laboratory experiments, were installed at

depths of 0.25 m, 0.75 m, 1.25 m, 1.75 m, and 2.25 m bgs. The sensors were inserted directly into undisturbed soils along the vertical profile of the excavated sidewalls. For the duration of the ERT field demonstration event, water content and temperature were continuously monitored and recorded by data-loggers at five-minute intervals. The soil moisture and temperature sensor data was later used to constrain the inversions of the ERT data, as well as provide baseline profiles for soil moisture contents and temperatures.

The first series of ERT surveys were designed to capture baseline profiles of the vadose zone bordering the western perimeter of the residential building, as shown in Figure 4.15. Then a moisture event was applied to the surface (via a residential irrigation system) in an effort to simulate a natural precipitation event and resurveyed the ERT profile several more times. Continuing to resurvey the ERT surface profile after the induced moisture event allowed us to capture the temporal and spatial change in moisture distributions in response to the induced surface moisture event, thus capturing the infiltration front moving downward and any lateral infiltration that might occur into the fine sand stringers. By combining the data collected using ERT and the data from the GC/MS, we predicted that this would allowed us to develop a spatial and temporal constraint on the intersection of vapor pathways with the induced wetting front, thus developing a novel characterization of the VI pathways in the vadose zone surrounding a VI-contaminated residential building.

4.9 Scenario Simulations

Field measurements of vapor intrusion often contain considerable uncertainty in part due to difficult-to-explain transience in monitoring data (McHugh et al., 2007; Folkes et al., 2009). One objective of this project is to apply the new knowledge generated from the other tasks to develop an understanding of what possible transient behavior may be expected at the field scale. To do this, a series of hypothetical scenarios were developed to simulate the behavior of vapors around an individual house using realistic values for field soils and household geometries. These scenarios were subjected to rainfall infiltration and water table fluctuation events of varied magnitudes, and the concentration response within the building was observed. As a further step to illustrate the affect these processes have on the conceptual model of VI, these scenarios were compared to the corresponding Johnson and Ettinger (1991) model for the same system. Using these scenarios, a practical sense for the magnitude, duration and effect of these transient processes on VI into buildings can be gained.

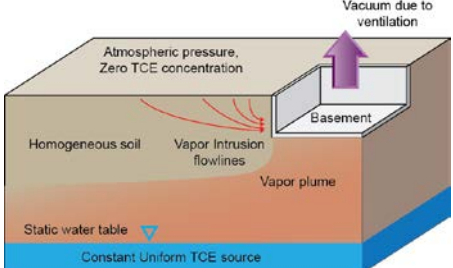
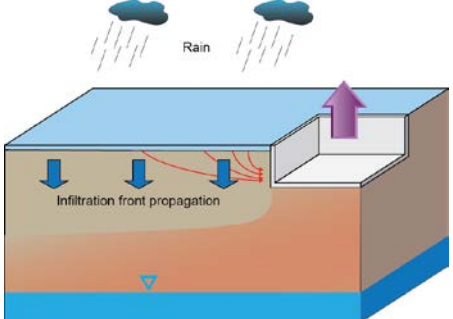
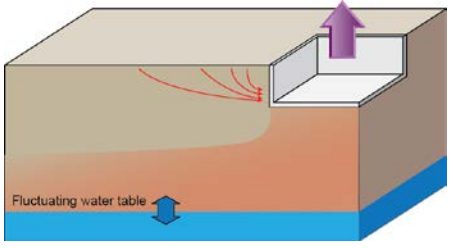
4.9.1 Approach

The approach used a series of fictitious VI scenarios based on the validated model with the goal of gaining insights into how infiltration and water table fluctuation may affect vapor intrusion into houses. The goal of this exercise was not to try and simulate every possible combination of the built environment or vadose zone heterogeneity, but rather to gain some insight into how systems may behave. Therefore, the scenarios started with a comparatively simple system around an individual house, and gradually became more complex. The knowledge generated from this exercise provides the basis for a more comprehensive conceptual model of the vapor intrusion pathway, and may lead to the development of decision support tools in the future.

Two-dimensional simulations approximating typical geometry were used in this study; while it is anticipated that the three-dimensional geometry of houses may have significant effects on the vapor observations, it proved to be too computationally intensive to solve these scenarios in 3-D using the current COMSOL software based model. An independent modeling code that is more efficient has been developed by collaborators at Czech Technical University (see appendix A), and is being tested and validated at the time of this report. It is anticipated that future more realistic field scenarios will be solved in 3-D with this more efficient code, possibly as part of a future ESTCP project.

The base case scenario consists of an isolated house surrounded by vacant land (open atmospheric boundary). The geometry of the house was the same as that used by Abreu and Johnson (2005) and Bozkurt et al. (2009) to facilitate comparison of results to other studies. The plume dynamics were held constant at depth, but conditions at the capillary fringe were allowed to change in accordance with infiltration and water table fluctuations. Upon this base case, three physical processes were simulated including a falling water table and a rain event at the soil surface. These scenarios are graphically outlined in table 4.7.

Table 4.7: Proposed scenarios demonstrating the effect of individual processes on vapor intrusion

Scenario	Conceptual model
<p>Base case scenario</p> <p>This provides a basis of comparison for all other scenarios using the simplest form of the model. Default values for house under pressurization will be used for all simulations. The model is steady-state.</p>	
<p>Case 1: Uniform rain at the land surface</p> <p>Rainfall uniformly applied to land surface. Vapor intrusion will be simulated until the system comes back to steady-state to demonstrate the full timing and effect of rain on VI. Independent variables include depth to groundwater, rainfall intensity and duration.</p>	
<p>Case 2: Volatilization from a falling water table.</p> <p>A falling water table is increasing the pathway distance between the capillary fringe and the house. Independent variables include depth to groundwater, rate of groundwater fall, and magnitude of groundwater drop.</p>	

4.10 References

- Abreu, Lilian D. V., and Paul C. Johnson. 2005. "Effect of Vapor Source-Building Separation and Building Construction on Soil Vapor Intrusion as Studied with a Three-Dimensional Numerical Model." *Environmental Science & Technology* no. 39 (12):4550-4561. doi: doi:10.1021/es049781k.
- Bozkurt, Ozgur, Kelly G. Pennell, and Eric M. Suuberg. 2009. "Simulation of the Vapor Intrusion Process for Nonhomogeneous Soils using a Three-Dimensional Numerical Model." *Ground Water Monitoring and Remediation* no. 29 (1):92-104.
- Braida, Washington, and S. K. Ong. 1998. "Air sparging: Air-water mass transfer coefficients." *Water Resour. Res.* no. 34 (12):3245-3253.
- Braida, Washington, and S. K. Ong. 2000. "Influence of porous media and airflow rate on the fate of NAPLs under air sparging." *Transport in Porous Media* no. 38 (1/2):29-42.
- Folkes, David, William Wertz, Jeffrey Kurtz, and Theodore Kuehster. 2009. "Observed Spatial and Temporal Distributions of CVOCs at Colorado and New York Vapor Intrusion Sites." *Ground Water Monitoring and Remediation* no. 29 (1):70-80.
- Illangasekare, Tissa H., Junko Munakata-Marr, R. L. Siegrist, K. Soga, Kent C. Glover, E. Moreno-Barbaro, J. L. Heiderscheidt, Satawat Saenton, Mini Matthew, Ann R. Kaplan, Yongcheol Kim, Dongping Dai, Jose L. Gago, and John W. E. Page. 2006. Mass Transfer from Entrapped DNAPL Sources Undergoing Remediation: Characterization Methods and Prediction Tools. In *Final Report: SERDP Project ER-1294*. Washington, D.C.: Strategic Environmental Research and Development Program. 437 p
- Johnson, Paul C., and Robert A. Ettinger. 1991. "Heuristic model for predicting the intrusion rate of contaminant vapors into buildings." *Environmental Science & Technology* no. 25 (8):1445-1452. doi: doi:10.1021/es00020a013.
- Lowry, G., T. Phenrat, F. Fagerlund, Tissa H. Illangasekare, P. Tratnyek, and Richard L. Johnson. 2012. Fundamental Study of the Delivery of Nanoiron to DNAPL Source Zones in Naturally Heterogeneous Field Systems. In *Final Report: SERDP Project ER-1485*. Washington, DC: Strategic Environmental Research and Development Program. 133 p
- McHugh, Thomas E., Tim N. Nickels, and Samuel Brock. 2007. Evaluation of Spatial and Temporal Variability in VOC Concentrations at Vapor Intrusion Investigation Sites. Paper read at Proceedings of Air & Waste Management Association's Vapor Intrusion: Learning from the Challenges, September 26-28, 2007, at Providence, RI.
- Miller, C. T., M. M. Poirier-McNeill, and A. S. Mayer. 1990. "Dissolution of Trapped Nonaqueous Phase Liquids: Mass Transfer Characteristics." *Water Resour. Res.* no. 26 (11):2783-2796.
- Moreno-Barbaro, Elena, Yongcheol Kim, Satawat Saenton, and Tissa H. Illangasekare. 2007. "Intermediate-Scale Investigation of Nonaqueous-Phase Liquid Architecture on Partitioning Tracer Test Performance." *Vadose Zone Journal* no. 6:725-735.

- Oostrom, M., J. H. Dane, and T. W. Wietsma. 2005. "Removal of Carbon Tetrachloride from a Layered Porous Medium by Means of Soil Vapor Extraction Enhanced by Dessication and Water Table Reduction." *Vadose Zone Journal* no. 4:1170-1182.
- Powers, Susan E., Linda M. Abriola, Joyce S. Dunkin, and Walter J. Weber, Jr. 1994. "Phenomenological Models for Transient NAPL-Water Mass-Transfer Processes." *Journal of Contaminant Hydrology* no. 16:1-33.
- Rodriguez, Derrick. 2006. *Significance of Diffused Zone Mass Storage and Rebound in Determining the Longevity of Solute Plumes Emanating from Heterogeneous DNAPL Source Zones*, Environmental Science and Engineering, Colorado School of Mines, Golden, Colorado.
- Rogers, Shane W., and Say Kee Ong. 2000. "Influence of Porous Media, Airflow Rate, and Air Channel Spacing on Benzene NAPL Removal during Air Sparging." *Environmental Science & Technology* no. 34 (5):764-770. doi: doi:10.1021/es9901112.
- Saba, T., and Tissa H. Illangasekare. 2000. "Effect of Groundwater Flow Dimensionality on Mass Transfer from Entrapped Nonaqueous Phase Liquid Contaminants." *Water Resour. Res.* no. 36 (4):971-979.
- Sakaki, Toshihiro, and Tissa H. Illangasekare. 2007. "Comparison of Height-Averaged and Point-Measured Capillary Pressure-Saturation Relations for Sands using a Modified Tempe Cell." *Water Resour. Res.* no. 43:W12502.
- Sakaki, Toshihiro, Anuchit Limsuwat, and Tissa H. Illangasekare. 2011a. "An Improved Air Pressure Measuring Method and Demonstrated Application to Drainage in Heterogeneous Soils." *Vadose Zone Journal* no. 10:706-715.
- Sakaki, Toshihiro, Anuchit Limsuwat, and Tissa H. Illangasekare. 2011b. "A Simple Method for Calibrating Dielectric Soil Moisture Sensors: Laboratory Validation in Sands." *Vadose Zone Journal* no. 10:526-531.
- Shannon, Luke. 2012. *Evaluating a novel approach for locating preferential vapor transport pathways in the vadose zone: joint-interpretation of soft data from electrical resistivity tomography with hard data*, M.Sc. Thesis. Advisor: Kathleen Smits, Civil and Environmental Engineering, Colorado School of Mines, Golden, CO.
- Sheriff, R. E. 2004. *Encyclopedic Dictionary of Exploration Geophysics*. 4th ed: Society of Exploration Geophysicists.266
- Siegrist, R. L., M. Crimi, Junko Munakata-Marr, Tissa H. Illangasekare, K. Lowe, S. van Cuyk, P. Dugan, J. L. Heiderscheidt, S. Jackson, B. G. Petri, J. Sahl, and S. Seitz. 2006. Reaction and Transport Processes Controlling In Situ Chemical Oxidation of DNAPLs. In *Final Report: SERDP Project ER-1290*. Washington, D.C.: Strategic Environmental Research and Development Program. 235 p
- Siegrist, R. L., R. C. Oesterreich, L. Woods, and M. Crimi. 2010. Improved Monitoring Methods for Performance Assessment During Remediation of DNAPL Source Zones. In *Final*

Report: SERDP Project ER-1490. Washington, D.C.: Strategic Environmental Research and Development Program. 116 p

Smits, Kathleen M. 2010. *Non-isothermal soil moisture processes in the shallow subsurface influenced by atmospheric boundary conditions: numerical and experimental study*, Environmental Science and Engineering, Ph.D dissertation. Advisor: Tissa Illangasekare, Colorado School of Mines, Golden, Colorado.

van Genuchten, M. Th., F. J. Leij, and S. R. Yates. 1991. The RETC code for quantifying the hydraulic functions of unsaturated soils, Version 1.0. edited by USDA U.S. Salinity Laboratory, ARS. Riverside, CA. p

Wilkins, M. D., Linda M. Abriola, and Kurt D. Pennell. 1995. "An Experimental Investigation of Rate-Limited Nonaqueous Phase Liquid Volatilization in Unsaturated Porous Media: Steady State Mass Transfer." *Water Resour. Res.* no. 31 (9):2159-2172.

Yoon, Hongkyu, Joong Hoon Kim, Howard M. Liljestrand, and Jeehyeong Khim. 2002. "Effect of Water Content on Transient Nonequilibrium NAPL-Gas Mass Transfer During Soil Vapor Extraction." *Journal of Contaminant Hydrology* no. 54:1-18.

Chapter 5: Results and Discussion

5.0 Introduction

This chapter presents results and discussion from the experimental and modeling studies outlined in chapter 4. Special emphasis is made on the scientific and practical observations that yield new insight into vapor intrusion and related contaminant fate and transport mechanisms. This work resulted in a series of publications, master and PhD theses, book chapter and conference presentations that are summarized in Appendix B.

5.1 Vadose zone NAPL source volatilization studies

The objective of the NAPL volatilization studies was to evaluate the mass transfer behavior of NAPL sources in the vadose zone under varied soil moisture conditions, and determine how these sources might impact loading to vapor plumes that affect VI. A number of scenarios of NAPL sources in the vadose zone are possible. One is a NAPL source that is trapped in the saturated zone becoming exposed when the water table drops. It is also possible that a source that did not is completely removed during remediation, especially if it is entrapped in a high water content zone. The vadose zone NAPL source volatilization studies measured VOC concentration and flux data from NAPL sources, as well as temperature, pressure, and airflow rate. The results for the case 1 (occluded NAPL source studies) and case 2 (exposed NAPL source studies) experiments are discussed separately. Modeling results, based on the experiments are used as a data analysis tool to determine the role of advection-diffusion transport given the two NAPL configurations and to determine how well existing physical transport theory can capture the observed mass transfer behavior.

5.1.1 Occluded NAPL experimental results (Case 1)

Figures 5.1a and 5.1b show the measured effluent TCE vapor concentration and the gas phase Darcy flux through the unsaturated portion of the tank for the “thick” and “thin” occlusion experiments, respectively (see section 4.3.3 for description). Stepwise changes in the flow rate resulted in step-like behavior in the effluent concentration response, with slower flow rates yielding higher effluent concentrations. The saturation concentration of TCE in the gas phase, estimated from measured temperature data (which fluctuated between 19°C and 26°C) and the TCE saturation vapor pressure curve reported by Boublík et al. (1973), is also given in figure 5.1 to show the departure from equilibrium contaminant transfer. Clearly, observed effluent concentrations are lower than the equilibrium saturation concentration, often by two orders of magnitude or more, suggesting that the occlusion layer provides significant resistance to mass transfer. Interestingly, effluent concentrations adjusted rapidly to new pseudo steady-state values following decreases in the air phase flow rate. The measured effluent concentration variations with time are generally steady with only minor “blips” on the concentration plot, which correspond to ambient temperature changes in the laboratory that affects the vapor partitioning. Note that there was a no flow period in the “thick” occlusions system that resulted from a power failure.

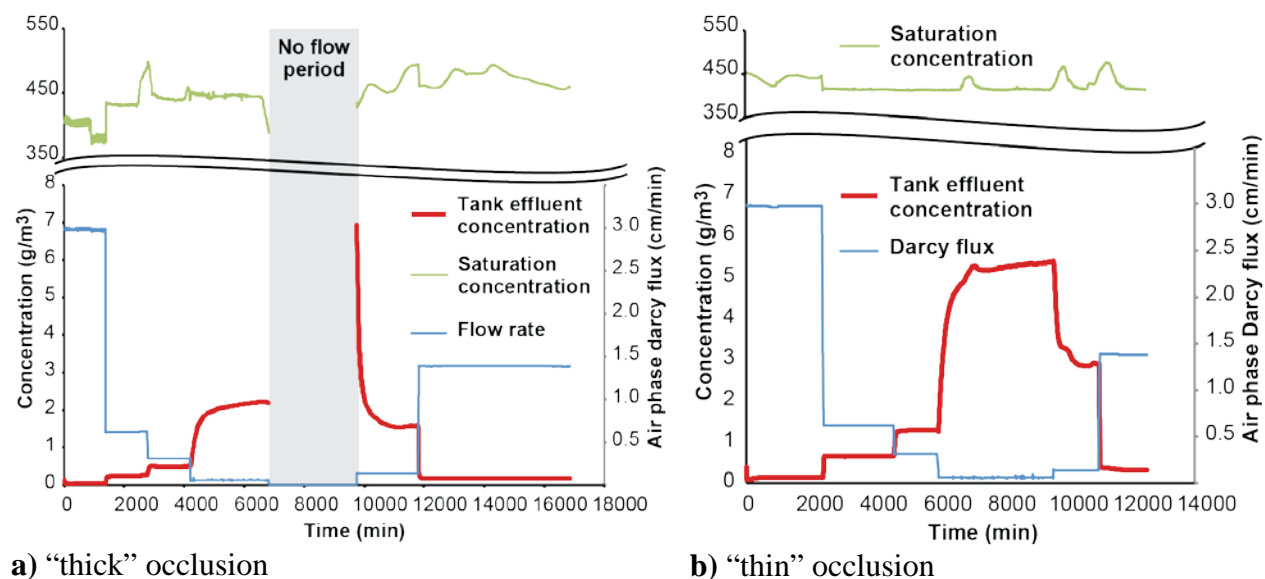


Figure 5.1: Measured TCE effluent vapor concentration versus time for a) the 13.8 mm “thick” occlusion and b) the 8.5 mm “thin” occlusion. The red line represents the concentration of TCE in the effluent soil gas (g/m³), green line represents the saturation concentration of TCE estimated from temperature data using values from Boublík et al. (1973)(g/m³) (note y-axis break), and the blue line represents the air phase Darcy flux in the unsaturated portion of the tank.

Table 5.1 presents a summary of the experimental results, including the average pseudo steady-state concentration for each flow rate tested in both the “thick” and “thin” occlusion tank experiments, as well as the average TCE mass flux eluting from the tank (product of gas phase concentration and flow rate).

The rapid response of the system to air phase velocity changes may be partly explained by strong rate limitations caused by diffusion across the water phase occlusion. Table 5.1 data indicate that despite large shifts in air-phase concentrations (range of 0.04 to 2.1 g/m³ in the thick occlusion, 0.14 to 5.3 g/m³ for the thin occlusion), the average TCE mass flux rate from the occluded sources for all velocities varies over a narrow range (mean, standard deviation of 3.28 ± 0.89 $\mu\text{g}/\text{min}$ for the thick occlusion, 7.74 ± 0.74 $\mu\text{g}/\text{min}$ for the thin occlusion), suggesting shifts in flow rate largely dilute the relatively constant flux emanating from the occluded source.

Table 5.1: Summary of experimental results

Run	NAPL configuration	Airflow rate (standard $\text{cm}^3\text{min}^{-1}$)	Average pore velocity (m/d^{-1})	Observed Steady State concentration (gm^{-3})*	Mass flux rate (mg/min)	Fraction of saturation vapor pressure	Modeled steady state concentration (gm^{-3})
1	Case 1: Thick Occlusion	50.0	145	0.0401 +/- 0.0009	0.002	0.01%	0.0971
2	Case 1: Thick Occlusion	22.5	67.9	0.1754 +/- 0.0001	0.005	0.04%	0.2080
3	Case 1: Thick Occlusion	10.0	30.2	0.2467 +/- 0.0013	0.003	0.06%	0.4620
4	Case 1: Thick Occlusion	5.00	15.1	0.4999 +/- 0.0008	0.003	0.11%	0.9185
5	Case 1: Thick Occlusion	2.25	6.72	1.5656 +/- 0.0024	0.004	0.33%	2.0093
6	Case 1: Thick Occlusion	1.00	2.88	2.1389 +/- 0.0086	0.003	0.48%	4.5421
7	Case 1: Thin Occlusion	50.0	145	0.1412 +/- 0.0003	0.008	0.03%	0.1483
8	Case 1: Thin Occlusion	22.5	67.4	0.3270 +/- 0.0025	0.009	0.08%	0.3114
9	Case 1: Thin Occlusion	10.0	30.2	0.6542 +/- 0.0003	0.008	0.16%	0.7088
10	Case 1: Thin Occlusion	5.00	15.1	1.2859 +/- 0.0012	0.008	0.31%	1.4075
11	Case 1: Thin Occlusion	2.25	6.72	2.8812 +/- 0.0048	0.008	0.68%	3.1789
12	Case 1: Thin Occlusion	1.00	2.88	5.2813 +/- 0.0076	0.006	1.27%	6.9203
13	Case 2: Free NAPL (Pool)	50.0	138	163.63 +/- 5.10	9.442	33%	transient
14	Case 2: Free NAPL (Pool)	10.0	29.0	323.78 +/- 8.51	3.921	67%	transient
15	Case 2: Free NAPL (Pool)	5.00	14.6	426.68 +/- 5.30	2.591	87%	transient
16	Case 2: Free NAPL (Pool)	1.00	3.84	415.91 +/- 3.00	0.484	97%	transient

* mean +/- 95% confidence interval of the mean

**Atmospheric pressure in Golden Colorado averages ~82000 Pa.

The reason the source flux does not respond strongly to changes in airflow can be explained by conventional advection-diffusion theory. Because the “occlusion layer” in this system is stagnant, and fully water saturated, it isolates the NAPL source from the flowing air phase in the coarse sand above. To volatilize, the NAPL must first dissolve within the source zone, then diffuse through the water phase occlusion to transfer mass to the gas phase. This diffusive flux is controlled by the concentration gradient across the water occlusion. On the NAPL side of the occlusion, the aqueous TCE concentration is near the solubility limit, while at the air-water occlusion interface, the concentration reflects that of the bulk flowing air, which under these experimental conditions is around 1% or less of the gas-phase saturation concentration. Thus, within this experimental system, the concentration gradient across the occlusion layer is near the maximum value, which results in a source flux that is relatively insensitive to the airflow velocity. This gradient will only reduce significantly if gas phase TCE concentrations in the bulk gas phase accumulate to significant levels, reducing the net change in concentration across the occlusion. In this event, gas phase transport processes such as bulk advection and diffusion may begin to affect source flux. The case 1 results are also consistent with what can be explained through the theory of diffusion, since experimental results demonstrate that the occluded layer thickness affects the source flux, i.e., a thicker occlusion has a longer diffusion distance and therefore lower concentration gradient (see table 5.1). These findings helps to conceptualize the mass transfer processes through occluded NAPL sources through traditional advection-diffusion theory.

5.1.2 Comparison of numerical and experimental results for occluded NAPL case

The steady-state concentrations predicted by the model presented in chapter 3 for each experimental run are presented in table 5.1, while a comparison of model and experimental

values for each run is presented in figure 5.2. The figure shows that without any fitting or calibration, the model predicts values within the range of the experimental observations, though with a positive bias in that the model predicts 144 +/- 29% of the observed steady-state effluent concentrations on average. However, the fit of the model is considerably better for all of the “thin” occlusion experiments, as well as both “thick” occlusion experiments that occurred after the unexpected flow shutdown, predicting 113 +/- 12% of the experimental value on average. Here the model prediction nearly brackets the experimental observations. It is important to note that in the case 1 model results, none of the model parameters are fitted through calibration, and only literature values for all basic process parameters are used. This is to ensure that the model yields insight into the physical process, rather than just fitting curves to unknown physics.

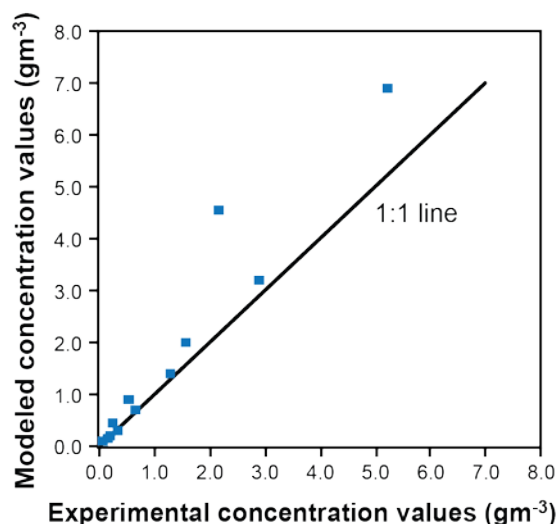
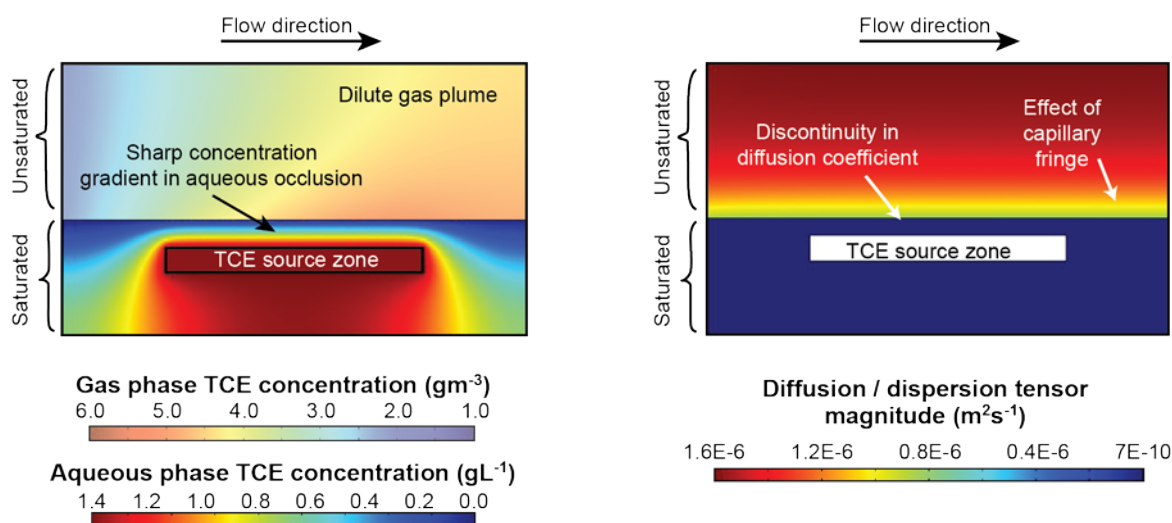


Figure 5.2: Comparison of steady-state model with experimental effluent concentration values for case 1 runs.

Over-prediction by the model is possibly due to inaccuracies in the precise representation of source zone geometry and NAPL phase distribution, which could control the contaminant flux through the occluded layer. In the model, the source is assumed to be at the TCE solubility limit everywhere within the source zone, based on the assumption that the NAPL is uniformly distributed. However, in practice, it is difficult to create uniform saturations in multiphase systems, and in this case TCE visibly pooled at the bottom of the source zone. Thus, the actual diffusion path in the experimental system might be longer than assumed within the model, leading to over-prediction of the simulated mass transfer rate. In the specific case of the “thick” occlusion system where the model over predicts by a much higher amount, it appears that the no flow period affected the observed mass transfer behavior. It is possible that prior to the unexpected no flow period, the system was not fully steady-state, and that no flow conditions may have given additional time to bring the system up to a steady state. Figure 5.3 shows a plot of the simulated total TCE concentration (sum of gas and aqueous phases) throughout the tank, as well as the magnitude of the diffusion dispersion tensor term (e.g. equation 11). The plot shows a steep concentration gradient is present within the occlusion layer. Likewise, the dispersion tensor shows a strong discontinuity across the occluding layer. It is this gradient, in combination with the dispersion tensor, that governs mass transfer within the tank. Only a very

dilute gas phase plume (<1% of saturation) extends downstream from the source, supporting the finding that aqueous phase diffusion is limiting this mass transfer process.



a) Concentration profile: pastel scale shows gas phase concentrations, dark axis shows aqueous concentrations

b) Diffusion / dispersion tensor magnitude profile

Figure 5.3: a) Simulated concentration profile and b) diffusion / dispersion tensor magnitude profile for run #12, 8.5 mm occlusion run at a pore velocity of 2.88 md⁻¹. TCE source zone outlined in white (at saturation concentration)

5.1.2 "Exposed" Source Experimental Results (case 2)

Results from the exposed source experiments (runs 13 – 16 in table 5.1) are presented in figure 5.4. The data are normalized by the saturation concentration of TCE to reduce the effect of ambient temperature fluctuations, which caused higher or lower effluent concentrations in response to ambient warming and cooling in the laboratory. In contrast to the occluded systems where effluent concentrations never exceeded more than 1% of the saturation concentration, the concentrations in the “exposed” NAPL systems clearly approached the saturation concentration. Upon NAPL injection, the effluent concentration rises quickly and approaches the saturation concentration until the NAPL source is depleted, after which concentrations diminish. Unlike the occluded systems, the exposed sources experiments were run until depletion of the NAPL was visually confirmed. The overall NAPL recovery mass balance on runs 13 through 16 (conducted sequentially in the same tank) was 97.8%

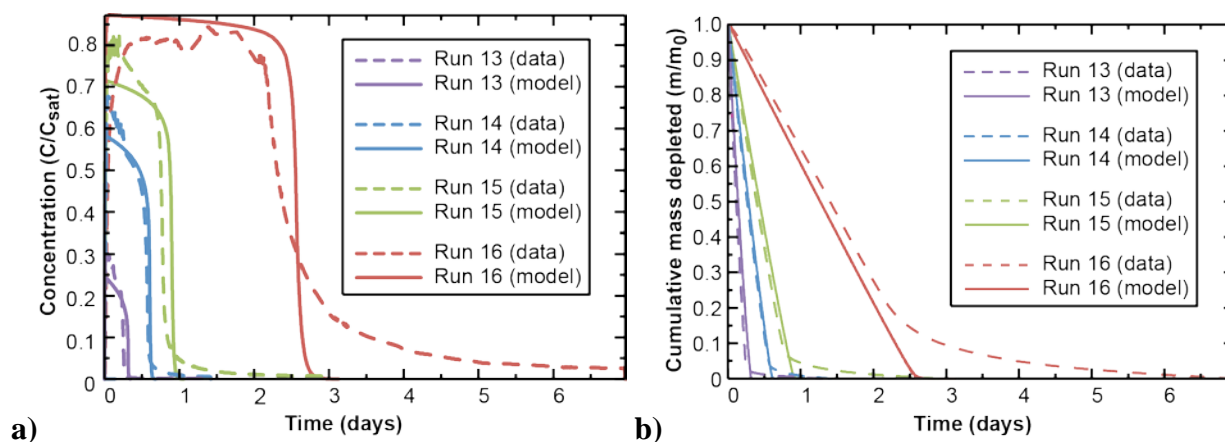


Figure 5.4: Concentration versus time for exposed source NAPL systems (a), the model (solid line) and measured data (dashed) outflow concentrations and (b) the model (solid line) and measured data (dashed) mass depletion curves.

Compared to the occluded systems, the exposed sources exhibit much higher average mass transfer rates and hence breakthrough concentrations (see table 5.1). This is expected, as the absence of an occlusion aqueous barrier to mass transport allows the NAPL to diffuse and disperse more rapidly within the soil gas. Additionally, the mass flux rate in NAPL exposed systems is dependent on air velocity, which contrasts with the occluded systems that had mass flux rates that were independent of velocity. This suggests that mass transfer in exposed systems is limited by gas phase advection.

To explore the role of advection in the mass transfer from exposed pools, a transport model was designed to simulate the mass transfer from the NAPL source. The original intent of running the “exposed” sources was to provide a basis of comparison to the occluded mass transfer systems within a similar porous media. A Gilliland-Sherwood mass transfer expression (see section 2.2.3.1 for description) was tested to determine if such a relation could accurately reproduce the experimental observations. As it was not the original intent of this study to produce a Gilliland-Sherwood mass transfer model, only a narrow range of experiments were run to investigate the mass transfer. However, these experiments do allow the estimation of a simple mass transfer rate coefficient as a function of the Peclet number, and it is insightful to compare this system to other volatilization mass transfer models in the literature (see table 5.2).

For the purpose of estimating a Gilliland-Sherwood relationship, the numerical model was used to simulate the tank and the Gilliland-Sherwood parameters were adjusted to best-fit the data. Fitted parameters included the regression constant (γ), Peclet number exponent (δ), and the mass tailing parameter (β). The model output was compared to the experimental breakthrough curve. The goal of the fitting procedure was to find a set of fitting parameter values γ , δ and β for which the difference between the simulated and experimental dissolution curves in all four airflow regimes is minimized. The best fit was obtained using a mixture of least squares linear regression, which gave $\beta = 0.2$, $\gamma = 1.1 \times 10^{-3}$, and $\delta = 0.05$.

In general, when comparing data to the model in figure 5.4, the model fits well to the initial mass transfer rate (i.e. the initial peak concentration), as well as the time at which the NAPL mass is

depleted (the sharp drop in concentrations). However, the model does not fit the mass tailing, as it predicts a much more rapid drop in concentrations. This is likely due to the model not properly considering back diffusion from water-saturated areas within the tank. This is particularly apparent in run 16, where considerable mass tailing was observed. Since this was the slowed flowing system, the NAPL was present considerably longer than in the other runs (~1.5 days) which would allow considerably more diffusion into the saturated zone at the bottom of the tank. The model did not attempt to capture this behavior, and neglecting this diffusion process may have lead to some of the discrepancy between the model and data. It is also worth noting that run 16 had a small amount NAPL mass escape the source trough and sink into the capillary fringe. This was not considered by the model, but may have affected the experiment.

The best-fit mass transfer correlation described above is presented in table 5.2, along with other mass transfer correlations that have been used to quantify volatilization in porous media in the literature. Several differences between the proposed and existing mass transfer correlations are noted: the range of Peclet values (0.003-0.15), and the corresponding vapor phase velocities tested in this system (3-145 m/day), are much smaller than those examined in previous studies. Given that equilibrium is expected in a system with no advection, it is logical to conclude that as the velocity decreases, the system approaches equilibrium. This behavior is evident in the much smaller Peclet number exponent in this study (0.05), which is likely at the boundary of applicability for the Gilliland-Sherwood type model, and approaching a local equilibrium condition. Under local equilibrium, volatilization effectively becomes instantaneous. As a result, the observed NAPL mass flux is a function of the transport of the NAPL vapor away from the NAPL source via diffusion, advection and dispersion. This contrasts with the occluded NAPL source where the mass flux was insensitive to the bulk diffusion and advection, and controlled instead by diffusion within the occlusion.

Table 5.2: Volatilization Mass Transfer Correlations

Reference	System type	Flow Regime	Pore velocity range (m/d)	VOC source configuration	Source zone water content	Gaseous diffusion / dispersion term	Correlation(s)	Peclet range
Wilkins et al. 1995	1-D column	Bulk gas flow	~ 50 – 1300	Homogeneous NAPL residual	Residual	Neglected	$Sh_0 = 10^{-2.79} Pe^{0.62} d_0^{1.82}$	$0.05 < Pe < 2$
Yoon et al. 2002	1-D column	Bulk gas flow	~ 50 – 1100	Homogeneous NAPL residual	Residual	Diffusion only	$Sh_0 = 10^{-2.77} Pe^{0.68} d_0^{1.68}$	$0.02 < Pe < 1.5$
van der Ham and Brouwer 1998	1-D column	Bulk gas flow	~ 8300 – 38000	Homogeneous NAPL residual	Residual	Neglected	$Sh_0 = 10^{-3.03} Pe^{0.88} d_0^{1.82}$	$5 < Pe < 60$
Anwar et al. 2003	1-D column	Bulk gas flow	~ 90 – 1700	Homogeneous NAPL residual	None	Diffusion only	$Sh_0 = 10^{-3.30} Pe^{1.15} \theta_n^{-0.30}$	$0.03 < Pe < 3.7$
Chao et al. 1998	1-D column	Air channels	Not reported	Homogeneous aqueous phase	Saturated	Neglected	$Sh_0 = 10^{-4.71} Pe^{0.84} d_0^{1.71} H^{-0.61}$	Not reported
Braida and Ong, 1998	2-D cell	Single air channel	~ 173 – 2160	Homogeneous aqueous phase	Saturated	Neglected	$Sh_0 = 10^{-7.14} Pe^{0.16} d_0^{1.66} H^{-0.83}$ $Dam = 10^{-4.81} Pe^{-0.79} H^{-0.83}$	$0.05 < Pe < 1.5$
This study	2-D cell	Bulk gas flow	3 – 145	Exposed NAPL pool	Residual	Both included	$Sh_0 = 10^{-2.82} Pe^{0.05}$	$0.003 < Pe < 0.15$

5.2 Capillary Fringe Volatilization Studies

In many vapor intrusion cases, shallow groundwater plumes serve as the primary source of vapors. Thus, the mass transfer of VOCs from groundwater to soil vapor is a process of considerable importance. Also, the assumptions made in commonly used screening type models with respect to vapor loading from the water table are questionable because they do not fully incorporate the capillary fringe. The capillary fringe acts as the interface between the vadose zone and groundwater, and plays a critical role in this process mass transfer. The transport processes within the capillary fringe that govern mass transfer across the fringe are complex because they entail simultaneous advective and diffusive transport of the volatile contaminant in both water and air phases. These processes are in turn affected by the physical properties of the porous media such as permeability, porosity, and especially the retention characteristics. In order to gain a better understanding of how vapor phase contaminants are loaded into the vadose from groundwater, it is important to explore the role of advection and diffusion within the capillary fringe region.

As an example, Figure 5.5 shows the calculated retention curves (van Genuchten, 1980 model), the saturation dependent air and water relative permeability (Mualem, 1976 model), and the saturation dependent effective diffusivity for trichloroethylene for the 20/30 Accusand expressed as a function of capillary head (Millington-Quirk 1961 model). Also included are hysteresis curves for the primary drainage, main wetting and secondary drainage cycles. Since relative permeability is the primary parameter that controls lateral advection in each phase, and diffusivity is the primary parameter that controls diffusion in each phase, it is important to note the strong gradients in the values of each parameter within the capillary fringe. For example, because diffusion coefficients in gases are much larger than in liquids, the effective diffusivity increases sharply with increasing gas saturation (or decreasing water saturation). Furthermore, effective diffusivity is quite sensitive to the hysteresis cycle as it changes with water phase content. With the primary drainage curve the effective diffusivity of TCE increases by nearly 4 orders of magnitude within a narrow region of capillarity (e.g. ~5 cm between 12-17 cm). However, for the main wetting and secondary drainage cycles, the entrapped air serves to increase the minimum diffusivity by only about 2 orders of magnitude by comparison to the primary drainage curve. The region of capillarity that affects the diffusivity is also wider especially for the main wetting cycle (e.g. ~10 cm between 3-13 cm). Likewise, relative permeability for each respective phase drops rapidly in the capillary fringe, and also depends on the drainage cycle.

These strong gradients in the transport parameters can have an important influence on the mass transfer regime at the capillary fringe. For example, in many groundwater systems, the natural movement of groundwater is often primarily horizontal, and advection is assumed the primary transport process. Meanwhile, in the vadose zone, water flow is usually vertical due to infiltration from the land surface, and gaseous diffusion is often the dominant transport process. Thus, in the capillary fringe, the advection transport of contaminants can be quite complex as it merges this vertically dominant transport domain into the horizontally dominant domain, all within a region where the relative permeability is changing rapidly. Likewise, the diffusive transport transitions from a groundwater region where diffusion is typically very small and often neglected to the vadose zone where diffusion is of great importance.

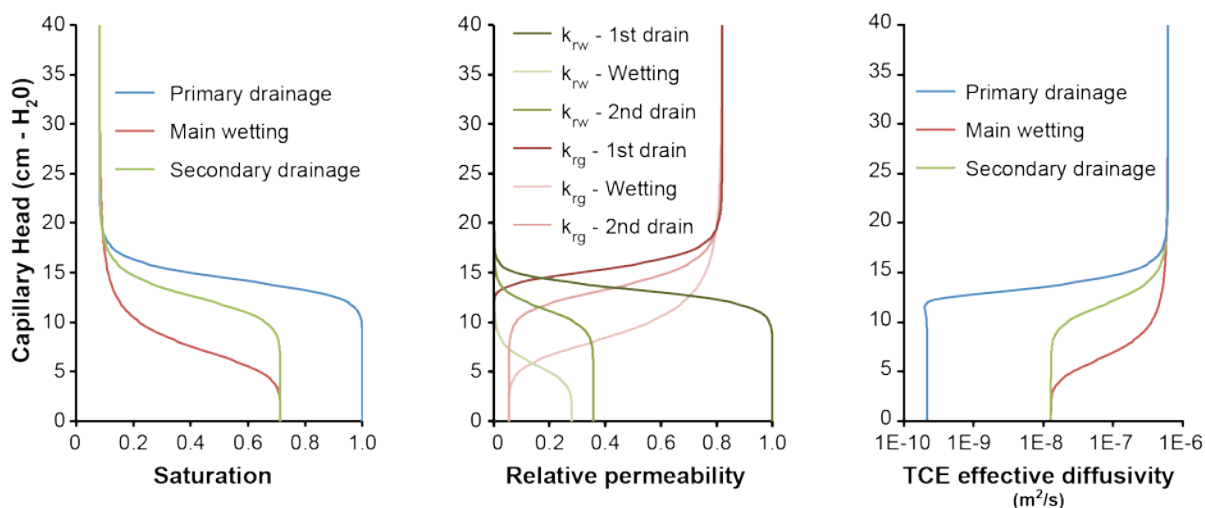


Figure 5.5: Estimated van Genuchten saturation, Mualem air and water relative permeability and Millington-Quirk effective diffusivity curves for the 20/30 Accusand used in the study. Included are curves for primary drainage cycle, main wetting cycle, and the secondary drainage cycle. Note logarithmic axis for diffusivity curves.

The experiments presented in this section were conducted to explore this capillary fringe mass transfer process and gain insight into what sort of assumptions are appropriate. A series of 4 experimental test cases were run, which are summarized in Table 5.3. These air phase linear velocities are within the same order of magnitudes as those measured in previous field studies (Eberling et al. 1998; Choi et al. 2001).

Table 5.3: Experimental Results Cases 1-4

Experimental Case	Air Phase Linear Pore Velocity [m d ⁻¹]	Initial TCE Aqueous Concentration [mg L ⁻¹]	Vapor phase equilibrium Concentration (calculated from Henry's Coefficient) [g m ⁻³]	Peak TCE Vapor Concentration [mg L ⁻¹] (% of equilibrium)
1	0.864	429	138	24 (17%)
2	21.6	389	124	3.7 (3%)
3	1.05	118	36	9 (25%)
4	26.3	410	120	14.5 (12%)

The observed effluent TCE vapor concentrations as a function of time are plotted for each of the experimental cases in Figure 5.6. Each test case shows a spike in vapor concentrations at the start of flow following the equilibration period. Each of the multiple spikes represents a cycle of re-saturation resulting from the raising and lowering of the water table and hence essentially represents a duplicate experiment for each case. The peak vapor phase concentration listed in table 5.3 represents the highest vapor concentrations observed in each test case and is expressed as the percent of equilibrium concentration with the TCE contaminant within the groundwater zone. By comparing the peak effluent concentrations in Figure 5.6 to the equilibrium concentrations given in Table 5.3, it is observed that the measured effluent concentration is only a fraction of the estimated maximum equilibrium vapor phase concentration. This is significant because it is typical in vapor intrusion investigations to assume equilibrium exists between contaminants within the shallow groundwater and the soil gas immediately above the capillary

fringe. The non-equilibrium condition that occurs between the dissolved groundwater plume and the vadose zone even in this small apparatus may suggest that the commonly employed assumption may overestimate mass transfer without factoring in processes in the capillary fringe. Another observation is that the degree of deviation from equilibrium conditions is larger when the flow velocity is high. This observation supports the argument that higher air flow reduces the residence time, thus mass transfer to be rate limited and the effluent concentrations further reducing due to dilution.

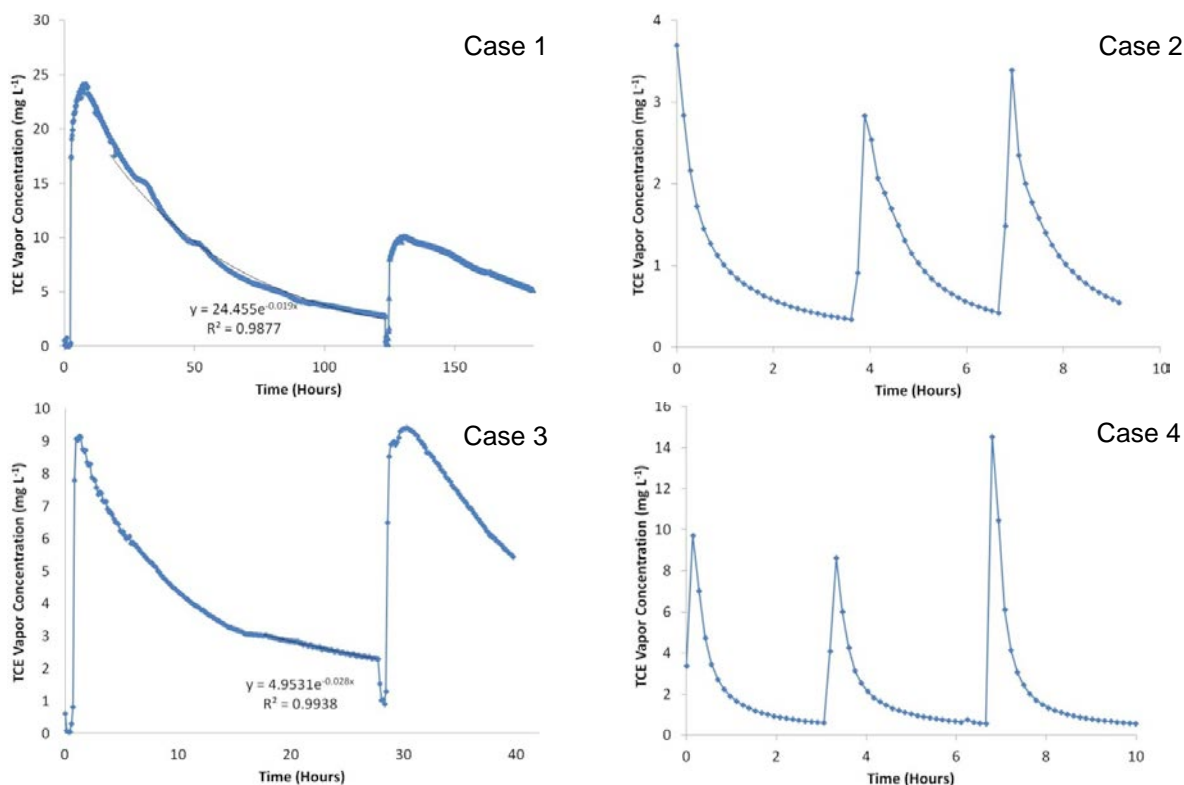


Figure 5.6: Effluent vapor concentration over time for all 4 cases. Spikes indicate separate experiments where the system is stopped, re-saturated, drained and resumed.

The concentrations of dissolved TCE in water in the vadose zone are substantially lower than that in the groundwater in the saturated zone, indicating that there should be a sharp concentration gradient across the capillary fringe. Aqueous phase samples were withdrawn from two vertical transects over time in the case 1 test in order to determine whether this concentration gradient could be observed. This data is presented in Figure 5.7. As can be seen, samples from both transects have nearly the same starting concentration, which is in keeping with the near uniform initial condition for each experiment. However, as the experiment proceeds, the concentration at the sample points located nearest the vadose zone (1W and 5W in the figures) drop off rapidly, indicating that mass transfer is rapidly depleting the TCE from this area. This also mirrors the vapor concentration trend in figure 5.6. However, as time progresses, the concentration gradient in the capillary fringe and saturated zone gradually declines, causing the diffusive flux to decline in time as well. The concentrations at the other sampling intervals show no clear trends, indicating that they are much slower to respond. It may be that in this experimental system these other sampling intervals are located too far below the capillary fringe to observe the propagation of the diffusion front at the timescale of these experiments. This may

be due to the relatively large spacing between aqueous sample points, which is approximately 2.5 cm, combined with the fact that aqueous diffusion is a very slow process. However, since the groundwater in this experiment is not flowing, over time the concentration gradient in the groundwater zone is expected to flatten out and disperse, and the mass-loading rate to the vadose zone would decay in an exponential fashion.

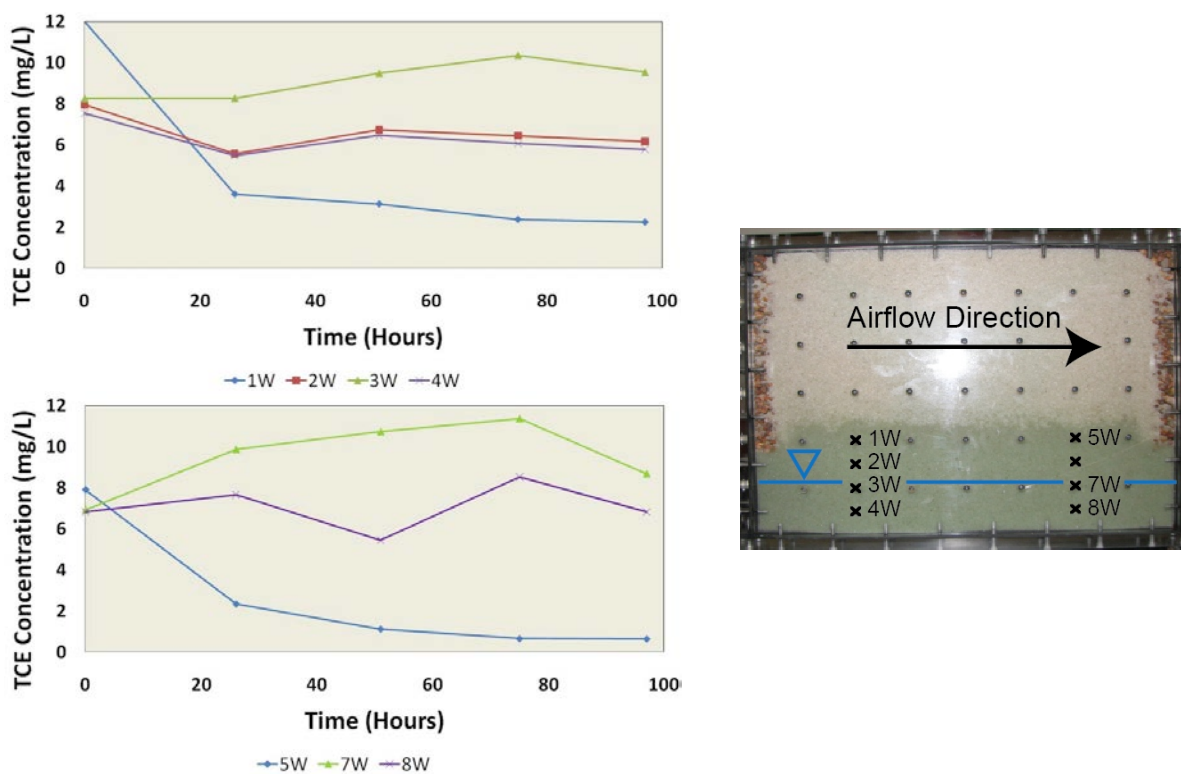


Figure 5.7: Aqueous TCE concentrations in the capillary fringe from experiment 3. Tank diagram at right shows locations of sample points. Water phase is dyed green for ease of viewing, while the vadose zone above the fringe appears as clean sand.

5.3 Dynamic air pathway experiments

The dynamic air pathway experiments tested the hypothesis that soil vapor pathways can be affected by changes in soil moisture resulting from infiltration and heat-induced evaporation from the soil surface. These experiments were conducted in a 1.2m x 2.4m 2-dimensional sand tank with multiple sand layers with varying soil water retention properties (see figure 4.7 for tank packing). The tank is operated in what is in essence a reverse vapor intrusion setting, where airflow is forced into soil from a point in the subsurface, and the air flows outward toward the land atmospheric boundary. This created an easier layout to test how vapor movement responded to changes in saturation. A series of soil moisture sensors, air pressure sensors and air flow meters measure the physical movement of the air and water phases in response to infiltration and heating applied at the sand surface. Numerical modeling was used to determine whether the observed soil moisture distribution could be captured using the physical theory.

The goal of these experiments was not to duplicate field case scenarios. Rather, the experimental design was developed that allowed rapid testing of numerous infiltration cases to validate the

numerical model. The sandy media used in the tank is much more permeable than a typical field soil, and airflow rates, infiltration rates, and heat application rates are much higher than typical field values. This notwithstanding, the conclusions drawn from this research are still informative as they indicate what may occur at the field scale, though the overall magnitudes and timeframes of observed effects may differ with the lower flow rates and permeabilities encountered in the field.

5.3.1 Infiltration experimental results

The first series of experiments tested the effect of infiltration at the soil surface on the vapor pathways. Rain was applied for a 3 hour time period, and Figure 5.8 shows the observed surface flow fractions in sand layers 1 through 4. Also shown is the proportion of the injected airflow that exits the tank via the soil surface (the remaining air exits the tank through the subsurface layers). The saturation value in each layer was averaged over six measuring sections (columns A-F in Figure 4.7). Although some degree of instability (fingering) in the infiltrating water was observed initially, the soil water saturation data indicated that the wetting front was fairly uniform with only 3% variation in layers 1 and 2, and up to 7-9% in layers 3 and 4. As soon as the rainfall started at $t = 0$, the water infiltrated and no ponding on the soil surface was observed. The wetting front advanced downward through layers 1 through 3. As seen in the soil moisture data in figure 5.8, by the end of the 3 hour rainfall period, the saturation profile nears a steady-state condition. The high permeability of the system allows the propagation of the wetting front and stabilization of the flow regime in this relatively short time period. The soil water saturation in layers 1 and 2 increased from an initial saturation of ~ 0.08 to $0.22 - 0.25$. The highest saturation of $0.26 - 0.31$ was observed in layer 3, which consisted of fine sand that retains more water. Due to the low relative water permeability in transitioning from finer layer 3 to coarser layer 4 water accumulated in layer 3 before penetrating into layer 4, which is consistent with observations by Walser et al., (1999). Layer 4 generally showed the lowest saturation of $0.20 - 0.23$. However, these values were measured at the mid-depth in each layer and do not necessarily represent the average soil water saturation. Thus, water saturation immediately above the interface between layers 3 and 4 was probably higher than the measured values that led to an *internal capping* due to water accumulation along the interface. The air pressure data (not shown) showed that there was a pressure difference as high as 0.87 kPa in layer 4 and 0.03 kPa or less in layers 1-3 between the upstream and down stream during the rainfall event.

Figure 5.9 plots transient changes in the air inflow and outflow normalized to the total flow of air into the tank. At $t = 0$, the total outflow rate measured at the downstream boundary was only 20% of the inflow. This suggests that 80% of the air injected in layer 4 was flowing out through the soil surface (also shown in Figure 5.9) and the initial saturation in layers 1 - 3 had only a minor effect on the air flow. However, as the wetting front migrated downward, outflow rates from the subsurface soil layers 1 through 4 increased. At about $t = 0.33$ hours, a sudden increase in airflow through layer 4 was observed. This is slightly before the water saturation in layer 4 increased (Figure 5.9). Therefore, $t = 0.33$ hours corresponds to when the water started to form an internal cap at the interface between layers 3 and 4. Following this time, a significant fraction ($\sim 60\%$) of the airflow was confined within layer 4.

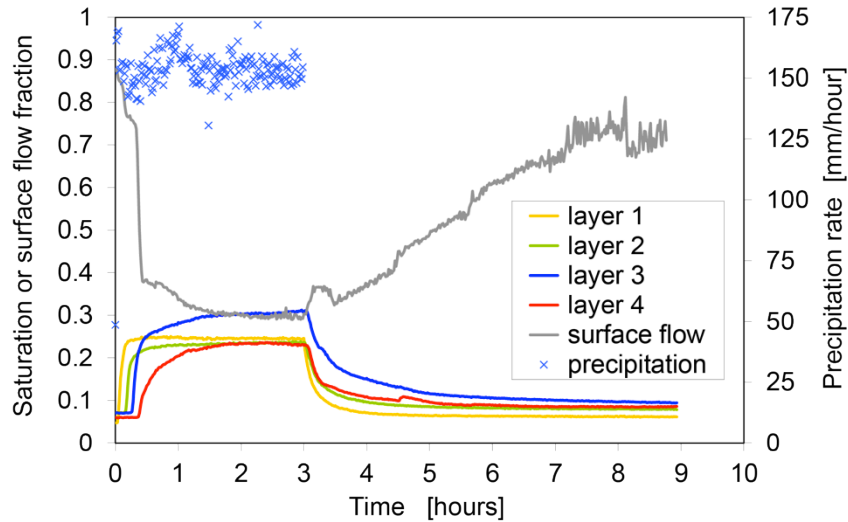


Figure 5.8. Soil water saturation by layer and total surface flow fraction (Rainfall experiment). The surface flow fraction was obtained based on the difference between the inflow and the total outflow from the four layers. Precipitation was applied for the first 3 hours.

Airflow rates in layer 1 remained very low throughout the experiment. Those in layers 2 and 3 increased slightly after the precipitation started due to confinement of flow at the moderate saturations observed in layer 1. However, the increase in layers 2 and 3 were not as distinct as that in layer 4. In total, about 70% of the injected air flowed within the soil layers without leaving through the soil surface (i.e., layers 1-4) during the precipitation event, which corresponds to a nearly 3-fold increase in subsurface vapor transport.

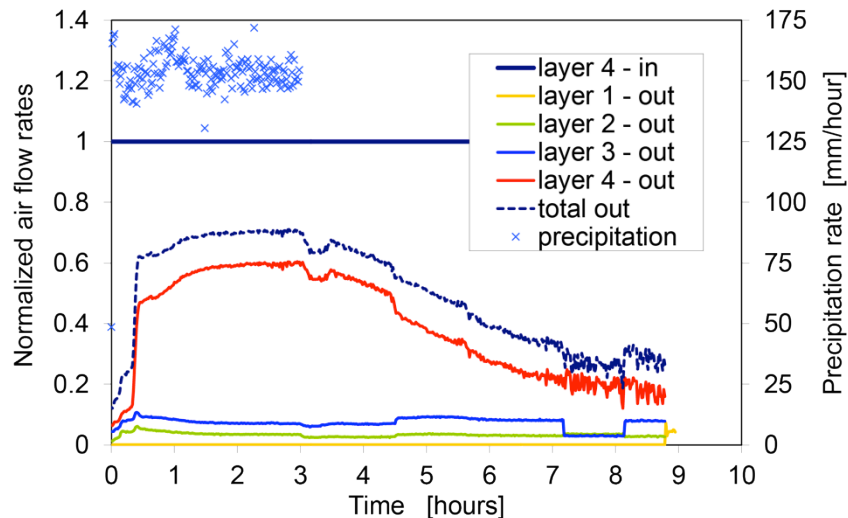


Figure 5.9. Total air inflow, individual layer air outflow rates and precipitation rate (Rainfall experiment). “Total out” is the sum of the outflow rates from layers 1 through 4. Air leaving through the surface is the area above the total out, air confined within subsurface is below the total out.

After precipitation ceased, saturation decreased as water drained toward the water table. Airflow in layer 4 gradually decreased as the effect of capping at the interface between layers 3 and 4 diminished and drainage proceeded. *This rainfall experiment demonstrated that airflow pathways may be significantly affected by preferential flow channels (layers) and precipitation due to the internal capping effect caused by heterogeneity-induced soil moisture distributions.*

5.3.2 Heat experiment results

In the heat experiments, heat was applied at the soil surface via a radiant heating element after a 3 hour precipitation event to simulate the effect of heat flux at the soil surface. Initial experimental results showed little effect because the drainage of layer 1 is rapid and the drying of this layer did not significantly effect the saturation or permeability of the sand pack. However, in later heat experiments placed a very fine sand layer at the soil surface to simulate fine topsoil that would retain significant water. The data obtained from this experiment is depicted in figure 5.10 The general behavior in soil moisture was similar to that of the rainfall experiment except that the surface fine layer became highly wet (saturation as high as ~0.9) at the start of the rainfall event ($t = 0$). No ponding was observed. As before, layer 4 generally showed the lowest saturation (~0.20) due to the internal capping at the interface between layers 3 and 4.

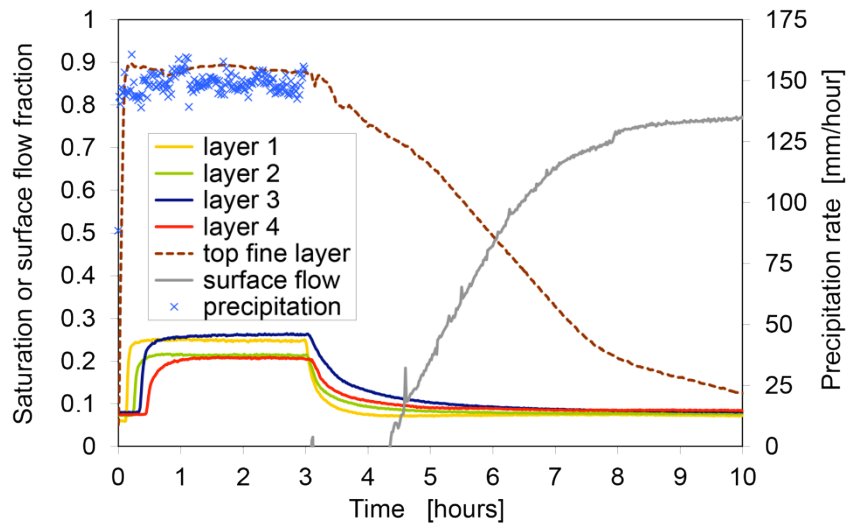


Figure 5.10. Soil water saturation and surface flow fraction (Heat experiment). The surface flow fraction was obtained based on the difference between the inflow and the total outflow from the four layers. Precipitation was applied for $0 < t < 3$ hours, heat was applied for $3 < t < 10$ hours.

Corresponding inflow and outflow rates normalized to the inflow rate for this heat experiment are depicted in 5.11. As described previously, rainfall occurs for the first 3 hours and was followed by the application of heat for the following 7 hours. Within several minutes after the start of the precipitation event, almost 100% of the injected air was confined in the soil, i.e., no significant flow through the soil surface was observed. Also noteworthy is the total air out flow rate that is higher than the inflow rate for the first ~45 minutes. It is most likely that the air phase initially filling the pore prior to the rainfall was forced to flow out through the outflow boundary. This effect was caused by the high saturation of the surface fine layer, which did not allow air flow through the surface, serving essentially as a cap, or barrier to air migration. Due

to this strong surface capping effect, the air initially filling the pore space was pushed downward by the wetting front and was, together with the injected air, forced to flow through layers 1 through 3 in addition to layer 4. No surface flow was observed until roughly $t = 4.3$ hours, that is 1.3 hours after precipitation had ceased and surface heat had been activated. The initiation of heat at the surface induced evaporation at the cap layer and air migration through this layer was observed when the layer saturation reached ~ 0.70 . Although not shown, the air pressure data indicated that there was a pressure difference as high as 0.57 kPa in layer 4 and about 0.27 kPa in layers 1-3 between the upstream and downstream during the rainfall event, confirming significant air migration.

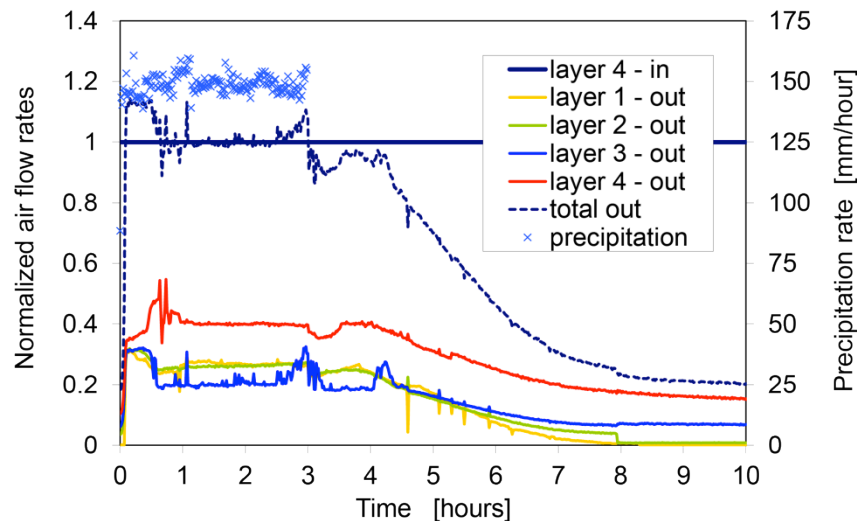


Figure 5.11. Air inflow and outflow rates and precipitation rate (Heat experiment). Precipitation was stopped and heat was turned on at $t = 3$ hours. “Total out” is the sum of the outflow rates from layers 1 through 4. Air leaving through the surface is the area above the total out, air confined within subsurface is below the total out.

In the absence of heat, it is expected that the surface fine layer would have remained saturated for a significantly longer period of time, resulting in a prolonged period of subsurface vapor migration. Heat in the absence of precipitation, however, had a negligible effect on subsurface airflow. *Therefore, this heat experiment suggests that the effect of diurnal heat fluxes on the airflow pathway dynamics will be significant only when the surface layer retains water due to its capillarity and evaporation is the dominant process that contributes to the reduction of water saturation in this surface.*

5.3.3 Comparison to numerical results

In this section, numerical simulation results are compared with the experimental results. Figures 5.12 and 5.13 show the simulated and measured vertical water saturation profiles obtained from the soil-moisture sensors in vertical array C of the sand tank and the saturation distribution and corresponding airflow field for the entire tank, respectively. The numerical results in Figure 5.12 seemed to capture the general trend in saturation along the vertical length of the tank both immediately following the precipitation event and 6 hours after the precipitation event ended (i.e., $t = 9$ hours). However, the lack of measurements at the interface prevented the testing of the capillary trapping of water between layers 1 and 2 and layers 3 and 4 simulated in the model.

The saturation distribution and velocity vectors of airflow in Figure 5.13 clearly show the capillary trapping at the interfaces. At $t = 3$ hours, the simulation shows this trapping is preventing the significant migration of air to the upper layers (layers 1 – 3) resulting in nearly parallel migration along layer 4. At $t = 9$ hours, however, the saturation has diminished and breakthrough of air from layer 4 to layers 1 through 3 is occurring, resulting in more flow through the upper layers and the surface boundary. These results agree qualitatively with the point-measured data obtained in the experiment depicted in Figures 5.8 and 5.9.

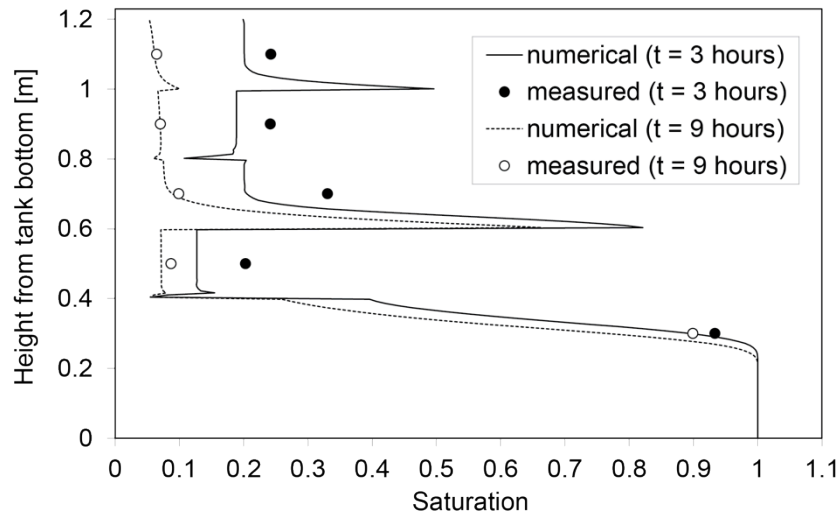


Figure 5.12. Vertical water saturation profile along sensor array C at $t = 3$ hours (when the rainfall stopped) and at $t = 9$ hours. Note that the larger the contrast at the fine-to-coarse interface, the higher the water saturation above the interface that leads to more significant capping effect.

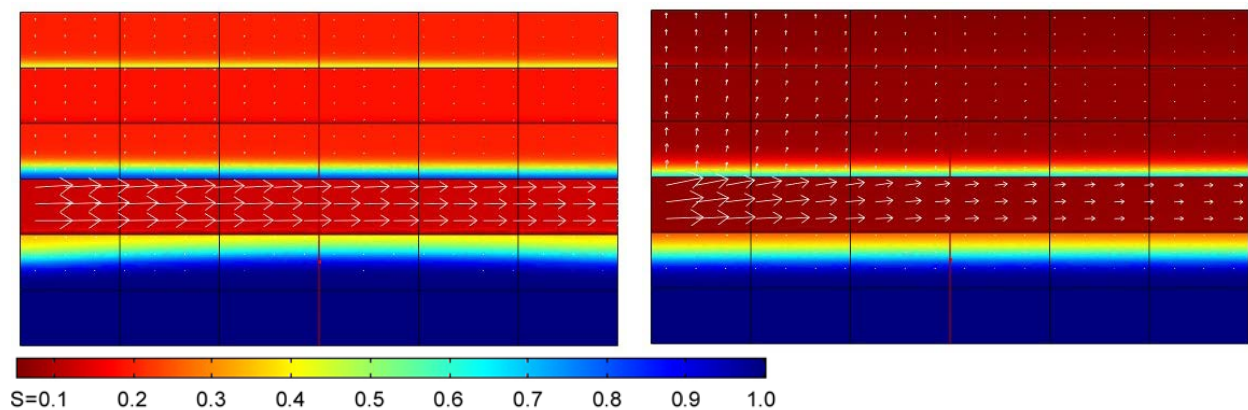


Figure 5.13. Soil water saturation distribution and air flow field (left) $t = 3$ hours, (right) $t = 9$ hours. Note that most of the injected air flows through layer 4 at $t = 3$ hours due to high saturation at the capping interface (i.e., large area of influence), whereas a significant portion passes through the capping interface at $t = 9$ hours and the flow in layer 4 diminishes over distance (i.e., small area of influence).

Figure 5.14 compares the numerical and experimental results for the transient soil water saturation at the midpoint of layers 1 through 4 in column C. These results generally agree with

those observed in the experiment where the highest saturation occurred in layer 3 and the lowest occurred in layer 4. The model however was not able to predict the magnitude of the saturation perfectly. This discrepancy partly results from the flat P_c - S relationships of the uniform test sands used in the model, for which a small change in P_c causes a large change in S . Nonetheless, the model does provide insight and a useful tool that is able to predict the general trends in subsurface airflow behavior affected by heterogeneity and soil moisture dynamics. More fine adjustments of the parameters in the constitutive relationships would probably lead to a better match of the numerical results with the experimental data, however, model calibration was not the goal of this study. The goal to test the ability of numerical models to capture the processes in the conceptual model developed from the observations in the experiments was achieved.

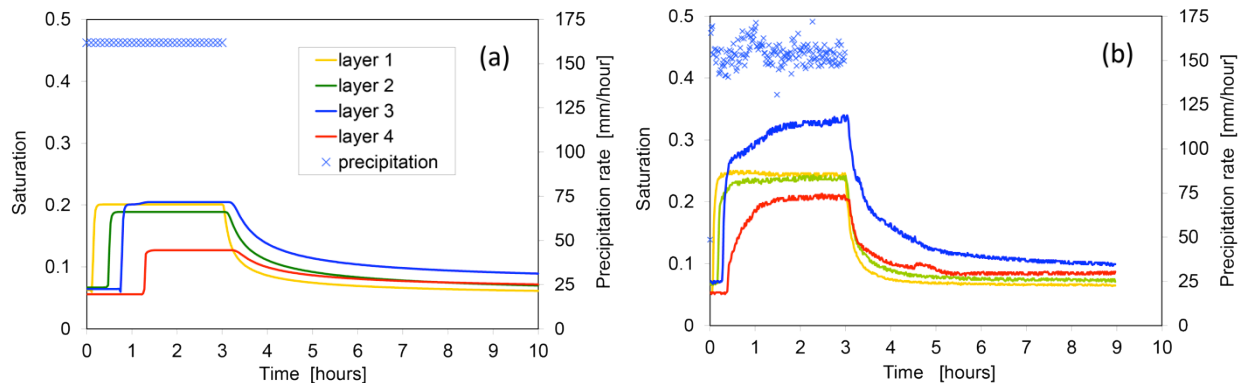


Figure 5.14. Transient change in soil water saturation in layers 1-4 in column C; (a) simulated results, (b) experimental data.

In Figure 5.15, transient changes in air inflow and outflow rates normalized to the inflow rate for both rainfall and heat experiments are plotted. Despite some minor differences, the numerical model captured most of the key features such as confinement of airflow within the subsurface due to internal and/or surface capping observed in the experiments presented in Figures 5.9 and 5.11. The simulation for the rainfall experiment showed that airflow is dominant in layer 4 (most permeable layer) before the rainfall event. As precipitation infiltrates into the soil, air migration through layer 4 increases. The model tends to have a delayed effect with the onset of significant flow through layer 4 not occurring until approximately 1 hour of infiltration, while significant flow through layer 4 due to capping occurred in the experiment at approximately $t = 0.3$ hours. This delay is largely associated with the difference in observed and simulated water infiltration rates as in Figure 5.14. Minor discrepancies could lead to significant effects at the interface leading to the relatively mild difference between the model and the experimental results. Nevertheless, this experiment/simulation illustrates: 1) the air flow pathways are largely controlled by heterogeneity, 2) the air flow rate in the preferential pathway is strongly enhanced by the spatial/temporal soil moisture distribution (i.e., the internal capping), and 3) air flow through the soil surface is significantly reduced during rainfall, which may increase the zone of influence from which air is drawn to underground structures in the case of the VI.

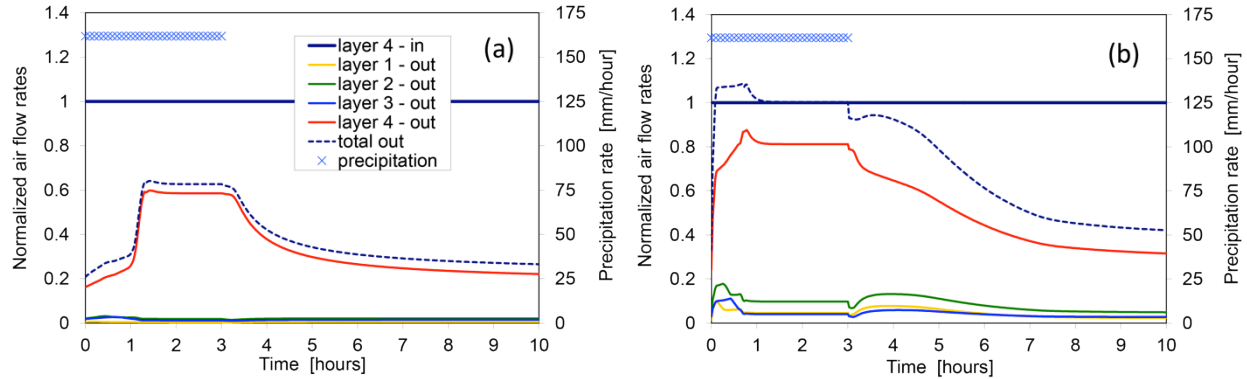


Figure 5.15. Transient change in airflow rates (a) Rainfall experiment (b) Heat experiment. These are comparable to Figures 5.9 and 5.11, respectively. Air leaving through the surface is the area above the total out, air confined within subsurface is below the total out.

The simulation for the heat experiment indicated that the numerical model was able to reproduce the key features observed in the heat experiment. The simulation also reproduced the air outflow rate higher than the inflow rate for the first ~45 minutes due to pore air pushed out by the wetting front as noted earlier. This specific case showed that the airflow is significantly confined to the subsurface without any connection to the atmosphere when the soil surface remains highly wet (e.g., a fine material is present at the soil surface that serves as a capping layer). Similar to the rainfall experiment/simulation, the airflow pathway was largely controlled by the heterogeneity for which the air permeability of the layers was spatially and temporarily affected by soil moisture.

5.3.4 Case studies with different degree of heterogeneity

In the foregoing sections, it was shown experimentally and numerically that soil moisture conditions affect the airflow pathway in the subsurface. The soil moisture was controlled both by the climate conditions at the soil surface as well as the subsurface heterogeneity. In this section, using the numerical tool that was shown to reproduce key features in the observed behavior, we investigated the effect of “degree” of heterogeneity on the soil moisture distribution and airflow pathways. Unlike the experiments where the air was “injected” into the soil, we considered and simulated a situation where air intrudes into the basement of a residential or commercial building as illustrated in Figure 5.16. In particular, we focused on how the fraction of subsurface-origin air (that could be contaminated) is affected under spatio-temporal soil moisture distributions with different degrees of heterogeneity.

In this study, the degree of heterogeneity was varied as follows. We considered the same layered structure that was used in the rainfall experiment but the “contrast” in the material properties was varied. Starting with the contrast used in the experiments that showed a distinct airflow pathway evolution as a function of soil moisture distribution, the contrast in the permeability k and VG model α parameter was reduced. For example, $k_{i,\text{scaled}} = k_{40/50} + (k_{i,\text{orig}} - k_{40/50}) \times F$, where $k_{i,\text{scaled}}$ is the scaled permeability of i th sand, $k_{i,\text{orig}}$ is the original permeability of i th sand, and F is the scaling factor. For the base case where the soil had the same degree of heterogeneity as the experiments, $F = 1$. Then, F was reduced to 0.5, 0.25 and 0.0, where $F = 0.0$ yielded a homogeneous #40/50 sand. The α parameters were varied in a similar manner. The sequence of the soils, the effect of which was examined by *Bozkurt et al.* [2009], remained unchanged, i.e.,

layer 4 is the coarsest in all cases. It has to be emphasized that it was assumed here that the method of varying the contrast in material properties would be sufficient to yield insight on the effect of “degree of heterogeneity (while the same geologic structure was kept)” on how air flow pathways are dynamically affected by soil moisture distribution controlled by the heterogeneity. The boundary conditions adopted were the same as those described in the previous section except that the air flow direction was reversed, i.e., a constant air flow rate of $3,000 \text{ cm}^3/\text{min}$ for $0 < t < 10$ hours, a rainfall intensity of $150 \text{ mm}/\text{hour}$ was applied at the soil surface for $0 < t < 3$ hours.

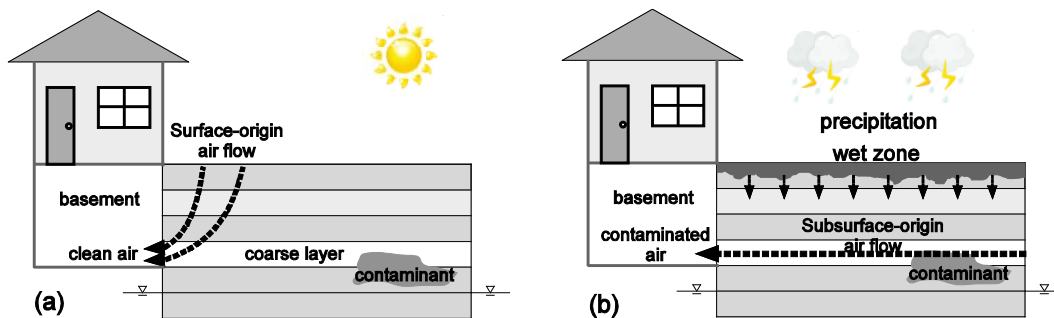


Figure 5.16. Schematic images of air flow pathway dynamics under different climatic conditions at the soil surface; (a) surface-origin air flow with small area of influence under no rainfall conditions, (b) subsurface-origin air flow with larger area of influence under rainfall conditions.

Figure 5.17 shows the transient change in the fraction of subsurface-origin airflow under different degrees of heterogeneity. In Case 1, where the degree of heterogeneity was the same as that in the experiments, roughly 70% of the air was of subsurface-origin (Figure 5.17a) during the rainfall event. As soon as the rainfall ceased, the fraction decreased down to about 20% at $t = 10$ hours, i.e., 80% is surface-origin as observed in Figure 5.17a. This suggests that airflow pathways change from that shown in Figure 5.16a before the rainfall, to Figure 5.16b during rain, and goes back to that in Figure 5.16a after rainfall. Cases 2 through 4 show that as the degree of heterogeneity decreases, the surface-origin air flow becomes more dominant (Figures 5.17b-d), i.e., air flow pathways do not change much. If less permeable, realistic soils were used in this layered system, it is likely that the finest layer would retain higher water saturation (even under more realistic rainfall rates), which could cause capping of the injected air under the finest layer as was observed in the heat experiment. In the more realistic/random heterogeneity configurations, on the other hand, it is expected that soil moisture would be distributed in three dimensions and multiple air pathways could be developed. The spatial “connectivity” of the airflow pathways would also vary over time and the air flow pathway dynamics can be more complex.

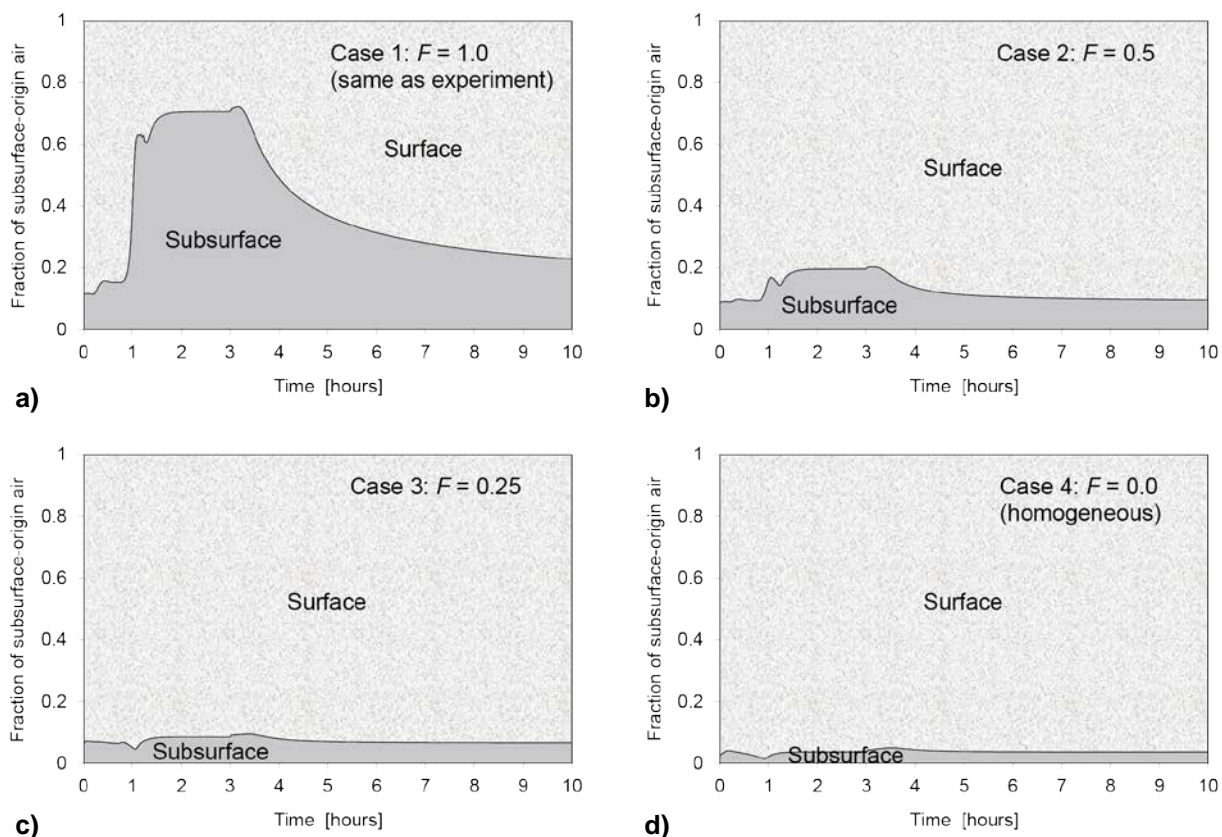


Figure 5.17. Fraction of subsurface- and surface-origin air flows under varied degree of heterogeneity (soil property contrast). Rainfall was applied for $0 < t < 3$ hours. For example, the following hydraulic conductivity values were used in each case; a) Case 1: as shown in experiment b) Case 2: $k_1=0.214$, $k_2=0.141$, $k_3=0.079$, $k_4=0.052$ cm/s, c) Case 3: $k_1=0.133$, $k_2=0.097$, $k_3=0.066$, $k_4=0.052$ cm/s, d) Case 4: $k_1=k_2=k_3=k_4=0.052$ cm/s. Note that as the subsurface-origin flow increases, it expands the area of influence around the building, resulting in potential activation of vapor sources further away from the building.

5.3.5 Discussion

Both the experimental and numerical results clearly showed that airflow preferential pathways could be affected by soil moisture distributions that varied in space and time due to heterogeneity and precipitation. In the rainfall experiment and simulation where there was no surface fine layer, the majority of the injected air flowed out through the soil surface prior to precipitation. Following the start of precipitation, however, precipitation generated internal capping at interfaces between different layers. As the result, a significant portion of the total airflow was confined in the soil with most of this airflow occurring in layer 4, the coarsest layer that showed the lowest water saturation during the experimental duration. These findings are analogous to a situation where a pressure drop in a basement structure results in vapor intrusion. When no precipitation is occurring and the surface boundary layer is relatively dry, significant exchange can occur between the atmosphere and the soil gas in the vicinity of the building. However, when precipitation events occur, the infiltration of water at the soil surface temporarily reduces this exchange by reducing the relative permeability of the surface layer. This may have implications for the vapor intrusion pathway because in most VI scenarios, the subsurface contaminant

concentrations are much higher than in the ambient atmosphere and the temporary “capping” effect of the precipitation may increase vapor intrusion into buildings.

The heat experiment and model simulations explored the role that heat induced evaporation at the surface may play in VI. The results suggested that the existence of a finer, poorly drained soils at the surface could remain wet and induce surface capping. The effect of this capping will, however, diminish as the surface dries due to soil water evaporation. The heat flux at the soil surface enhanced this evaporation, but the effect of heat is expected to be significant only at shallow depths. The fine sand layer on the surface used in this experiment led to a strong surface capping effect due to its high water saturation during precipitation. Because of this dominant capping effect, the infiltration mobilized the pore air downward. Therefore, immediately after precipitation started, not only the newly injected air but also the existing pore air was forced to flow through the subsurface and exit. This is analogous to a situation where all airflow into the basement of a building is of subsurface-origin and air can potentially travel over a larger distance when the soil surface is wet. Furthermore, the case studies with different soil property contrast also showed that the preferential air pathways induced by a building pressure drop could potentially expand the area of influence and result in potential activation of vapor sources further away from the building.

In making conclusions derived from the results and findings of a study where experiments are conducted in simplified laboratory test systems that do not capture all the complexities of field systems, some caution has to be exercised. Conclusions that could be generalized for all possible field settings and scenarios cannot be derived from a limited study such as the one that is presented. In more realistic field settings where the soil heterogeneity is not as simple as the two-dimensional layered case considered in this study, variation in the airflow pathway (three-dimensional spatial routings as well as travel distance) can be more complex. However, the findings still improve our fundamental understanding of the processes that will help to develop conceptual models and to obtain insights that are useful in practical problem solutions. Concluding statements drawn from these findings are summarized:

In heterogeneous subsurface systems with layers having contrasting soil properties (e.g. stratified alluvial formations), soil moisture variations created by precipitation could have significant effects on the generation of dynamic airflow pathways, which could lead to increased transport of contaminant vapor to subsurface structures. In systems with more complex heterogeneity, interconnected pathways may also lead to the surface, highlighting the need to understand the interconnected nature of subsurface airflow pathways. Given the importance of the capping effects observed in this study, the distribution and continuity of the capping formation would be a critical factor that controls the changes in airflow pathways.

Thermal boundary conditions at the land/atmospheric interface have a negligible effect on the soil moisture deep in the formation, and hence have little impact on the creation of airflow pathways. However, in a very specific situation where a finer soil layer exists on the land surface, the fine layer will retain water during a rainfall event. The airflow pathways across the fine layer that brings fresh atmospheric air to the building gets blocked (capping). This results in more air with subsurface-origin that can potentially be contaminated intruding into the building. During dry periods, heat flux at the soil surface dries this layer removing the barrier to fresh air.

Although the specific scenario of effects of paving the land surface or surface vegetation on air pathway generation was not tested, the capping effect of the wet fine layer implies that when the air flow pathway from the atmosphere is blocked, the influence zone of the pressure fluctuation in the building may be extended to locations much farther away from the building. Such change may persist temporarily or permanently depending on the nature of the blockage. If contamination sources are present in this zone, it provides potential for VI into the building. The findings of this study also suggest an explanation for some of the uncertainty that results when homes are sampled at different times and record vastly different vapor concentrations.

The conclusions presented above were obtained under the specific laboratory conditions used in this study. For example, for more realistic soil (i.e., less permeable, three dimensionally distributed) and climate conditions (i.e., lower rainfall intensity, diurnal heating cycle), it is important to examine to what extent these findings are valid. If more realistic soils were used in these layered experiments, we anticipate that similar changes in the air pathways (although air flow rates would be lower) would have been observed under more realistic (i.e., lower) rainfall intensity because more realistic soils tend to retain more water leading to a slower infiltration and sufficient capping effects at the soil surface or interfaces.

Intermittent airflow activation is also possible under real field conditions, e.g., due to intermittent usage of indoor air conditioning. The intermittent air flow activation as well as cyclic heating due to the diurnal cycle would reduce changes in the airflow pathways. These factors are left for future investigations.

5.4 Integrated dynamic flow and vapor transport experimental results

The objective of the up-scaled large test system experiments was to combine elements of the previous tests in a simulated vapor intrusion system to better evaluate the observations resulting from the rainfall events and water table fluctuations made previously. The experiments generated very large data sets, including continuous time series data of the vapor phase TCE concentrations, the airflow rates, the soil moisture data from 30 sensors and air pressure from 30 pressure transducers. This large data set was used for various tasks that includes improving conceptual models, identify and quantify critical processes that contribute to VI that cannot be accomplished in field setting, design of numerical models and testing. The following discussion of results presents an overview of the data, and focuses discussion on key observations.

5.4.1 Homogenous tank experiment

The effluent air phase TCE concentrations for the entire 106 day period of the experiment are presented in figure 5.18. Experimental event in this case is defined as a scenario of water table fluctuation and rainfall application. For the purposes of testing our conceptual model, the concentrations in this effluent serve as a surrogate for the vapor signal that might be observed entering into a building (e.g. subslab soil gas) under the influence of VI. Over the course of the experiment, concentrations at the effluent line varied from a high of $0.0978 \text{ g}\cdot\text{m}^{-3}$ on day 57 to a low of $0.0009 \text{ g}\cdot\text{m}^{-3}$ on day 82, indicating concentrations ranged overall by a factor of 109 (two orders of magnitude).

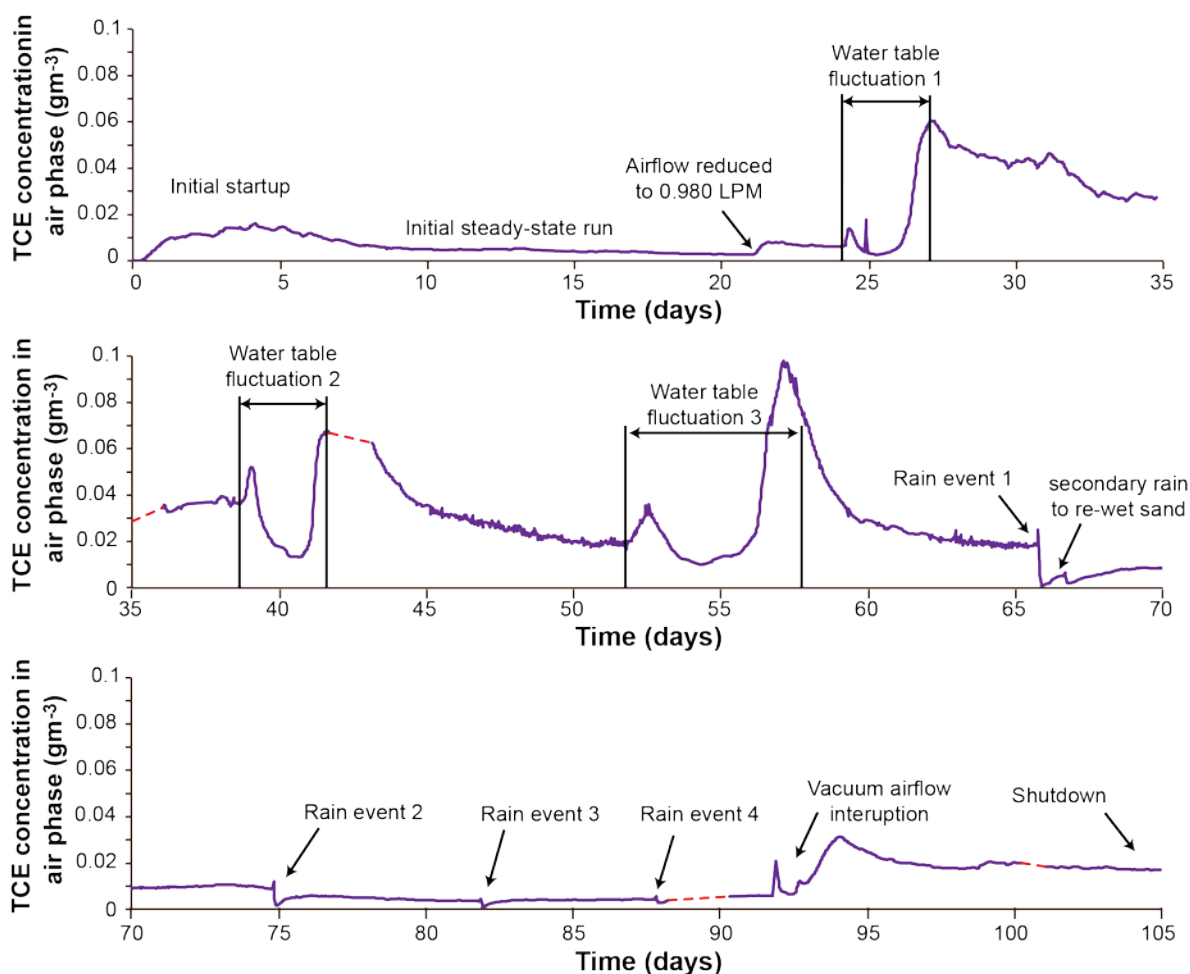


Figure 5.18: Effluent vapor concentrations over the entire 106 day homogeneous experiment. Experimental events are noted. Red dashed lines indicate gaps in the data.

During the initial startup, the concentrations rose rapidly as TCE contaminated water was introduced to the tank from the groundwater plume when the water table rose, and declined as the system stabilized and reached its first steady state condition. When the vacuum airflow was reduced on day 21, an immediate baseline shift was noted. At day 24, the first water table fluctuation was implemented, registering a short-term peak in TCE concentration during the water table rise, followed by a dip during the elevated steady water table, and then a rapid sustained rise in concentrations during the falling water table. An anomalous spike also occurred during WT1 that was corroborated by observed pressure data, but not by the flow meters or soil moisture sensors, leading to speculation that this was a pressure spike in the vacuum line. After this first water table fluctuation (WT1), the concentrations declined slowly but the baseline remained elevated through the next two water table fluctuations. Water table fluctuations 2 (WT2) and 3 (WT3) showed similar behavior as WT1, though with different initial baseline starting concentrations, and the WT3 event was longer due to the slower timescale of the fluctuation. The first rain event (R1) followed and observed an immediate rapid spike (statistically significant) in concentrations, followed immediately afterward by a rapid drop in

concentrations, and a slow rebound to baseline. A second drop during R1 was due to a secondary rain application that was intended to re-wet the sand pack. The baseline does not recover fully to the value preceding R1, indicating some baseline hysteresis between rain events and water table fluctuation events. Rain events 2, 3, and 4 (R2, R3 and R4) showed similar behavior, though with R4 the effects are muted partly due to the application of rain in only chambers 1 and 2 instead of across the whole tank. From days 92 to 95, a vacuum flow interruption caused erratic tank behavior, and at day 106, the experiment was terminated.

To focus the presentation of results and gain insight into the physical observations made from the homogeneous experiment, two steady state cases, as well as one water table event (WT3) and one rain event (R2), a sub-set of the time series is presented in detail. The two steady state cases relate to the high flow period during the first 21 days of the experiment and the medium flow period of days 21-66. Although all three water table fluctuations showed similar but unique behavior, WT3 was selected as it had the clearest data set for interpretation: WT2 was missing data immediately after the water table fluctuation due to a gas chromatograph shutdown, and WT1 appears to be influenced by hysteresis in the baseline concentration resulting from the water table fluctuation. R2 was selected for analysis, since R1 was qualitative due to the secondary rain application, and R3 and R4 behaved very similarly.

5.4.1.1 Steady-state cases: Steady-state conditions are of interest because investigations of transient phenomena need a known initial condition in order to understand and model the behavior that is observed. Steady-state conditions also provide a basis of comparison since many models treat VI as a steady-state process (e.g. Johnson and Ettinger, 1991; Abreu and Johnson 2005; Bozkurt et al., 2009). Because the homogeneous tank was subjected to two different flow rates for much of the experiment, pseudo steady-state conditions for both flow periods may be evaluated. The “high flow steady-state case” presents averaged data from day 20, which represents a pseudo steady-state condition during the high flow period (vacuum flow rate = 3.82 SLPM), and the “medium flow pseudo steady-state case” presents averaged data from day 65, which represents a pseudo steady-state condition between the end water table fluctuation events and the beginning of the rain events (vacuum flow rate = 0.980 SLPM).

At the end of the high flow period (day 20), the TCE concentration in the vacuum outflow stabilized between $0.00281 \text{ g}\cdot\text{m}^{-3}$, and $0.0186 \text{ g}\cdot\text{m}^{-3}$ for the day 65 medium flow steady-state period. Evaluation of the soil moisture data during the steady state conditions revealed generally not very useful results, as all moisture probes were placed above the capillary fringe and indicated only a constant residual saturation. However, the air pressure data were more interesting and provided useful insights. A contour plot of average pressure values at steady-state is shown in figure 5.19 and a table of the average atmospheric chamber flows is given in table 5.4. As expected, the magnitudes of the differential pressure were larger in the high flow case. In both high and medium flow cases, a strong pressure gradient was noted on the right side of the tank where airflow was created through vacuum, and the pressure gradients extend asymmetrically away from this point. The steepest pressure gradient extends directly to the atmospheric boundary at the land surface, indicating the bulk of the soil gas flow was occurring here, and was corroborated by the average airflows reported in table 5.4; Chamber 1, closest to the vacuum line showed the highest overall airflow, and the flows declined as the chambers got further away from the vacuum source. One clear difference between the steady state cases is that for the high flow experiment, a considerable lateral pressure gradient existed across the tank,

while this was more subdued in the medium flow case. This was also corroborated by the wider distribution of flow across the tank at high flow, as the proportion of airflow in chamber 3 is higher during the high flow period than the low flow period, indicating more lateral flow was occurring.

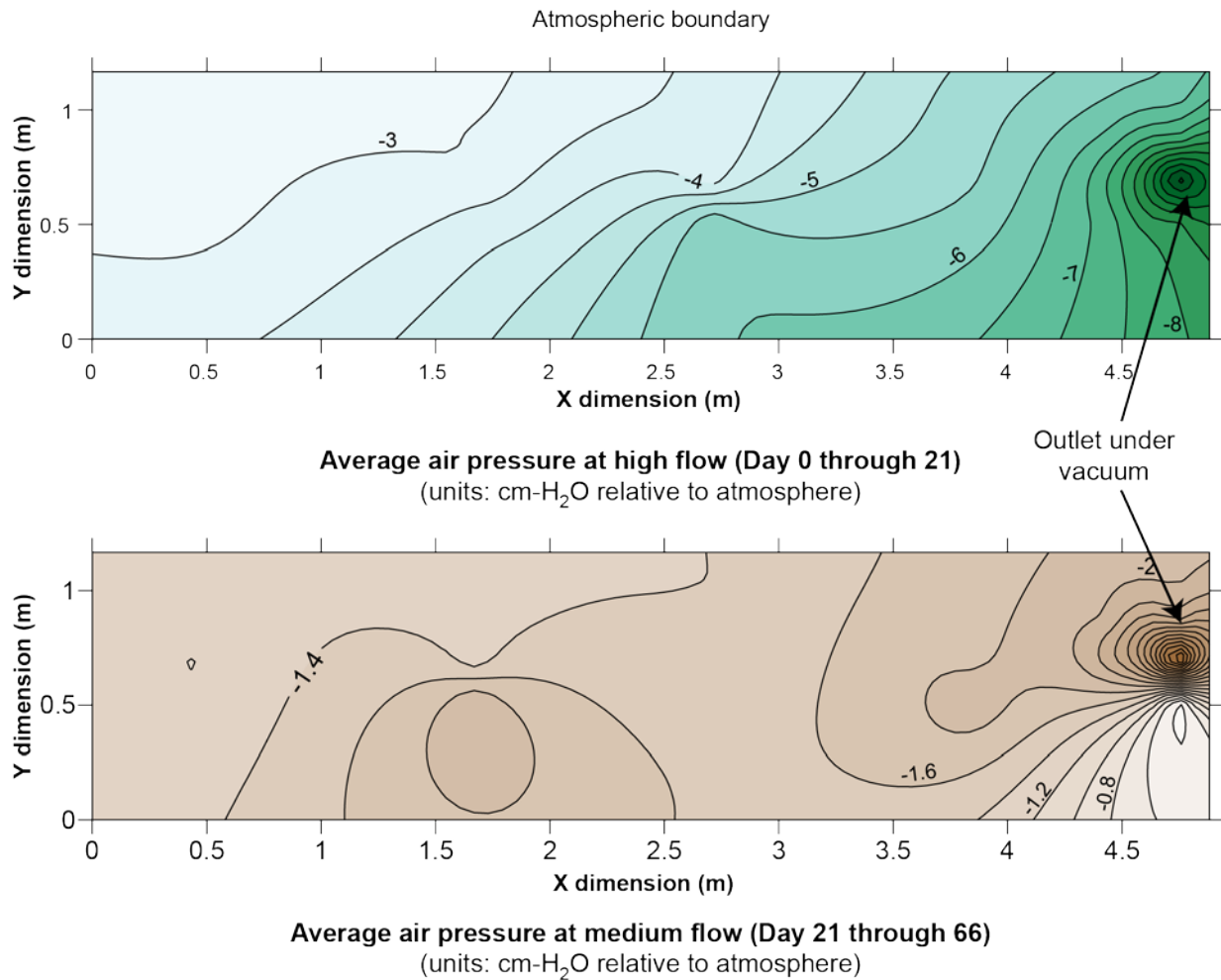


Figure 5.19: Observed average air pressure distributions for high flow and medium flow periods. Darker colors indicate more negative pressure relative to gauge pressure (higher vacuum). Note that while data are interpolated across the entire tank area, the lowest elevation of pressure sensors was array 4, located at 0.514 m above the tank bottom, and there is no data below this point. Extrapolation of the contour map below this point is uncertain.

Table 5.4: Airflow in atmospheric chambers during steady-state periods (SLPM)

Experiment	Chamber 1	Chamber 2	Chamber 3	Chamber 4
High flow (day 20)	2.33	1.15	0.313	0.028
Medium flow (day 65)	0.57	0.36	0.044	0.008

Important findings can be derived from the data. Firstly, the fundamental flow properties and geometry of the tank were essentially the same for both cases, yet the concentration in the medium flow case was about 6.5 times larger than in the high flow case, despite the flow rate changing only by a factor of 4. The dilution effect due to higher airflow rate partly explains this

reduction, but shows that it is not a simple 1:1 relationship. Rather, the asymmetry of the flow regime may be an important consideration. In this intermediate scale tank experiment, the vacuum line that is simulating airflow into a “building” is located only about 25 cm above the capillary fringe, and therefore the mass transfer response of the fringe to airflow may be quite high. However, in a field scenario where groundwater may be several meters below the surface, the affect of airflow on mass transfer from the capillary fringe may be less significant. It is also possible that the hysteresis of the soil-water may play a role. The steady state condition at day 20 resulted from the initial drainage of the clean tank with the subsequent introduction of TCE through groundwater flow. The day 65 state came after three water table fluctuation events, and there may be some hysteresis effect from these experiments as they affect the capillary fringe saturation distribution and related mass transfer across the fringe.

5.4.1.2 Water table fluctuation discussion: Air phase effluent TCE concentrations as well as water saturation at the bottom row of sensors (array 5, closest to the water table) are presented in figure 5.20 for the third water table fluctuation (WT3). The water table fluctuation events all showed similar TCE effluent vapor concentration behavior. Firstly all values showed an initial concentration increase in the influent during the period of the rising water table. However, midway through the water table rise, this increase abruptly stopped and then started to decrease to baseline or lower concentrations. Looking at the water saturation data, it is apparent that during the first part of the rising water table, the water content at sensor array 5 (the bottom row of sensors, see figure 4.10) rises slowly. Then late in the water table fluctuation, the saturation rises rapidly to near the maximum water saturation condition (0.81 for #40/50 sand). During the later phase the concentration begins to decrease.

It is believed that displacement of accumulated vapor in the unsaturated zone may explain this short-lived concentration spike during the water table rise, which may be partly explained by capillary fringe hysteresis. For the initial condition of this experiment it is expected that the capillary fringe was following the secondary drainage curve because the tank was last subjected to a drainage cycle during the previous water table experiment, followed by a steady water table period with no imbibition between the experiments. Thus, once the water table rise was initiated, the tank must transition from the secondary drainage curve to the imbibition curve. During this transition, with the water constant head devices rising at a steady rate, the imbibing water may have been displacing soil gas out of the capillary fringe, causing a TCE vapor spike. However, as soon as the transition was complete, the rapidly rising water table began to accumulate residual water from the vadose zone on the capillary fringe. Note, however, this vadose zone is relatively clean compared to the more highly contaminated saturated zone, and as it builds on the fringe, it forms a clean water lens that temporarily reduces mass transfer.

The next phase was the water table remaining steady at a higher elevation. In general, not much unique behavior was observed other than a plateauing of concentrations. However, in a field setting, a high water table is expected to generate higher diffusive fluxes due to the shortened diffusion pathway between the water table and the building (Abreu and Johnson, 2005; Tillman and Weaver, 2007b). However, the water table rise simulated in this 4 ft high tank is relatively small (18 cm), so this effect may not be observable in the data.

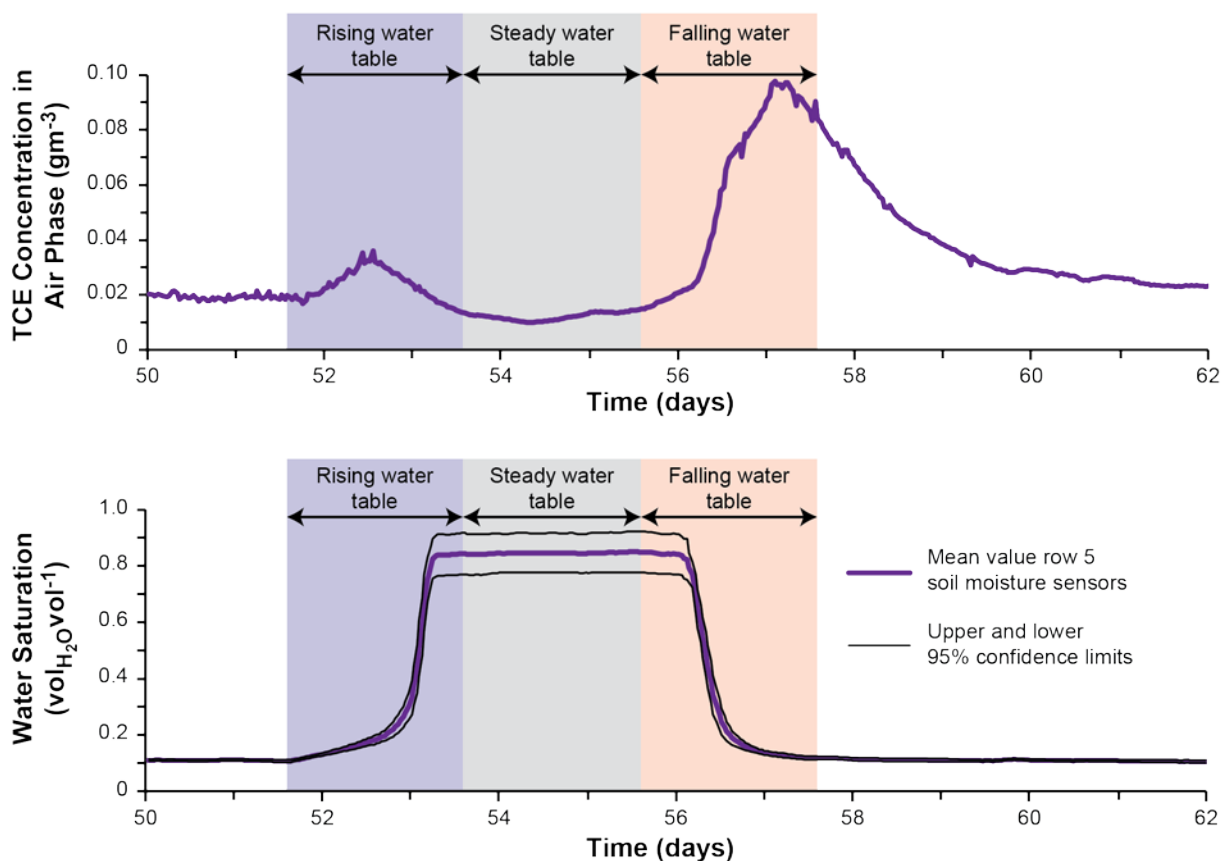


Figure 5.20: TCE airflow concentrations and water saturations a sensor array 5 during water table fluctuation three (WT3).

The next phase was the water table drop. As shown in figure 5.20, concentrations began to increase at the beginning of the water table drop. However, the TCE concentration increase accelerated midway through the water table drop, roughly corresponding to the first incidence of drainage at sensor array 5. Again, hysteresis may be involved in this initial delay as the flow transitioned from the imbibition curve back to the drainage curve. However, once the drainage began in earnest, it is understandable that a large spike in concentrations may occur because the drainage exposes more concentrated TCE contaminated water to the air phase. The concentration increase continued almost throughout the remainder of the water table drop, and only subsided after the fluctuation was complete. Overall, while the soil moisture distribution recovered to its initial condition quite rapidly by day 58, the vapor concentrations took considerably longer, not fully reaching the initial condition until around day 62. Thus, the effect of the fluctuation on the vapor plume may outlast the observable multiphase flow event that drives the dynamic behavior.

5.4.1.3. Rain event discussion: The rain events also showed a dynamic TCE vapor response. Compared with the other observed fluctuations, the effect of the rain event was shorter, but more complex as a number of processes that are interacting contribute to the dynamics. Unlike the water table fluctuation where the effect on the airflow regime was largely unremarkable, the rain event induced immediate effects on the airflow. The data from rain event 2 (R2) is presented in figure 5.21, including the TCE vapor concentrations, a vertical profile of soil moisture data averaged across each row of sensors, the airflow rates in the vacuum line and atmospheric

chambers 1-3 (chamber 4 flow was non-detectable), and air pressure from the first row of sensors across the tank. The right side plots show the effects of rainfall application in more detail showing observations at higher measurement frequencies, while the left side plots show the larger timescale of the rain event. 6.5 minutes of rain was applied at a rate of about 0.088 m-hr⁻¹ across the entire atmospheric surface. This is brief and intense, but necessary to create a fast moving wetting front in the permeable sands used, while a field soil with a silt and clay content would retain a considerable moisture front at much lower intensity rainfall. This 6.5 minute rainfall period is shown on the right side plots as the thin grey rectangle. Immediately upon the onset of rainfall, a spike in effluent concentrations was observed, and this spike continued for about 30 minutes after the rainfall event. This corresponds to the time period in which the wetting front was propagating downward. Once the wetting front passed the elevation of the effluent line, a “washout” effect was observed where concentrations rapidly dropped to a minimum. Based on the soil moisture data the wetting front migrated rapidly within about 30 minutes and was dissipating through the sensor rows 1-4. However, once it reached row 5, the saturation increased considerably and only dissipated very slowly over almost a full day. This was likely because array 5 is just above the capillary fringe and the rainfall event raised the water table enough to temporarily saturate these sensors. Thus, the slower drainage out of the capillary fringe was likely controlled by the dissipation of the groundwater mound. Evaluating the longer term TCE concentration data, this period of slow water dissipation at array 5 also corresponds roughly to the rebound timeframe, indicating that the clean water on the capillary fringe may reduce the vapor mass transfer into the vadose zone.

With respect to the airflow regime, the response to the rainfall event is immediate, and the rebound is also immediate after the rainfall ceases. The vacuum line outlet flux (representing the flow into the building) is completely unaffected by the rain application. However, the airflows in atmospheric chambers 1 and 2, which ordinarily carry the most airflow, drop immediately, and rebound immediately. Likewise, the pressure data show an immediate pressure increase during this same period. This may be explained as the wetting front displaced the pore air downward as it infiltrates, and thus airflow into the building continues unaffected, while the pressure increases due to the compression from the wetting front. This may partly explain why such an immediate concentration spike is observed - this downward propagation of the front may displace the vapor plume into the “building.” Several additional pressure anomalies were also present in the data set, but were not corroborated by any observations in the airflow or soil moisture data. These are unexplained, but given all of the air pressures sensors are referenced to the laboratory atmosphere, any indoor pressure shift in the laboratory due to ventilation equipment may manifest itself in the data, and is the most likely explanation. It should be noted that the anomalous pressures all deviate downward from the baseline pressure, which is consistent with an increase in laboratory atmospheric pressure due to building ventilation equipment.

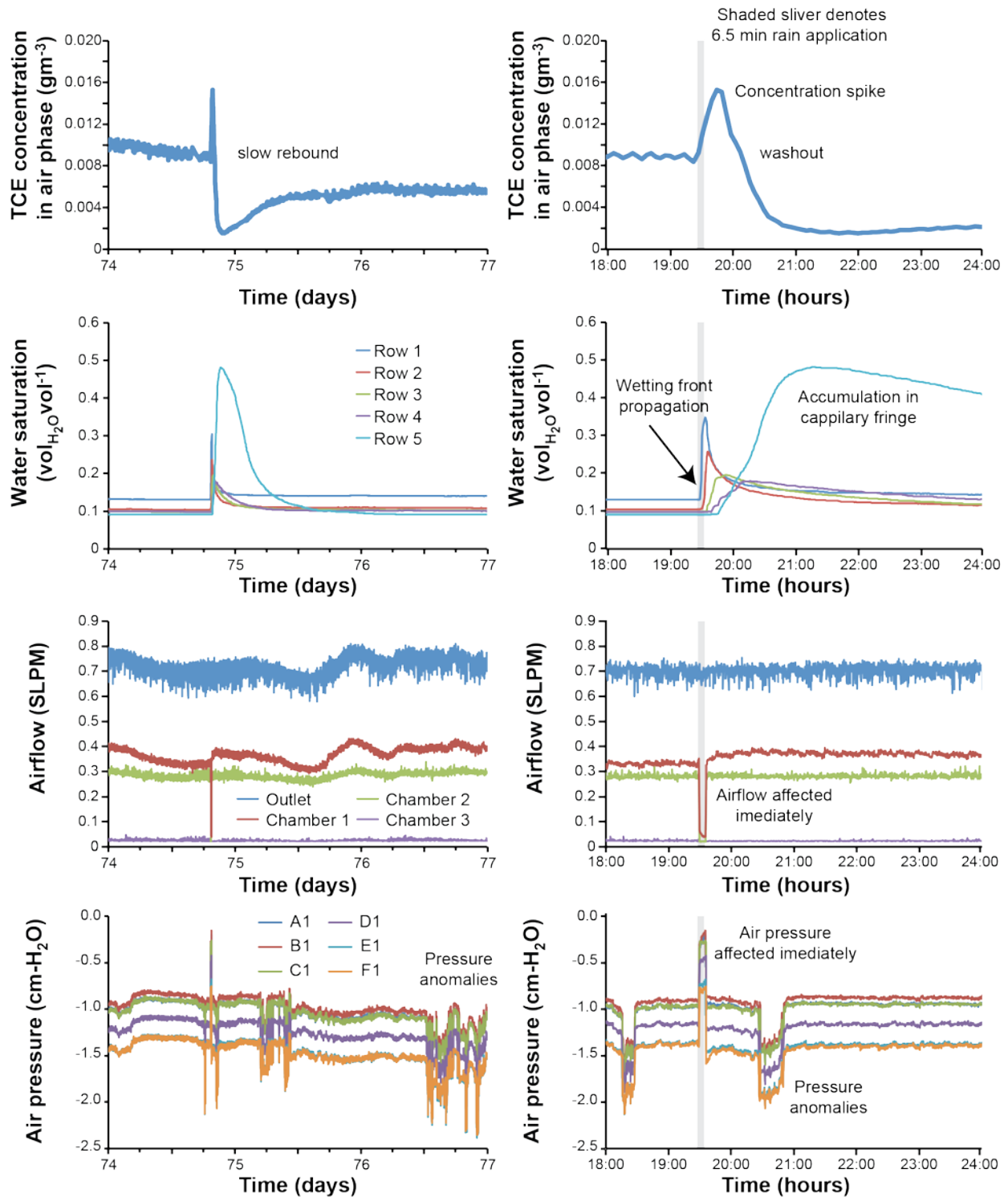


Figure 5.21: TCE airflow concentrations, water saturations, airflow, and air pressure data from rain event 2 (R2). Left column shows data from the wider timescale of the 3 full days surrounding the rainfall event. Right column presents the same data at higher temporal resolution, showing the 1.5 hours leading to the rainfall event, and 4.5 hours after the rainfall.

5.4.2 Heterogeneous tank experiment

The overall effluent TCE concentration data in the heterogeneous tank are presented in figure 4.22. Compared with the homogeneous tank, the heterogeneous tank recorded less variation in concentration magnitude once the experiment reached its initial steady-state condition. For instance, from day 20, when pseudo steady-state was achieved until day 77 shortly before malfunction during rain event 7, the TCE concentrations in the air phase effluent only varied by a factor of 4.8. This contrasts with the homogeneous case where the concentrations varied by a factor of 109, even though the heterogeneous tank was subjected to 3 water table fluctuations and 2 rain events in this timeframe. Interestingly, while range of variation was smaller in the heterogeneous system, the overall average TCE concentrations over the entire experiment was nearly the same ($0.0181 \pm 0.001 \text{ gm}^{-3}$ in the homogeneous case, $0.01753 \pm 0.00005 \text{ gm}^{-3}$ in the heterogeneous case). However, the vacuum flow rate in the heterogeneous case was considerably higher (3.001 SLPM) than the majority of the homogeneous experiment (0.980 SLPM) resulting in a larger overall mass flux. These statistics illustrate the effect of the low permeability confining layer on vapor transport. This confining layer had higher water content and lower permeability, which served as a barrier to both diffusive and advective TCE fluxes. Since clean air was entering the tank above the layer, the vadose zone above the heterogeneity was at a lower concentration, and because the lower permeability layer acted as an advection and diffusion barrier, the vadose zone below the confining layer became more concentrated. Since the vacuum line draws airflow from under the confining layer, it was representative of soil gas that was contained between the layer and the capillary fringe. The decreased variation in concentrations observed due to the experiment was also likely due to the trapping of the TCE below the layer, rendering the vapor concentrations less sensitive to the surface boundary condition.

Examining the individual events in the data set, it is apparent that water table fluctuation behavior is different in the heterogeneous case. Water table fluctuation 4 was a complex fluctuation that consisted of raising, then lowering then again raising the water table. The behavior observed was complex. It is perhaps easier to try and understand water table fluctuations 5 and 6 since they consisted of a simple rise and fall of the water table. With respect to the rising table, a vapor spike was noted, that dissipated after the rise was complete. Meanwhile, during the falling water table, a dip in concentrations was observed. One plausible explanation for this behavior is that the water table's proximity to the confining layer in the tank resulted in an increasing saturation in the confining layer during the rising water table. Meanwhile, under the falling water table, the fine layer is under higher suction and possibly draining, reducing the role of the confining layer. In either event, *the observations from these water table fluctuations show that heterogeneity may considerably alter observed transient dynamics.*

As discussed earlier, the rain events in the heterogeneous tank were compromised by the rainmaker malfunction. The first two rain events were intended to re-wet the sand as excessive drying and fingering of flow occurred at the atmospheric boundary. Thus, their observations are qualitative. However, it is interesting to note that for rain events 5 and 6, the wetting front stopped at the fine layer. The concentration increase corresponding to these events may be the result of increased saturation of the fine layer "capping" the TCE vapor. However, during rain event 7, when compartments 3 and 4 swamped, a very large wetting front propagated all the way

through the tank. In this case, the observation is much like the rain event seen in the homogeneous case, with a concentration spike, washout and rebound.

At the conclusion of the rain event, NAPL was injected into the tank to demonstrate the effect of water table fluctuation on NAPL (see figure 5.22). The entire water table was raised above the level of the source trough, and NAPL was injected such that it resided below the capillary fringe. Large concentration increases occurred at this time as exposed NAPL volatilized, but then quickly fell as the NAPL retreated into the capillary fringe and was occluded by water. A pseudo-steady-state condition was reached. Then the water table was dropped at a steady rate. This caused the highest peaks as NAPL rapidly volatilized upon exposure.

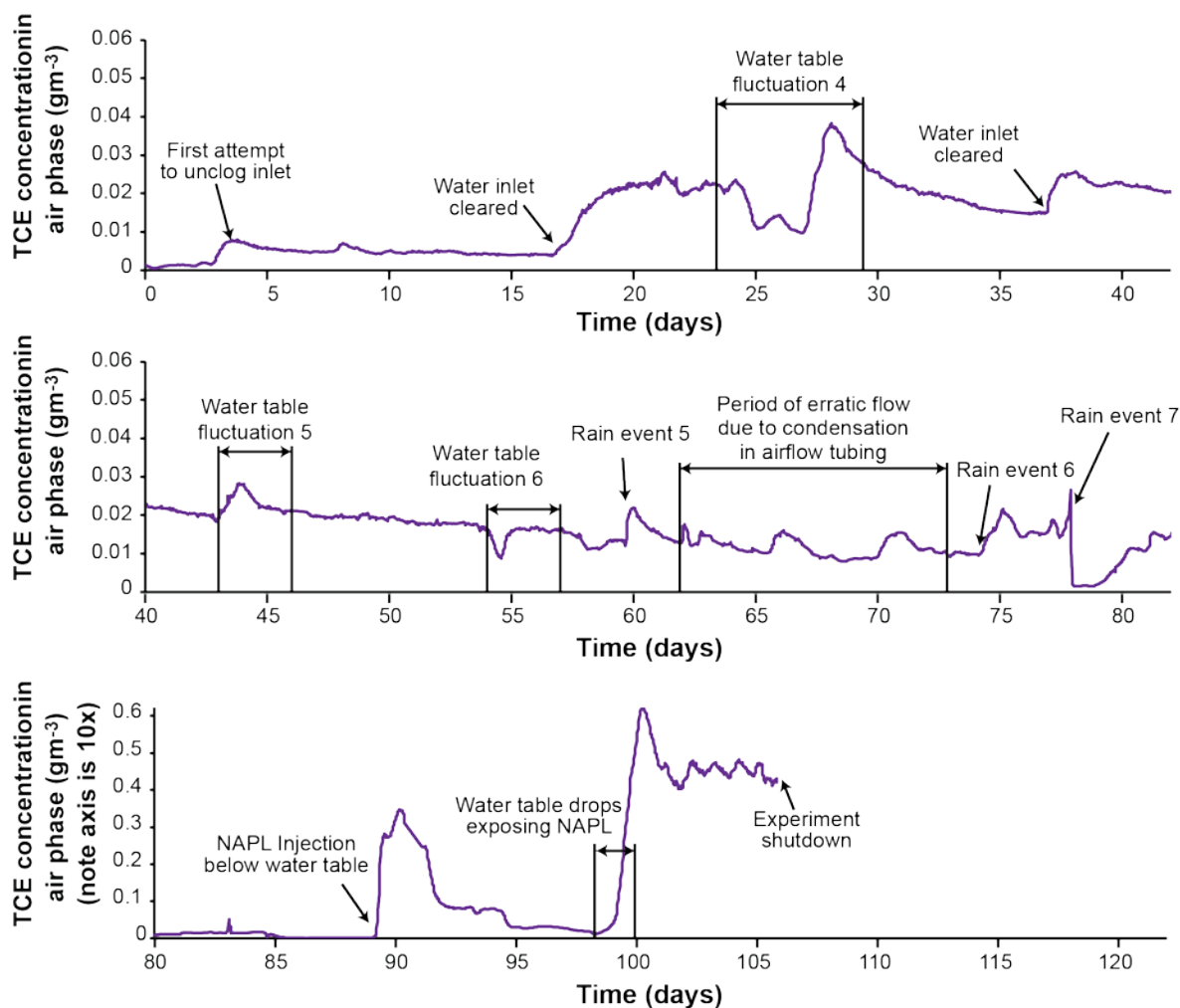


Figure 5.22: Effluent vapor concentrations over the entire 106 day experiment. Experimental events are denoted. Also note scale change for NAPL experiments on days 80-105.

5.4.3 Mass balance calculations

Obtaining accurate mass balances on volatile organic compounds is difficult, especially in applications where atmospheric exposure occurs, in large part due to the potential for large negative bias in the sampling and measurement results (Oesterreich and Siegrist, 2009). This

experiment proved no different. The assessment of mass balance was based on a comparison of average inflowing TCE mass flux with average outflowing mass flux, and assuming that accumulation of TCE within the tank is negligible after the tank reaches its initial steady state condition. In this experiment, the air phase outflow and TCE concentration from the tank were the primary focus of research and was characterized with a high degree of confidence. For instance, the 95% confidence intervals of the mean outflow TCE concentration are tightly bounded at 2.5% of the mean even when averaging over the entire 106 data set and ignoring the obvious temporal trends that are the focus of this study (a running average will yield even tighter confidence intervals). This tight confidence interval is the product of the very large number of measurements of eluting gas phase TCE concentrations (~31000 in each tank). However, this flux of TCE only represents about 2.5% of the total aqueous TCE flux entering the tank, with the rest of the TCE flux exiting the water phase effluent constant head device. Thus, the overall tank mass balance is more dependent on the inflowing and outflowing water concentrations than the gas phase fluxes. While great care was used at the influent end of the tank to avoid atmospheric exposure while introducing the TCE contaminated water to the tank (the head device overflow rate was 3x the tank flow rate and the inflow was located in Viton tubing 20 cm below the atmospheric surface in the head device), atmospheric exposure was unavoidable at the effluent device. It was determined during the homogeneous experiment that this resulted in large unavoidable mass losses from the effluent after it exited the tank, which manifested themselves in the sampling data. As a result, only 26% of the overall estimated TCE inflow was recovered from the constant head device, and it was not possible to close a mass balance on the homogeneous tank. Considerable variability also was present in the data, as the estimated variance in this outflow was 73% of the mean.

For the heterogeneous tank, an attempt to improve the mass balance estimate was made by drilling a hole in the tank adjacent to the water phase outlet and moving the effluent sampling location to this point within the tank. This change immediately showed higher concentrations than had been found in the effluent, though it represents a point sample, rather than an averaged effluent sample. Nonetheless, this confirmed the negative bias in the effluent data and the mass balance improved to 74% of the influent +/- 18% standard deviation. This was compared to the influent mass flux (which had a +/- 13% standard deviation) via a 2-sample t-test and it was determined that the estimated flux differences were still statistically significant (i.e. the mass balance is not statistically closed). However, further analysis revealed that when comparing the individual influent and effluent samples taken at each time point, a total of 51 out of 67 effluent samples indicated mass fluxes that lay within 2 standard deviations of influent flux. Given this analysis, the mass balance cannot be closed statistically, but it is noted that considerable overlap of the variance between inflows and outflows occurs, and that a relatively smaller number of strongly negatively biased samples may be throwing off the mass balance. Furthermore, given that the airflow mass balance is closed and quality control measures in ensuring the tank is airtight, there is no evidence of any leaks in the tank. There is also no evidence of TCE accumulation, as this should register increased gas concentrations. Thus, it appears that the inability to close a TCE mass balance is primarily due to negative biases associated with the effluent sampling location. This is an important finding for those wishing to model this data set, because although the effluent data will be unusable, there is high confidence in the gas phase TCE fluxes exiting the tank as well as a good assessment of the average influent TCE concentration, allowing the modeler to set the water phase effluent flux as the balance.

5.5 Model analysis of rain infiltration and water table fluctuation experiments

As one of the goals of the project was to make an assessment of the current use of models, a significant effort was made on modeling analysis to facilitate detailed interpretation of the large tank experimental results. Using a model for this analysis allows insight into the physical processes occurring during transient rain and water table events, and builds confidence in the pathway conceptual model. The objective here was not to exactly reproduce experimental results, but rather to test the model conception and develop scenarios to identify practical implications.

5.5.1 Model testing

The COMSOL model was used to analyze and explore the large tank experimental results. While the COMSOL modeling software itself is used by industry and has undergone validation and verification steps by COMSOL Inc., the formulation of the model is customizable for each application. Thus, the model needs to be validated with other models and datasets to ensure that the model formulation correct, and that the model properly captures the physical processes being explored. Toward this end, the COMSOL model was compared to C++ code developed at Czech Technical University as part of a long-term collaboration with the Colorado School of Mines. The C++ code (see appendix A) was used to analyze the results from the NAPL volatilization experiment (sections 4.3 and 5.1) and the multiphase flow formulation and validation approach for this model has been previously published (Fucik et al 2007). However, the solute transport portion of this model is new and requires validation. Thus, both the C++ as well as the COMSOL model were cross compared to the NAPL experimental results (section 5.1). This comparison is presented in figure 5.23.

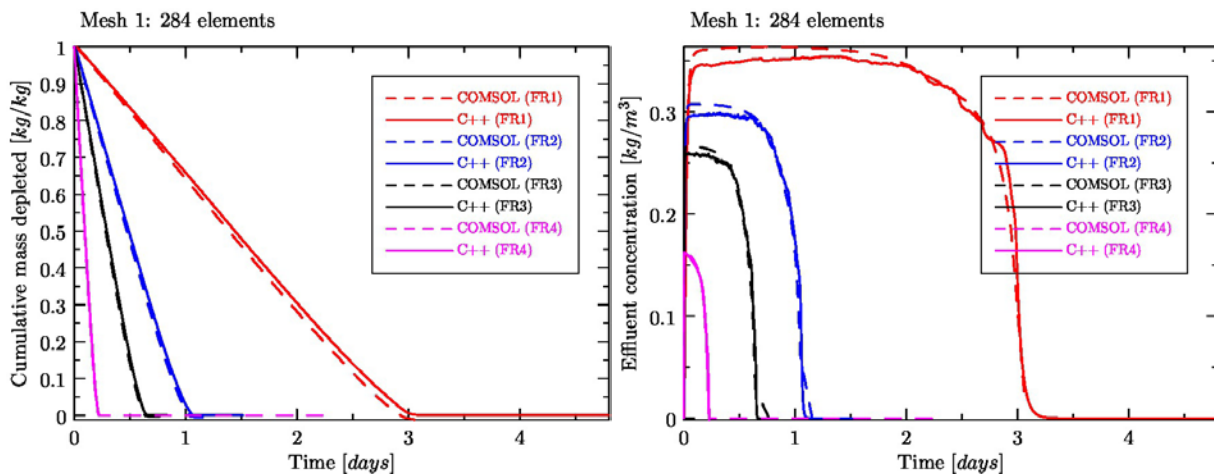


Figure 5.23: COMSOL model and C++ model compared to each other simulating the experiments in section 5.1.

The results demonstrate the models satisfactorily reproduce the concentration profiles within the margins of experimental error and attain reasonable mass balance closure. However, while the experiments from section 5.1 included NAPL mass transfer and vapor transport, the role of the capillary fringe in the experiments was strongly controlled; the “occluded” NAPL experiments

were conducted in such a way that the capillary fringe was reduced to a sharp saturation front that is simple to model, while the “exposed” NAPL experiments saw direct NAPL mass transfer to the vapor phase overwhelm any mass transfer from the capillary fringe. Since mass transfer across the capillary fringe was an important process in the large tank experiments, the model was also tested against data sets that present capillary fringe volatilization. Few experimental data sets exist with sufficient detailed description and data to validate a capillary fringe volatilization model. However, such a data set was identified in the study by McCarthy and Johnson (1993). They presented a small tank experiment where TCE contaminated water was flowing horizontally across the bottom of the tank, while the top of the tank was unsaturated with an open boundary condition along the tank top. TCE volatilization occurred across the capillary fringe and vertically through the sand pack. They brought the system to steady state and they sampled several vertical transects for soil vapor concentrations. We set up their experiment was set up in the COMSOL model to determine whether the model could match their steady-state experimental data. Steady-state horizontal groundwater flow was present in their experiment and incorporated into the model, which means that the model accounts for horizontal flow in the tension saturated region of the capillary fringe. The results are presented in figure 5.24.

Also shown in figure 5.24 are the results of a simple analytical solution to 1-dimensional Fickian diffusion through a hydrostatic capillary fringe. This model represents the type of transport model commonly used in vapor intrusion screening models. This analytical model solves the equation

$$D_z \frac{\partial^2 C_g}{\partial z^2} = 0 \quad (1)$$

subjected to boundary conditions $C = 0$ at $z = 0.6\text{m}$ (the top of the soil column) and $C = C_{\text{sat}}$ at $z = 0\text{m}$ (the elevation of the groundwater free surface). C_g is the gas concentration, z is the coordinate in the vertical dimension, and the diffusion coefficient D_z is defined by

$$D_z = \phi S_g \tau_g D_g^* + \phi S_w \tau_w D_w^* / H \quad (2)$$

where ϕ is porosity, g denotes the gas phase, w denotes the water phase, S_i is the saturation of phase i , D_i^* is the molecular diffusion coefficient of phase i , and τ_i is the tortuosity of phase i given by Millington-Quirk (1961) relationship in (3).

$$\tau_i = \phi^{4/3} S_i^{10/3} \quad (3)$$

In this simple analytical approach, the saturation profile was taken from the van Genuchten retention function curve for the media used by McCarthy and Johnson (1993).

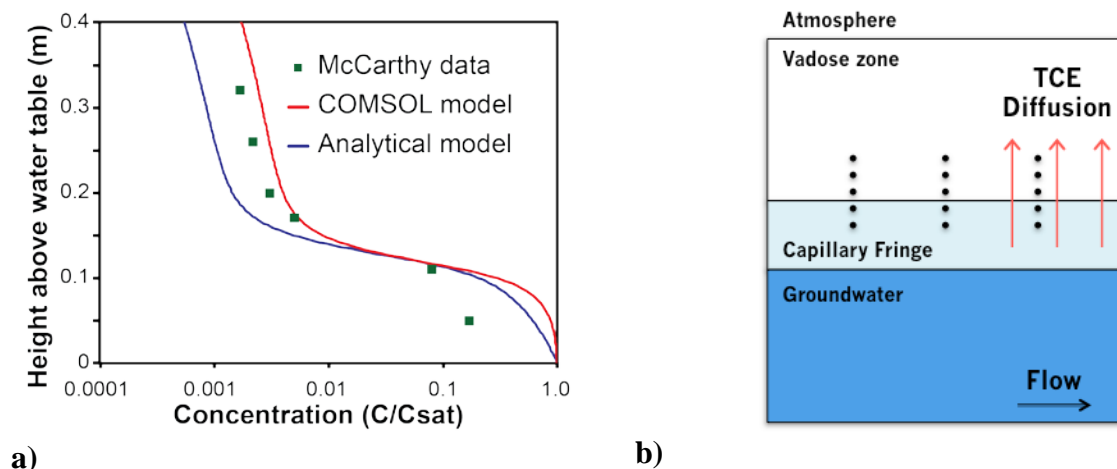


Figure 5.24: a) COMSOL model compared against McCarthy and Johnson (1996) data and analytical model. Note that the error bars for McCarthy and Johnson data are smaller than the data marker. Note logarithmic concentration axis. b) diagram of McCarthy and Johnson experimental apparatus (1 m x 1 m).

This model comparison to experimental data indicates that the two models effectively bracket the experimental data, with the experiment being more closely matched by the COMSOL model. A deviation was expected between the two models because they do not solve the same governing equations; the COMSOL model included the groundwater flow present in the McCarthy experiment whereas the analytical model only solves diffusion. Given that almost a half order of magnitude exists between the two models, this suggests that flow within the capillary fringe may be an important mechanism to include to adequately capture the delivery of higher mass transfer across the fringe. The only data point that the COMSOL model widely missed was the lowermost point located within the high saturation region of the capillary fringe. This may be a more difficult location for the model to capture because the gradients in saturation and concentration are very large in this region and therefore are sensitive to exact incorporation of the retention function parameters. Nonetheless, the test of the model against the McCarthy and Johnson (1996) data add to the confidence that the model is able to capture the physical processes correctly.

5.5.2 Steady-state analysis of the intermediate scale tank system

The focus of the modeling work is on simulation and analysis of the homogeneous large tank experiment (see section 5.4.1). This was because the added complexity of the heterogeneity, while insightful, may have masked other important findings from the data and model. Before simulating the rain and water table fluctuation events, the model was first tested to determine if the flow regime could be adequately reproduced by the model. The experimental flow regime was monitored via a series of airflow meters, soil moisture and air pressure sensors, constant head devices at the groundwater inlet and outlets, and occasional spot measurements of the tank effluent flow rate. This produced a large data set to which the model could be compared. Please note that when comparing the data, a traditional model “calibration” process was avoided because our objective was to ensure that the correct physical representation of the system was

incorporated within the model, in contrast to using a somewhat arbitrary fitting process. Thus, all physical properties of porous media, liquids, gases and the TCE contaminant were set to their literature or laboratory measured values, and no fitting parameters were used in the model.

Although the experiment ran for a total of 106 days and contained a series of water table fluctuations and rain events, large periods of time during the experiment were committed to equilibrating the experiment to a steady-state condition. This was by design to improve the model analysis because it was easier to simulate a system in steady state where the solution is a function of boundary conditions, in contrast to the difficulty of matching a model to a system that has some initial transience. This steady state solution then served as the initial condition for the transient model as the rainfall or water table fluctuation perturbation is initiated.

5.5.2.1 Flow system validation. The first step in testing the model against the experimental data required effective capture of the flow system to solve for the steady state initial condition. This proved challenging because while our conceptual model of the tank viewed the top tank boundary as a uniform atmospheric pressure boundary typical of the land surface, the subdivision of this boundary into a series of flux chambers (see figure 4.10) resulted in small but significant differential air pressures between the chambers. These pressure differentials resulted from friction losses associated with flow through the tubing that connected the humidifier to the chambers and their flow meters. It was later proven that these pressure differentials could be adequately incorporated into the model using the Darcy-Weisbach friction loss equation. Ultimately, only two of seven friction factors had to be fitted to match the model data, while the remainder were effectively estimated using with the Darcy-Weisbach equation.

The effect that these friction losses had on airflow within the large tank can be seen in figure 5.25. In 5.25a, where the uniform atmospheric pressure boundary was applied, airflow curves inward toward the outlet in a simple, clear pattern where the largest airflow occurs at the surface nearest to the outlet, and gradually declines as the distance from the outlet increases. In figure 5.25b where the Darcy-Weisbach correction is used, two key differences are observed: 1) the airflow spreads further toward the left side of the tank than under the uniform atmospheric conditions, and 2) several local zones of flow short-circuiting between flux chambers were observed, especially between flux chambers 1 and 2. It was only by including these frictions losses that the data from the airflow meters could be adequately matched with the model, seen in figure 5.26.

Several step changes in airflow rate (figure 5.26) occur during the experiment, and this is a result of deliberate changes made to control the airflow. These correspond to a “high” flow period for the first 21 days, a “medium” flow period for days 21-65 and 74-106, and a low flow period between days 65-74. Also seen in the experimental data is a fluctuation in the airflow with a regular frequency. This corresponds to daily temperature fluctuations in the laboratory that affect the density of air and therefor the mass flow rate of air pulled into the tank outlet. However, these fluctuations were found to have only a minor influence on vapor concentrations. Average temperatures over the entire experiment were used to calculate thermodynamic parameters. Thus, the model shows straight lines that neglect this daily fluctuation. Overall, the model fit to the airflow rates was quite good, with the largest errors corresponding to the first 20 days of the experiment when airflow was relatively high.

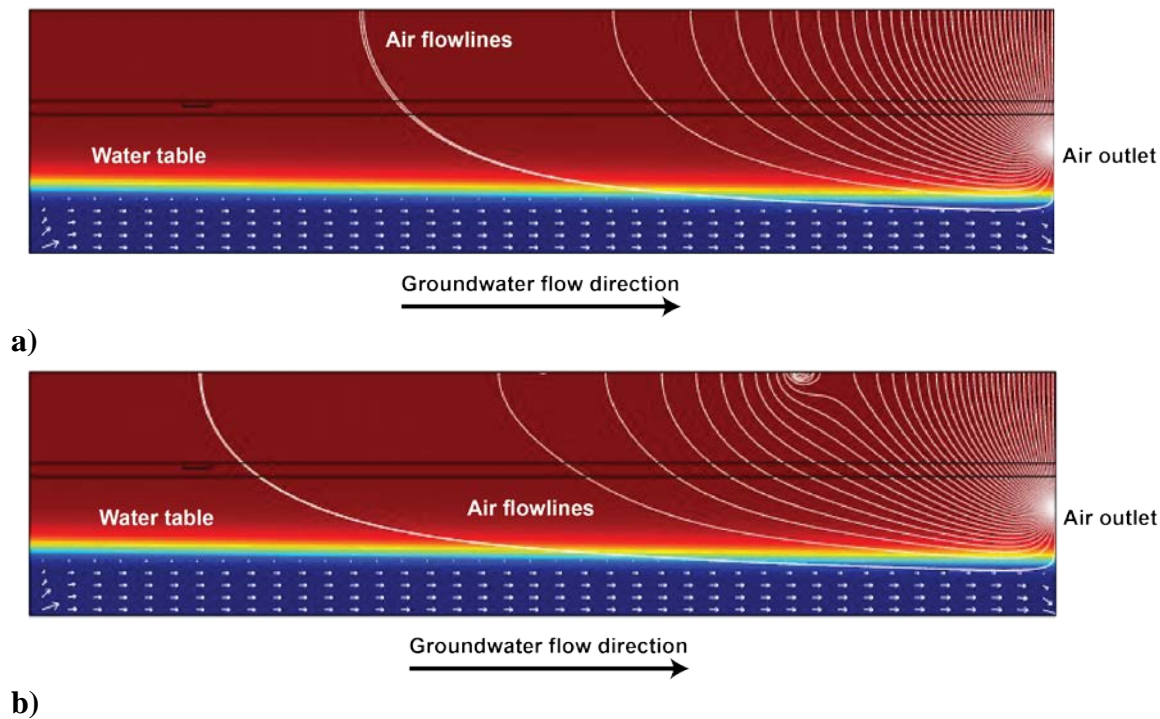


Figure 5.25: Effect of friction losses on airflow streamlines within the tank: a) airflow with uniform atmospheric pressure boundary condition at tank top, b) airflow with differential air pressures in each flux chamber. White lines represent streamlines for airflow from soil surface to the air outlet. Rainbow plot represents water saturation with red area representing drained porous media at residual water saturation, and blue zones representing the saturated zone of the tank. White arrows represent groundwater flow.

The model was also compared against air pressure (measured at 24 locations) and soil moisture data (measured at 30 locations) for the steady-state simulations. In general, for steady-state conditions, the soil moisture sensors gave largely unremarkable data (not presented) because they were located far enough above the capillary fringe that they merely registered the value for residual water saturation. The model likewise showed near residual values. However, the air pressure data did show a dependence on location and airflow rate, which was expected given the asymmetric airflow pattern and that larger pressure differentials expected at higher airflow rates. The mean air pressure values for each pressure sensor from the experiment and the model fit are presented in Table 5.5, including separate data for each of the three major flow regimes (high, medium and low) described previously.

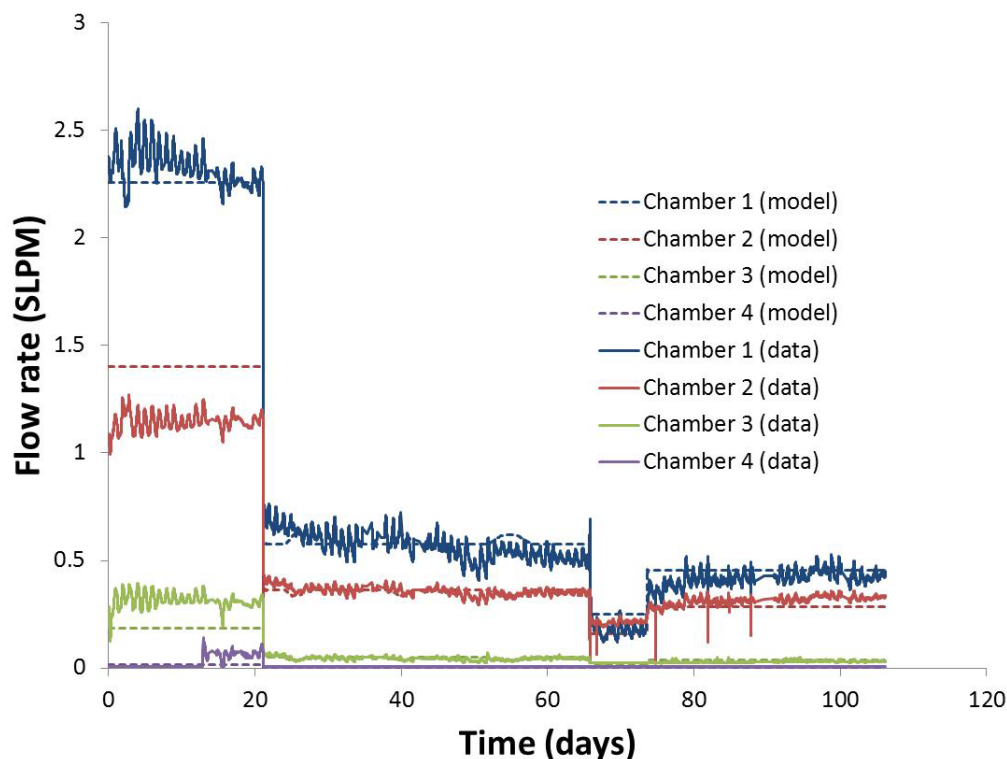


Figure 5.26: Simulated vs. observed data for airflow rates in the 4 flux chambers (units = standard liters per minute). Flux chambers are numbered 1-4 with decreasing proximity to the air outlet (see figure 4.10).

Table 5.5: Comparison of model fit to mean steady-state air pressure values as a function of airflow

Flow	Sensor location ¹	Column A		Column B		Column C		Column D		Column E		Column F	
		Data ²	Model ³										
Medium	Row 1	-132 +/- 230	ok	-125 +/- 166	ok	-137 +/- 24	ok	-165 +/- 120	ok	-191 +/- 77	ok	-193 +/- 57	ok
	Row 2	-132 +/- 53	ok	-133 +/- 54	ok	-140 +/- 87	ok	-170 +/- 90	ok	-199 +/- 57	ok	-225 +/- 83	ok
	Row 3	-116 +/- 86	ok	-126 +/- 34	ok	-141 +/- 66	ok	-171 +/- 46	ok	-227 +/- 75	ok	-460 +/- 368	ok
	Row 4	-122 +/- 90	ok	-195 +/- 160	ok	-354 +/- 359	ok	-192 +/- 137	ok	-160 +/- 112	ok	-28 +/- 500	ok
Low	Row 1	-111 +/- 230	ok	-105 +/- 166	ok	-106 +/- 24	under	-114 +/- 120	ok	-132 +/- 77	ok	-129 +/- 57	ok
	Row 2	-113 +/- 53	under	-112 +/- 54	ok	-111 +/- 87	ok	-117 +/- 90	ok	-131 +/- 57	ok	-143 +/- 83	ok
	Row 3	-98 +/- 86	ok	-103 +/- 34	under	-111 +/- 66	ok	-119 +/- 46	ok	-145 +/- 75	ok	-352 +/- 368	ok
	Row 4	-102 +/- 90	ok	-176 +/- 160	ok	-325 +/- 359	ok	-139 +/- 137	ok	-69 +/- 112	ok	104 +/- 500	ok
High	Row 1	-290 +/- 230	ok	-287 +/- 166	ok	-365 +/- 24	over	-515 +/- 120	ok	-589 +/- 77	ok	-617 +/- 57	ok
	Row 2	-287 +/- 53	over	-299 +/- 54	over	-360 +/- 87	over	-520 +/- 90	ok	-652 +/- 57	ok	-747 +/- 83	ok
	Row 3	-273 +/- 86	over	-297 +/- 34	over	-365 +/- 66	over	-531 +/- 46	ok	-737 +/- 75	ok	-1117 +/- 368	ok
	Row 4	-281 +/- 90	over	-367 +/- 160	over	-577 +/- 359	ok	-557 +/- 137	over	-710 +/- 112	over	-826 +/- 500	over

¹See Figure 4.10 for sensor locations and indexing

²Pressures (units = Pa, +/- 95% prediction interval) are under vacuum, referenced to atmosphere (~82000 Pa in Golden CO)

³Model fit described as follows: "ok" = model fit within 95% PI, "under" = model underpredicted pressure differential, "over" = model overpredicted pressure differential.

The model fit was described as “ok” if the model produced pressure values that fit within the 95% prediction interval for a given sensor and airflow. The air pressure sensors proved to be quite variable in measurement quality, some with relatively tight prediction intervals about the mean and others having very wide prediction intervals. This was, in part, due to many of the sensors reading air pressure values that were near the sensor detection limit, such that voltage background noise in the sensor can register larger errors in the data. Thus, the model often had quite wide prediction intervals to target. The model was observed to fit the medium flow range across all of the sensors very well. This flow regime is the most important because the water table and rainfall experiments were all conducted under this flow regime. The low and high flow regimes also observed generally good matches in sensor columns D, E and F, which are the pressure sensors closest to the airflow outlet. This indicates that the flow field is also well matched in this area of the tank, where the pressure differentials are also larger. However, in the portion of the tank distal to airflow outlet, where arrays A, B and C are located, a larger number of mismatches are observed, especially for the high flow case. This is likely due the effective narrowing of the prediction interval with higher flow giving the model a smaller target to meet. Because the high airflow period did not contain any of the key transient events that were the target of the modeling study, no effort was expended to improve the model fit to these values.

These data from the flow system indicate that the COMSOL model is able to reproduce flow fields, saturation profiles, and air pressures that are consistent with the experimental data. This steady-state flow system forms the basis for the solute transport simulations that follow.

5.5.2.2 Steady-state TCE vapor transport: Unlike the flow system, which was highly instrumented at both the tank boundaries and within the sand pack, it was only possible to instrument the TCE vapor transport system at the boundaries of the tank, specifically the airflow outlet, and the groundwater inlet and outlets. Limited sampling data were collected from within the sand pack, but these were subject to large sampling errors, especially where vapor was present. Thus, the dataset is primarily highly accurate with high temporal resolution (every 4 minutes) data of the vapor concentrations exiting the tank, and daily grab sampling of the groundwater influent and effluent concentrations. The influent groundwater TCE concentrations were relatively steady with a mean concentration 317 ± 19 mg/L. However, of the groundwater effluent data that were found to be valid (some data were negatively biased due to inadvertent sample exposure to incompatible materials), the effluent concentrations were statistically the same as the influent concentrations, limiting the utility of this data for model comparison. Thus, the primary experimental evidence that may be used to compare the model consists of the high-resolution vapor phase effluent concentration breakthrough curves.

For steady-state model analysis, the airflow effluent concentration must be reduced to a single baseline value for TCE concentration in vapor effluent. In practice, this was observed to fluctuate, but was generally between about $0.02\text{-}0.04$ g/m³. This baseline value proved difficult to match with the model, as the model had a tendency to overestimate this concentration. The solute transport portion of the model was setup using literature values for TCE properties, and assumes local equilibrium between phases. A major limitation of the model is related to the assumptions about the retention function. For example, in figure 5.24 showing the McCarthy and Johnson (1996) data, it can be seen that the effective concentrations drop by 2-3 orders of magnitude across the capillary fringe. This steep concentration gradient is a function of the water saturation profile within the fringe. A particular challenge for this model was the decision

of which retention function to use (primary drainage, imbibition, secondary drainage) in the absence of incorporating full multiphase flow hysteresis into the model. In the experiment, the tank is first wet packed and then drained with a saturated zone in the bottom of the tank remaining fully saturated. Thus, in this region primary drainage is the most appropriate curve. However, when subjecting the tank to rain events and water table fluctuation, these transient events occur in the unsaturated portion of the tank where residual air entrapment was expected under imbibition. Thus, the imbibition and secondary drainage curves are more relevant in the unsaturated zone. This poses a problem for solute transport because while the retention had relatively minor effects on the flow field, small changes in water saturation have strong effects on the diffusive flux of TCE. For example, using the secondary drainage curve versus the primary drainage curve nearly doubled the effluent concentration, only because the higher gas saturation in the capillary fringe promoted more diffusive transport. However, this value ($\sim 0.10 \text{ g/m}^3$) was significantly higher than the observed value ($0.02\text{-}0.04 \text{ g/m}^3$). Using the primary drainage curve brought these concentrations closer to the real value ($\sim 0.05 \text{ g/m}^3$), but unrealistically increased water saturations during the transient events, particularly in the rainfall infiltration front. Thus, while the model fit was not perfect for the baseline concentration, the objective of the model was to test whether the model could adequately explain the physical behavior of the transient events.

5.5.3 Rainfall infiltration simulation

The rainfall scenario posed an interesting problem for analysis because while the scenario was conceptually simple, the data from the experiment indicated a complex response. Simulating the rainfall event not only tested the model, but also gave insights into the physical processes. The model simulation was focused on the second rainfall event (rain-2). This event was selected because the first rain experiment had severe flow fingering due to a dry sand pack, rain event 3 was a duplicate of rain 2, and rain-4 was a deliberately non-uniform rain distribution. The model was first compared to the water saturation data to ensure that the infiltration front was adequately captured by the model. Initial model runs had difficulty in matching both the magnitude and velocity of the infiltration front, and it was hypothesized that the relative permeability model assumed in the model may play a role. The model assumes the commonly used van-Genuchten-Mualem (VGM) relative permeability model (Mualem 1976, van Genuchten 1980), given in equations (4-5).

$$k_{rw} = \sqrt{S_{we}} \cdot \left(1 - \left(1 - (S_{we})^{1/m}\right)^m\right)^2 \quad (4)$$

$$k_{rg} = \sqrt[3]{1 - S_{we}} \cdot \left(1 - (S_{we})^{1/m}\right)^{2m} \quad (5)$$

However, measurements made in our laboratory indicated that for the Accusands used in the study, the VGM model tends to underestimate water relative permeability, and overestimate non-wetting relative permeability (Mori, 2013). Therefore, the model was also run using the Mori (2013) relative permeability equations to determine the effect of the relation on the wetting front. The empirical curves derived from the Mori data set are given in (6-7). The comparison of the simulated infiltration front propagation to the experimental data are presented in figure 5.27.

$$k_{rw} = 1.626 \cdot S_w^2 - 0.557 \cdot S_w^3 \tag{6}$$

$$k_{rg} = 0.95 \cdot (1 - S_w)^{5.3} \tag{7}$$

The experimental data showed an initially sharp saturation front that began to dissipate when the front reached sensor array 3. A long slow tailing of water saturations followed the initial front. It is worth noting that the error bands on the experimental data were quite wide for the infiltration front propagation. This was due to several factors. First, each sensor array had only 6 sensors at the same vertical elevation throughout the tank, and these values were averaged. This low number of measurements resulted in relatively wide 95% confidence intervals. Secondly, despite the careful design of the rainmakers to try to distribute the infiltration as evenly as possible across the sand surface, there was nonetheless some variation in application rate. This can result in somewhat faster or slower propagation of the front, as well as variation in the magnitude of saturations observed. Thus, while the sensor-by-sensor breakthrough curves may be quite smooth and uniform, averaging across the whole level registers a much wider prediction interval. Finally, despite efforts to prevent drying of the sand surface by humidifying the airflow, ultimately some evaporation in the surface boundary layer occurred, which may have resulted in some flow fingering and non-uniform flow, despite the homogeneous sand pack.

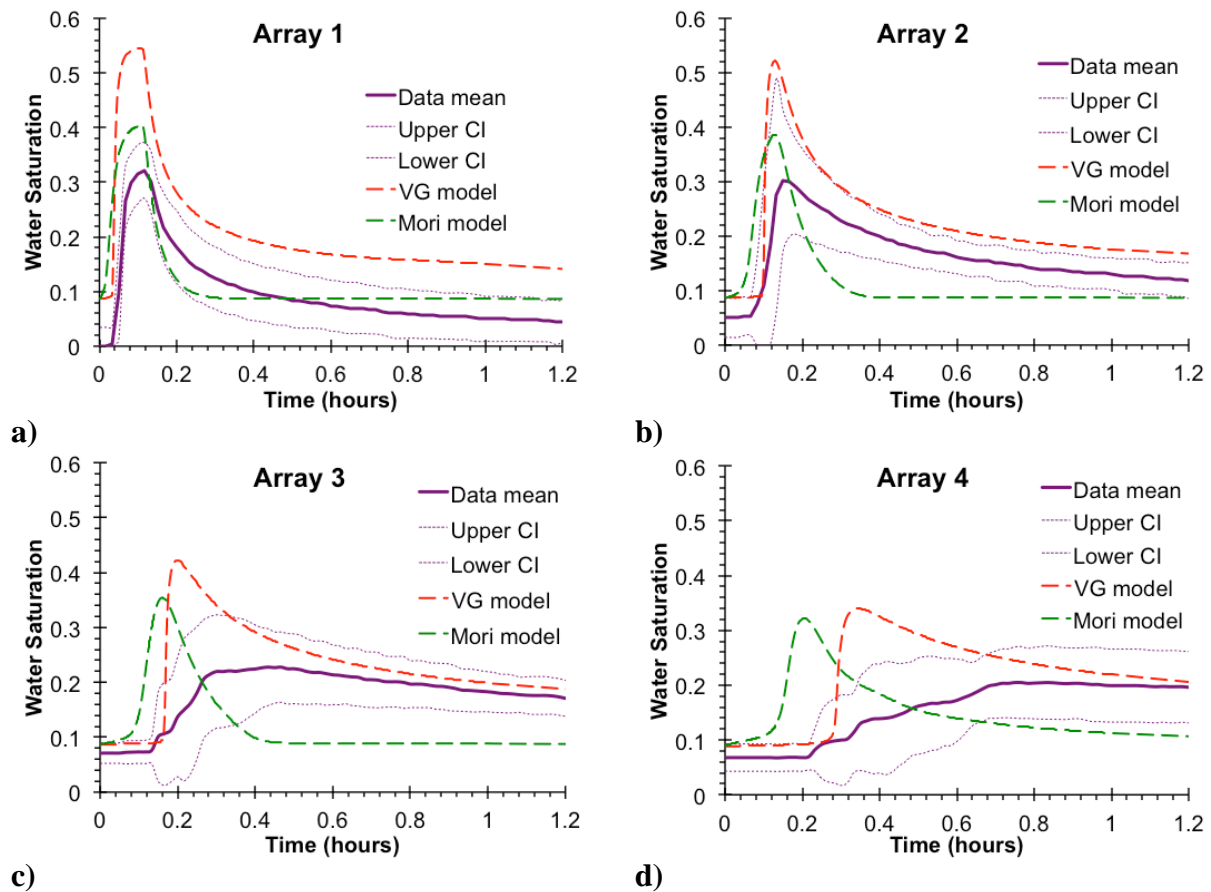


Figure 5.27: Water saturation profiles for model(s) and experimental data as a function of sensor array elevation. Sensor arrays increase in depth from 1 to 4, showing the propagation of the wetting front with time. Shown also are the 95% confidence intervals for the mean.

For sensor array 1 (figure 5.27a), which is the first sensor array that the infiltration front intercepts, the Mori model initially seemed a better fit, predicting saturations on a similar order of magnitude as the data, while the VGM model overshoots the saturations to a large degree. However, as the front propagates downward through arrays 2-4 (figure 5.27b-d), the Mori model tended to predict an early saturation front arrival, as well as too rapid of a return to initial saturations after the passing of the front. This suggests that perhaps the relative permeabilities for water are too high for the water phase. Meanwhile, the VGM model fit improves as the front propagates downward, and approximately matches the front arrival time, though it continues to overshoot the saturations within the front, and predicts too rapid of a rise in saturations. Overall, the VGM model produced the better fit as it returned predictions near or within the confidence interval of the data more frequently than the Mori model.

After the flow regime during the rain experiment was adequately captured, analysis focused on the concentration response of the system to the rain event. This is presented in Figure 5.28. Throughout the experiment and simulation, the airflow at the outlet was held constant, so the concentration response, and the TCE flux leaving the tank are directly proportional.

The model analysis predicted three primary phases of the rainfall affect on vapor concentration, which agreed well with the experimental observations. The first phase was a short-term rapid spike in vapor concentration. Other studies have termed this a so-called “capping effect” (Sakaki et al. 2013, Shen et al. 2012), referring to the ability of the infiltration front to reduce diffusivity and relative permeability, blocking atmospheric exchange of TCE vapors and leading to higher concentrations intruding into a building. In our model analysis, however, the rapid propagation of the infiltration front primarily displaced the vapors within the tank, causing the spike in vapor concentrations. Atmospheric exchange is not possible here because the tank is sealed into 4 flux chambers that do not allow outward flow of the TCE vapors. The second phase of the rainfall effect was an almost equally rapid drop in vapor concentrations to values well below the baseline concentration. This drop was due to a so-called “washout effect”, where the relatively cleaner water from the infiltration front displaces the TCE vapors downward, and effectively flushes these concentrations out of the tank. Here it is worth noting that the permeable sand used in the experiment allows a relatively rapid infiltration front propagation (~ 1 m downward in 1 hour), and the infiltration front does not fully dissipate by the time it reaches the water table. This allows a relatively large “washout effect” because the rapid downward advection and reduced dispersion of the front flush more of the TCE from the vadose zone. However, in lower permeability field soils, this effect may be much smaller when the infiltration front dissipates more quickly. Finally, the third phase is a much slower rebound back to the initial baseline concentration. After the infiltration front intercepts the water table, the water from the infiltration front must drain via groundwater flow. For a time, this causes a vertical downward flow of water within the capillary fringe, such that solute advection acts in a direction counter to solute diffusion from the source, keeping concentrations depressed. The higher water content of the capillary fringe also depresses the effective diffusion coefficient, reducing diffusive mass transfer. However, eventually this downward flow ceases as the infiltration front dissipates completely, and given time, the capillary fringe slowly rebounds back to its initial steady-state condition.

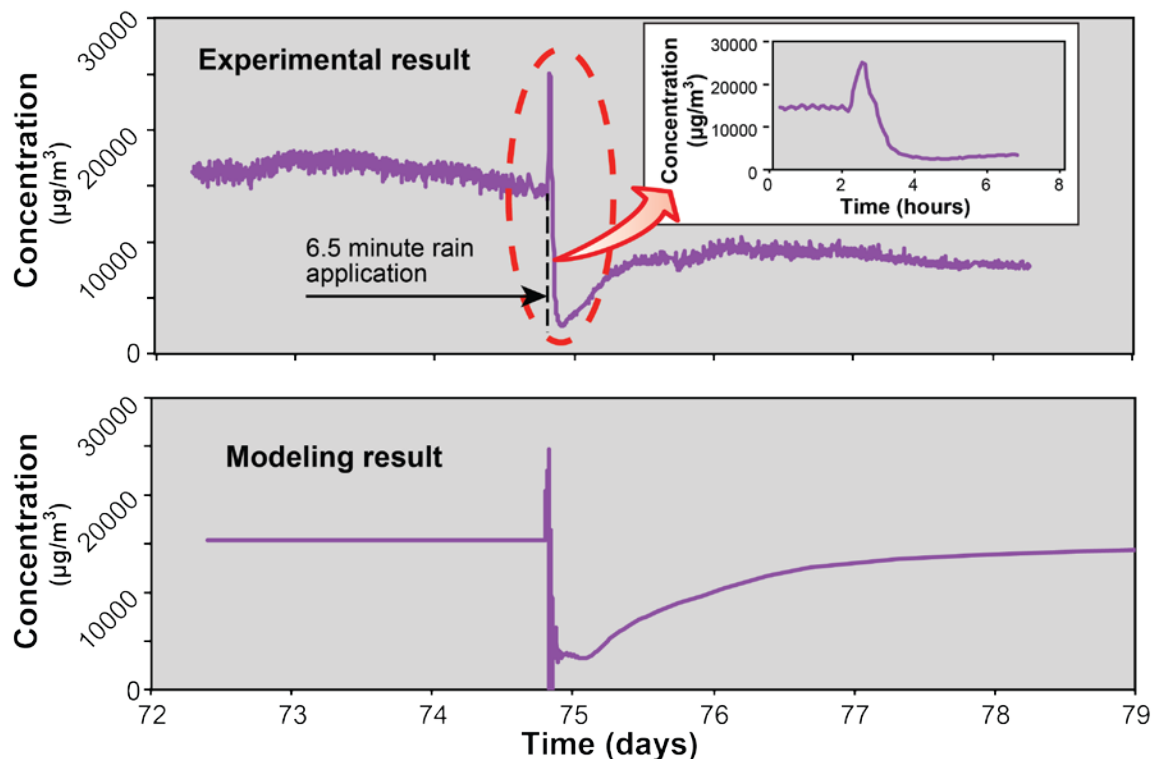


Figure 5.28: Comparison of model and experimental concentration responses in the effluent airflow from the tank.

Ultimately, this experimental and modeling exercises show that a fairly complex vapor response may result from a simple infiltration event. While these types of effects have been postulated to occur within natural systems by others (e.g. Fitzpatrick and Fitzgerald (2002), Tillman and Weaver (2007), Sakaki et al. 2013), or predicted through simulation (Shen et al. 2012), this is first major experimental and modeling analysis that confirms the effects, and builds support for the controlling mechanisms. While the specific porous media, tank dimensions, TCE concentrations and flow rates used in this experiment make direct extrapolation of these results to field systems inappropriate, they do nonetheless prove that these complicated phenomena can be captured by current models, and ultimately further sensitivity analysis and scenario modeling is necessary to understand their implications for vapor intrusion.

5.5.4 Water table fluctuation simulation

The water table fluctuation scenario also presented an important transient problem for analysis with the transport model. Mass transfer across capillary interfaces is a complex process, involving diffusion, dispersion and advection within the capillary fringe. However, determining the interactions between these processes requires use of controlled experiments and models. Much of the existing literature evaluating volatilization from groundwater emphasizes the role of vertical transverse dispersion (Klenk and Grathwhol, 2002; Swallow and Gschwend, 1983), as well as diffusion (McCarthy and Johnson, 1993; Thomson et al., 1997) in driving mass transfer across the fringe. However, the studies provide a conflicting portrait of whether diffusion or dispersion dominates (Klenk and Grathwhol, 2002), and under which conditions. They also do not fully explore the interactions between multiphase flow and solute transport that occur within

the fringe. Because mass transfer occurs across the fringe, any shifting of the capillary fringe has the potential to affect this mass transfer into the vadose zone. Water table fluctuations have been postulated to cause important mass transfer effects, but few studies have explored the role of water table fluctuation in detail (McCarthy and Johnson, 1993; Thomson et al. 1997). McCarthy and Johnson (1993) conducted a laboratory flow cell experiment in which concentrations in the unsaturated zone were observed during a water table fluctuation. During a water table reduction, they observed temporary increases in VOC concentrations, which diminished once the water table was restored to its initial level. However, they observed a long-term hysteresis effect where the concentrations remained depressed after the system reached steady state. Thomson et al. (1997) conducted a modeling study to evaluate the effect of a regular sinusoidal fluctuation of the water table (e.g. a diurnal or tidal effect), and predicted this to greatly increase the mass transfer to the vadose zone, often by orders of magnitude. The magnitude of the mass transfer rate increase correlated positively with increasing frequency and amplitude of the fluctuation. However, despite this body of work, more work is necessary to gain confidence in our ability to predict the true physical behavior of a dynamic water table. For example, the water table fluctuation simulation by Thomson et al. (1997) did not have data to validate against, and used assumed values for a rate-limited mass transfer coefficient. This study was also conducted on a vertical 1-dimensional domain that may negate important multi-dimensional flow and transport effects. The experiment by McCarthy and Johnson (1993) was conducted in 2-dimensions, but contains a sparse concentration dataset and did not present soil moisture data. The data and model analysis that follows is unique because the combination of soil moisture data and observed VOC concentrations gives insight into the dynamic behavior and important processes that need to be included.

5.5.4.1 Comparison model to soil moisture data: The third water table fluctuation was chosen for analysis because it was conducted at a slower experimental pace (over 6 days instead of 3) than water table fluctuations 1 and 2, and presented a clearer overall dataset. As with the rain model, the first simulation step comparing to focused on capturing the transient soil moisture distribution to determine whether the model could reproduce the flow system. Figure 5.29 presents the data from the bottom array (array #5) of soil moisture sensors during the water table fluctuation. This row of sensors is initially above the capillary fringe, but the rising water table eventually inundates these sensors causing the saturation to rise to a fully saturated condition (with residual air entrapment).

The experimental data show a different saturation profile at the array 5 sensors than the model. The water table fluctuation begins with a rising water table at time ~51.7 (days), continuing on through time ~53.7 (days). In the experimental data, the saturation is observed to start slowly rising until about halfway through the water table rise period, at which the saturation rapidly increased to the fully saturated value. The water saturation then stays steady at this value through the rest of the water table increase. A period of steady high water table proceeds between 53.7 and 55.7 days. Then the water table recession begins at 55.7 (days) and ends at 57.7 (days). The water table recession effectively mirrors the behavior seen in the water table rise, though with slight differences in slope and curvature. Meanwhile, the model predicts a evenly placed rise in saturation between these time points, and nearly identical behavior during the water table drop. The model does generally reach the correct steady state saturations at the correct times for the water table fluctuation, but it mostly misses the transition period between the drained and saturated condition.

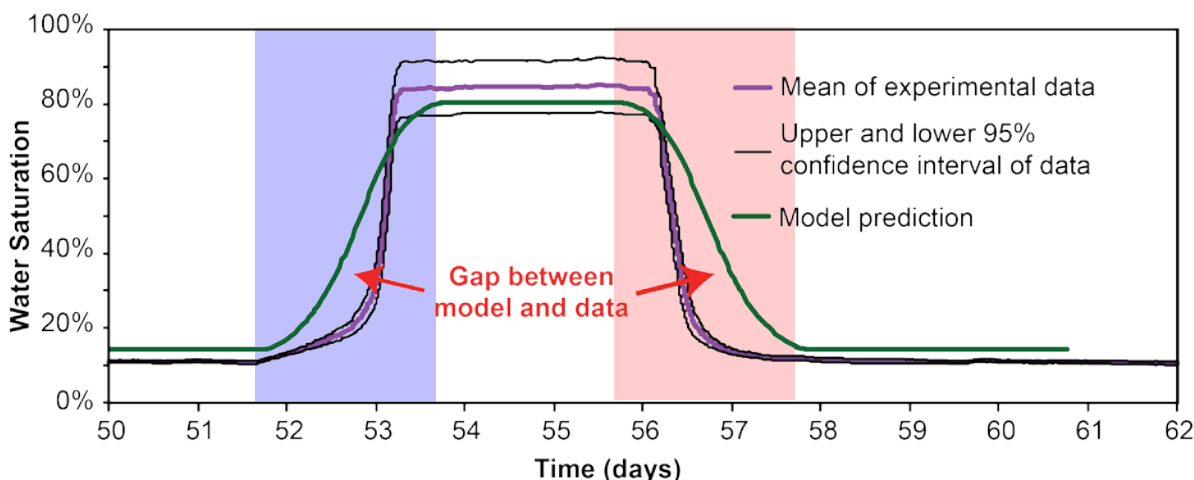


Figure 5.29: Model and experimental comparison of mean soil moisture values in array 5 during the water table fluctuation event. Blue time period corresponds to rising water table and pink time period corresponds to the dropping water table.

The deviation between the model and the experiment in figure 5.29 may be caused by the assumptions about the capillary characteristics of the media in the model, versus the “true” physical behavior within the experimental system. One possibility is that the van Genuchten model for capillary pressure-saturation relationships (P_c - S_w) used in the model presents a smoother capillary curve for the 40/50 Accusand than is actually physically observed within the tank. The Accusand has very high uniformity and thus a sharper capillary curve than is typical of many field soils for which the van Genuchten (1980) model was developed. This might explain the relatively abrupt increase in saturation that occurs midway through the water table rise. As such, a Brooks-Corey (1966) type model, which incorporates this more abrupt transition, may be more appropriate for this porous media.

Another possible cause of the model-experiment discrepancy is that multiphase flow hysteresis may be affecting the capillary region. The model neglects hysteresis and uses a single retention curve relationship to define P_c - S_w relationships within the media. Thus a reversal of the water table merely results in a reversal of direction on the P_c - S_w curve used to define saturation. However, in the physical experiment, the water table increase causes the capillary fringe to shift from the drainage curve to the wetting curve. Since the imbibition curve lags below the drainage curve for equivalent values of capillary pressure, a decrease in capillary pressure (as occurs during the rising water table) will cause the water saturations to increase more slowly than would be predicted if hysteresis is neglected. Evidence of this exists in the data for approximately the first full day of the fluctuation (e.g. time ~51.7 to 52.7 in figure 5.29), where the saturations in array 5 increase much slower than predicted by the model. The reverse occurs during the water table reduction that followed the water table rise. Here the P_c - S_w relationships transition from the imbibition curves to the secondary drainage curve. Since this hysteresis loop still lies below the drainage curve used by the model as the P_c - S_w relation, the model will continue to over-predict saturations through the water table reduction as well.

5.5.4.2 TCE Solute transport: The comparison of the experimental and modeled airflow outlet concentrations are presented in figure 5.30. Here it can be seen model also encountered

difficulties in matching the experimental concentration data. The most perplexing observation was that the model predicted an immediate *decrease* in concentrations during the water table rise, while the experiment observed a clear, temporary *increase* in concentrations that extends about halfway through the water table rise. This “bump” in concentrations was also observed in the first and second water table fluctuations (WT1 and WT2 as described in section 5.4.1), indicating the repeatability of this experimental observation. This suggests that some physical process in the experiment is not being captured. A plausible explanation for this the mismatch is that the inability to completely capture the soil moisture dynamics within the capillary fringe, and a considerable level of effort, including hundreds of model runs were dedicated to trying to determine the source of this model-experiment discrepancy. These model runs included exploration of boundary conditions, physical parameters, and hysteresis to determine which processes could capture this “bump” at the beginning of the water table rise. These model runs will be archived in the PhD dissertation by Ben Petri (see appendix B).

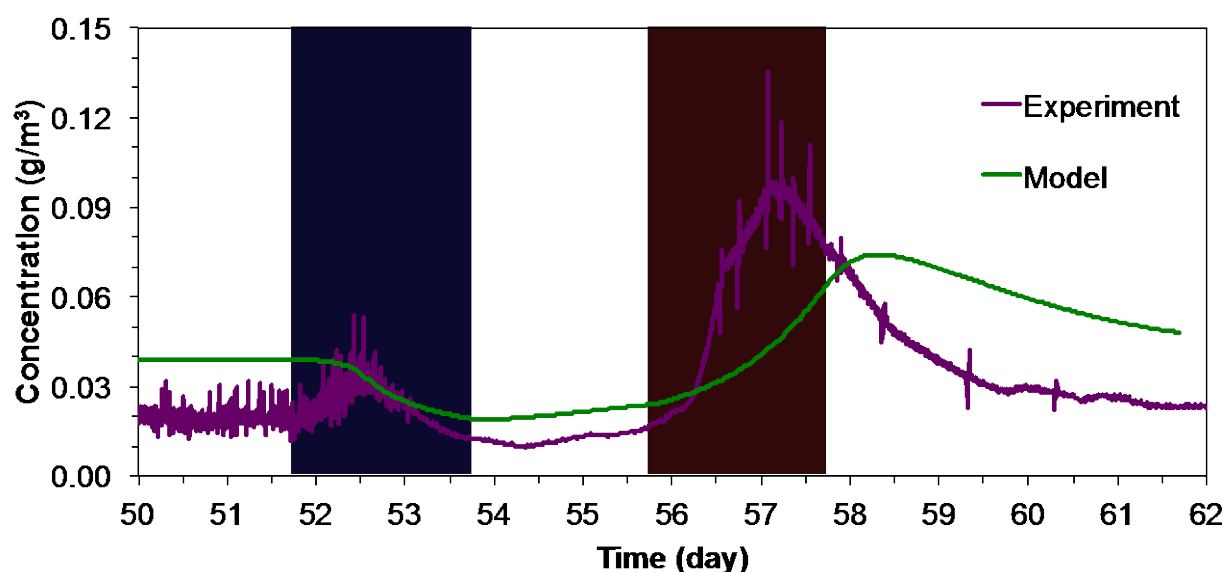


Figure 5.30: Comparison of experiment and model for TCE concentrations at tank outlet. Blue shaded region represents rising water table interval and pink shaded region indicates falling water table.

One of the factors explored was multiphase flow hysteresis. The model was modified to incorporate a hysteresis formulation proposed by Kool and Parker (1987). The Kool and Parker (1987) model effectively combines the van Genuchten (1980) retention function model with Scott et al.’s (1983) empirical hysteresis model resulting in a relatively simple system of scanning curves that can be incorporated into the model. The scanning curves use the same α and n parameters for the van Genuchten model, but scales the residual air and water saturations to obtain the scanning curves. Figure 5.31 presents the results obtained for water table rise portion of the fluctuation only for the hysteresis model, versus a non-hysteresis model, which uses the secondary drainage curve as the only saturation curve.

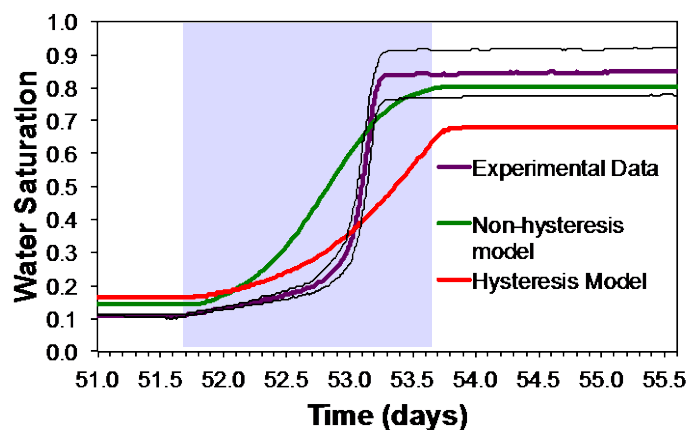


Figure 5.31: Comparison of water saturations at array 5 for the hysteresis model, non-hysteresis model and data for the water table rise.

While neither model fits the data well, what can be seen is that the initial upward curvature of the hysteresis model is more gradual than the non-hysteresis model, and a similar gradual curvature is observed in the experimental data. This corresponds with the transition between the drainage and imbibition curves as discussed previously. The hysteresis model predicts a more abrupt transition to the saturated condition that is also in closer agreement with the experimental observation. However, the hysteresis model misses the overall maximum saturation observed at the end of the water table rise, as well as the sharp increase in water saturation midway through the rise that results in the maximum saturation being achieved much sooner than either model predicts. Unfortunately, while model was able to generate a stable solution for the flow system response with hysteresis, the solute transport component of the model was destabilized by the hysteresis formulation. Incorporation the transition from the drainage curve to the imbibition scanning curves caused a transient change in the concentrations in the model domain even without the applied water table rise. This is likely due to numerical errors in the effective diffusion coefficient, which is highly sensitive to water saturation. Therefore the hysteresis model results for the airflow outlet concentration are inconclusive. Ultimately, better models will be necessary to fully capture the capillary fringe dynamic behavior. Hysteresis may be a factor worth evaluating because the typical assumption of a single van Genuchten scanning curve does not appear to capture the saturation behavior, and this may have implications for solute transport.

Initial model results did indicate that the model could predict an immediate increase in concentrations when the water table dropped, which was consistent with experimental observations. Thus a separate modeling effort to simulate only the water table drop portion of the experiment was conducted to determine if the model could fit this part of the experiment. The results from this simulation are presented in figure 5.32. Here, the physical behavior of the model is correct in predicting an increase in concentrations at the outlet, though the fit is poor as the experimental concentrations spike much higher and earlier than the model. This poor fit may partly be due the sequence of the experimental procedure (water table rise, water table drop); since the simulation in figure 5.32 neglects the previous water table rise, deviations between the model and experiment may propagate forward due to any remaining transience in the experiment from the water table rise. This might partly explain why the fit of the model to the water table reduction alone is poor, despite the ability of the model to predict an increasing concentration trend. As with the water table rise model, hysteresis might also play a role. Notwithstanding the

poor fit, this anticipated increase in concentrations does agree with results from section 5.2 and the experimental observations from McCarthy and Johnson (1993).

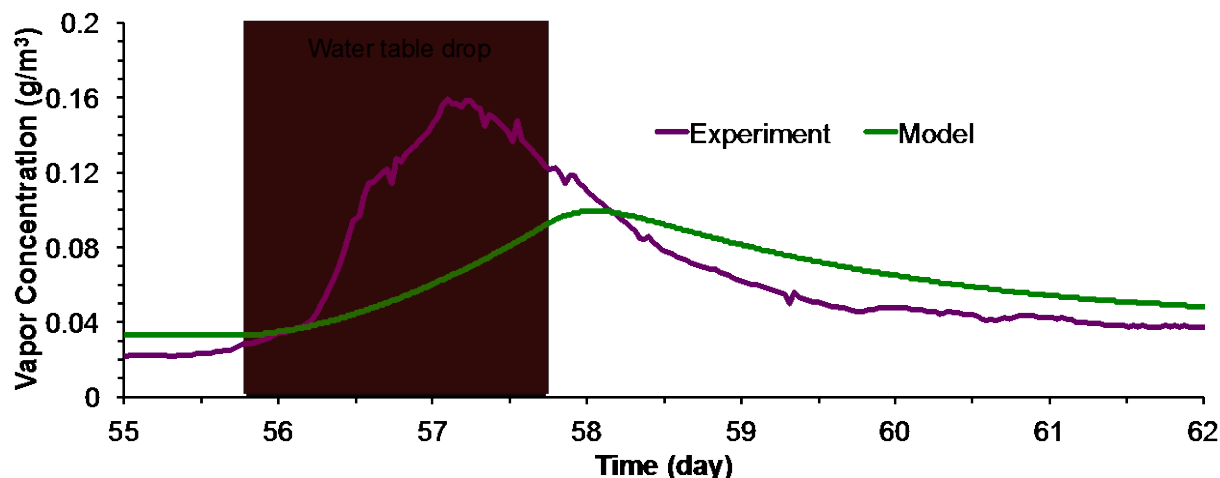


Figure 5.32: Model and experiment comparison for only water table reduction.

An analysis of the mass balance from the model for the water table reduction reveals some counterintuitive physical trends. Figure 5.33 shows the simulated boundary fluxes and total mass of TCE within the tank as a function of time throughout the water table reduction portion of the experiment. During steady-state operation, the TCE mass in the tank is constant, and TCE flux entering into the tank through the groundwater inlet (initially negative indicating inflow in figure 5.33) is counterbalanced by the TCE fluxes from the airflow and groundwater outlets. During the water table reduction, groundwater drains from the tank resulting in a net reduction of the water mass within the tank, primarily from the saturated zone. This water contains TCE at a considerably higher concentration than vapor within the unsaturated zone. Thus the water table drop results in an overall net loss of TCE mass from the tank (the dashed line in figure 5.33). The flux of TCE leaving the tank at all of the boundaries increases during the drainage, with the groundwater inlet reversing as TCE contaminated water exits the tank through the inlet constant head device. However, the mechanism of increased flux at the boundaries differs between the air outlet flux and the groundwater fluxes. In the case of the groundwater, which is almost uniformly contaminated with TCE, the increase in flux is primarily due to the momentary increase in water flow from drainage of the tank. However, for the air outlet flux, the flowrate is fixed and it is the increased concentrations in the air phase that drive the increased boundary flux, indicating this portion of the mass likely originates from the capillary fringe as the water table drops

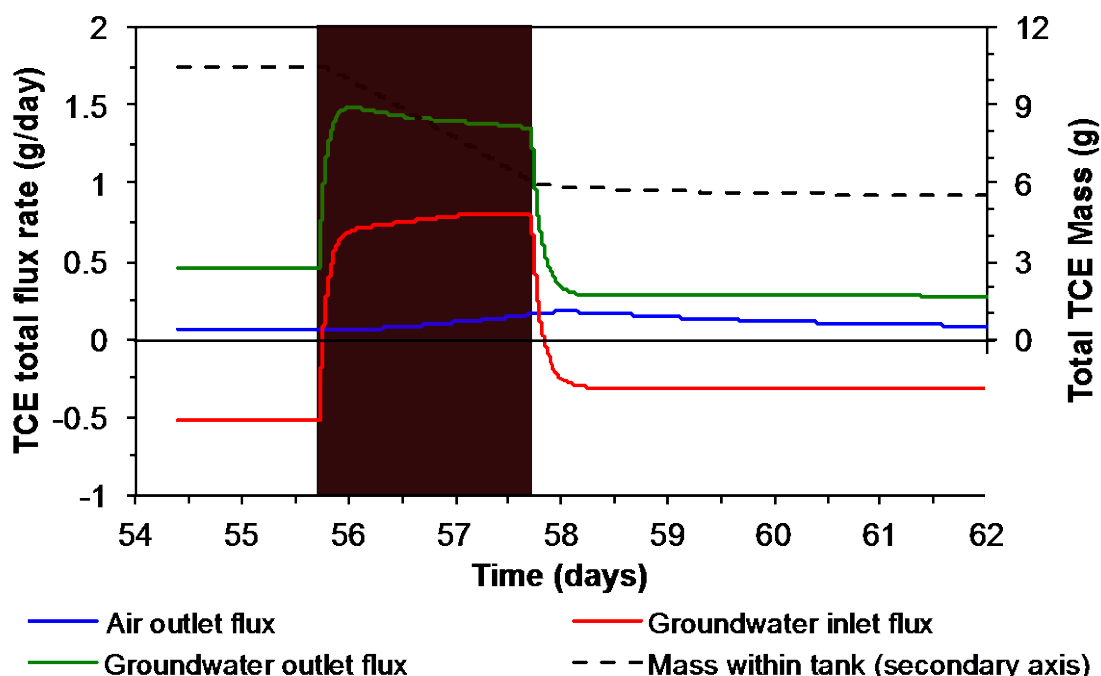


Figure 5.33: Mass balance and boundary fluxes from the model for the water table reduction

Overall, the results from the water table fluctuation simulations indicate more work is needed to fully understand the dynamic behavior observed. Clearly some physical process appears to be missing for the water table rise to capture the “bump” observed, and the water table reduction does not fully fit with the data either. On the basis of the water saturation data, it appears that the capillary characteristics within the model domain are not being adequately captured. The simulations run provide some evidence in support of the hypothesis that hysteresis may be important, but without effective simulation coupled with solute transport the results are inconclusive. Ultimately, despite the homogeneous sand pack, and relatively simple nature of the experimental procedure, the modeling results show that the interactions between flow and transport within the capillary fringe are complex and defy easy assumptions and modeling. It is hoped that future exploration and modeling of this dataset may eventually yield insight into the important processes within the capillary fringe, and yield a better understanding of the flow and transport interactions.

5.6 Two-Dimensional Geophysical Tank Experiment

In this series of experiments, three heterogeneous sand-pack configurations were tested in a two-dimensional intermediate-scale testing tank using a novel application of electrical resistant tomography (ERT) to characterize VI pathway evolution. The experimental design employed heterogeneous packing configurations and a variable water table in an effort to capture fundamental REV-scale hydrologic processes that affect VI pathway evolution in unsaturated environments. The ERT tests were performed on three sand tank packing configurations, each one with slightly more complex heterogeneity than the previous, in an effort to create a physical VI model that contained varied levels of complexity. During all stages of ERT sand tank experimentation, soil moisture, temperature, and electrical conductivity were continuously monitored and used to constrain the ERT inversions and produce a series of qualitative soil gas

diffusivity simulations. The observational results for soil moisture content, soil gas diffusivity simulations, and ERT inversions were then compared at three selected time steps (T0, T1, and T2) to evaluate ERT in a physical VI sand tank model at varying degrees of saturation.

The observed volumetric soil moisture contents during all stages of ERT testing are shown in Figure 5.34-5.36. Results are presented at three selected time steps (T0 - 0hrs, T1 - 2hrs, and T2 - 4hrs), each capturing a unique soil moisture distribution stage within the testing tank. The first time step (T0) shows the volumetric moisture content under full saturation conditions. Under these conditions, volumetric moisture content is equal to porosity. For the sands used during these tank experiments the total porosity values were $0.413 \text{ m}^3/\text{m}^3$, $0.330 \text{ m}^3/\text{m}^3$, $0.312 \text{ m}^3/\text{m}^3$, for #70 sand, #20/30 sand, and #12/20 sand, respectively (see Table 4.1 for additional sand properties). The second time step (T1) shows the volumetric moisture content at an intermediate step, with the water table set at approximately 20 cm bgs and immediately below the coarse sand-packed layer. At this water table elevation, the upper most region of fine sands (#70) are still relatively close to saturation, with the volumetric moisture contents ranging from $0.243 \text{ m}^3/\text{m}^3$ in the shallowest zones monitored (approximately 4 cm bgs) to full saturation in the lower zones (well below the water table). At this time step, the volumetric moisture contents for the coarse sand layer (#20/30) are beginning to drain, with observed values of approximately $0.111 \text{ m}^3/\text{m}^3$. The final water table elevation, set at approximately 30 cm below the coarse packed layer, shows the coarse layer almost completely drained, with an observed saturation of $0.027 \text{ m}^3/\text{m}^3$. The fine packed layers, however, still contain a significant amount of water, with observed saturation values ranging from $0.185 \text{ m}^3/\text{m}^3$ in the shallowest regions (approximately 4 cm bgs) to full saturation, $0.413 \text{ m}^3/\text{m}^3$, at the lowest monitored regions (approximately 45-55 cm bgs). The contrast in volumetric moisture contents between the fine sand packed layers and the coarse sand packed layers becomes most pronounced at the lowest water table elevations, as seen by comparing Figures 5.34-5.36 at time steps T0 to time step T2.

In an effort to examine the potential impact to VI pathway evolution that results from the strong volumetric moisture content contrasts between the coarse and fine sand layers in the testing tank, we used the experimentally observed moisture content values, along with known soil properties [Smits et al., 2010], as input values for a water induced linear reduction (WLR) soil gas diffusivity model [Moldrup et al., 2000]. As no observational studies on soil gas diffusion were performed during these sand tank experiments, the WLR model simulations performed for this task cannot be validated and therefore should serve in a limited capacity as a qualitative evaluation tool for determining the performance of ERT VI characterization methodologies.

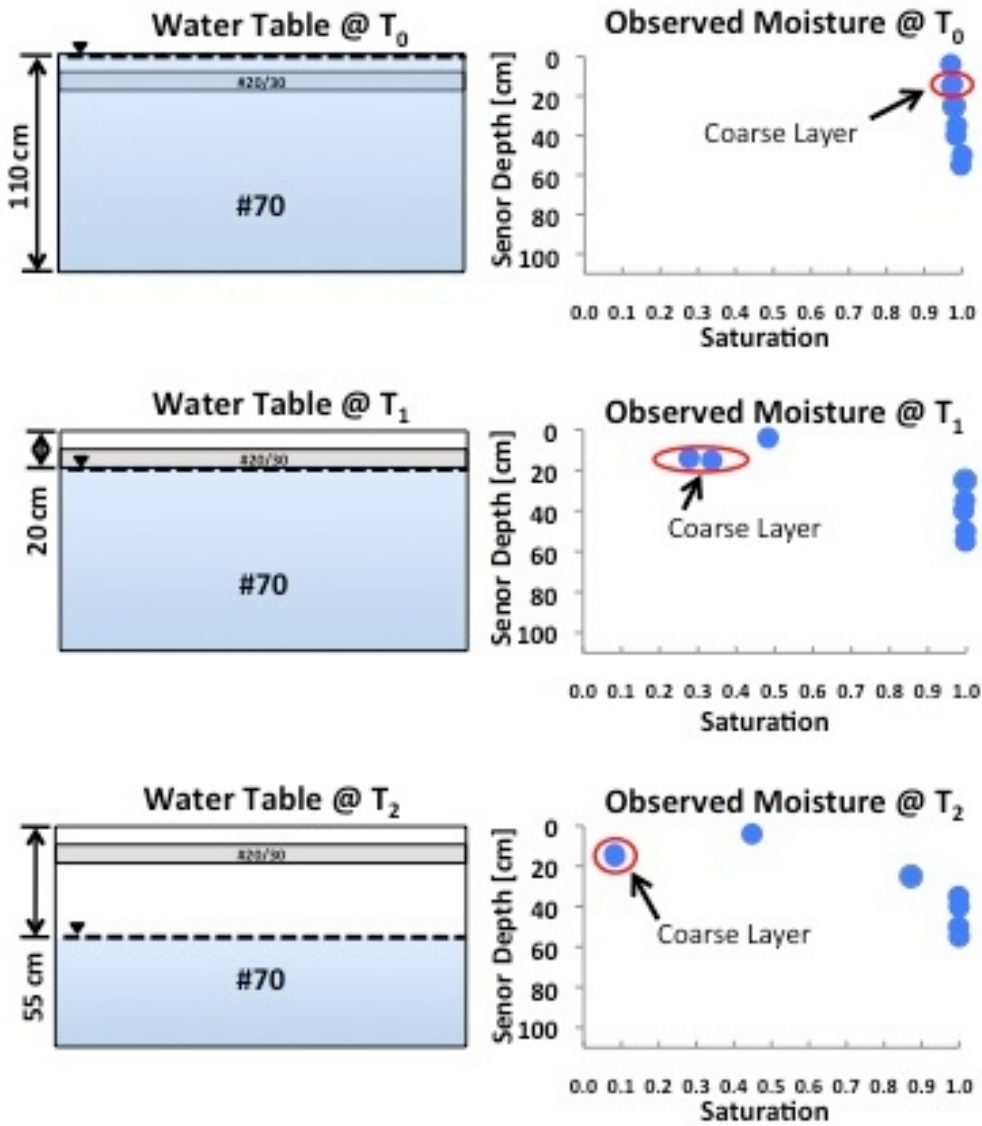


Figure 5.34: Schematic of packing configuration #1 and the calibrated volumetric moisture content data (e.g. Sakaki et al., 2011) with the water table set at the upper, mid and lower elevations (T_0 , T_1 , and T_2 , respectively).

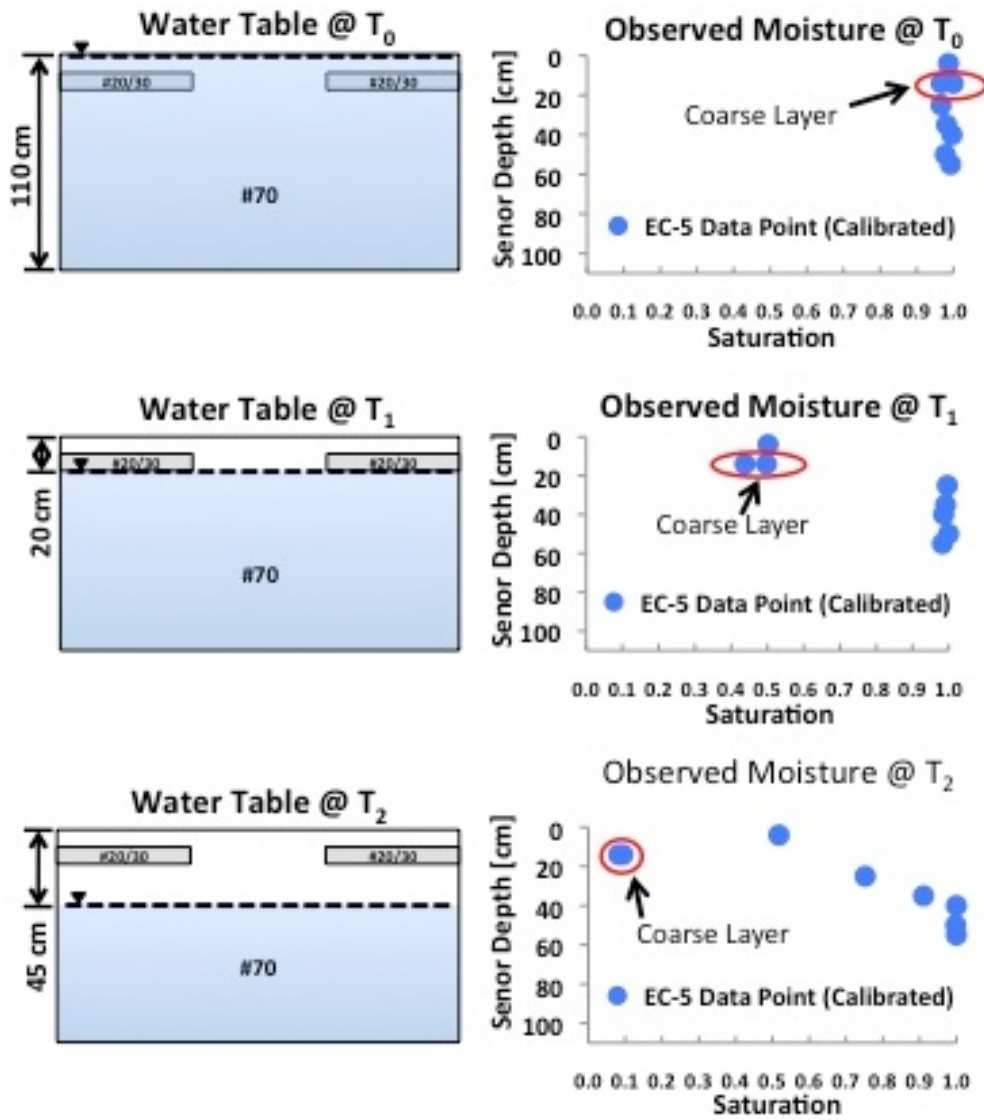


Figure 5.35: Schematic of packing configuration #2 and the calibrated volumetric moisture content data (e.g. Sakaki et al., 2011) with the water table set at the upper, mid and lower elevations (T_0 , T_1 , and T_2 , respectively).

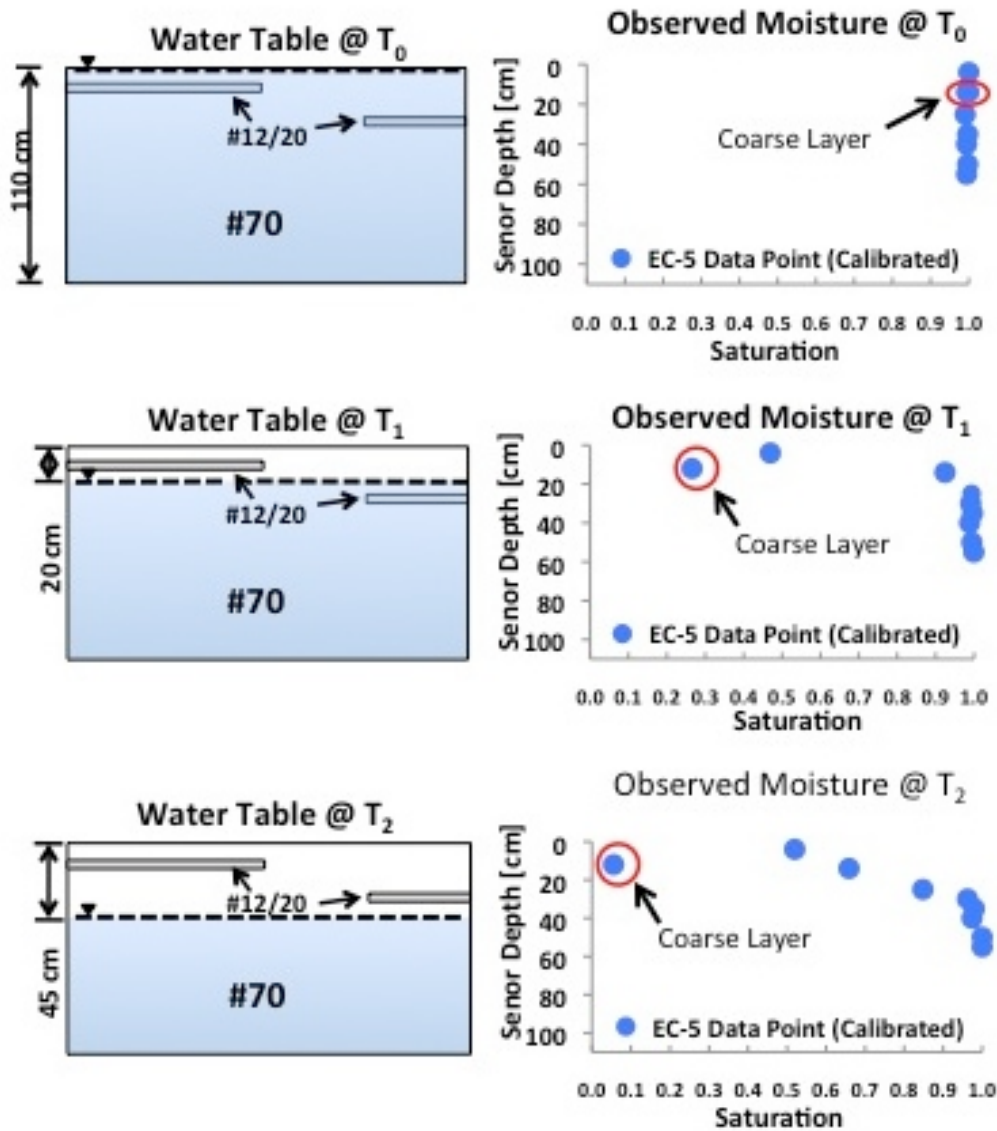


Figure 5.36: Schematic of packing configuration #3 and the calibrated volumetric moisture content data (e.g. Sakaki et al., 2011) with the water table set at the upper, mid and lower elevations (T_0 , T_1 , and T_2 , respectively).

Figures 5.37-5.39 show the simulations of soil gas diffusivity rates through the two-dimensional testing tank, using the WLR model [Moldrup et al., 2000] at three selected time steps (T_0 , T_1 , and T_2), for packing configuration #1, #2 and #3, respectively. The color gradient for all diffusivity simulations represents soil gas diffusion rates in m^3/m^3 ; the red and blue shaded regions are higher and lower diffusivity rates, respectively. The soil gas diffusivity simulations at time step T_0 are a simulation of the soil gas diffusivity with the water table at the top of the sand-pack. As no gas can pass through water-saturated soil pores, the simulated diffusivity rates for all packed sands at this time step (T_0) are zero, as indicated by the shaded blue regions in the figures. At time step T_1 the soil gas diffusivity simulations are produced with the water table set at a mid-point in the sand-pack, approximately 20 cm bgs. This time step shows the first initial stages of positive soil gas diffusivity rates developing in the testing tank. Based on an evaluation

of the diffusivity simulations, only the coarse material develops the potential for positive gas diffusivity fluxes. The shaded white regions in the model simulations support this interpretation. At time step T2 the soil gas diffusivity simulations are produced with the water table set at the lowest elevation in the sand-pack, at approximately 45-55 cm bgs. At this water table elevation, the simulated soil gas diffusivity rates reach the strongest contrast between the fine and coarse packed sands. In comparing the diffusivity simulation rates for packing configuration #1, #2 and #3 at time series T2 the results indicate that packing configuration #3 does not develop as high a gas diffusivity rate as configuration #1 and configuration #2. This is likely due to the increased area of coarse material in configuration #1 and configuration #2. The dark blue shaded region that only develops in packing configuration #1 and #2 supports this model interpretation. It should also be noted that, effective diffusion rates for site-specific contaminants of concern (COCs) should also include the influence associated with temperature fluctuations and physical partitioning of the COCs due to soil sorption and water solubility.

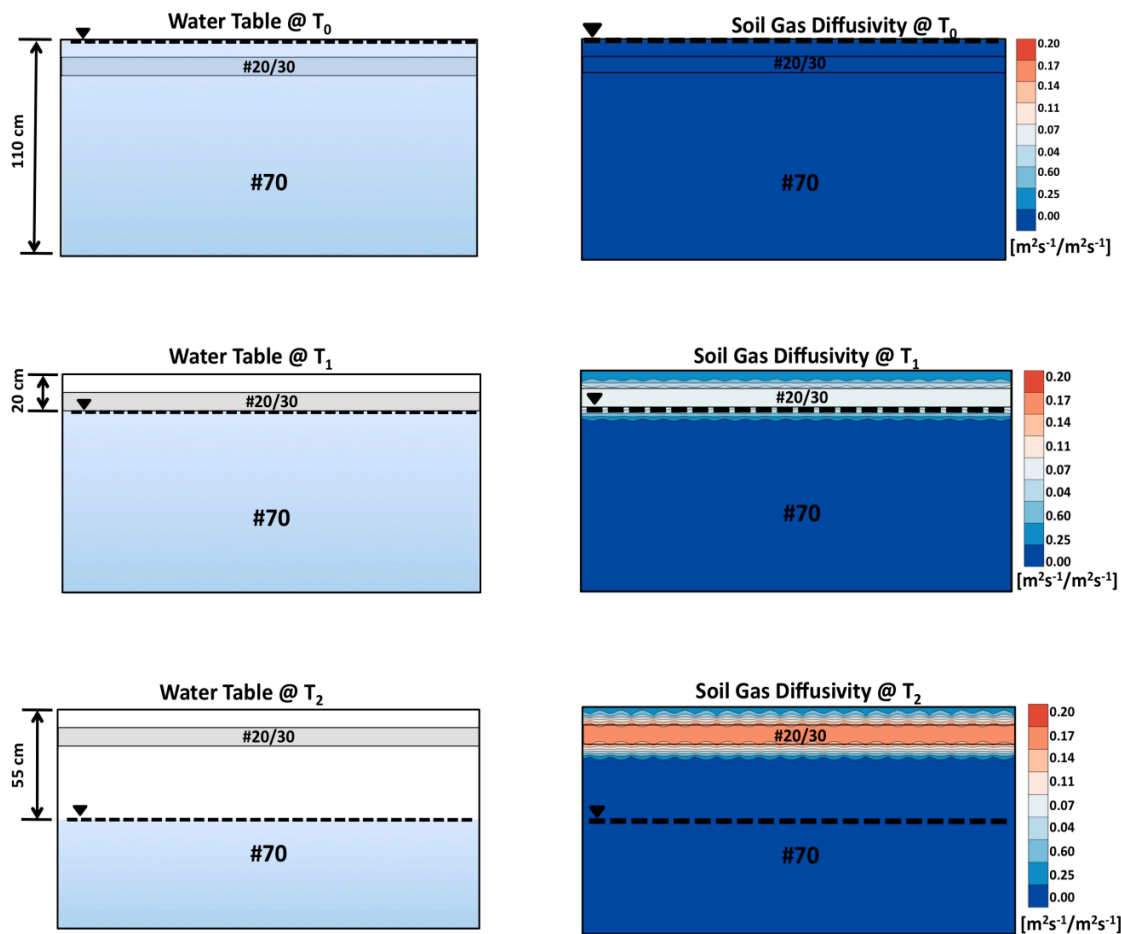


Figure 5.37: Schematic of packing configuration #1 and the soil gas diffusivity simulations (Moldrup et al., 2000) with the water table set at the upper, mid and lower elevations (T₀, T₁, and T₃, respectively).

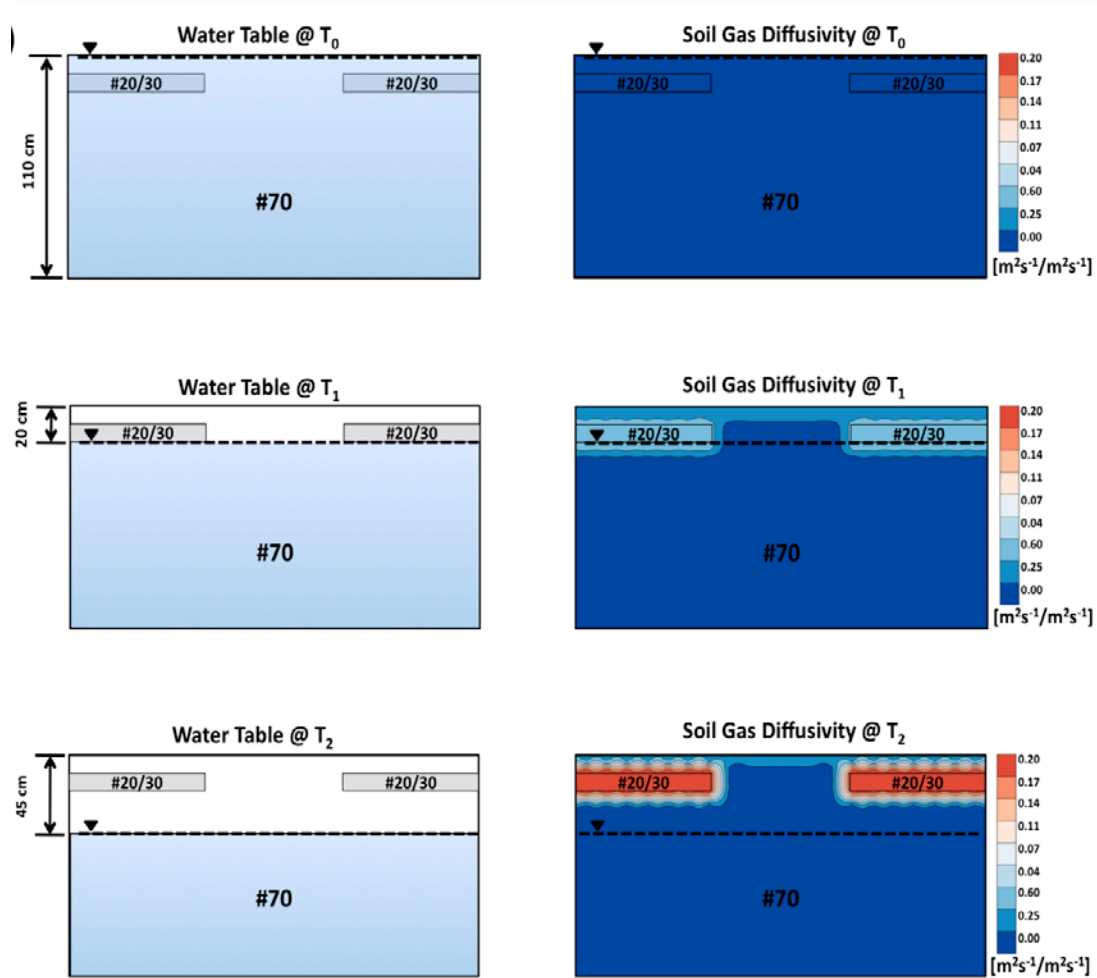


Figure 5.38: Schematic of packing configuration #2 and the soil gas diffusivity simulations (Moldrup et al., 2000) with the water table set at the upper, mid and lower elevations (T_0 , T_1 , and T_3 , respectively).

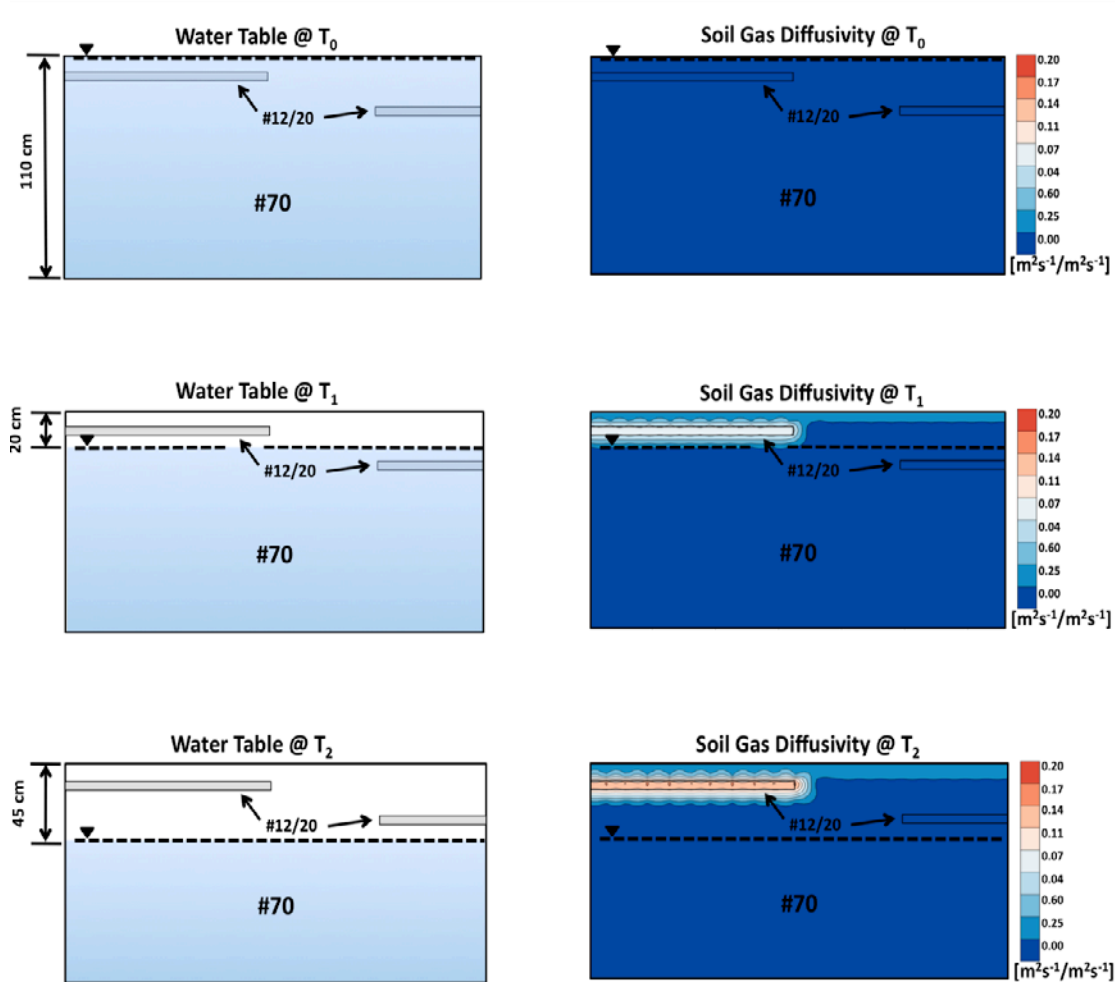


Figure 5.39: Schematic of packing configuration #3 and the soil gas diffusivity simulations (Moldrup et al., 2000) with the water table set at the upper, mid and lower elevations (T_0 , T_1 , and T_3 , respectively).

The ERT resistivity inversion model results are shown in Figures 5.40-5.42. All ERT resistivity inversion models results were produced by graduate student Brent Putman (CSM Geophysical Department, 2011-2012) using the University of British Columbia (UBC) Geophysical Inversion Facility (GIF) database model codes (Oldenburg and Li, 1994; Li and Oldenburg, 2000). The ERT surveys were performed along surface profiles using a Wenner electrode array configuration. During all stages of ERT testing, volumetric moisture content, temperature, and electrical conductivity were continuously monitored and recorded via automated data loggers. These values (volumetric moisture content, temperature, and electrical conductivity) were then used to constrain the ERT inversion models. By using these observed experimental values to constrain the ERT inversions, we were able to produce inversions that were theoretically closer representations of true subsurface conditions. The color gradients shown in Figures 5.40-5.42 represent geoelectrical observations of the sand pack material by recording the resistance (in $\text{Ohm}\cdot\text{m}$) in response to induced DC currents and performing inversions of the observed resistivity values. The blue shaded region indicates high resistance and the red shaded region

represent low resistance or high conductance (also see color gradient key to right of ERT inversion cross sections).

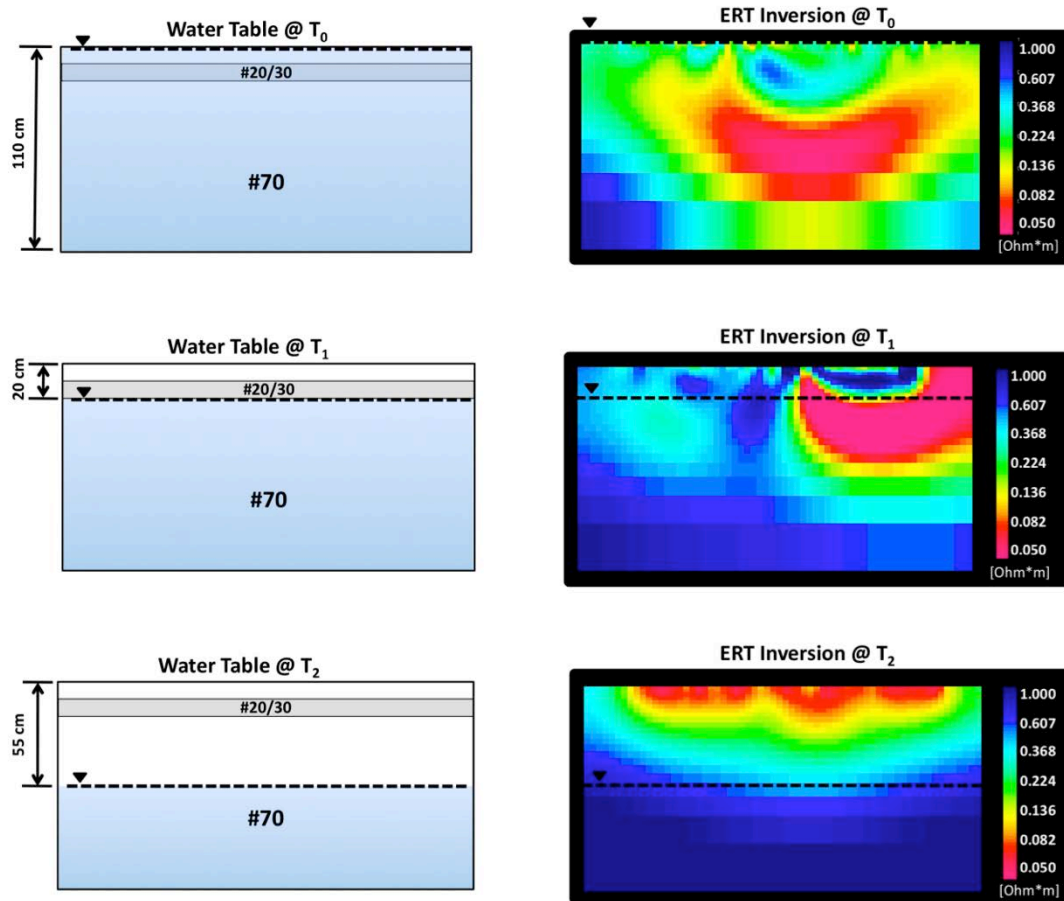


Figure 5.40: Schematic of packing configuration #1 and the ERT inversions with the water table set at the upper, mid and lower elevations (T_0 , T_1 , and T_3 , respectively). The ERT inversion color gradients represent resistivity values with ranges from 0.05 $\text{Ohm}\cdot\text{m}$ to 1.00 $\text{Ohm}\cdot\text{m}$.

In Figure 5.40, at time step T_0 , the upper region is shown with low levels of resistance, as indicated by the high amounts of shaded red area shown in the model domain. The lower resistance values are most likely associated with the higher amounts of pore space water, as water has a much higher conductance compared to the packed sands. However, this interpretation is not supported by the graphs shown in Figures 5.34-5.36 that quantifies the volumetric moisture contents present in the sand pack material layers at each time step. Therefore, given the conceptual understanding that porous materials containing higher moisture contents (i.e. the fine sands in my sand pack) should theoretically pass electrical current much easier than porous materials containing lower moisture contents (i.e. the coarse sands in my sand pack) and using the moisture content values from Figures 5.34-5.36 as a reference, the ERT inversions should reflect this contrast in moisture contents.

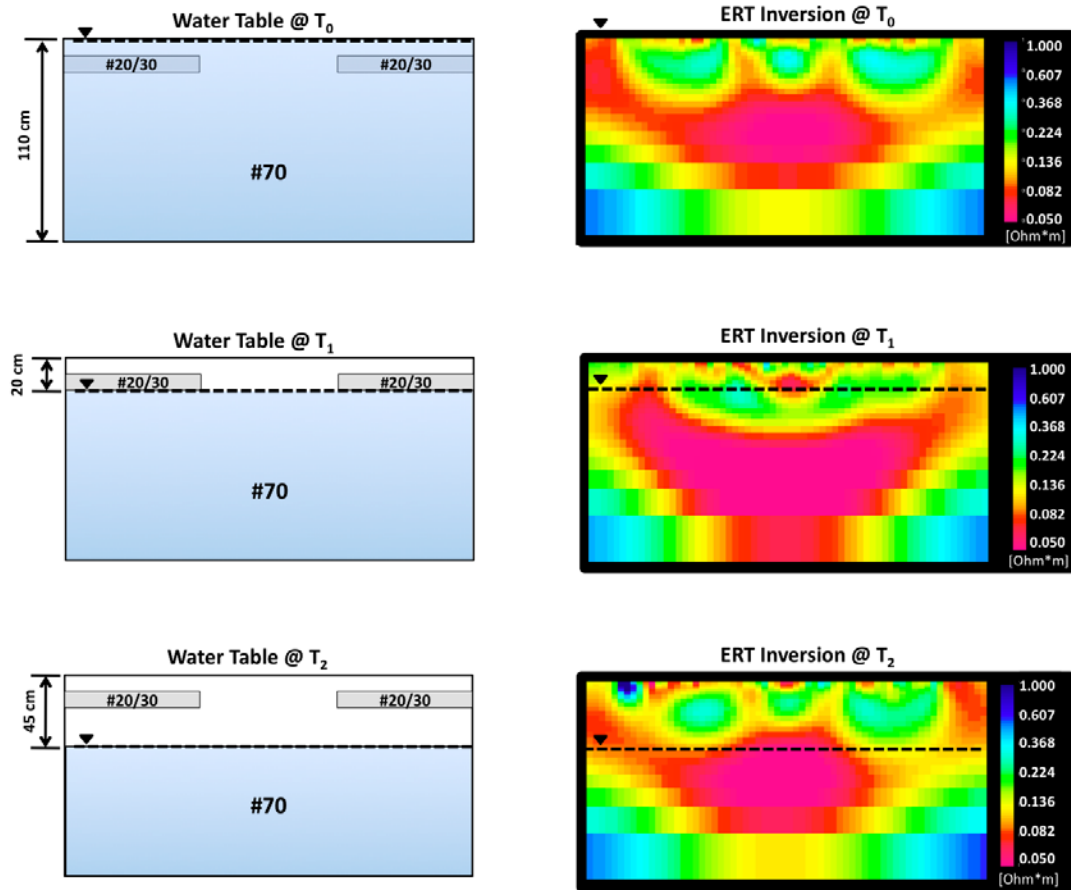


Figure 5.41: Schematic of packing configuration #2 and the ERT inversions with the water table set at the upper, mid and lower elevations (T_0 , T_1 , and T_3 , respectively). The ERT inversion color gradients represent resistivity values with ranges from 0.05 $\text{Ohm}\cdot\text{m}$ to 1.00 $\text{Ohm}\cdot\text{m}$.

After close examination of the ERT inversion cross sections, there appears to be no consistent relationship seen in the inversions that capture the relative moisture contents associated with the fine versus coarse sand pack layers. The next time step, T_1 , shown in Figures 5.40-5.42, shows the ERT inversion cross sections with the water table at a mid-point. This time step does not capture the moisture distributions, as indicated by Figure 5.35, or the fine versus coarse packed layers. The next time step, T_2 , shown in Figures 5.40-5.42 shows the ERT inversion cross-sections with the water table at the lowest elevation. This time step does not capture the moisture distributions, which are at the highest contrast levels, as indicated by Figure 5.36, or the fine versus coarse packed layers. Thus ERT failed to capture the moisture distribution within the laboratory tank. However, much more promising results were found in the field, as discussed in section 5.7. It was later found that, unknown at the time, a current leakage from tank may have occurred, which would comprise results and explain the erratic ERT behavior. Thus the apparent inability of ERT to capture soil moisture in this experiment may represent a problem with this particular experimental apparatus, instead of a failing of the ERT method.

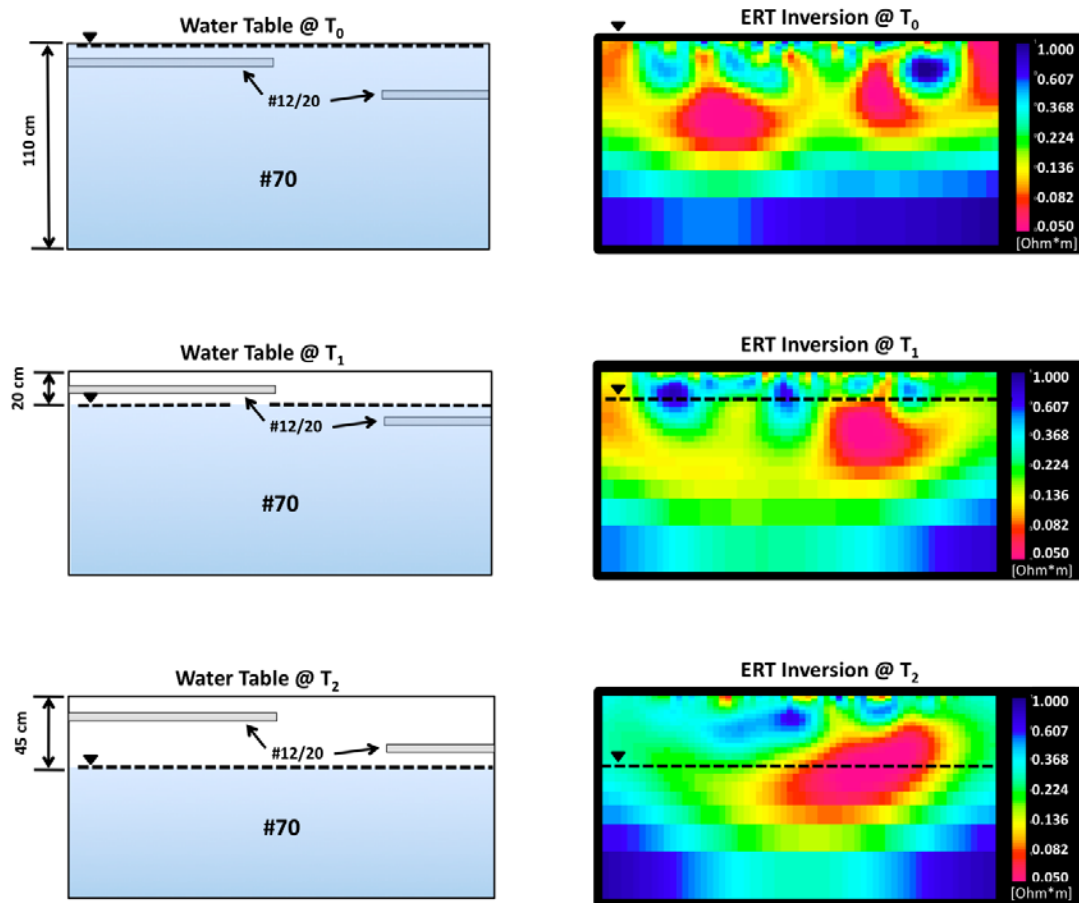


Figure 5.42: Schematic of packing configuration #3 and the ERT inversions with the water table set at the upper, mid and lower elevations (T₀, T₁, and T₃, respectively). The ERT inversion color gradients represent resistivity values with ranges from 0.05 Ohm*m to 1.00 Ohm*m.

5.7 Site demonstration of geophysical methods and observation of infiltration effect

The field demonstration served as a proof-of-concept evaluation of the practical application of ERT for vadose characterization at VI impacted field sites. The approach was based on providing a qualitative evaluation of the ERT VI characterization methodologies developed in the laboratory sand tank tests and ERT inversion model simulations. The general experimental design of our field demonstration was based on the concept of inducing a disturbance (via a simulated precipitation event) in the unsaturated zone that would create an observable change in the VI signal entering the building. By using an induced surface moisture event we were able to successfully observe the response in the system using both soft geophysical methods and hard analytical methods and use the observed values to develop a joint-interpretation of hard and soft data applied to moisture induced perturbations in an active VI signal.

5.7.1 Site Specific Historical Surface Moisture Events

Using data available from an onsite Meteorological Station (MET) station [Ongoing VI site study by Johnson et al., 2010-2012], we were able to statistically analyze all local precipitation events over the previous 16 months and determine an appropriate volume of water to release on the surface during the induced moisture event. The observed MET station data is shown in Figure 5.43a and the statistical analysis is shown in Figure 5.43b.

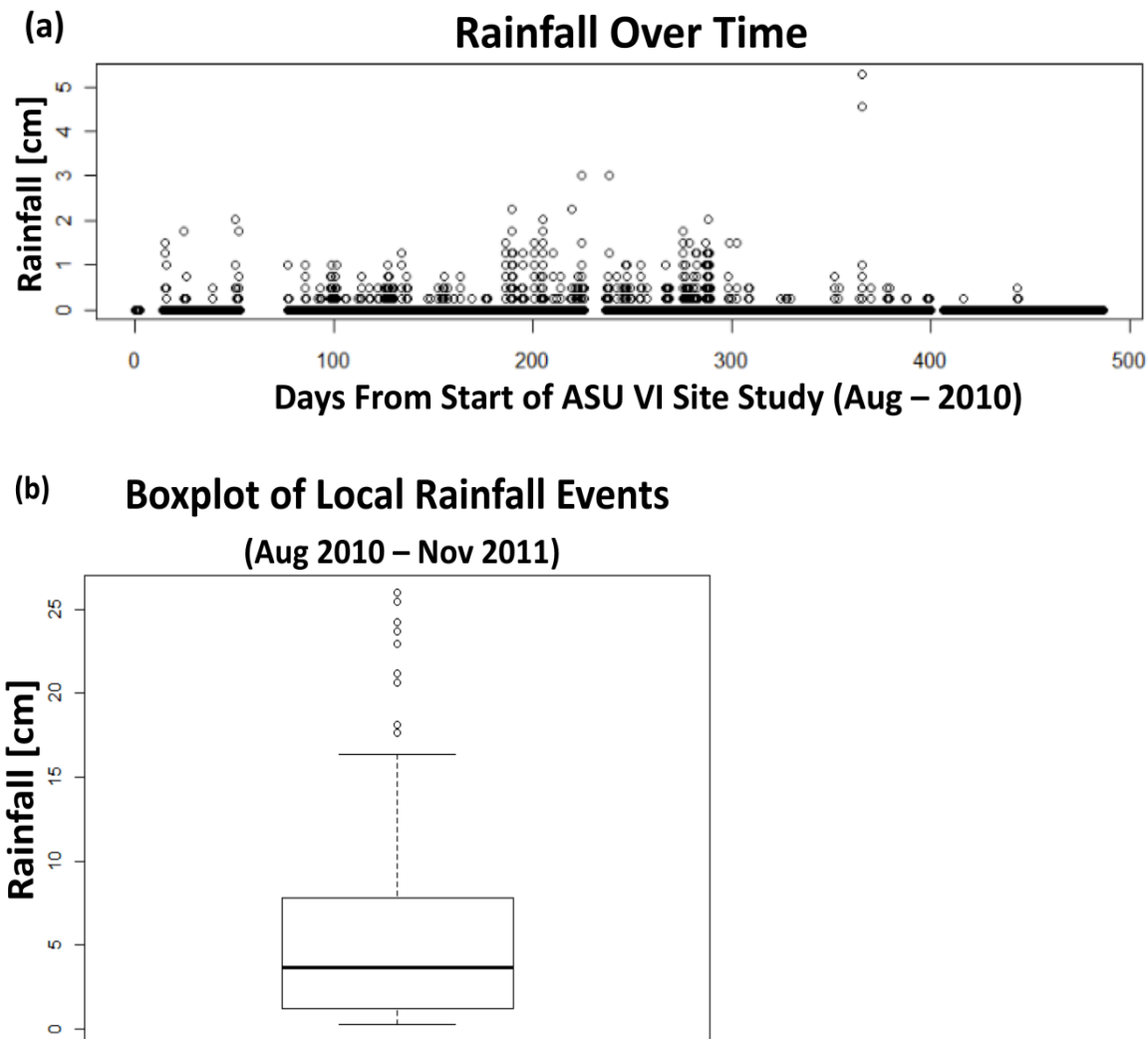


Figure 5.43: (a) MET station precipitation data from field site and (b) Statistical analysis of local precipitation events from field site.

Using statistical analysis of local precipitation events to create a Boxplot of the precipitation data collected on-site over the past 16 months, (Figure 5.43 (a) and (b)), we were able to recreate a moisture event (using the residential sprinkler system available on-site) that was volumetrically proportional to the largest 10-percentile precipitation events (approximately 1.8 - 2.5 cm). The Boxplot, seen in Figure 5.43 (b), quantifies the mean 50-percentile (indicated by the boxed region in the plot) and the upper and lower 25-percentile data points (identified by the upper and lower whisker regions in the plot). To quantify the volume of water absorbed by the ground

surface, moisture and temperature sensors were installed (at approximately 1 ft bgs) in undisturbed soils directly adjacent to ERT profiles. In addition, several rain gauges were placed along the surface profiles to record the volumes released. By combining the historical statistical analysis with observed induced precipitation data, we were able to validate the volume of water applied to the ground surface during our ERT field demonstration. Validating the volume of water applied to the ground surface was important because the results from this study could potentially be used by residential home owners to make more informed decisions about the potential for inducing VI into their homes based on when and how much water they apply during irrigation. Additionally, the result from this study may also be used for future regulatory screening standards.

5.7.2 Observed Temperature and Moisture Content Values

Figure 5.44 shows temperature and volumetric moisture changes in the unsaturated zone (at approximately 1 ft bgs) immediately before, during, and after the simulated precipitation event. The general hypothesis driving the experimental approach of our field demonstration was the prediction that, at REV-scales, wetting fronts migrate vertically downward, producing a compression effect on the VI channels, which in turn create an associated spike in VI concentrations entering the building; this compression effect was observed in recent sand tank studies by Sakaki et al. [2012]. For this field demonstration, ERT was used to capture the induced moisture event, the associated wetting front, and lateral migration of displaced and infiltrating water into interconnected channels of highest relative permeability.

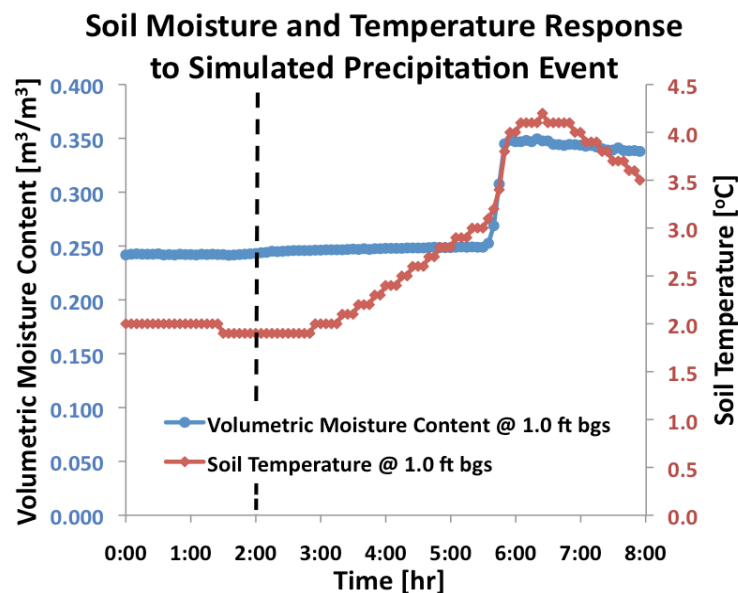


Figure 5.44: Temperature and volumetric moisture content changes in response to simulated moisture event.

5.7.3 ERT Inversions

Figure 5.45 (a-d) shows time-series snap shots of ERT inversion before, immediately after, and approximately 2 and 4 hours after the induced precipitation event. (Please note, due to an equipment operator error in which the SuperSting hard drive was inadvertently reformatted

resulted in the loss of the initial {T₀} ERT simulation data files. The initial ERT simulation {@ T₀} that is used in Figure 5.45 (a) is a profile captured along the exact same spatial profile as the inversions used in Figure 5.45 (b-d), however, it was collected during a site visit in November of 2011, approximately 5 months earlier. This is also the reason the resistivity scale is different for Figure 5.45 (a) as compared to the later time steps). The scale used in Figure 5.45 (a-d) is Ohm*m, with the blue shaded regions representing material with high electrical resistivity and the red shaded regions representing the lower electrical resistivity values. The white crosshatched region, seen along the lower sections of Figure 5.45 (a-d), represent regions of the model domain where the model predictions are no longer reliable. The depth of investigation (indicated by the colored region in the model domain) is approximately 6-7 m. bgs.

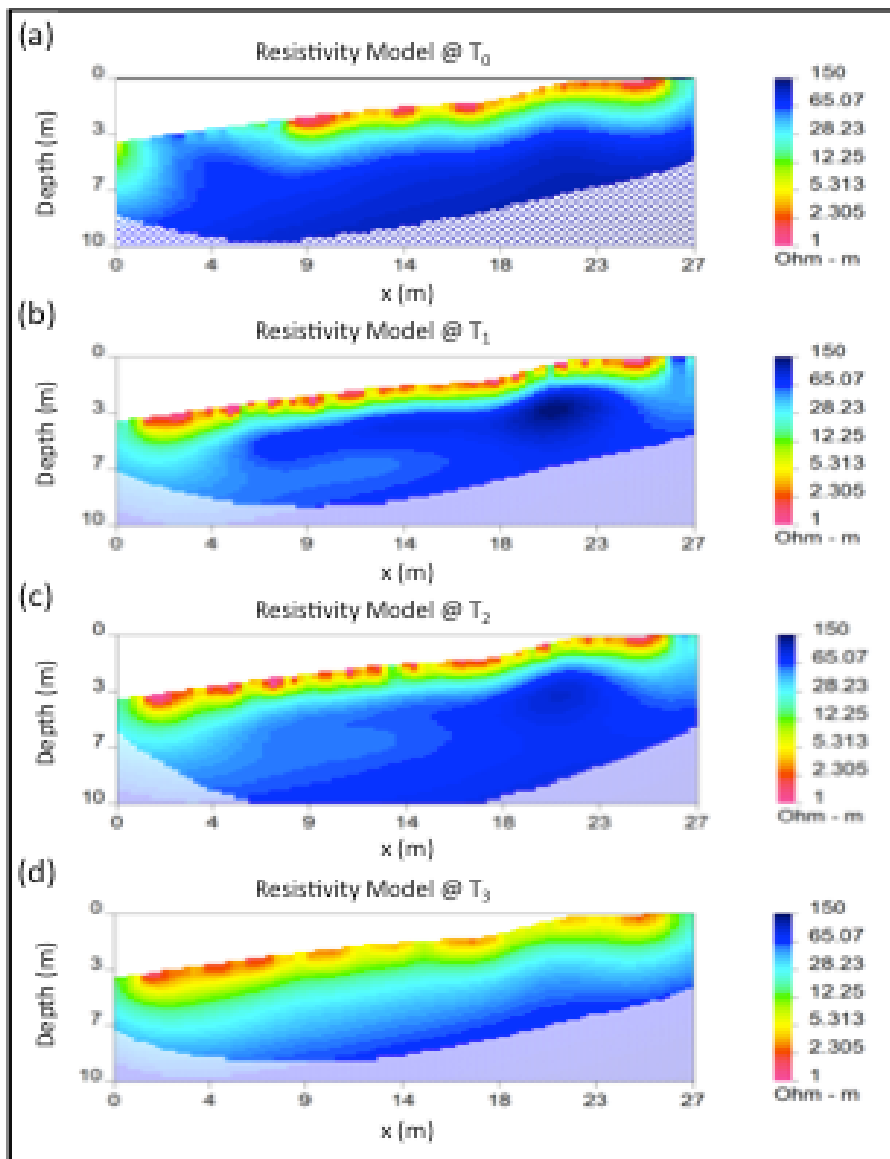


Figure 5.45: Time-series snap shots of ERT surveys capturing initial site conditions and the infiltrating wetting front induced by our simulated precipitation event.

Comparing the inversions seen in Figure 5.45 (a), at time step T0, to the inversions seen in Figure 5.45 (b-d), at time step T1, T2, and T3, respectively, we can observe the change in geoelectrical properties associated with the water introduced during the simulated precipitation event. This is seen in the inversions by a slight decrease in the concentration of the red shaded region along the ground surface, especially on the left sides of the cross section where the surface elevation is lower. At the initial time step (T0), a potential boundary layer can also be seen at approximately 2 m bgs. This interpretation is supported by the sharp contrast in geoelectrical properties (and corresponding color gradients) at approximately 2 m depth that appear to be horizontally (relative to ground surface) continuous in the inversions. At later time steps (T1 - 2hrs, T2 - 4hrs, T3 - 6 hrs), the higher resistive regions (indicated by the blue shaded region) below the potential boundary layer begin to become infiltrated with the water induced from the simulated precipitation event and the upper regions begin to drain. This interpretation is supported by closely evaluating the geoelectrical changes, indicated by the transitional steps from dark blue to light blue, seen in the regions below the boundary layer in time-series T1, T2, and T3, respectively. The inversions also show that the wetting front does not infiltrate evenly throughout the horizontal (relative to ground surface) profile captured in our ERT resistivity data. The wetting front appears to preferentially infiltrate along the left side of the inversion cross sections and indicates a lateral infiltration up gradient, as seen in Figure 5.45 (b) and (c).

By capturing time-series snap shot profiles of the vadose zone in response to the simulated moisture event using ERT, we were able to successfully distinguish the wetting front infiltrating the unsaturated zone, capture a region of lateral infiltration, and develop a joint-interpretation using both hard and soft data. The observation in the ERT simulations of lateral infiltration between T0, T1, and T2 temporally coincides with a spike in the VI signal observed in the study site building using a GC/MS. The VI signal data, collected by the ASU research group [Ongoing VI site study by Johnson et al., 2010-2012] provided the hard VI data used to spatially and temporally constrain the infiltrating water's impact on the vapor pathways. By combining these soft and hard data sets, we have demonstrated a novel joint-interpretation of ERT data with GC/MS data and have developed a more comprehensive conceptual site model of the VI pathway locations in the subsurface surrounding a VI impacted building.

5.7.4 Comparison of ERT Inversions to VI Signal Observations

Figure 5.46 shows the Hapsite GC/MS readings over a five-day window that captured our simulated precipitation event and the response in the VI signal. As shown in Figure 5.46, the VI signal over the previous four days showed no positive values from approximately 6:00AM in the morning till 12:00AM midnight. This diurnal cycle is likely a result of the pressure differentials created by nightly use of a central heating unit. The use of a central heating unit results in decreased interior pressures due to a chimney effect developing inside the building as the heat rises and exits through the roof. After performing the simulated precipitation event, we observed a mid-day spike in TCE, at approximately 0.044 ppb_v, from a portable on-site gas chromatograph and mass spectrometer (Hapsite GC/MS ER, Inficon, Syracuse, New York).

By observing this VI signal in response to our simulated precipitation event, we were able to develop a novel joint-interpretation using the soft geophysical data, produced by ERT resistivity inversions, and the hard analytic data, produced from the onsite GC/MS unit. Combining these

hard and soft data sets suggested that the water infiltrated coarse VI channels, which forced the VI signal to spike as the air was displaced by infiltrating water.

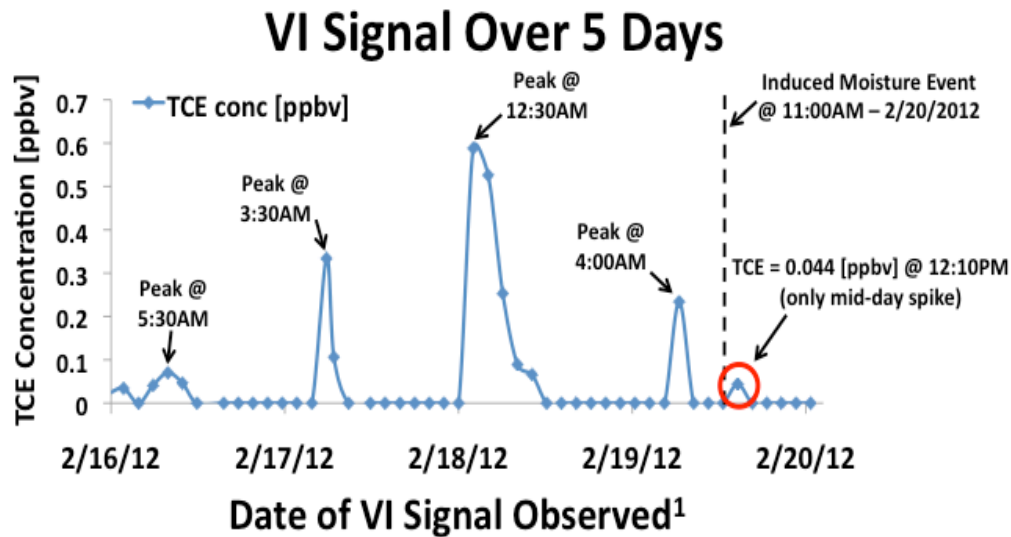


Figure 5.46: Graph of the VI signal (TCE in ppbv) entering study site building over a five-day window that included our field demonstration and simulated precipitation event. [Ongoing VI site study by Johnson et al., 2010-2012].

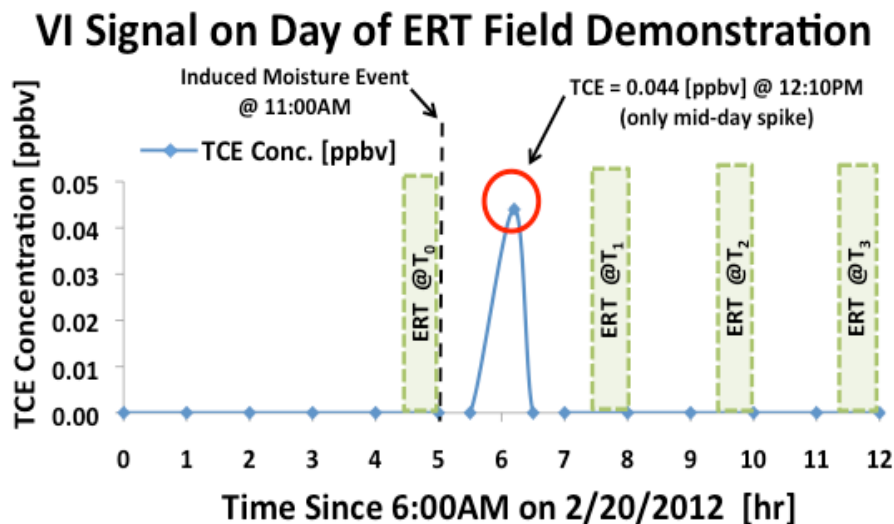


Figure 5.47: Graph of the VI signal (TCE in ppbv) entering study site building over 1-day window during our ERT field demonstration with ERT time-series snapshots overlaid on the VI signal timeline [Ongoing VI site study by Johnson et al., 2010-2012].

Figure 5.47 shows a conceptual diagram of the joint-interpretation method applied temporally by overlapping the soft and hard observational methods. This figure helps visually conceptualize the joint-interpretation method used and how the data sets relate temporally. Performing a joint-interpretation of hard and soft observational methods allowed us to constrain the spatial regions in the vadose zone surrounding the house where preferential VI channels likely exist. For our

specific field demonstration site, the joint-interpretation indicates that the front yard in the southeast corner of the residential lot most likely contains preferential VI pathways.

5.8 Practical implications of transient vapor dynamics through simulation of hypothetical scenarios:

As was stated earlier, the scope of the modeling effort does not include calibrating the developed model and use as a prediction tools. Such an exercise that needed field data that is not readily available to cover all possible geologic and climate conditions of VI sites. It was demonstrated that the model developed based on an improved conceptual understanding was able to capture some of the important to of the processes and their interactions. Hence, instead of conducting case studies that covers different expected site conditions, the model was used to conduct a limited set of hypothetical scenario simulations with the goal of demonstrating the practical implications of the research findings that will lead to guideline development and better monitoring of VI sites.

Many numerical modeling studies simulating hypothetical vapor intrusion scenarios have already been presented in the literature (see table 2.2 for review of other scenario studies). However, our model generally differs from these previous studies based on a few major characteristics. These are outlined in Table 5.6 versus the typical assumptions made in other VI models.

Table 5.6: Characteristics differentiating this study's model from previous scenario simulations

Characteristic	Our model	Typical assumption
Simulation type	Transient	Steady-state
Vapor source	Mass transport across capillary fringe from flowing groundwater plume loading the vapor plume in the unsaturated zone	Assumed constant source concentration at water table
Fluid flow formulation	Fully coupled multiphase flow	Single phase flow
Phenomena evaluated	Effects of rainfall, water table fluctuation	Effects of soil properties, heterogeneity

As reported in literature, only Yu et al., (2009) and Wang et al. (2012) present models that are similar to this study in that they include a groundwater plume source with capillary fringe volatilization, a transient simulation and fully coupled multiphase flow. However, their models contain a significant error in that they treat the land surface boundary as being impervious to diffusive exchange of VOCs from the soil to the atmosphere, yet allow advective vapor exchange across the same boundary. This is physically unrealistic because any atmospheric surface that is open to advective exchange (e.g. not paved) will be open to diffusion as well. The result in their model is that concentrations build up in the vadose in an unrealistic manner. Most other models of vapor intrusion (e.g. Hers eta al., 2000; Abreu and Johnson, 2005; Bozkurt et al., 2009) simulate the atmospheric boundary with the concentration set to zero, which inherently allows for both diffusive and advective exchange. This is also the approach used in this study. Thus, to-date, these scenarios are to our knowledge the first simulations that consider the full coupling of all of these processes for field scale scenario simulation.

Hypothetical scenario simulations are useful because the complexity of interactions between flow and transport explored during this study do not allow easy extrapolation of laboratory observations to field case studies. The scenarios simulated here are not intended to present a comprehensive exploration of the many field scale conditions that could be encountered, but rather present some basic understanding of how these interactions might affect a VI in real systems. *The scenarios focused on water table fluctuation and rainfall infiltration, evaluating the transient response to vapor intrusion that may be anticipated within a building during such events.* A homogeneous domain was used to create a simplified scenario that allows for a more straightforward physical explanation of the observed vapor responses. It is hoped that future work beyond this project may allow for a more thorough sensitivity analysis of the scenario model than is presented here to fully elucidate the sensitive parameters and range of interactions that may occur in field systems.

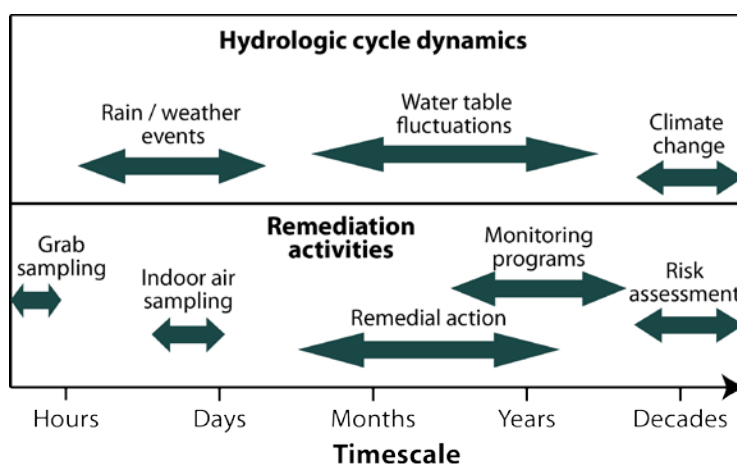


Figure 5.48: Timescales of typical hydrologic cycle dynamic events and remediation activities.

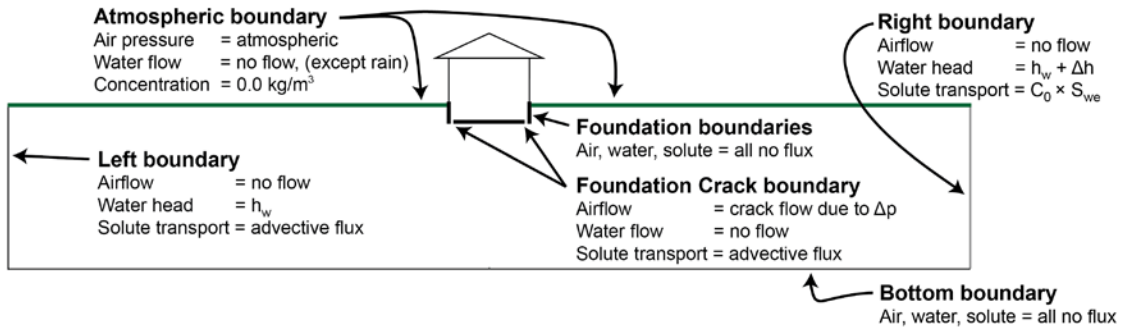
When evaluating the vapor intrusion response to transient hydrologic cycle dynamics, it is useful to consider the timescales involved with typical remediation activities at a field site, illustrated in figure 5.48. For example, some radiation activities, such as grab sampling or indoor air sampling occur over relatively short timescales of hours to days. Meanwhile, remedial action may occur on a medium timescale of months to years, while monitoring programs and risk forecasting may occur over long timescales of years to decades. Since weather events overlap the timescale of short term activities such as sampling, a short-term temporal response of vapor intrusion due to weather may bias sampling results, while the longer timescale processes and activities may be unaffected. However, if sampling data gathered in the short term are used to extrapolate risk or assess remediation effectiveness over a long timescale, then biases from short timescale disturbances may propagate forward into the long-term risk assessment. Meanwhile, medium and long timescale factors such as water table fluctuation or climate change may not cause interferences with short timescale remediation activities such as sampling. However, they may be more difficult to detect from short timescale data, and might have significant implications for the longer-term remedial action, monitoring and risk assessment. Thus it is important to understand what types of temporal vapor responses may occur from hydrologic cycle dynamics (e.g. rain fall, recharge, water table fluctuations), and their implications for vapor intrusion at all timescales. Overall, it may be that the significance of temporal variability in vapor intrusion signals in buildings does not lie in the significance of any single spike in vapor intrusion anywhere over a multi-decadal risk assessment period, but rather in understanding the

overlapping temporal responses to various weather and climate factors that may be occurring simultaneously, in order to make the best decisions about the observed VI pathway in the field.

5.8.1 Scenario Characteristics and Steady State Simulation

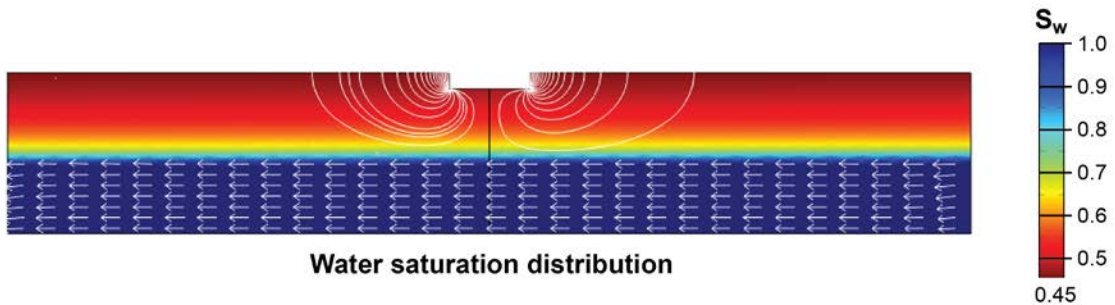
Even though many scenarios that vary subsurface and climate factors are possible, the primary objective of the scenarios selected for evaluation was to probe the vapor intrusion responses to rainfall events and water table fluctuations that were found to be important in controlling the transient vapor signals. This has significant consequences for model simulations because not only must the vadose zone and capillary fringe be simulated, but the model also needs to simulate an entire groundwater plume to provide a vapor source. Thus there is a need to apply appropriate boundary conditions to create a realistic groundwater plume. A model domain was created using the dimensions of a house consistent with previous studies such as Abreu and Johnson (2005) and Bozkurt et al., (2009). The domain and boundary conditions are shown in figure 5.49a.

While the groundwater flow field is established by setting head boundaries at the right (inflowing) and left (outflowing) sides of the problem domain, an arbitrary source concentration distribution must be imparted to create a plume. To focus the scenarios on the rainfall and water table fluctuation cases on vapor generation, it was desired to simulate as uniform a groundwater plume concentration along the plume length to remove some of complexities that are not relevant in the scenarios that are selected. Thus a concentration of 1 mg/L of TCE that is low enough to avoid vapor density effects, but high enough to be of concern in a field setting was assumed for the baseline plume concentration. However, if a constant source concentration is assumed across the entire inflowing boundary, this results in an unrealistic “mounding” of vapor concentrations at this boundary, with strong horizontal concentration gradients that are uncharacteristic of typical vadose zone environments; vadose zone vapor concentration gradients are generally directed in the vertical direction due to upward diffusion to the atmosphere. A boundary condition where the incoming groundwater concentrations were scaled by the effective water saturation on the boundary was found to give the best result that reduced this horizontal gradient, through it was not eliminated entirely. Because of these boundary affects, a larger domain had to be simulated than the one used in the Abrue and Johnson (2005) and Bozkurt et al. (2009) models in order to place the zone influenced by the boundary away from the simulated house. It was found that simulating scenarios on a 2-D domain (180m long x 20m deep) was effective in reducing the boundary effects. A deeper model domain (20 m) versus the ones use in the other studies (typically 10 m) was also used to allow testing of multiple water table elevations within the same domain, and give room for water table fluctuations. Another effect of including the capillary fringe and flowing groundwater plume within the simulation is the plume slowly dissipates as it travels across the domain (see figure 5.49c). This is caused by diffusion and dispersion transferring and depleting the VOC mass from the capillary fringe as it traverses the domain. Thus, despite the apparent symmetry of the model domain, the problem itself is not symmetric due to attenuation of the plume with distance. At the outflow (left) boundary, advective flux of TCE was allowed to exit.

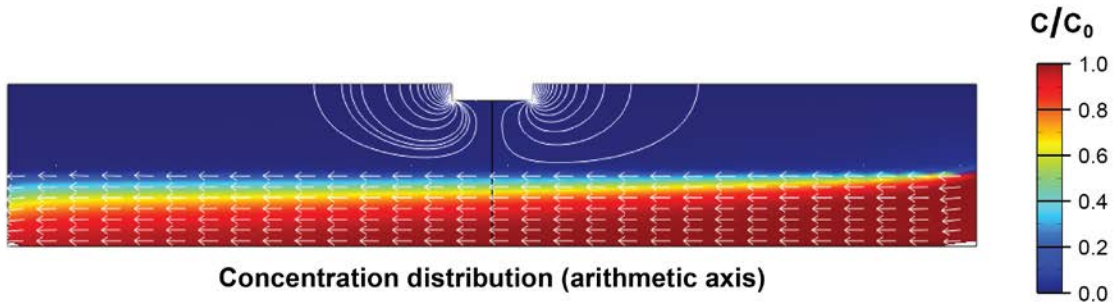


Boundary conditions

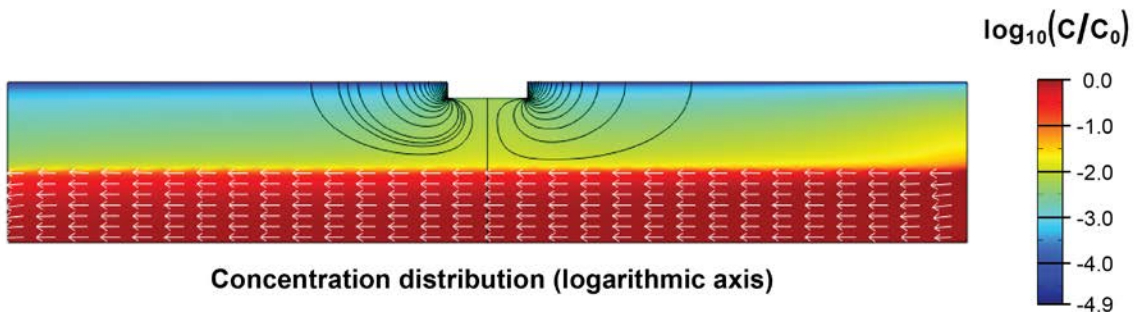
a)



b)



c)



d)

Figure 5.49: Steady-state initial condition for scenarios. a) boundary conditions, b) water saturation distribution, c) and d) concentration distributions with arithmetic and logarithmic axis, respectively. White arrows indicate groundwater flow vectors, and streamlines indicate airflow pattern into the house.

At the land surface, atmospheric pressure was assumed the gas flow equation, no flow for the water flow equation (except when rain was applied), and was set to zero TCE concentration, which is consistent with other studies (Abreu and Johnson, 2005; Bozkurt et al., 2009). For airflow through the foundation crack, the formulation presented by Abreu and Johnson (2005) was used as given in equation (8).

$$Q_{ck} = \frac{-w_{ck}^3}{12\mu_g d_{ck}} (p - p_{indoor}) \quad (8)$$

where, Q_{ck} is the volumetric flow of air through the crack per unit length of crack [$m^3/m\cdot s$], w_{ck} is the width of the crack [m], d_{ck} is the thickness of the floor slab, and p_{indoor} is the indoor air pressure. A indoor-outdoor pressure differential of 5 Pa (vacuum) was assumed. The water flow equation was set to no flux for the crack, and the solute transport equation allowed advective flux. The foundation crack is assumed to be a perimeter crack located at the corners of the foundation. All other foundation boundaries, as well as the model domain bottom boundary were set to no flux for all equations.

The scenarios were simulated using two different soil textural classes for porous media characteristics, which include a sandy soil and a silty clay loam. The permeabilities and retention function characteristics for each soil texture were derived from the average values for each texture derived from the Rosetta (v1.2) database provided by Schaap (2000), and are given in Table 5.7. The initial height of the water table in most of the scenarios was set to 10 m, though this was tested as a sensitivity parameter for some scenarios.

Table 5.7: Soil properties of media used in scenario simulations

Media	K_{sat} (cm/day)	ϕ	S_{rw}	α (1/cm)	n
Sand	643	0.375	0.141	0.0352	3.177
Sandy Clay Loam	13.2	0.384	0.164	0.0211	1.330

Results for the base case with silty clay loam soil are shown in figures 5.49b – 5.49d. In figure 5.49b, the water saturation distribution is shown along the air and water flow fields. The saturation distribution shows the saturated zone and water table as the blue area in the bottom of the domain. The white streamlines show the airflow converging into the perimeter crack in a roughly symmetrical pattern on both sides of the building. White vector arrows show the groundwater flow directions and their magnitudes, which are very uniform and horizontal within the saturated zone. Concentration plots are presented with an arithmetic axis in figure 5.49c, and a logarithmic axis in figure 5.49d. Both plots were included because the arithmetic axis presents the aqueous plume better than the logarithmic plot, while the logarithmic plot displays the vapor plume concentrations better. As can be seen in 5.49c, significant widening of the aqueous diffusion boundary layer occurs as the plume travels across the domain. In the logarithmic plot (figure 5.49d), elevated vapor concentrations are encountered underneath the building due to the combination of the foundation serving as a diffusion barrier, as well as the low rate of advection from the building-pulling vapor up from the capillary fringe. Also seen in this plot is the boundary effect (concentration mounding) on the right (inflowing) side, which necessitates a larger domain to prevent this from influencing the house. Similar baseline conditions were

derived also for the sandy soil as well. These base cases comprise the starting point for the rainfall and water table fluctuation scenarios.

5.8.2 Rainfall Scenarios

A series of rain scenarios were simulated in the COMSOL model. The primary rainfall scenario applied rainfall infiltration at varied intensities for a duration of 3 hours. A plot showing the influence of infiltration rate on the concentration of soil gas entering the building for the first 24 hours of the rainfall event is presented in figure 5.50. As can be seen, there is little effect from rainfall on the concentrations in these scenarios, showing only an almost undetectable, momentary decrease in concentrations. This suggests that little effect may be anticipated to subsurface soil gas concentrations during or immediately after a rainfall event of moderate duration and intensity. This lack of an effect is largely because the infiltration front propagation through the sandy clay loam media is slow, such that it only infiltrates about 0.2 m into the soil during the 24-hour simulation period. Since the water table is at 10 m, and the building foundation is at a depth of 2 m, this relatively short penetration of the infiltration front does not cause an appreciable effect to concentrations at much greater depth on this timescale.

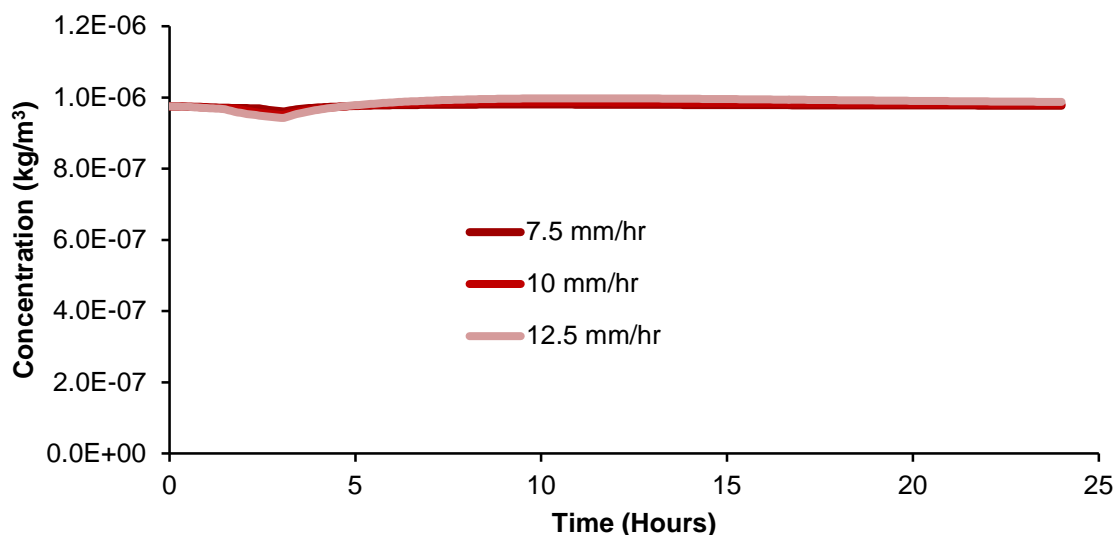


Figure 5.50: Effect of rainfall intensity on TCE concentrations of soil gas entering the building for the silty clay loam soil.

However, it is important to note that vapor intrusion pathway dynamics are not a function of soil gas concentrations alone. Figure 5.51 shows the effect of the infiltration rate on the airflow rate through the crack for the same rainfall events used. As can be seen, the crack airflow rate spikes during the 3-hour rainfall event, with the magnitude of the spike directly proportional to the infiltration rate. This increase is considerable, with the airflow rate increasing by nearly a factor of 10 for the highest infiltration rate tested. Since the vapor loading to a building by soil gas advection is the product of the crack airflow rate and soil gas concentration, this shows that while the concentration of the soil gas may be quite constant or small, the vapor mass loading may still increase causing elevated indoor air concentrations in response to rain. The driving force for this increase in airflow is the downward displacement of soil gas by the infiltration front.

Since the building indoor-outdoor air pressure differential is held constant, the increase in air pressure from the infiltration front causes a corresponding increase in the crack flow rate. After infiltration stops, this flow rate rapidly receded to its initial value, indicating this effect is limited primarily to the period during which rain is falling.

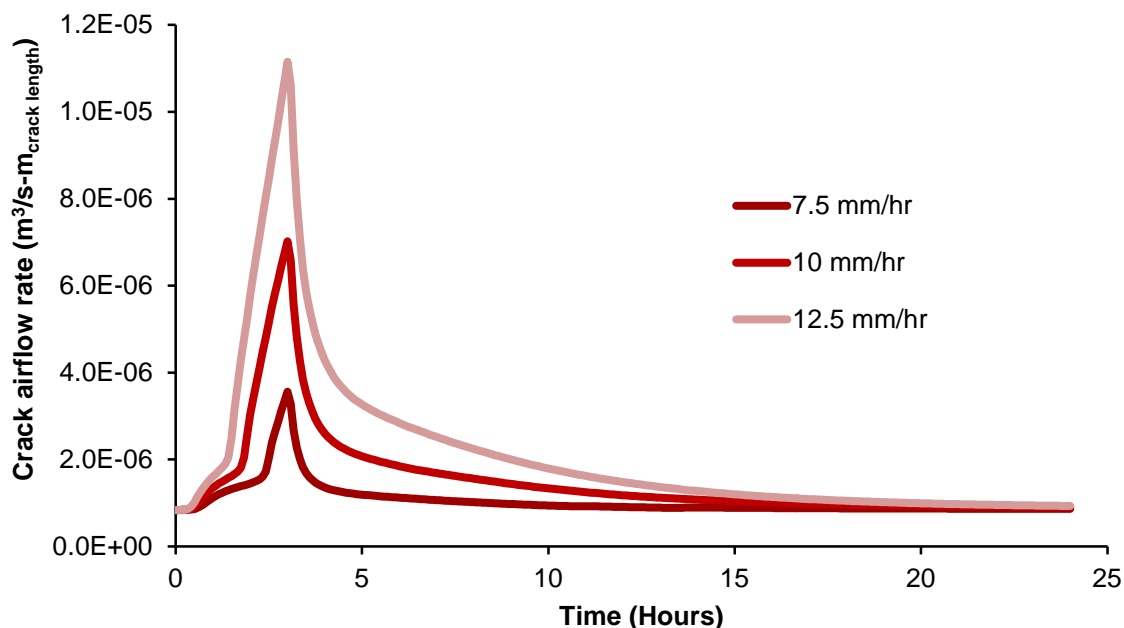


Figure 5.51: Scenarios showing effect of precipitation rate on airflow rate into building. Simulation was for sandy clay loam soil with a water table at 10m depth, and 5 Pa indoor-outdoor pressure differential.

Since the concentration was not strongly affected in the first 24 hours of the rainfall, and the airflow rate approached the initial value after about 24 hours of the rainfall event, it would seem likely that the rain scenario would return to steady-state conditions relatively quickly. However, additional analysis indicated that the model continued to predict transient behavior well after the first 24 hours of the rainfall event. This is demonstrated in figure 5.51, where a rainfall event of 24 hours duration at 1 mm/hr intensity was simulated, corresponding to a minor rainfall event. The figure shows the crack airflow rate, soil gas concentration and TCE vapor flux (product of concentration and airflow) versus time, with time displayed on a logarithmic axis. Here, as in figure 5.51 above, the concentration in the subslab soil gas is relatively static while vapor spikes due to the vapor displacement. However, also noteworthy is that the concentrations begin to slowly increase long after the infiltration event, reaching a peak concentration about 1 year later. This is significant because it indicates that there may be multiple effects from rainfall at multiple timescales. The much later and slower concentration increase is primarily due to the slow downward migration of water from the dissipated infiltration front. This has the effect of increasing saturations around the house, which reduces upward diffusion to the atmosphere, causing vapor concentrations to increase under the house. Tillman and Weaver (2007) observed a similar effect in that that a “rain shadow” formed underneath buildings while the soil outside the building foot print remained wetter. They postulated that this might form a preferential pathway for vapor contaminants, but they did not have a fully coupled model to simulate VOC concentrations.

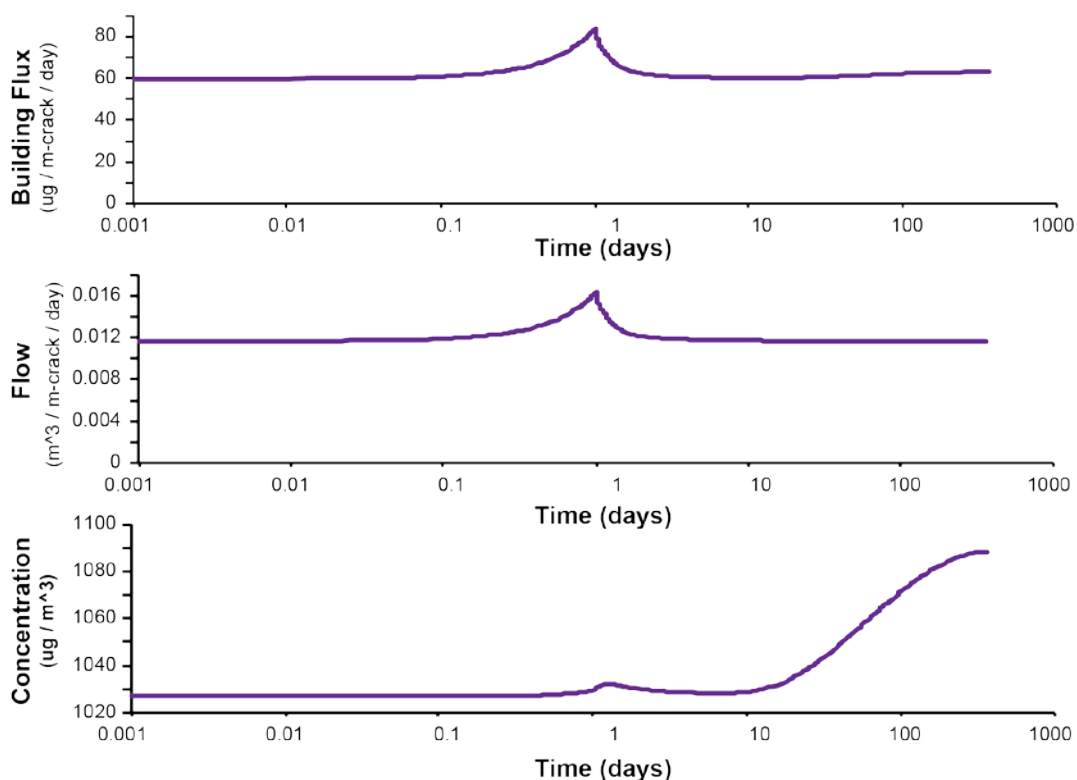


Figure 5.52: Effect of infiltration at 1 mm/hr for 24 hours on vapor signals in sandy clay loam scenario.

While the overall magnitude of subslab concentration changes, crack airflow rate and TCE vapor flux are relatively minor in figure 5.52, it should be noted that this rainfall intensity and duration was small. Larger storm events may have stronger effects, such as those shown in figure 5.51 above. Furthermore, it is unrealistic that only one storm event would occur per year in most climates. Thus a more realistic scenario would consider multiple rain events, and more rainfall scenarios need to be simulated before the full range of effects can be understood. One limitation of the COMSOL model was that the rainfall scenarios were cumbersome to simulate. Each simulation generally required multiple rounds of mesh, solver and time stepping optimization in order to get a valid solution. This is due in part to the challenge of modeling infiltration at this scale, because finer vertical discretization is necessary along the atmospheric boundary at the land surface due to the sharp gradient in water saturation at this interface. Using the meshing algorithms available in COMSOL, fine vertical discretization of the large model domain results in a very large mesh that takes the solver long time to solve, as well as requiring fine time steps. Furthermore, the COMSOL model is not presently programmed to solve a ponded boundary condition as may occur with heavy rainfall. Thus simulations were limited to events whose intensity and duration are below the ponding threshold for the soil. However, the scenarios above are informative because they do provide an insight how rainfall may affect VI. It is hoped that the future work with a more efficient production code, such as that outlined in Appendix A will allow a much thorough analysis of rainfall scenarios in the future.

5.8.3 Water table reduction scenarios

A series of scenarios simulating the effect of a falling water table were also analyzed with same COMSOL model. As with the rainfall scenarios, these falling water table scenarios started with an initially steady-state simulation. At the beginning of the scenario, the water table begins to drop at a slow steady rate, which is accomplished by slowly reducing the water pressure at the side boundaries at a steady rate. These scenarios were relatively easier to solve in comparison to the infiltration scenarios in part because the gradients in saturation and capillary pressure are more gradual, making meshing and time stepping easier. As a result, a larger number of water table reduction scenarios were simulated. The simulation period was for 290 days. Data from these simulations is summarized in Table 5.8, while typical trends in the simulations are presented in figures 5.53. Figure 5.53 shows that vapor concentrations in the soil gas rise during a water table reduction, and the rate and amount of increase is proportional to the rate at which the water table is falling. Concentrations rise continuously as long as the water table is falls, but the rate of increase declines with time. This is partly because the distance the TCE vapor must diffuse is increasing as the water table drops.

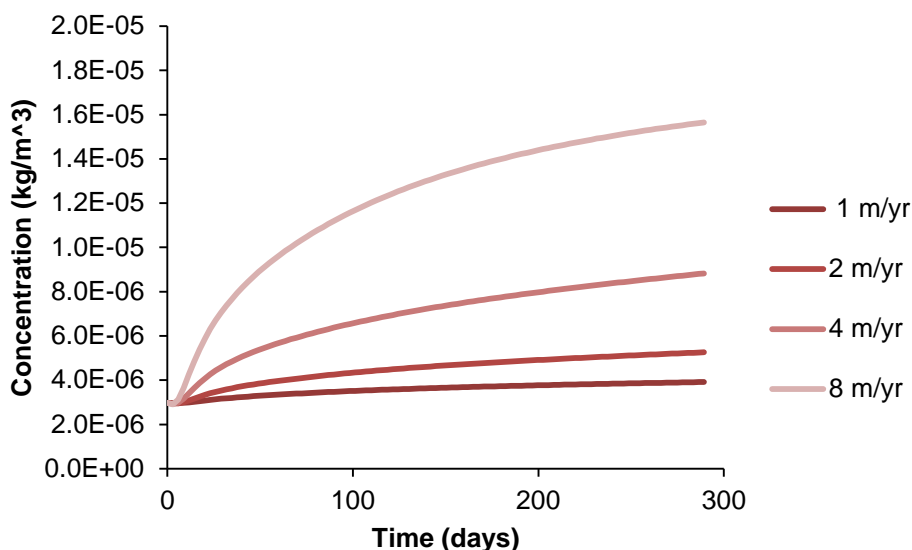


Figure 5.53: Effect of water table drop rate on subslab vapor concentrations (initial water table depth at 3 m, sandy soil media).

Figure 5.54 shows the effect of the water table depth on the concentration trends. As is to be expected, larger changes in concentration are observed for shallower water tables, in part because shallower systems place the contaminated groundwater in closer proximity to the house. However, a counter-intuitive phenomena is also observed in that the model predicted higher subslab soil gas concentrations for the deeper water tables; this is opposite to what would be expected from the Johnson and Ettinger (1991) model. However, this is due to the simulation of a flowing groundwater plume coupled with the vadose zone, in contrast to most screening type VI models, which simulate only the vadose zone and impart an arbitrary concentration at the water table. As the groundwater flows across the domain (velocity 1 cm/day for sand), TCE volatilizes into the vadose zone and exits the atmospheric boundary. This causes the concentration gradient at the capillary fringe, which is initially very steep at the right side of the domain, to slowly decrease as water flows across the domain. Since this concentration gradient is

the driving force for diffusive mass-transfer through the capillary fringe, the flux of TCE from the capillary fringe declines as the water flows across the domain (see figure 5.49c). When comparing the shallow and deep groundwater systems to each other, more TCE volatilizes upstream of the house in the shallow groundwater scenario because the atmospheric boundary is closer to the capillary fringe, and promotes more rapid mass transfer. Thus vapor flux is lower by the time it reaches the house 90m into the domain than it is when the water table is deeper. This is why there is an apparently lower concentration in the shallow subslab soil gas, despite the water table being closer to the building foundation. This illustrates yet another complexity of the VI pathway, since the physical characteristics of the coupled groundwater-vadose-zone system may interact differently than one may expect an idealized decoupled vadose zone to behave.

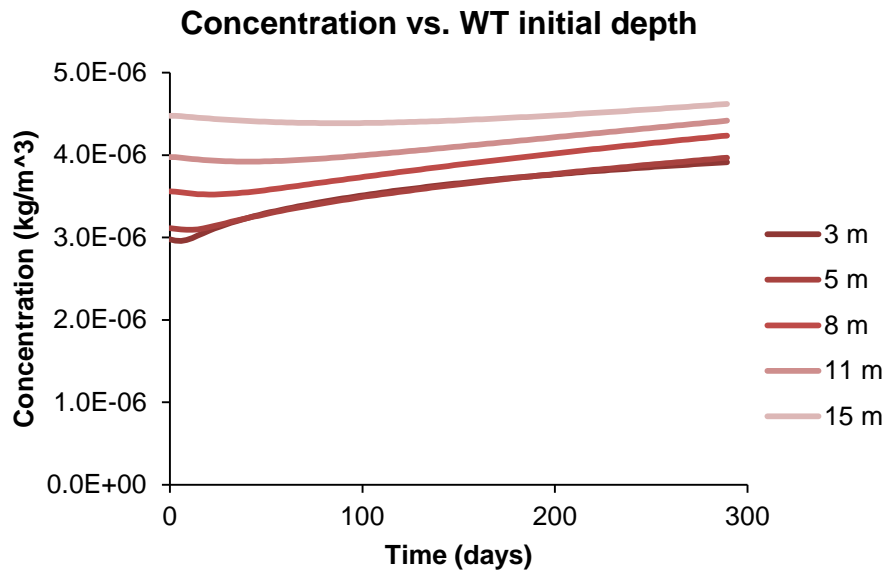


Figure 5.54: Effect of water table depth on subslab vapor concentrations from a water table dropping at a rate of 1 m/year in sandy soil.

The water table reduction scenarios also showed some potential to affect the crack airflow rate, though generally these effects were minor. This is shown in figure 5.55. The main effect was for shallow water table systems, and as the depth to groundwater increased, the airflow rate converged on a single value. This is because when the water table is close to the foundation, the capillary fringe extends high enough to reduce relative permeability for the gas phase causing a lower crack flux rate. As the water table drops lower, this effect diminishes and the crack airflow rate becomes solely a function of building geometry, soil permeability and the crack properties.

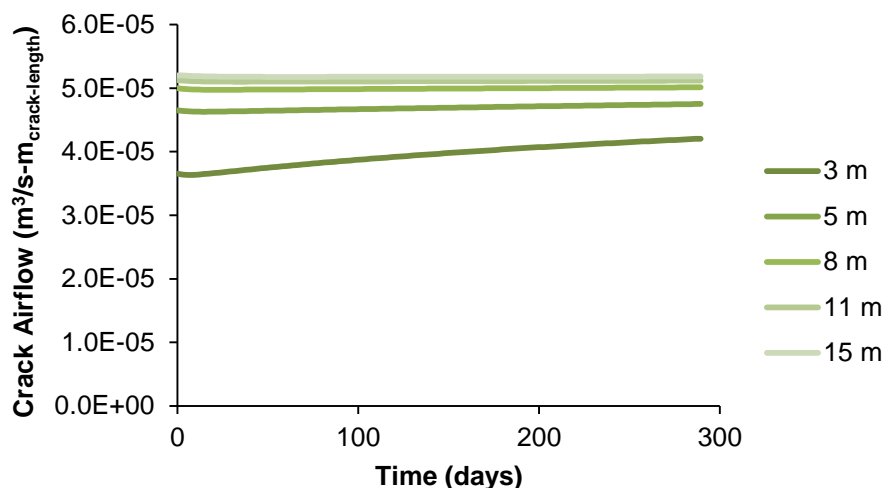


Figure 5.55: Effect of water table reduction on airflow rate. Initial water table depth is 3m and sandy soil media.

Table 5.8 presents summary parameters for all of the water table drop scenarios. Included are the initial concentrations, crack airflow rates, and the contaminant fluxes, as well as the ratios describing the maximum value of each of these parameters observed during the scenario versus the initial rate. From these summary statistics, the scenarios that have the largest effect and highest risk associated with water table reduction become apparent. Based on the conditions of these simulations, these are primarily the sandy soil scenarios with shallow water tables, as well as water tables that drop at faster rate. These produced the largest vapor intrusion increases, in one case causing a 7 fold increase in vapor loading to the building over the baseline condition.

Table 5.8: Water table fluctuation scenarios

Scenario case	Media	WT init depth (m)	WT Drop Rate (m/yr)	Time length (d)	C _{init} (µg/m ³)	C _{max} /C _{init}	Q _{init} (m ³ /d-m)	q _{max} /q _{init}	F _{init} (µg/m-d)	f _{max} /f _{init}
1	S	3	1	289	2978	1.31	3.156	1.15	9398	1.51
2	S	5	1	289	3114	1.27	4.019	1.02	12512	1.30
3	S	8	1	289	3559	1.19	4.319	1.00	15369	1.19
4	S	11	1	289	3978	1.11	4.429	1.00	17616	1.11
5	S	15	1	289	4477	1.03	4.494	1.00	20117	1.03
6	S	3	1	289	2978	1.31	3.156	1.15	9398	1.51
7	S	3	2	289	2978	1.77	3.156	1.22	9398	2.15
8	S	3	4	289	2978	2.96	3.156	1.28	9398	3.79
9	S	3	8	289	2978	5.26	3.156	1.31	9398	6.91
10	SCL	3	1	289	4454	1.20	0.039	1.00	175	1.13
11	SCL	5	1	289	2291	1.00	0.060	1.00	137	1.00
12	SCL	8	1	289	1304	1.00	0.070	1.00	91	1.00
13	SCL	11	1	289	958	1.00	0.074	1.00	71	1.00
14	SCL	15	1	289	754	1.00	0.078	1.00	59	1.00

These scenarios provide an initial insight into the role water table fluctuation affects vapor intrusion. However, more exploration of this phenomena under more realistic conditions is needed. These scenarios have so far been limited to exploring the water table reduction process, since the experimental data and model in section 5.5 did not agree for the water table rise process. Ultimately the rising water table needs to be included in the exploration as well. As discussed in section 5.5, the role of hysteresis also may be important to include. Furthermore, it is unlikely that a fluctuating water table in the field will behave in the ideal manner simulated in these scenarios. For instance, many fluctuations may be cyclical such as from tidal effects or seasonal cycles. Pumping or injection wells at remediation sites may be turned on and off, causing varied drawdown behavior. Heterogeneous soil systems are also likely to interact with the fluctuations. It is suggested that future work focus on exploring the range of scenarios that may occur with water table fluctuations in order to identify conditions that may lead to high vapor loading variability and vapor risk.

5.9 References:

- Abreu, Lilian D. V., and Paul C. Johnson. 2005. "Effect of Vapor Source-Building Separation and Building Construction on Soil Vapor Intrusion as Studied with a Three-Dimensional Numerical Model." *Environmental Science & Technology* no. 39 (12):4550-4561. doi: doi:10.1021/es049781k.
- Anwar, A. H. M. Faisal, Truong Hong Tien, Yasushi Inoue, and Fusetsu Takagi. 2003. "Mass transfer correlation for nonaqueous phase liquid volatilization in porous media." *Environ. Sci. Technol.* no. 37:1277-1283.
- Boublík, T., V. Fried, and E. Hála. 1973. *The Vapour Pressures of Pure Substances: Selected Values of the Temperature Dependence of the Vapour Pressures of Some Pure Substances in the Normal and Low Pressure Region*. New York: Elsevier
- Bozkurt, Ozgur, Kelly G. Pennell, and Eric M. Suuberg. 2009. "Simulation of the Vapor Intrusion Process for Nonhomogeneous Soils using a Three-Dimensional Numerical Model." *Ground Water Monitoring and Remediation* no. 29 (1):92-104.
- Braida, Washington, and S. K. Ong. 1998. "Air sparging: Air-water mass transfer coefficients." *Water Resour. Res.* no. 34 (12):3245-3253.
- Brooks, Royal H., and Arthur T. Corey. 1966. "Properties of porous media affecting fluid flow." *J. Irrig. Drain. Div. Amer. Soc. Civil Eng.* no. 92 (IR2):61-88.
- Chao, K-P., S. K. Ong, and A. Protopapas. 1998. "Water-to-Air Mass Transfer of VOCs: Laboratory Scale Air Sparging System." *Journal of Environmental Engineering* no. 124 (11):1054-1060.
- Choi, Jee-Won, Fred D. Tillman, and James A. Smith. 2002. "Relative Importance of Gas-Phase Diffusive and Advective Trichloroethene (TCE) Fluxes in the Unsaturated Zone under Natural Conditions." *Environmental Science & Technology* no. 36 (14):3157-3164. doi: doi:10.1021/es011348c.
- Elberling, Bo, Flemming Larsen, Steen Christensen, and Dieke Postma. 1998. "Gas transport in a confined unsaturated zone during atmospheric pressure cycles." *Water Resour. Res.* no. 34 (11):2855-2862.

- Fitzpatrick, Nancy A., and John J. Fitzgerald. 2002. "An evaluation of vapor intrusion into buildings through a study of field data." *Soil & Sediment Contamination* no. 11 (4):603-623.
- Fučík, Radek, J. Mikyška, M. Beneš, and Tissa H. Illangasekare. 2007. "An Improved Semi-Analytical Solution for Verification of Numerical Models of Two-Phase Flow in Porous Media." *Vadose Zone Journal* no. 6:93-104.
- Hers, Ian, Jim Atwater, Loretta Li, and Reidar Zapf-Gilje. 2000. "Evaluation of vadose zone biodegradation of BTX vapours." *Journal of Contaminant Hydrology* no. 46 (3-4):233.
- Johnson, Paul C., and Robert A. Ettinger. 1991. "Heuristic model for predicting the intrusion rate of contaminant vapors into buildings." *Environmental Science & Technology* no. 25 (8):1445-1452. doi: doi:10.1021/es00020a013.
- Klenk, I. D., and Peter Grathwhol. 2002. "Transverse verticle dispersion in groundwater and the capillary fringe." *J. Contam. Hydrol.* no. 2002:111-128.
- Kool, J. B., and Jack C. Parker. 1987. "Development and Evaluation of Closed-Form Expressions for Hysteretic Soil Hydraulic Properties." *Water Resour. Res.* no. 23 (1):105-114.
- McCarthy, Kathleen A., and Richard L. Johnson. 1993. "Transport of Volatile Organic Compounds Across the Capillary Fringe." *Water Resour. Res.* no. 29 (6):1675-1683.
- Millington, R. J., and J. P. Quirk. 1961. "Permeability of Porous Solids." *Trans. Faraday. Soc.* no. 57:1200-1207.
- Mori, Hiroko. 2013. *The study of constitutive relationships of multi-phase flow for geologic carbon sequestration*, M.Sc. Thesis. Advisor: Tissa Illangasekare. Civil and Environmental Engineering, Colorado School of Mines, Golden, CO.
- Mualem, Yechezkel. 1976. "A New Model for Predicting the Hydraulic Conductivity of Unsaturated Porous Media." *Water Resour. Res.* no. 12 (3):513-522.
- Oesterreich, R. C., and R. L. Siegrist. 2009. "Quantifying Volatile Organic Compounds in Porous Media: Effects of Sampling Method Attributes, Contaminant Characteristics, and Environmental Conditions." *Environ. Sci. Technol.* no. 43:2891-2898.
- Sakaki, Toshihiro, Anuchit Limsuwat, and Tissa H. Illangasekare. 2011. "A Simple Method for Calibrating Dielectric Soil Moisture Sensors: Laboratory Validation in Sands." *Vadose Zone Journal* no. 10:526-531.
- Sakaki, Toshihiro, Paul. E. Schulte, Abdullah Cihan, John A. Christ, and Tissa H. Illangasekare. 2013. "Airflow Pathway Development as Affected by Soil Moisture Variability in Heterogeneous Soils." *Vadose Zone Journal* (doi:10.2136/vzj2011.0118):14.
- Rosetta 1.2. U.S. Salinity Laboratory, USDA.
- Scott, P. S., Graham Farquhar, and N. Kouwen. 1983. Hysteretic effects on net infiltration. Paper read at Advanced in Infiltration, at St. Joseph, MI.
- Shen, Rui, Kelly G. Pennell, and Eric M. Suuberg. 2012. "A Numerical Investigation of Vapor Intrusion - The Dynamic Response of Contaminant Vapors to Rainfall Events." *Science of The Total Environment*:110-120.

- Smits, Kathleen M. 2010. *Non-isothermal soil moisture processes in the shallow subsurface influenced by atmospheric boundary conditions: numerical and experimental study*, Ph.D. Thesis, Advisor: Tissa Illangasekare. Environmental Science and Engineering, Colorado School of Mines, Golden, Colorado.
- Swallow, J. A., and P. M. Gschwend. 1983. Volatilization of Organic Compounds from Unconfined Aquifers. Paper read at NWWA/API Third National Symposium on Aquifer Restoration and Groundwater Monitoring, May 1983, at Columbus, Ohio.
- Thomson, N. R., J. F. Sykes, and D. Van Vliet. 1997. "A numerical investigation into factors affecting gas and aqueous phase plumes in the subsurface." *Journal of Contaminant Hydrology* no. 28 (1-2):39.
- Tillman, Fred D., and James W. Weaver. 2007. "Temporal moisture content variability beneath and external to a building and the potential effects on vapor intrusion risk assessment." *Science of The Total Environment* no. 379 (1):1.
- van der Ham, A. G. J., and H. J. H. Brouwers. 1998. "Modeling and experimental investigation of transient, nonequilibrium mass transfer during steam stripping of a nonaqueous phase liquid in unsaturated porous media." *Water Resour. Res.* no. 34 (1):47-54.
- van Genuchten, M. Th. 1980. "A closed-form analytical equation for predicting the hydraulic conductivity of unsaturated soils." *Soil Sci. Soc. Am. J.* no. 44 (5):892-898.
- Walser, Gabriele S., Tissa H. Illangasekare, and Arthur T. Corey. 1999. "Retention of liquid contaminants in layered soils." *J. Contam. Hydrol.* no. 39:91-108.
- Wang, Xiaomin, A. J. A. Unger, and B. Parker. 2012. "Simulating an Exclusion Zone for Vapour Intrusion of TCE from Groundwater into Indoor Air." *J. Contam. Hydrol.* no. 140-141:128-134.
- Wilkins, M. D., Linda M. Abriola, and Kurt D. Pennell. 1995. "An Experimental Investigation of Rate-Limited Nonaqueous Phase Liquid Volatilization in Unsaturated Porous Media: Steady State Mass Transfer." *Water Resour. Res.* no. 31 (9):2159-2172.
- Yoon, Hongkyu, Joong Hoon Kim, Howard M. Liljestrang, and Jeehyeong Khim. 2002. "Effect of Water Content on Transient Nonequilibrium NAPL-Gas Mass Transfer During Soil Vapor Extraction." *Journal of Contaminant Hydrology* no. 54:1-18.
- Yu, S., A. J. A. Unger, and B. Parker. 2009. "Simulating the Fate and Transport of TCE from Groundwater to Indoor Air." *Journal of Contaminant Hydrology* no. 107:140-161.

Chapter 6: Summary, Conclusions and Recommendations

6.1 Summary of Research

This project included a variety of different experimental and modeling activities at varied scales to investigate interactions of the vapor intrusion pathway dynamics in subsurface environment. The primary goal of this project was to improve our understanding of factors that contribute to the uncertainty and variability of measured vapor concentrations in subsurface structures resulting from NAPL sources trapped in the unsaturated zone and NAPL constituents dissolved in groundwater. In developing the research approach and tasks, we hypothesized that processes associated with atmospheric, climatic and subsurface geologic heterogeneity factors contribute to those uncertainties and transients. The basic premise under which the fundamental component of this research was planned was that it is not feasible to control all the factors that contribute to the VI in field settings to get accurate data. Also, findings from site-specific case studies cannot be generalized for all sites variable climatic and geohydrologic conditions with potential VI risks. Hence, the approach we used relied on multi-scale laboratory experiments conducted in small to intermediate scale tanks. The small tank experiments were designed to obtain data for the improvement of fundamental process understanding. The intermediate scale tank experiments allowed for the creation of different boundary conditions and excitations expected in field settings to obtain data on different process interactions and dynamics contributing to transient system behavior. Concurrently with experiments, various research level modeling tools with limited capabilities were developed to interpret data, obtain new insights for improving conceptual understanding and provide the basis for development of more comprehensive models for field applications. Even though the development of such a model was not within the scope of this project, using the findings from the research models and improved conceptual models, the development of a comprehensive model that can be used for predictions was initiated.

At the time this project was initiated, little was known about the practical effect of weather and climate factors, such as rainfall, wind, water table fluctuation, daytime heating, and heterogeneity on the vapor intrusion exposure pathway, especially with regards to their role on temporal variability. The new knowledge gained from these activities was used to propose and validate an improved conceptual model of the pathway, giving insights into how these various factors may be anticipated to influence VI. A schematic of this conceptual model that was developed based on this research is presented in figure 1.1. This work has culminated in a large amount of experimental and modeling data, which has been included in this report. A series of conference presentations and papers and theses have also been prepared on the basis of this work, and will continue to be disseminated after this project has concluded.

A number of different experiments and modeling studies were conducted throughout the project to explore the proposed conceptual model. The scope of work included bench scale laboratory experiments, intermediate-scale sand tank experiments, field-testing of geophysical methods, and numerical modeling at all relevant scales of the experiments. Much of this work emphasized the effect of soil moisture on VOC mass transfer, vapor diffusion and vapor advection with particular emphasis on dynamic conditions that exist as a result of transient weather and climate effects. Trichloroethylene (TCE) was the model VOC used throughout all experiments. The experimental and modeling initiatives performed as part of this work are summarized as follows:

- *Bench scale flow cell studies of NAPL volatilization under different source morphologies.* The experiments evaluated exposed (pooled) and occluded NAPL sources, including multiple occlusion layer thicknesses. This situation corresponds to either an entrapped NAPL source in the unsaturated zone that was not removed during remediation or a source that was below the water table getting exposed due to water table drop, as a result of local event or due to regional effects of climate change. Airflow at varied rates was used to drive mass transfer from these sources, and the breakthrough curves evaluated. A numerical model was used to simulate the data and confirm the mechanisms behind the observed behavior.
- *Bench scale flow cell studies of volatilization across a dynamic capillary fringe.* These studies evaluated volatilization of dissolved phase TCE from a falling water table in both homogeneous and heterogeneous formations. This situation corresponds to a groundwater plume containing a dissolved NAPL components residing in vicinity of the building and the water table dropping due to either a local or a regional climate event. Airflow at varied rates was used to drive vapor mass transfer, diffusion and advection. Gathered data demonstrated the concentration profiles that developed within the capillary fringe as well as the water phase and effluent breakthrough curves.
- *Intermediate scale sand tank experiments evaluating the effect of heat flux (e.g. solar heating) and rain infiltration on dynamic vapor pathways.* In these up-scaled experiments, a large tank with layered heterogeneities was tested with rainfall at different rates on the soil surface, as well as the application of heat to the soil surface using a heating element. These experiments simulated scenarios of different possible climate conditions at the land surface that affects VI pathways. . The tank was instrumented with a series of soil moisture sensors, air pressure sensors and airflow meters. Air was injected at one end of the tank and the changes in airflow patterns were used to determine how vapor migration pathways respond to heat and rain.
- *Intermediate scale sand tank experiment integrating vapor generation, transport and intrusion under the influence of rainfall, water table fluctuation and NAPL volatilization.* This large tank experiment evaluated the full vapor transport regime set up as a physically simulated vapor intrusion setting, including volatilization across a capillary fringe from a groundwater plume, along with vadose zone diffusion and advection. Both a homogeneous and layered heterogeneous systems were tested. The system was subjected to multiple events of water table fluctuations and rainfall infiltration and dynamics of vapor generation and intrusion pathways were observed during a long time period of several months. A NAPL source was emplaced for one experiment. High temporal resolution measurements were made of concentrations, soil moisture, air pressure and airflow rates through the system.
- *Development of multiple numerical models to simulate the series of experiments conducted in multi-scale test systems presented above.* Developed models evaluated the role of multiple physical processes and their interactions, including flow in both air and water phases represented as a multiphase flow system, mass transfer from NAPL sources, solute diffusion and advection in both air and water phases, partitioning, and heat

transport. Models were implemented in the analysis of nearly all experiments as well as hypothetical field scenarios.

- *Intermediate scale tank experiments to test the feasibility of using shallow subsurface geophysical measurement to identify dynamic VI pathways due to changes in soil moisture.* Direct-current resistivity measurement was the method used to analyze water retention from multiple heterogeneous sand packs, to determine the measurement potential of the method.
- *Field scale demonstration of rainfall infiltration with application of geophysics to track infiltration front propagation.* Through collaboration with SERDP project ER-1686, sprinklers were used at the Sun Devil Manor site adjacent to Hill AFB to determine the practical effect of infiltration on the VI pathway. DC-resistivity was used to track the propagation of the infiltration front, while vapor signals in the house were monitored.

6.2 General Conclusions

The results of each series of experiments, explained in detail in the results section, provide the basis for some generalized conclusions that may be drawn from the body of work summarized above. These are described as follows.

- Subsurface VI pathway can be dynamic and complex, sometimes resulting in counter-intuitive cause-effect relationships. Numerical modeling based on improved conceptual models can be informative to understand the processes that govern VI in complex systems. For example:
 - Currently used steady-state models of VI predict that a water table that has dropped should exhibit lower vapor fluxes because the increased length of the diffusion pathway from the water table to the subsurface structure reduces the driving force for vapor diffusion. However, on the basis of transient modeling done in our work, a dropping water table causes a temporal increase in concentrations due to the introduction of more contaminants into the soil water in the unsaturated zone that will partition into the air. The more heavily contaminated zone below the initial capillary fringe before the water table dropped will now be in the unsaturated zone where vapor is generated through partitioning
 - In the intermediate scale tank experiment, a rainfall infiltration event caused a temporal spike in vapor *concentrations* intruding into the simulated building while holding the airflow rate constant. However, model simulations of scenarios predicted no concentration change in the intruding air, but did predict immediate increases the *rate of airflow* in the simulated crack in the structure resulting from propagation of the infiltration front that displaced the air in the soil that was directed to the structure. Thus both the laboratory experiment and hypothetical scenario predicted spikes in vapor intrusion, but different causal mechanisms due to the differences in conditions. This highlights the complexity inherent in data

interpretation without an effective conceptual model because in the field, indoor concentrations might spike with no observable changes in subslab concentration.

- Heterogeneity in the dynamic pathway experiments (section 5.3) indicated enhanced preferential airflow during an infiltration event in a heterogeneous environment. However, the integrated vapor generation, transport and intrusion experiments (section 5.4) showed that the effect of heterogeneity was to dampen the observed transient vapor responses when compared to equivalent homogeneous experimental results. The first set experiments (section 5.3) were for a simplified situation, where only the air pathway development was studied without considering vapor generation. Whereas, in the second set of experiments (section 5.4), the vapor generation was integrated with airflow. This finding suggests the importance of considering process interactions in both conceptualization and model development to accurately capture the dynamics that contribute to transient concentrations in the building.
- VI pathway development is transient as a result of weather and climate factors, and may be important in designing monitoring strategies and remedial action.
 - Temporal behavior can occur at different timescales, with different driving forces dominating. For example, in the rainfall scenario there is an immediate short-term spike in vapor intrusion due to increase airflow through the crack, but there is also a longer-lived increase in concentration that occurs long after the rain event has ceased. Meanwhile, water table reductions cause temporal increases in VOC concentrations over a medium to long-term timescale.
 - The timescales of transient effects and the factors that contribute those effects may be important considerations when incorporating this new knowledge into conceptual models and remediation activities. For example, the immediate rainfall spike may only affect a sampling round that occurs during or shortly after the rain event. However, if a particularly significant rain event or even a flood causes a significant long-term concentration shift, this may be of more importance for longer-term site management.
- Rainfall exerts a complex, condition dependent response to the VI pathway.
 - Vapor intrusion will likely spike in the near term during a rain event due to gas phase displacement from the initial infiltration front propagation. This observation is supported on the basis of observations from multiple laboratory experiments, model scenario simulations, and field-testing.
 - The “capping” effect where infiltration blocked diffusive and advective exchange with the atmosphere was significant in the laboratory experiment, but appeared to be negligible in the scenarios for the conditions simulated. Concentration shifts in the near term were negligible. The capping effect may be an artifact of the constrained flow in the 2-D tank. However, other scenarios such as snow accumulation all around the building grounds may produce similar capping effects where the atmospheric air is not connected to the soil air and air pathways through unsaturated zone has the potential to direct vapor from subsurface sources to the building.

- A “washout effect” due to the "cleaner water" of the infiltration front diluting the "dirtier water" of the vadose was significant in the laboratory experiment and corroborated by the model, but was not readily observed in the rainfall scenarios. The infiltration front in the scenarios travelled more slowly, and the front dissipated before reaching the bottom of the foundation, thus there was no appreciable dilution effect.
- After the dissipation of the infiltration front, there is a long slow tailing in soil moisture saturations as water very slowly percolates downward. During this "redistribution period," significant changes in concentrations were observed in both the experiments and the scenarios. In the experiments, a slow rebound over several days to the initial condition was observed. In the scenarios, the redistribution was much slower, still affecting vapor concentrations more than one year later. In the scenario simulated over this long timeframe, concentration changes at one year were actually larger than the initial concentration shift during the infiltration event. Furthermore, this scenario merely simulated a very mild rain event. More sensitivity analysis is needed to discern the significance of the redistribution period.
- Water table fluctuation imparts very complex transport behavior within the capillary fringe that has significant effects on vapor loading from the groundwater plumes that defied simplified models used in screening.
 - A falling water table is likely to cause short and medium term increases in vapor concentrations due to entry of air into more contaminated regions of the capillary fringe, exposing more contaminant mass. This was corroborated by experimental observations as well as numerical modeling of the experiment and scenario simulations. The magnitude of this increase depends on a variety of factors, including depth to groundwater from the building, the rate of water table drop, and soil properties.
 - A rising water table exerts a complex behavior contributing to vapor loading, resulting in a momentary rise in concentrations, followed by a decrease. The numerical model was unable to fully capture this behavior. Multiphase flow hysteresis may be an important factor within the rising capillary fringe, especially in regards to the vapor loading, but more work is needed to fully explore this effect.
- Trapped NAPL sources in the unsaturated zone are capable of loading significant mass into the vadose zone, but the loading rate is a strong function of the moisture distribution within and in the vicinity of the source
 - Source zones with high water content and occluded NAPL will tend to have lower mass loading rates, as demonstrated through experiments and modeling.
 - Pooled sources with direct exposure will have high mass loading rates
 - A fluctuating water table may periodically expose or occlude a NAPL source causing corresponding increases or decreases to vapor loading.
- Transient thermal effects for subsurface vapor transport are mostly negligible.

- The heating effect was largely limited to the near surface and generally didn't affect vadose zone transport pathways below the surface layer.
- Temperatures did not increase significantly below the surface layer.
- The primary effect of heat was to dry out the surface layer, which was only significant when fine media was present at the soil surface.
- While heating did not cause large temporal effects, it is important to use appropriate temperatures for all relevant physical parameters in models, such as diffusion coefficients, solubility limits, Henry's constants and others.
- Subsurface heterogeneity can interact with vapor transport to cause complex effect.
 - Soil moisture may interact with heterogeneity to "activate" preferential pathways, especially in response to heavy infiltration
 - Wet layers serve as barriers to vapor diffusion, which can have the effect of damping transient behavior.
- Shallow surface geophysical methods may have the potential to provide tracking of soil moisture distributions in field soils, but further development is needed.
 - This was corroborated by the field demonstration of the ERT measurements.
 - The laboratory demonstrations were unsuccessful with ERT, likely due to current bleeding from the intermediate scale tank from an unknown electrical ground.
- Controlled experiments in intermediate scale settings are valuable for assessing complex interactions between multiple processes and factors within the subsurface
 - Models alone may overlook important phenomena if they are not compared against data sets generated in highly controlled experiments that are not feasible in field settings.
 - Even though homogenous packing in test tanks are not representative of field settings, their value should not be overlooked. The experiments from section 5.4.1 provided much insight when evaluating the model because the very complex interactions were observed even from a comparatively "simple" homogeneous case. Heterogeneity may complicate an experiment to such an extent that effective analysis becomes difficult.

6.3 Practical implications:

For the purposes of defining the practical effects these weather and climate factors may have for the vapor intrusion pathway, it is useful to discuss the possible effects that may be anticipated based on this work.

Table 6.1: Practical implications of weather and climate factors for VI.

Factor	Anticipated temporal effect based study results
Rainfall	<ul style="list-style-type: none"> • Likely short-term spike in vapor intrusion. This may interfere with indoor air sampling if it occurs during a rainfall event. • Possible short – to medium term washout of concentrations due to infiltration front movement. This may or may not occur depending on how fast the infiltration front propagates and dissipates as controlled by the soil conditions. Could give artificially low vapor results if sampling occurs after a large storm event. • Long term rebound or concentration rise possible as system equilibrates. The significance of this is not as clear. One would expect a regular series of rainfall events to reach a pseudo-steady state in terms of long-term effect. However, an unusually large rain event (e.g. a flood) might cause unusually long rebound with effects playing out over years.
Water table drop	<ul style="list-style-type: none"> • Short to medium term increase in vapor concentrations likely if water table reduction exposes source zones or zones of contaminated groundwater. In the field, evaluation of well data may give an indication of water table history. Well drawdown could be a factor. • Effect likely more significant for shallow water tables (e.g. 10-15 ft) and more rapid rates of water table reduction. • Long-term steady state should come to a reduced concentration.
Water table rise	<ul style="list-style-type: none"> • The overall effect is unclear based on conflicting information from the model and the experiment. The experiment suggests a momentary increase in vapor concentrations will be observed. The model predicts concentrations to fall during the rising water table. • At long term steady-state, the concentrations should increase in proportion to the decrease in diffusion pathway length.
Heterogeneity	<ul style="list-style-type: none"> • Layering of soils has a complex effect. The layering may dampen transient vapor responses reducing temporal variability. More water-wet, heavily layered systems in the field may be less likely to exhibit dynamic behavior • Infiltration within a layered system may periodically causes a dry layer to re-wet, or likewise a dry spell causes a wet layer to drain. These could cause changes to the diffusion and advection pathways causing vapor increases or decreases depending on the configuration.

Factor	Anticipated temporal effect based study results
Heat at soil surface	<ul style="list-style-type: none"> • The laboratory data suggest the primary effect of heating is to increase evaporation from the soil surface layer. This is unlikely to penetrate deep enough to cause major changes. • While heat had a negligible effect, it is important to use relevant temperatures when estimating diffusion coefficients, partitioning coefficients, and other temperature dependent parameters.

6.4 Recommendations for Future Work:

The work conducted under project ER-1687 provides a solid foundation for understanding the dynamic response of vapor intrusion to complex factors such as weather, climate, and hydrologic cycle dynamics. This study emphasized experimental exploration of mass transfer, vapor diffusion, and vapor advection in homogeneous and heterogeneous multiphase systems, as well as characterization methods to monitor or observe these in field settings. This informed the development of an improved conceptual model of the vapor intrusion pathway. However, this model has only explored only a limited number of possible range field scale scenarios that might be encountered in real world systems, and more work is needed to develop a better understanding of the implications of these factors for VI. In particular, modeling and field sensitivity analysis of realistic complex systems is needed to elucidate more information about best and worst case VI scenarios that give more detailed information about spatial and temporal variability. A separate, collaborative effort to develop a more efficient production code (Appendix A) has only just begun to allow for a more thorough analysis of field scale systems. It is recommended that a more comprehensive scenario sensitivity analysis be performed to generate a clearer understanding of best and worst case scenarios for vapor intrusion dynamics, and to evaluate the contributing factors that cause such behavior. Furthermore, it field validation and verification of such scenarios could improve confidence in in the model, and allow for development of better guidance for assessment of the VI pathway, based on an improved overall conceptual model of the factors that affect VI. Suggested factors are included in table 6.2.

Additionally, more work is needed to improve characterization practices in the field, which would allow for improved identification of site-specific pathways and risk factors. Tomographic methods such as ERT can provide 2-D or 3-D images of the subsurface that provide a much greater level of detail than traditional borehole or sampling analysis. This project explored ERT for mapping heterogeneous soil moisture, and results show promise through a proof-of-concept type of experiment. However, more work is needed to determine if such a technology is implemented and practicable for large sites and sites that will have accessibility issues due to both natural conditions and existing urban infrastructure and how such new information can be best incorporated into models and decision-making.

Table 6.2: Factors suggested for future analysis.

Scenario Cases	Suggested factors to evaluate
Base case	<ul style="list-style-type: none"> • Regional climate characteristics <ul style="list-style-type: none"> ○ Temperature ○ Annual infiltration ○ Cyclical seasonal effects • Heterogeneous soil systems <ul style="list-style-type: none"> ○ Layered systems ○ Random systems • Varied soil types <ul style="list-style-type: none"> ○ Permeable soils ○ Impermeable soils • Depth to water table
Rainfall / Irrigation	<ul style="list-style-type: none"> • Incorporate rainfall / irrigation analysis into base cases with additional sensitivity analysis on: <ul style="list-style-type: none"> ○ Infiltration event intensity ○ Infiltration event duration ○ Infiltration event frequency ○ Seasonal variation
Water table fluctuation	<ul style="list-style-type: none"> • Incorporate water table fluctuation analysis into base cases with additional sensitivity analysis on: <ul style="list-style-type: none"> ○ Water table drop / rise rate ○ Cyclical fluctuations (e.g. seasonal / tidal effects) ○ Responses to remediation activities such as pumping, SVE, etc.
Urban environment	<ul style="list-style-type: none"> • Explore the role that typical urban infrastructure and urban environments have on the VI model <ul style="list-style-type: none"> ○ Surface conditions <ul style="list-style-type: none"> ▪ Building footprints ▪ Pavement / sidewalks ▪ Lawns / Trees / vegetation ▪ Irrigation effects ○ Subsurface conditions <ul style="list-style-type: none"> ▪ Foundation types ▪ Utility corridors ▪ Foundation / French drains

Appendix A: Supporting Data

A.1: Introduction:

The ER-1687 project conducted a variety of experiments and models that generated very large data sets. Due to the unique nature of the data gathered, these data sets will likely continue to be of interest to other researchers for quite some time after the conclusion of this project. The laboratory tank experimental data sets in particular are useful for benchmarking and validating numerical models in a variety of disciplines, which may include vapor intrusion and beyond. Thus in order to provide a wider benefit to the broader community, these data sets will be achieved in a publically available manner. Some have already been published or defended as master's thesis (see Appendix B for list of publications), and at the time of this report, a PhD dissertation by Ben Petri is also being prepared for defense. This appendix describes the raw data set generated by the integrated dynamic flow and transport experiments and how to acquire the data, and also presents a model developed to run as an efficient production code for future exploration of VI, vapor transport, and scenarios.

A.2: Data sets from the integrated dynamic flow and vapor transport experiments

These experiments (described in section 5.4) produced very large data sets that may be of particular interest to researchers seeking to validate models. Briefly, these experiments encompassed two large sand tank experiments, one homogeneous and the other heterogeneous, which were each operated as a physical model of a coupled groundwater-vadose zone system, with airflow drawn at a point to simulate airflow into a building. Each tank was operated in the laboratory continuously for 106 days, during which the tank was subjected to a series of water table fluctuation, rainfall, and NAPL volatilization events. The tanks were highly instrumented. Within the tank, an array of 30 soil moisture sensors, 24 air pressure transducers, 5 airflow meters and 2 temperature transducers logged data throughout the entire experimental timeframe. At the airflow outlet, a gas chromatograph (GC) also continuously measures the gas phase TCE concentration. All of this automated instrumentation logged measurements around the clock with a temporal resolution of approximately 4.25 minutes (corresponding to the GC method run time). As a result, the raw data sets for each tank experiment consist of ~32000 lines of data with each line of data recording 61 measurements from all of the sensors, for a total of roughly 2 million independent measurements per tank experiment. Since it would be wholly impractical to include this enormous data set within this document, the data will be archived electronically instead. Versions of the data in both a MS Excel file as well as a text file will be archived in Ben Petri's PhD dissertation pending his defense in summer 2014. These datasets will also be available upon request from either Ben Petri (Colorado School of Mines, bpetri@mymail.mines.edu) or Dr. Tissa Illangasekare (Colorado School of Mines, tissa@mines.edu).

A.3 Development and testing of an efficient model for simulation of vapor transport

A numerical model was developed in collaboration with Dr. Radek Fucik at Czech Technical University in Prague, Czech Republic. The objective of this code was to build a more efficient numerical model than the COMSOL-based model so that a wider range of sensitivity analysis and scenarios could be explored. Though COMSOL has many advantages, especially in terms of ease of use and flexibility of the formulation, it also has disadvantages in terms of model stability and model run times when simulating very complex problems. These limitations manifested themselves particularly with regard to the simulations in section 5.5 (large tank experiments) and section 5.8 (scenarios), severely limiting the number of simulations that could be achieved within a reasonable timeframe. Since many of the findings from this project suggest more work needs to be done to understand the sensitivity of the VI pathway to the spatio-temporal variability that was explored in this project, a more efficient code was built. This code was tested against the small-scale NAPL volatilization studies (section 5.1) for proof concept. The new formulation made possible the simulation of several thousand transient model runs to develop a Gilliland-Sherwood correlation from the data. This would have been impractical in the COMSOL code. Presented below is a draft manuscript prepared on this work, which describes the code and the initial results.

A computational study of complete TCE volatilization in unsaturated porous medium

We present a two-dimensional computational model for mass transfer and mass transport within the framework of immiscible flow of compressible gas and incompressible water phases in unsaturated porous media. The model is used to test a hypothesis whether the Gilliland-Sherwood model for the mass transfer rate coefficient can be applied to model a complete volatilization of an exposed TCE pool under four different air flow velocities. In the model, the TCE phase is assumed to be immobile and located in the source zone under initially known saturation from which a mass transfer process of TCE volatilization into the gas phase is considered only. The mathematical model is implemented using the C++ library NumDwarf that is being developed by the author and verified against another model built using the COMSOL Multiphysics commercial software.

1. Introduction

We present a two-dimensional computational model that includes mass transfer and mass transport within the framework of immiscible flow of compressible gas and incompressible water phases in unsaturated porous media. In this report, the model is used to test a hypothesis whether the Gilliland-Sherwood model [Saba et al., 2001, Saenton and Illangasekare, 2007] for the mass transfer rate coefficient can be applied to model a complete dissolution of the exposed TCE pool under variable air flow. In the model, the TCE phase is assumed to be immobile and located in the source zone under initially known saturation from which a mass transfer process of TCE volatilization into the gas phase is considered only.

In the first section, we describe the governing equations of the two-phase flow, mass transfer and

transport in the porous medium. In the following section, we show how the NumDwarf computational library is used to discretize and solve the mathematical model. The numerical scheme is then compared against another computational model developed using a commercial software COMSOL Multiphysics for an arbitrary set of model parameters. In Section 5, the numerical model is employed in an extensive computational study where the objective is to determine a set of model parameters that fit data measured in a laboratory experiment.

2. Model Equations

A commonly used concept of modeling immiscible two-phase flow processes in porous media is based on the assumption that every fluid phase is governed by the continuity theorem and Darcy's law. In the following, a flow of an incompressible wetting phase (indexed by w) and a compressible gas phase (indexed by g) is considered. Additionally to the gas and water phase, we consider an immobile NAPL (TCE) phase (indexed by n) to be present in the source zone.

The α -phase mass continuity equation for $\alpha \in \{w, g, n\}$ has the following form

$$\frac{\partial(\phi\rho_\alpha S_\alpha)}{\partial t} + \nabla \cdot (\rho_\alpha u_\alpha) = F_\alpha, \quad (1)$$

and the Darcy's law for the phase $\alpha \in \{w, g\}$ is given by

$$u_\alpha = -\lambda_\alpha K (\nabla p_\alpha - \rho_\alpha \mathbf{g}), \quad (2)$$

where $\phi[-]$ is the porosity, $K[m^2]$ is the intrinsic permeability tensor, and $\mathbf{g}[m s^{-2}]$ is the gravitational acceleration vector. Note that we assume zero velocity for the NAPL phase, i.e. $u_n = 0$. The symbols $\rho_\alpha[kg m^{-3}]$, $S_\alpha[-]$, $u_\alpha[m s^{-1}]$, $F_\alpha[kg m^{-3} s^{-1}]$, $\lambda_\alpha = k_{r,\alpha} \mu_\alpha[kg m^{-1} s^{-1}]$, $\mu_\alpha[kg m^{-1} s^{-1}]$, $k_{r,\alpha}[-]$, and $p_\alpha[Pa]$ stand for the α -phase density, volumetric saturation, apparent macroscopic velocity, specific source/sink term, mobility, dynamic viscosity, relative permeability, and pressure, respectively. The relative permeability functions $k_{r,w}$ and $k_{r,g}$ are assumed to be nonlinear functions of the wetting phase saturation S_w and the empirical model by Mualem [Mualem, 1975] is employed. Assuming no other liquid is present in the porous medium, we get

$$S_w + S_g + S_n = 1. \quad (3)$$

The system of equations is closed by introducing the capillary pressure $p_c[Pa]$ as the difference between the phase pressures, $p_c = p_g - p_w$, for which the van Genuchten model is used [Genuchten, 1980].

2.1 Water Phase Equation

The water phase is assumed to be incompressible and its Darcy's velocity u_w can be written in terms of the gas phase pressure p_g and the capillary pressure p_c as

$$u_w = -\lambda_w K (\nabla p_w - \rho_w \mathbf{g}) = -\lambda_w K (\nabla p_g - \nabla p_c - \rho_w \mathbf{g}), \quad (4)$$

where p_c is defined as $p_c = p_g - p_w$. For the wetting phase, the continuity equation (1) reads as

$$\boxed{-\phi \rho_w \frac{dS_w}{dp_c} \frac{\partial p_c}{\partial t} + \phi \rho_w S_w^e \frac{\partial S_n}{\partial t} + \nabla \cdot (-\rho_w \lambda_w K \nabla p_c + \rho_w \lambda_w K \nabla p_g - \lambda_w \rho_w^2 K \mathbf{g}) = F_w}, \quad (5)$$

where the modified van Genuchten model for the $p_c \leftrightarrow S_w$ relationship is used:

$$S_w^e = \frac{S_w - S_{w,r}}{1 - S_{w,r} - S_{g,r} - S_n} = [1 + (\alpha p_c)^n]^{-m}, \quad (6)$$

$$\frac{dS_w}{dp_c} = -mn\alpha^n (1 - S_{w,r} - S_{g,r} - S_n) p_c^{n-1} (1 + (\alpha p_c)^n)^{-m-1}, \quad (7)$$

where $S_{w,r} [-]$ and $S_{g,r} [-]$ are the residual wetting and non-wetting phase saturations, respectively, and S_n is the immobile NAPL saturation. In (6), $S_w^e [-]$ denotes the effective wetting phase saturation, $\alpha [Pa^{-1}]$, $n [-]$, and $m [-]$ are the van Genuchten model parameters.

2.2 Gas Phase Equation

We consider the gas phase to be a mixture of 100% humidified air (indexed by a) and NAPL (TCE) vapor (indexed by n). The mixture density is assumed to be given by the ideal gas law

$$\rho_g = p_g \frac{M_g}{RT}, \quad (8)$$

where $R [J mol^{-1} K^{-1}]$ is the gas constant, $T [K]$ is the temperature and $M_g [g mol^{-1}]$ is the molar weight of the mixture given by

$$M_g = \left(\frac{X_n}{M_n} + \frac{X_a}{M_a} \right)^{-1}, \quad (9)$$

where $M_a [g mol^{-1}]$ and $M_n [g mol^{-1}]$ are molar weights of the humidified air and NAPL vapor, respectively. In (9), $X_a [-]$ and $X_n [-]$ are the mass fractions of the humidified air and NAPL vapor in the gas phase, respectively, with

$$X_n + X_a = 1. \quad (10)$$

In terms of the mass fraction X_n , the gas density reads as

$$\rho_g = \frac{p_g M_a}{RT} \frac{1}{1 + X_n \left(\frac{M_a}{M_n} - 1 \right)}. \quad (11)$$

In terms of the mass concentration $c_n [kg m^{-3}]$ of the NAPL vapor in the gas phase defined as $c_n = X_n \rho_g$, the gas density is given by

$$\rho_g = \frac{p_g M_a}{RT} + c_n \left(1 - \frac{M_a}{M_n} \right). \quad (12)$$

The continuity equation (1) for the gas mixture is given by

$$\frac{\partial(\phi \rho_g S_g)}{\partial t} + \nabla \cdot (\rho_g u_g) = F_g, \quad (13)$$

where $S_g + S_w + S_n = 1$, i.e.,

$$\boxed{-\phi \rho_g \frac{dS_w}{dp_c} \frac{\partial p_c}{\partial t} - \phi \rho_g (1 - S_w^e) \frac{\partial S_n}{\partial t} + \phi S_g \frac{\rho_g}{p_g} \frac{\partial p_g}{\partial t} + \phi S_g \frac{\partial \rho_g}{\partial X_n} \frac{\partial X_n}{\partial t} + \nabla \cdot (-\rho_g \lambda_g K \nabla p_g + \rho_g^2 \lambda_g K \mathbf{g}) = F_g,} \quad (14)$$

2.3 NAPL Vapor Transport in Gas Phase

Transport of the components in the gas phase is described by the Advection–Diffusion–Dispersion Equation (ADDE) [Bear, 1988]

$$\frac{\partial(\phi S_g X_n \rho_g)}{\partial t} + \nabla \cdot (\rho_g u_x) = F_x, \quad (15)$$

where $F_x [kg m^{-3} s^{-1}]$ is the source/sink term and u_x denotes the velocity of the component X_n given by

$$u_x = X_n u_g - D_{ng} \nabla X_n. \quad (16)$$

By virtue of (13) and (16), Eq. (15) can be written as

$$\boxed{\phi S_g \rho_g \frac{\partial X_n}{\partial t} + \rho_g u_g \nabla X_n + \nabla \cdot (-\rho_g D_{ng} \nabla X_n) = F_X - X_n F_g}, \quad (17)$$

with

$$D_{ng} = (a_L - a_T) \frac{u_g u_g^T}{|u_g|} + (a_T |u_g| + \tau \phi S_g D_n) I, \quad (18)$$

where $D_n [m^2 s^{-1}]$ is the free fluid molecular diffusion of NAPL ($D_n = 8.35 \cdot 10^{-6} m^2 s^{-1}$ for TCE vapor in the air in this study), $\tau [-]$ is the tortuosity given by [Millington and Quirk, 1961]

$$\tau = \Phi^{13} S_g^{73},$$

and $a_L [m]$ and $a_T [m]$ are the longitudinal and transversal dispersivity coefficients, respectively.

In the latter, a simplified isotropic diffusion–dispersion coefficient, denoted by D_{ng}^{iso} , is used in (17) instead of D_{ng} in the form

$$D_{ng}^{iso} = (a_D |u_g| + \tau \phi S_g D_n) I, \quad (19)$$

where $a_D [m]$ is the isotropic dispersivity coefficient.

The dispersivity coefficients a_L , a_T , and a_D are empirical quantities that describe dispersion of the NAPL vapor plume due to solid matrix.

2.4 NAPL Mass Transfer (Volatilization)

The volatilization of the immobile liquid NAPL is described by

$$\boxed{\phi \rho_n \frac{\partial S_n}{\partial t} = F_n}, \quad (20)$$

where $\rho_n [kg m^{-3}]$ is the density of the liquid NAPL.

Mass transfer from the immobile liquid NAPL pool into the gas phase due to volatilization is described by $R_{ng} [kg m^{-3} s^{-1}]$ and based on [Yoon et al., 2002],

$$R_{ng} = \text{Sh} \frac{D_n}{d_{50}^2} (c_s - X_n \rho_g), \quad (21)$$

where d_{50} [m] is log-normal distribution mass median diameter, Sh [-] is the Sherwood number, S_n [-] is the NAPL volumetric saturation, S_n^{ini} [-] is the initial NAPL saturation, and c_s [kg m^{-3}] is the saturated mass concentration of NAPL in the gas phase. Assuming no other sinks or sources are present in the problem description, we set $F_w = 0$, $F_g = R_{ng}$, $F_x = R_{ng}$, and $F_n = -R_{ng}$.

The model for the Sherwood number in (21) is assumed in the form [Yoon et al., 2002]

$$\text{Sh} = \gamma \text{Pe}^\delta \left(\frac{S_n}{S_n^{ini}} \right)^\beta d_0^{1.68} \quad (22)$$

where Pe denotes the dimensionless Péclet number, d_0 [m] is the normalized mean grain size defined as $d_0 = d_{50}/d_m$, d_m [m] is the mean grain size of sand and β , γ , and δ are empirical fitting parameters.

2.5 Initial and Boundary Conditions

The objective of the formulation is to find functions $p_g = p_g(t, x)$, $p_c = p_c(t, x)$, $S_n = S_n(t, x)$, and $X_n = X_n(t, x)$ for all t [s] in $[0, T]$ and all x in the computational domain $\Omega \subset \mathbb{R}^2$. The system of equations (5), (14), (17), and (20) is subject to initial condition for all $x \in \Omega$ at $t = 0$:

$$p_g = p_g^{ini}, \quad (23)$$

$$p_c = p_c^{ini}, \quad (24)$$

$$S_n = S_n^{ini}, \quad (25)$$

$$X_n = X_n^{ini}, \quad (26)$$

and boundary conditions for all $t > 0$:

$$u_w \cdot n = u_w^N, \quad \text{on } \Gamma_{u_w} \subset \partial\Omega, \quad (27)$$

$$u_g \cdot n = u_g^N, \quad \text{on } \Gamma_{u_g} \subset \partial\Omega, \quad (28)$$

$$u_x \cdot n = u_x^N, \quad \text{on } \Gamma_{u_x} \subset \partial\Omega, \quad (29)$$

$$\rho_g D_{ng} \nabla X_n \cdot n = 0, \quad \text{on } \Gamma_{ad} \subset \partial\Omega, \quad (30)$$

$$p_g = p_g^D, \quad \text{on } \Gamma_{p_g} \subset \partial\Omega, \quad (31)$$

$$p_c = p_c^D, \quad \text{on } \Gamma_{p_w} \subset \partial\Omega, \quad (32)$$

$$S_n = S_n^D, \quad \text{on } \Gamma_{S_n} \subset \partial\Omega, \quad (33)$$

$$X_n = X_n^D, \quad \text{on } \Gamma_{X_n} \subset \partial\Omega, \quad (34)$$

where Γ_{u_w} , Γ_{u_g} , Γ_{u_X} , Γ_{p_g} , Γ_{p_w} , Γ_{S_n} , and Γ_{X_n} denote the subsets of the domain boundary $\partial\Omega$ where the boundary conditions for u_w , u_g , u_X , p_g , p_w , S_n , and X_n are prescribed. By Γ_{ad} , we denote the boundary segment where the advective flux boundary condition for the NAPL component X_n is prescribed.

3. Numerical Model

3.1 Implementation in C++ using NumDwarf Library

The system of equations is discretized and solved using the C++ computational library NumDwarf which is being developed by the author [Fučík, 2014]. The library allows to solve a system of n nonlinear partial differential equations (PDEs) in a general coefficient form using the mixed hybrid finite element (MHFEM) discretization in space and semi-implicit discretization in time similar to numerical methods reported in [Hoteit and Firoozabadi 2008, Fučík and Mikyška, 2011, Fučík and Mikyška, 2012]. The general coefficient form of the system of PDEs is denoted by

$$\sum_{j=1}^n N_{i,j} \frac{\partial Z_j}{\partial t} + \sum_{j=1}^n u_{i,j} \cdot \nabla Z_j + \nabla \cdot \left(m_i \left(-\sum_{j=1}^n D_{i,j} \nabla Z_j + w_i \right) + \sum_{j=1}^n Z_j a_{i,j} \right) + \sum_{j=1}^n r_{i,j} Z_j = f_i, \quad (35)$$

for $i = 1, \dots, n$. By v_i , we denote the conservative flux given by

$$v_i = m_i \left(-\sum_{j=1}^n D_{i,j} \nabla Z_j + w_i \right), \quad (36)$$

where the unknown vector function $Z = [Z_1, \dots, Z_n]^T$ is a function of time $t [s]$ and space $x [m]^d$ where d denotes the spatial dimension. In (35), the coefficients have the following meaning:

Symbol	Meaning	Assumptions
$N_{i,j}$	damping matrix	non-singular
u_i	convection	
m_i	mobility of the flux v_i	non-negative
$D_{i,j}$	diffusion tensor	positive definite (or zero)
w_i	external forces / source term	

a_i	conservative flux convection	
r_i	reaction term	
f_i	source term	

At each discrete time step t_i , the system of equations (5), (14), (17), and (20) is solved sequentially in the following order.

In the **first step (STEP 1)** (indexed by superscript (1)), the two-phase flow equations (5) and (14) together with the mass transfer equation (20) are solved using the NumDwarf library (with $n^{(1)} = 3$) setting the unknown vector $Z^{(1)}$ to represent primary unknown variables as $Z^{(1)} = (p_c, p_g, S_n)^T$ and the coefficients in (35) are assigned as follows:

Symbol	Assignment	Meaning
N	$\begin{pmatrix} -\phi\rho_w \frac{dS_w}{dp_c} & 0 & \phi\rho_w S_w^e \\ -\phi\rho_g \frac{dS_w}{dp_c} & \phi S_g \frac{\rho_g}{p_g} & -\phi\rho_g (1 - S_w^e) \\ 0 & 0 & \phi\rho_n \end{pmatrix}$	damping matrix
u	0	convection
m	$\begin{pmatrix} \rho_w f_w \\ \rho_g f_g \\ 0 \end{pmatrix}$	mobility of the flux v_i
D	$\begin{pmatrix} \lambda_t K & -\lambda_t K & 0 \\ 0 & \lambda_t K & 0 \\ 0 & 0 & 0 \end{pmatrix}$	diffusion tensor
w_i	$\begin{pmatrix} -\lambda_t \rho_w K g \\ \lambda_t \rho_w K g \\ 0 \end{pmatrix}$	external forces / source term
a_i	0	conservative flux convection
r_i	0	reaction term
f_i	$\begin{pmatrix} 0 \\ R_{ng} - \phi S_g \frac{\partial \rho_g}{\partial X_n} \frac{\partial X_n}{\partial t} \\ -R_{ng} \end{pmatrix}$	source term

where $f_\alpha = \frac{\lambda_\alpha}{\lambda_t}$ denotes the fractional flow function of the phase α , $\alpha \in \{w, g\}$, and $\lambda_t = \lambda_w + \lambda_g$.

Note that all coefficients in the previous listing are evaluated on the previous time level t_k or using the initial condition (2.5).

In the **second step (STEP 2)** (indexed by superscript (2)), the transport equation (20) is solved using the NumDwarf library (with $n^{(2)} = 1$) setting the unknown vector $Z^{(2)}$ to represent the primary unknown variable as $Z^{(2)} = (X_n)$ and the coefficients in (35) are assigned as follows:

Symbol	Assignment	Meaning
N	$\phi S_g \rho_g$	damping matrix
u	$\rho_g u_g$	convection
m	1	mobility of the flux v_i
D	$\rho_g D_{ng}$	diffusion tensor
w_i	0	external forces / source term
a_i	0	conservative flux convection
r_i	0	reaction term
f_i	$(1 - X_n) R_{ng}$	source term

Again, all coefficients in the previous listing are evaluated on the previous time level t_k or using the initial conditions (23-26). The boundary conditions (27-34) are also included in the implementation using the NumDwarf library.

In both local steps STEP 1 and STEP 2, the MHFEM implementation in the NumDwarf library requires to solve many small local systems of linear equations (per element) and one large system of linear equations with a sparse, positive definite matrix whose size is given by the total number of sides in the mesh multiplied by the number of equations. The size of the local system per element K is the number of sides of the element and the size of the global system is given by the total number of sides in the mesh multiplied by the number of equations considered [c.f. Fučík, 2014]. The solution of the local and global systems is done by using the LAPACK [Anderson, 1999] and UMFPACK [Davis, 2005] library, respectively.

4. Exposed Pool Scenario Problem Description

We use the computational model described in the previous section to model an *exposed pool scenario* described in detail in [Petri *et al.* 2013]. In this scenario, a process of a complete volatilization of an entrapped TCE pool is investigated under four different flow regimes of the gas phase (denoted as FR1, FR2, FR3, and FR4, see Table 1). The computational domain, shown in Figure 1, represents a 2D longitudinal slice of the 3D experimental tank of dimensions 28 cm

x 14 cm x 2.54 cm. Three different sands were used in the packing of the experimental tank and their properties are given in Table 1. Initially, the pressures p_w and p_g are chosen such that the water distribution corresponds to the observed water table in the experiment:

$$p_w = p_{atm} - (y + 0.093)\rho_w g, \quad p_g = p_{atm} - y\rho_g g, \quad (37)$$

where p_{atm} denotes the atmospheric (referential) pressure. The initial TCE source saturation S_n^{ini} is assumed to be uniformly distributed in the source zone (see Figure 1) and is computed from the injected TCE mass m_{TCE}^{ini} [kg] given in Table 1 for each of the four flow regimes as

$$S_n^{ini} = \frac{m_{TCE}^{ini}}{\rho_n V_{source} \phi}, \quad (38)$$

where V_{source} [m^3] is the volume of the source zone. The initial TCE vapor content in the gas phase is assumed to be zero throughout the computational domain. The boundary conditions that are consistent with the experimental tank setup are displayed in Figure 1. The inlet air is 100% humidified to ensure that no evaporation from the pore water can occur during the experiment and thus the humidified air and the TCE vapor are the only gas phase components considered.

At $t = 0$, the entrapped TCE starts to volatilize into the flowing air until the entire TCE content is depleted from the source zone. The objective of the computational study is to simulate the non-stationary mass transfer and transport processes and to test a hypothesis whether the Sherwood model described by Eq. (22) can be used to describe the volatilization. The computational procedure involves fitting three empirical parameters β , γ , and δ in Eq. (22) and also estimation of the dispersivity parameters a_L , a_T , or a_D . In order to reduce the number of unknown parameters in the fitting procedure, we consider isotropic dispersion described by the dispersivity coefficient a_D in (19) only, i.e., we use D_{ng}^{iso} in (17) instead of D_{ng} in all simulations.

Table 1. Properties of the sands and fluids used in the simulation [Smits 2010].

Sand properties		Sand		
		Gravel	#20/#30	Sand #70
Porosity	ϕ [-]	0.33	0.33	0.418
Intrinsic permeability	K [$10^{-10} m^2$]	27.8	2.42	0.144
van Genuchten parameter	α [$10^{-4} Pa^{-1}$]	30.67	7.152	2.138
van Genuchten parameter	n [-]	6.47	15.68	11.53
van Genuchten parameter	$m = 1 - \frac{1}{n}$	0.85	0.94	0.91
Residual water saturation	S_{wr} [-]	0.067	0.082	0.079
Median distribution diameter	d_{50} [mm]	n/a	0.75	n/a
Mean grain size of sand	d_m [mm]	n/a	0.50	n/a

Fluid properties		Water	Air	TCE	
Density	$\rho [kg\ m^{-3}]$	1000	1.2047	1460	
Dynamic viscosity	$\mu [\cdot 10^{-5}\ Pa\ s]$	100	1.82	90	
Molar weight	$M [kg\ mol^{-1}]$	0.018	0.02897	0.1314	
Simulations' parameters		FR 1	FR 2	FR 3	FR 4
Temperature	$T [K]$	24.72	22.35	25.13	25.25
Reference pressure	$p_{atm} [kPa]$	82.94	82.09	82.49	87.10
Inlet air flux	$q_{air} [ml\ min^{-1}]$	12.55	1.188	6.302	59.74
Injected TCE mass	$m_{TCE}^{ini} [g]$	2.941	2.935	2.909	2.916
Saturated TCE concentration	$c_n^{sat} [kg\ m^{-3}]$	0.514	0.463	0.523	0.526

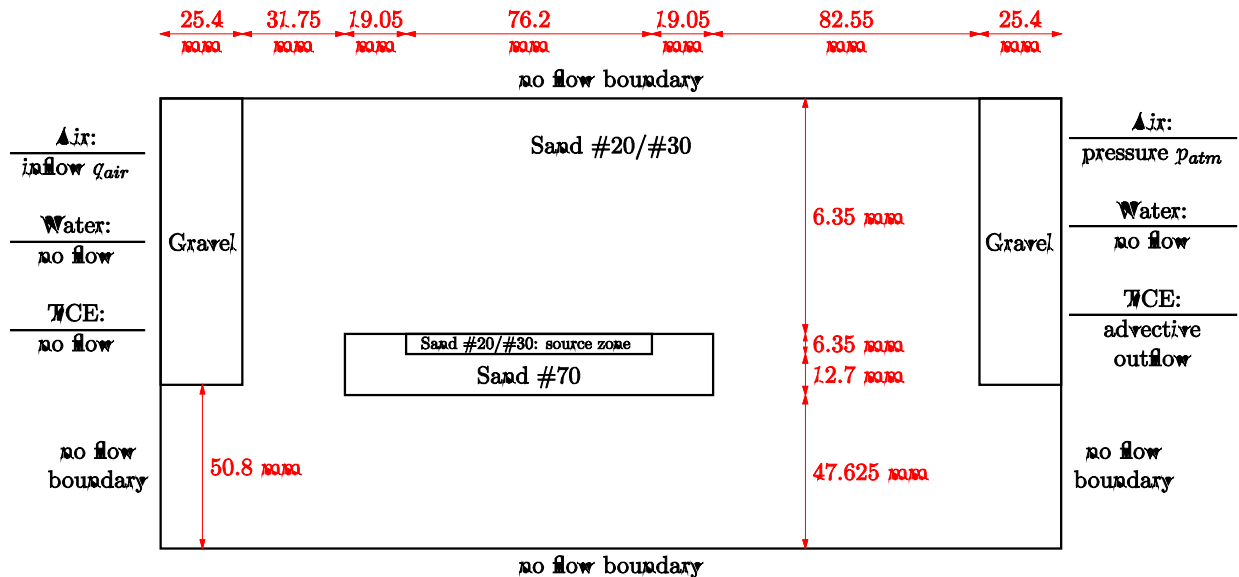


Figure 1. Computational domain description.

5. Computational Study

The computational study for determining the unknown fitting parameters contains two separate procedures. In the first approach (see Section 5.1), we include the isotropic dispersion coefficient a_D among the parameters to be fitted. In the other procedure (see Section 5.2), we use the common literature value [Fetter, 1993] for dispersivity equal to $a_D = 0.1 \times L$, where $L[m]$ is the length of the model domain.

The objective of each fitting procedure is to find a set of parameters for which all *effluent concentration curves* under four different flow regimes (FR1, FR2, FR3, and FR4) match the measured effluent concentration during the laboratory experiments. The simulated effluent

concentration curve is compared to the measured concentration curve and their difference is measured in the L_2 norm as

$$\eta_i = \|c_{n,FRi} - c_{n,FRi}^{ex}\|_2 = \left(\int_0^{T_{FRi}} |c_{n,FRi} - c_{n,FRi}^{ex}|^2 dt \right)^{\frac{1}{2}} \quad (39)$$

for $i = 1, 2, 3, 4$, where T_{FRi} [s] is the final time of the experiment/simulation when almost all TCE content is volatilized and driven out of the domain. In order to find the best fitting parameters to match the experimental data, we seek the minimum of the objective function η defined as

$$\eta = \left(\sum_{i=1}^4 \eta_i^2 \right)^{\frac{1}{2}} \quad (40)$$

through the set of all computed concentration curves.

All numerical simulations were computed on a single PC equipped with Intel i7 processor with 4 double threaded cores at 2.80 GHz and 8 GB RAM and running Linux Debian 7 (64 bit architecture). Every computation ran on a single CPU core. In order to speed up the computation, a comparison of the simulated concentration against the experimentally measured data was implemented directly in the C++ code to terminate the simulation when the difference between the simulated and measured data was beyond a threshold of 20%.

5.1. Four Fitting Parameters

In the first procedure, we seek the minimum of the objective function η as a function of four fitting parameters β , γ , δ , and a_D . The fitting procedure was done in the following steps:

1. **Coarse mesh run.**

The first step in the fitting procedure was done on a very coarse mesh (Mesh 1: 284 elements) and a total of 20827 simulations were computed. The minimum of the objective function was estimated for the range of parameters given in the first row of Table 3.

2. **Finer mesh run.**

Then, the fitting procedure was redone on a finer mesh (Mesh 2: 3517 elements) and a total of 10880 simulations were obtained. Based on the results from the previous step, we looked for the minimum of the objective function in a narrower set of parameters and the best fit was obtained for the range of parameters given in the second row of Table 3.

3. **Fine mesh run.**

To verify convergence of the numerical scheme, we computed the solution on a fine mesh (Mesh 3: 14068 elements) and compared the concentration and mass depletion profiles to those obtained in the previous two steps for the best fitted parameters found in the second step. This comparison is shown in Figure 2 where the simulated concentration and mass depletion profiles are compared to the experimentally measured data computed on three different meshes. Almost no difference between the plots in rows in Figure 2

indicates that the size of the mesh does not influence the simulated temporal profiles and thus the numerical solution as well as the whole fitting procedure is sufficiently accurate in solving the system of governing equations.

As a result of the four fitting parameters procedure, we found that the isotropic dispersivity coefficient a_D should be larger than common values reported in the literature [Fetter, 1993] and thus indicating that the estimated value of dispersivity coefficient may be unrealistic.

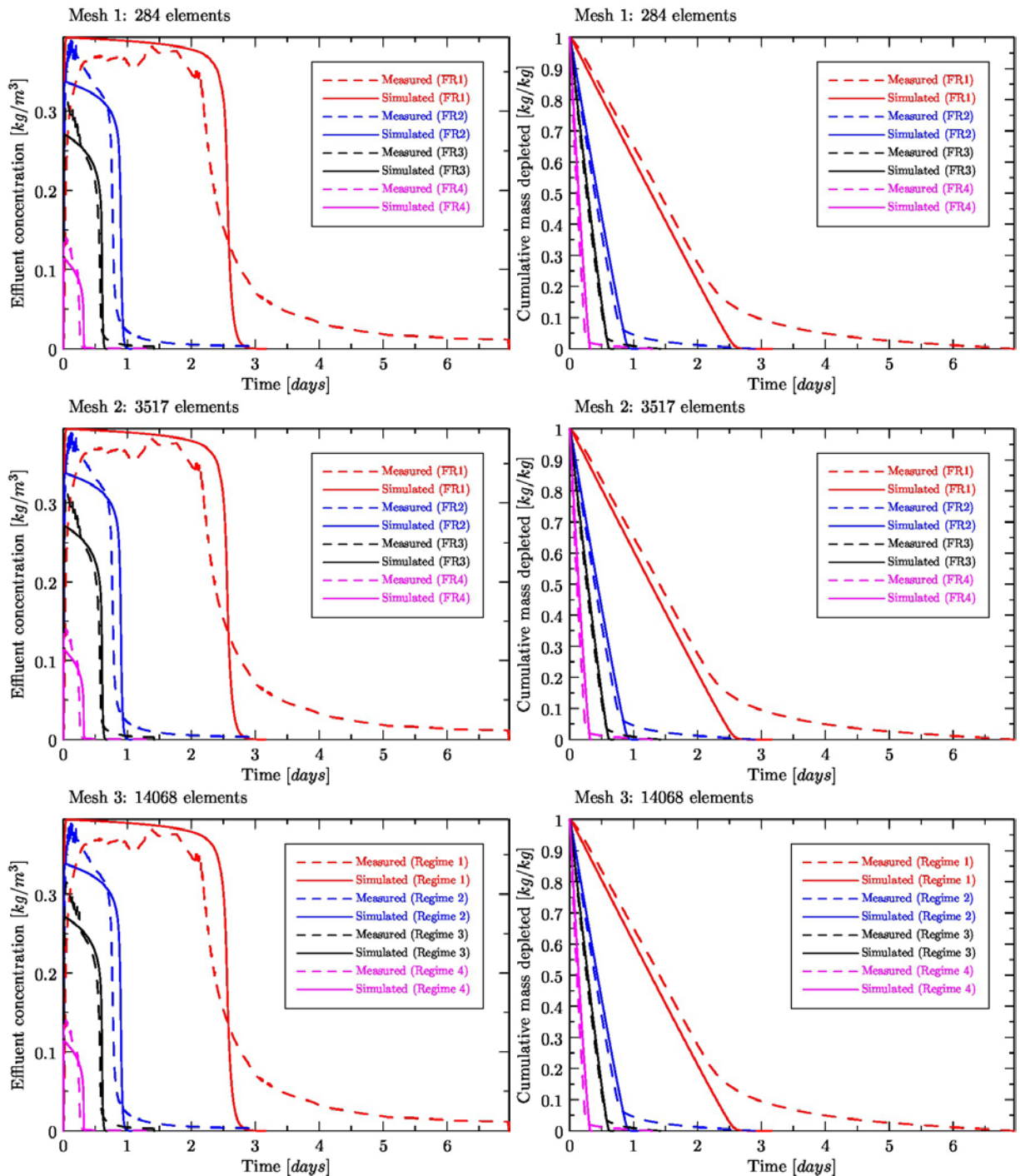


Figure 2: TCE concentration (left column) and cummulative TCE content depletion (right column) temporal profiles compared to laboratory measured data (dotted lines) for the best fitted parameters during the four fitting parameters procedure (Section 5.1) given in the second row in Table 2.

5.2. Three Fitting Parameters

In order to avoid unrealistic dispersivity values obtained in the previous fitting procedure, we set the dispersivity parameter ad to literature values [Fetter, 1993] $a_d = 0.1 \times L$, where $L = 28\text{ cm}$ in this study. The fitting procedure was done using the similar steps as in Section 5.1:

1. **Coarse mesh run.**

The first computational run was done on the coarse mesh (284 elements) and a total of 6000 simulations were computed. The estimated range of parameters where the minimum of the objective function lies in the third row of Table 3.

2. **Finer mesh run.**

The second computational run was done on the finer mesh (3517 elements) and a total of 3.000 simulations were computed using a narrower range for the fitting parameters based on the results from the previous step. The best fitted parameters are shown in the fourth row of Table 3.

3. **Fine mesh run.**

The convergence is verified using the numerical solution computed on the fine mesh (14068 elements) and shown in Figure 3 where the simulated concentration and mass depletion profiles are compared to the experimentally measured data.

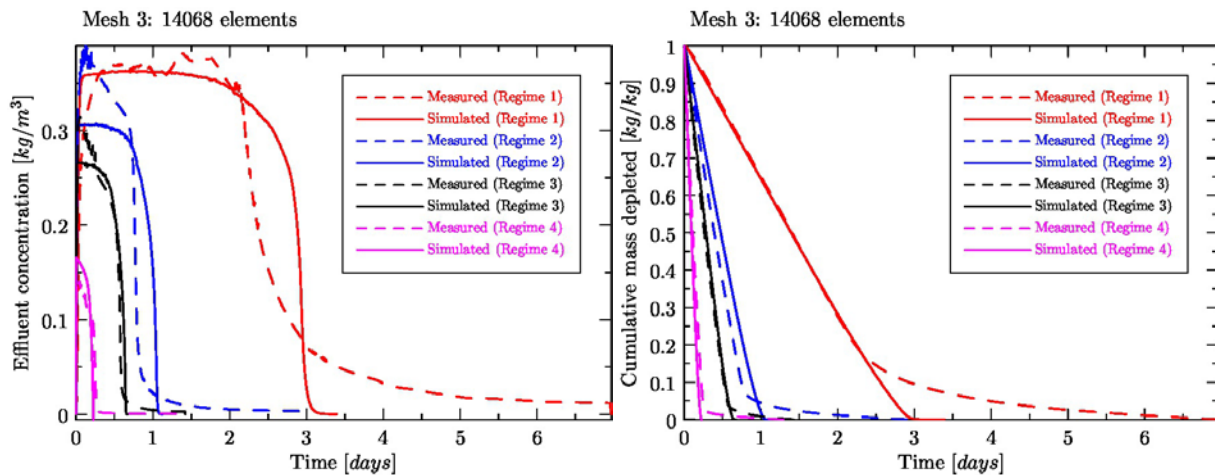


Figure 3: TCE concentration (left column) and cummulative TCE content depletion (right column) temporal profiles compared to laboratory measured data (dotted lines) for the best fitted parameters during the three fitting parameters procedure (Section 5.2) given in the fourth row in Table 2.

Table 2. Results of the fitting procedures described in Section 5.1 and 5.2. The fitted values are supplied with an estimated range of validity and the best fitted values (used in Figure 2 and Figure 3) are typed in bold.

Fitting Procedure Run	Step	a_d [cm]	β [10 ⁻²]	γ [10 ⁻⁴]	δ [10 ⁻²]
Four fitting parameters	Mesh 1	40 (\pm 10)	30 (\pm 10)	15 (\pm 5)	0 (\pm 10)

(Section 5.1)	Mesh 2	45 (± 5)	20 (± 5)	11 (± 2)	5 (± 5)
Three fitting parameters	Mesh 1	2.8	35 (± 10)	20 (± 5)	0 (± 10)
(Section 5.2)	Mesh 2	2.8	25 (± 5)	25 (± 2.5)	0 (± 5)

The second fitting procedure shows that for the dispersivity coefficient a_d given by the literature values, the fitted coefficients does not differ much from those obtained using the four fitting procedure (compare Figure 2 and Figure 3 and second and fourth row in Table 2). Therefore, the Gilliland-Sherwood model for the mass transfer and the transport model using the ADDE approach (17) can be reliably used to model complete volatilization of TCE. Moreover, a very low (almost zero) value of the Péclet exponent beta indicates that the mass transfer coefficient (Sherwood number) does not depend on the velocity of the flowing air. On the other hand, a larger value of the dispersivity coefficient may be necessary to correctly model the dynamics of the volatilization process observe during the laboratory experiments.

5.3. Verification Study

Along with the computational model in C++ using the NumDwarf library, another numerical model has been built using commercial software COMSOL Multiphysics version 3.5a. The model is implemented using the PDE Coefficient Form module with the coefficients described in the previous Section 3.2 (only with different symbols used, c.f. COMSOL Multiphysics version 3.5a documentation). The purpose of the COMSOL model is to verify the implementation of the computational model in C++.

Numerical experiments show that the COMSOL model has much lower computational performance and software stability than the developed C++ code. Therefore, the C++ code is suitable to be used in the fitting procedures that involve a large number of simulations. On the other hand, the COMSOL model allows to directly visualize parameters and solutions on-the-fly within the internal graphical user interface (GUI).

We computed the numerical solutions using the COMSOL model for the parameters given in Table 2 and found that the difference is almost negligible compared to the results obtained using the C++ code. The comparison is shown in Figure 4 on the coarsest mesh. On finer meshes (Mesh 2 and Mesh 3), the temporal profiles overlap completely and, therefore, the C++ implementation solves the system of governing equations reliably.

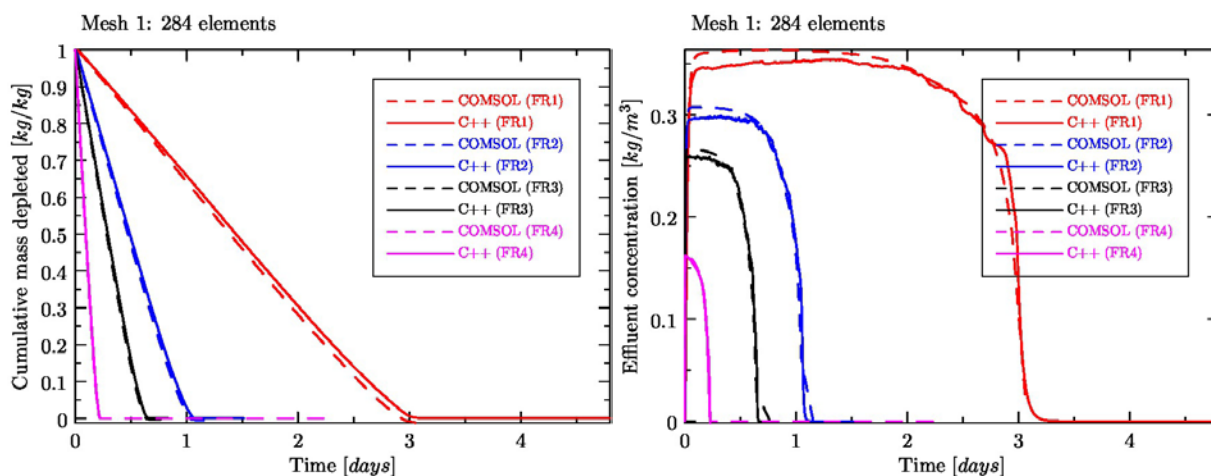


Figure 4: TCE concentration (left column) and cumulative TCE content depletion (right column) temporal profiles obtained using the C++ code using the NumDwarf library (solid line) compared to computational model built using COMSOL Multiphysics software version 3.5a (dashed line).

6. Conclusion

We developed a computational model that allows for solving mass transfer and mass transport processes within the framework of unsteady unsaturated flow in the porous medium. The computational model was implemented in the C++ programming language using the NumDwarf scientific library. We verified the numerical convergence of the numerical scheme using a comparison of numerical solutions on refined meshes and we demonstrated the correctness of the implementation using another computational model built in COMSOL Multiphysics.

We used the C++ implementation in an extensive computational study to find best fitted parameters of the volatilization and transport process in order to match laboratory measured data. As a result, we confirmed the hypothesis that the non-equilibrium Gilliland-Sherwood model can be used in the modeling of complete TCE volatilization in porous medium.

7. Acknowledgement

The author thank the Strategic Environmental Research and Development Program Grant ER-1687: Vapor Intrusion from Entrapped NAPL Sources and Groundwater Plumes: Process Understanding and Improved Modeling Tools for Pathway Assessment and Numerical Methods for Multiphase Flow, the project P105/11/1507: Development of computer models of CO₂ sequestration in the subsurface of the Czech Science Foundation, Transport in Subsurface Environmental Applications KONTAKT ME10009, Czech Ministry of Education, Youth and Sports for providing funding for this research.

8. References

- Anderson, E (1999) ed. LAPACK Users' guide. Vol. 9. Siam, 1999.
- Bear, J. (1988) Dynamics of fluids in porous media. Dover publications, 1988.
- Davis, T. A. (2005) Umfpack version 4.4 user guide. Department of Computer and Information Science and Engineering, University of Florida, Gainesville, FL.
- Fetter, C. W. (1993) *Contaminant Hydrogeology*: MacMillan. 458p.
- Fučík, R., and J. Mikyška (2011). "Discontinuous Galerkin and Mixed-Hybrid Finite Element Approach to Two-Phase Flow in Heterogeneous Porous Media with Different Capillary Pressures." *Procedia Computer Science*, 4, 908-917.
- Fučík R. and J. Mikyška (2012) Mixed-hybrid finite element method for modelling two-phase flow in porous media. *Journal of Math-for-Industry* Vol. 3 (2012) 9--19.
- Fučík, R. (2014). A general mixed-hybrid finite element numerical solver NumDwarf. *in preparation*.
- van Genuchten, M. T.(1980) A Closed-Form Equation for Predicting the Hydraulic Conductivity of Unsaturated Soils. *Soil Science Society of America Journal*, 44:892--898, 1980.
- Hoteit, H; Firoozabadi, A. Numerical Modeling of Two-Phase Flow in Heterogeneous Permeable Media with Different Capillarity Pressures, *Advances in Water Resources* 31 (2008) 56–73.
- Millington, R. J. and J. P. Quirk (1961). "Permeability of porous solids." *Trans. Faraday. Soc.* **57**: 1200-1207.
- Mualem, Y.(1975) A New Model for Predicting the Hydraulic Conductivity of Unsaturated Porous Media. *Water Resources Research*, 12(3), 1975.
- Petri, B., R. Fučík, T. H. Illangasekare, K. M. Smits, J. A. Christ, T. Sakaki, and C. C. Sauck (2013) Effect of Nonaqueous Phase Liquid Source Morphology on mass transfer in the vadose zone: Experimental and Modeling Study, submitted to *Groundwater Journal*.
- Saba, T., T.H. Illangasekare, and J. Ewing. (2001) Investigation of surfactant-enhanced dissolution of entrapped nonaqueous phase liquid chemicals in a two-dimensional groundwater flow field. *Journal of contaminant hydrology*, 51(1-2):63--82, 2001.
- Saenton, S. and T.H. Illangasekare, (2007) Upscaling of mass transfer rate coefficient for the numerical simulation of dense nonaqueous phase liquid dissolution in heterogeneous aquifers. *Water resources research*, 43(2):W02428, 2007.

- Yoon, H., M. Oostrom, T.W. Wietsma, C.J. Werth, and A.J. Valocchi. (2009) Numerical and experimental investigation of DNAPL removal mechanisms in a layered porous medium by means of soil vapor extraction. *Journal of contaminant hydrology*, 109(1):1--13, 2009.
- Yoon, H., J. H. Kim, H. M. Liljestrand, and J Khim. (2002) Effect of water content on transient nonequilibrium NAPL-gas mass transfer during soil vapor extraction *Journal of contaminant hydrology*, Elsevier, 54(1):1--18, 2002.

APPENDIX B: LIST OF SCIENTIFIC/TECHNICAL PUBLICATIONS

1. Articles in peer-reviewed journals (specify whether in print, accepted for publication, or submitted for publication).

Sakaki, T., A. Limsuwat, and T. H. Illangasekare, 2011. A Simple Method for Calibrating Dielectric Soil Moisture Sensors: Laboratory Validation in Sands, *Vadose Zone Journal*, May 2011, v. 10, p. 526-531
(<http://vzj.geoscienceworld.org/content/10/2/526.abstract?sid=c99ea641-946c-4793-a635-cdbf59383d9d>)

Sakaki, T., A. Limsuwat, A. Cihan, C. C. Frippiat, and T. H. Illangasekare, 2012. Water retention in a coarse pocket under wetting and drainage, *Vadose Zone Journal*, 11:223-230, doi:10.2136/vzj2011.0028.

Sakaki, T., P. E. Schulte, A. Cihan, J. A. Christ, and T. H. Illangasekare, 2013. Airflow pathway development as affected by soil moisture variability in heterogeneous soils, *Vadose Zone Journal*, doi:10.2136/vzj2011.0118.

Petri, B. G., R. Fučík, T. H. Illangasekare, K. M. Smits, J. A. Christ, T. Sakaki, C. C. Sauck, 2014. Effect of NAPL source morphology on mass transfer in the vadose zone, *Groundwater*, accepted for publication and in print.

Petri, B. G., R. Fučík, T. H. Illangasekare, K. M. Smits, T. Sakaki, 2014. The dynamic response of vapor intrusion to rainfall infiltration: experimental and modeling investigation. To be submitted to *Water Resources Research*, August 2014.

Petri, B. G., R. Fučík, T. H. Illangasekare, K. M. Smits, T. Sakaki, 2014. Effect of water table fluctuation on vapor plume transport and vapor intrusion: experiments and models. To be submitted to *Vadose Zone Journal*, September 2014.

2. Technical reports (specify whether in print, accepted for publication, or submitted for publication).

None

3. Conference or symposium proceedings scientifically recognized and referenced (other than abstracts).

C. Sauck, T. Illangasekare, T. Sakaki, B. Petri, J. Christ, 2011. Validation of a Conceptual Model for Partitioning of Volatile Chemicals from Dissolved Groundwater Plumes under Fluctuating Water Table Conditions, MODFLOW and More.

4. Conference or symposium abstracts

2009

Sakaki, T., A. Limsuwat, and T.H. Illangasekare, 2009. Role of air on local water retention behavior in the shallow heterogeneous vadose zone, American Geophysical Union, Fall 2009 meeting.

Illangasekare, T. H., T. Sakaki, B. Petri, and A. Limsuwat, 2009. Vapor intrusion from entrapped NAPL sources and groundwater plumes: Process understanding and improved modeling tools for pathway assessment, The SERDP/ESTCP Partners Symposium, December 1-3, 2009, Washington DC.

Illangasekare, T.H, 2009. Three Decades of Study and Experience: Understanding the Behavior of Non-aqueous Phase Liquids in Heterogeneous Porous Media- What have we learned to solve real-world problems?, Chinese Environmental Academy, Beijing, China, Sept. 2009.

Illangasekare, T.H, 2009. Three Decades of Study and Experience: Understanding the Behavior of Non-aqueous Phase Liquids in Heterogeneous Porous Media- What have we learned to solve real-world problems?, Technical University of Catalonia, Barcelona, Spain, Special Workshop, PROGRAMA JORNADA CONTAMINACIÓ D'AQUÍFERS PER ORGANOCORATS. June 2009.

2010

Christ, J. A., T. H. Illangasekare, T. Sakaki, B. Petri, and C. Sauck (2010), Vapor intrusion from entrapped NAPL sources and groundwater plumes : Process understanding and improved modeling tools for pathway assessment, Technical Exchange Meeting, August 16, 2010, Salt Lake City, Utah

Petri, B., T. H. Illangasekare, T. Sakaki, C. Sauck, and J. Christ (2010), Evaluation of volatilization from NAPL sources under low velocities with implications for the vapor intrusion pathway, Proceedings of the 30th Annual American Geophysical Union Hydrology Days, March 22-24, 2010, ed. J. A. Ramirez, Colorado State University, Fort Collins, CO.

Sauck, C., T. H. Illangasekare, T. Sakaki, B. Petri, and J. Christ (2010), Understanding TCE vapor generation from dissolved groundwater plumes under fluctuating water table conditions, Proceedings of the 30th Annual American Geophysical Union Hydrology Days, March 22-24, 2010, ed. J. A. Ramirez, Colorado State University, Fort Collins, CO.

2011

Petri, B; Sauck, C; Illangasekare, T; Sakaki, T; Christ, J. (2011) "Effects of Vadose Zone Soil Moisture Dynamics on the Mass-Transfer and Transport of Volatile Compounds: Investigations Using Physical Models at Multiple Scales," American Geophysical Union 2011 Fall Meeting, San Francisco, CA, December 5-9, 2011.

Petri, B; Illangasekare, T; Sakaki, T; Christ, J; Sauck, C. (2011) "Effect of Source Conditions on Mass-Transfer from Non-aqueous Phase Liquids to Soil Gas in the Vadose Zone" Fall 2011 National Meeting and Expo, American Chemical Society, Denver, CO, August 28 - September 1, 2011.

Petri, B; Illangasekare, T; Sakaki, T; Christ, J; Sauck, C. (2011) "Experimental and Numerical Investigation of Mass-Transfer Rate for Prediction of Vapor Generation from NAPLs for the Evaluation of the Vapor-to-Indoor Air Exposure Pathway," MODFLOW and More 2011, Colorado School of Mines, Golden Colorado, June 5-8, 2011.

2012

Illangasekare, T.H. 2012. "Multi-scale Laboratory Experimentation for Process Understanding and Up-scaling for Field Problem Solution, Lawrence Berkeley Laboratory, August 2012.

Illangasekare, T.H. 2012. "Multi-scale Laboratory Experimentation for Process Understanding and Up-scaling for Field Problem Solution, Jülich, Bonn, Germany, May 2012.

Petri, B., C. Sauck, T. H. Illangasekare, T. Sakaki, J. Christ, 2012. Experimental investigation of vadose zone transport of volatile organic compounds under dynamic hydrologic conditions with applications to vapor intrusion, AGU Hydrology Days 2012, Colorado State University, Ft. Collins, CO, March 2012.

Illangasekare, T.H., Multi-scale Laboratory Experimentation for Process Understanding and Up-scaling for Field Problem Solution, Plenary Talk, 4th International Conference on Porous Media & Annual Meeting of the International Society for Porous Media. May 14-16, 2012, Purdue University, West Lafayette, Indiana, USA.

Illangasekare, T.H., 2012. "Let us keep observing and play in sand boxes ", Distinguished Lecture , Global Climate Energy Program, Stanford University, May 2012.

Illangasekare, T.H., 2012. "Let us keep observing and play in sand boxes ", 2012 Darcy Medal Lecture, General Assembly of the European Geological Union, Vienna, Austria, April 2012.

2013

Illangasekare, T.H. and B. Petri, 2013, Vapor Intrusion from Entrapped NAPL Sources and Groundwater Plumes- Factors Contributing to Uncertainty, Groundwater

Quality 2013 Conference (GQ13) • April 21-26, 2013 , Gainesville, Florida • J. Wayne Reitz Union – University of Florida (invited key note)

Illangasekare, T.H. and B. Petri, 2013, Climate and Hydrogeologic Factors Contributing to Variability of Observed Vapor Concentrations in Buildings due to Vapor Intrusion: Experimental and Modeling Investigation, REMTEC Remediation Technology Summit 2013, The future of Remediation Technology, Broomfield, Colorado, March 4-6, 2013 (invited key note).

Illangasekare, T.H., 2013. Multi-scale Laboratory Experimentation for Process Understanding and Up-scaling for Field Problem Solution, International Symposium on Patterns in Soil-Vegetation-Atmospheric-Systems: Monitoring, Modeling & Data Assimilation, University of Bonn, Germany, March 11-14, 2013 (invited talk).

5. Text books or book chapters.

Illangasekare, T.H., 2012. Contributed to the NRC Report “Alternatives for Managing the Nation’s Complex Contaminated Groundwater Sites”, National Academy Press.

Illangasekare, T.H., K. M. Smits, R. Fučík, H. Davarzani, 2014. From pore to the Field: Upscaling challenges and opportunities in hydrogeological and land-atmospheric Systems, Book Chapter in Preparation published by World Scientific, London, UK.

Thesis and Dissertations:

Saucks. C., 2013. The Effects of Water Table Fluctuation On Vapor Generation From Dissolved Groundwater Plumes, MS Degree Independent Study Report, Department of Civil and Environmental Engineering, Colorado School of Mines, pp 82. February 2012.

Shannon, L., 2013. Evaluating a novel approach for locating preferential vapor transport pathways in the vadose zone – Coupling soft data from Electrical Resistivity Tomography to hard analytic data, MS Thesis, Department of Civil and Environmental Engineering, Colorado School of Mines, pp 124. March 2013.

Petri, B., 2014 Fundamental Study of Mechanisms of Dynamics of Vapor Generation and Intrusion into Subsurface Structures, PhD Dissertation in preparation to be completed in August 2014.